Max-Planck-Institut für Meteorologie

EXAMENSARBEIT Nr. 57

2-meter air temperature [°C]

ECHAM4/IMPL - ECHAM4 (JJA)

ON THE ROLE OF THE LAND SURFACE REPRESENTATION AND THE NUMERICAL COUPLING TO THE ATMOSPHERE FOR THE SIMULATED CLIMATE OF THE GLOBAL ECHAM4 MODEL

von

Jan-Peter Schulz

Dissertation zur Erlangung des Doktorgrades

Autor:

Jan-Peter Schulz   Max-Planck-Institut
                                    für Meteorologie

MAX-PLANCK-INSTITUT
FÜR METEOROLOGIE
BUNDESSTRASSE 55
D - 20146 HAMBURG
GERMANY

Tel.:   +49-(0)40-4 11 73-0
Telefax: +49-(0)40-4 11 73-298
E-Mail: <name> @ dkrz.de

On the Role of the Land Surface Representation
and the Numerical Coupling to the Atmosphere for
the Simulated Climate of the Global ECHAM4 Model

vorgelegt von

Jan–Peter Schulz

aus Kiel

Hamburg, 1998

Als Dissertation angenommen vom Fachbereich Geowissenschaften der Universität Hamburg auf Grund der Gutachten

von   Prof. Dr. Lennart Bengtsson
und   Dr. Erich Roeckner

Hamburg, den 29. Juni 1998

Prof. Dr. G. Miehlich

Dekan des Fachbereichs Geowissenschaften

Contents

Abstract

The continental surfaces represent an important component of the Earth's climate system. Meteorological models for climate simulations or numerical weather prediction therefore require a realistic description of the land surface processes. The degree of complexity needed for these land surface schemes is not yet completely determined. Another aspect of the meteorological models is the numerical realization of the coupling between land surface and atmosphere. This thesis investigates the sensitivity of the simulated climate to the parameterization of land surface processes compared to the effect of different numerical coupling techniques between land surface and atmosphere. For this reason, a detailed evaluation of the two land surface schemes ECHAM and SECHIBA in a hierarchy of model set-ups, from off-line through one-dimensional to global three-dimensional, is conducted. In the off-line experiments, ECHAM shows deficiencies in modelling the diurnal variations of surface temperature and ground heat flux. This is due to the conceptual inconsistency in that the top soil layer temperature is both used as part of the soil temperature finite difference scheme and also as surface value for computing the atmospheric surface energy fluxes. This is improved in SECHIBA by an extrapolation of heat capacity and ground heat flux toward the surface.

The standard ECHAM4 climate model utilizes a semi-implicit coupling technique between land surface and atmosphere in a way in which energy at the land surface–atmosphere interface is not conserved. This is a major deficiency. Two new model versions were developed as part of this thesis: ECHAM4/IMPL and ECHAM4/SECHIBA. They incorporate an implicit coupling technique which conserves energy. ECHAM4 and ECHAM4/IMPL are identical with respect to all physical parameterizations they apply; the only difference is the coupling. In ECHAM4/SECHIBA the ECHAM land surface scheme was replaced by SECHIBA. The intercomparison of one-dimensional versions of these three models shows that the energy residual term in ECHAM4, which is part of the semi-implicit coupling and represents an error in the surface/atmosphere energy balance, is not negligibly small. Rather, it is of the order of the physical fluxes and therefore serves as an artificial (numerical) sink or source of energy at the surface, significantly altering the surface energy balance. Biases of more than $1300~\text{W/m}^2$ are found due to the coupling technique. These are avoided in ECHAM4/IMPL, which results in a more pronounced diurnal cycle of surface temperature and generally higher temperature maxima during a warming phase.

In a global-scale intercomparison of the three models a significant impact of the altered coupling technique and land surface scheme on most surface variables and atmospheric surface fields is found. The surface air temperature over large continental areas in the Northern Hemisphere in summer is higher by up to 3–5°C in the two implicit models than in ECHAM4. For ECHAM4/IMPL this is attributed to the closure of the surface energy balance. This allows to use energy amounts of regionally more than $40~\text{W/m}^2$ in the seasonal mean, which are lost in ECHAM4, for physical processes, e. g. for heating the land surface and lower atmosphere. In ECHAM4/SECHIBA a further increased surface air temperature of up to 3°C is due to a different snow parameterization that allows an earlier snow melt. This is in good agreement with snow observations. Due to the changed temperature structure a considerably improved Asian summer monsoon circulation with respect to stream patterns, wind velocities and associated precipitation distributions is simulated by the implicit models. Furthermore, the computed evaporation in SECHIBA is more realistic, compared to measurements at some European sites, as consequence of a more sophisticated representation of vegetation.

4

Introduction

The continental surfaces, including vegetation cover, represent an important component of the Earth's climate system. On the one hand, they are the habitat of man, which makes it interesting to understand the governing processes and living conditions at the land surface and how they may evolve in the future. On the other hand, from the point of view of atmospheric sciences, the land surface and biosphere interact with the lower atmosphere, and they have a significant impact on near-surface meteorological and climatological phenomena.

Everyone will probably have noticed at some time certain meteorological processes, such as the heating of near-surface air during daytime, the development of cumulus clouds by the end of a summer day or the occurrence of a land-sea breeze in coastal regions and the change of its wind direction between night and day. Another phenomenon, occurring on a longer time scale, may be the wilting of plants after a long period without rain. All of these processes are consequences of a complex system of interactions between the surface and lower atmosphere. When the soil receives radiation, its temperature is generally altered and the energy is partially returned back to the atmosphere as sensible heat flux or used for evaporation of water, thus heating and humidifying the overlying air. Hence, the stratification of the lower atmosphere generally becomes more unstable, stimulating enhanced turbulent vertical mixing. Higher surface temperatures may also cause convection. Rising of moist air can lead to formation of clouds, and finally precipitation. A modified cloud cover will in turn affect the surface radiation budget. Therefore, it can be concluded, that the continental surface and the overlying atmosphere clearly interact. This has primarily an effect on the lower atmospheric layers, but the general circulation will distribute the energy in the whole global atmosphere.

Consequently, to more substantially assess the role of the land surface in the entire climate system, the question of interest is: How sensitive is the atmosphere or the climate of the Earth in general to land surface processes? In order to address this question, experiments with atmospheric *General Circulation Models (GCMs)* have been conducted which revealed a sensitivity of climate to various land surface characteristics (see the review by Mintz 1984). In these sensitivity experiments one or a few parameter values or a component of the land surface parameterization is (drastically) changed to investigate the impact on the atmosphere, including possible feedback effects. For instance, Shukla and Mintz (1982) found a large reduction of the precipitation over most continents when the land surface evapotranspiration is changed from the rate, which occurs in the case of a permanently moist soil that is completely covered by vegetation, to zero. The land surface temperature was drastically increased due to both the loss of evaporative cooling and an enhanced heating by solar radiation, the latter being a consequence of a reduced cloud cover. Therefore, they stated that "the surface vegetation, which produces the evapotranspiration, is an important factor in

the Earth's climate." Charney et al. (1977) showed that increasing the albedo in the Sahel region would lead to a significantly changed large scale circulation and a reduced rainfall. Sud et al. (1988) found that also changing the land surface roughness has a large influence on the distribution of precipitation. Furthermore, Milly and Dunne (1994) pointed out that the global water cycle of the land-ocean-atmosphere system and the atmospheric circulation are sensitive to the water-holding capacity of land.

In this context it is interesting to explore the sources of water which precipitates on regions in the interior of the continents. It may be supplied either by advection from the surroundings or by evapotranspiration within the region. The latter mechanism is denoted as recycling of precipitation. Koster et al. (1986) found that its contribution to the total precipitation in continental regions tends to vary substantially with location and season. This result was confirmed by Brubaker et al. (1993) who used analysed observational data for their study. It is an example for a land surface–atmosphere interaction, which may contribute to regional climate variability and may be important for the occurrence and persistence of droughts.

The models used in these early studies often conceptualized the land surface hydrology as a "bucket" (Manabe 1969). Its water level is lowered when evaporation exceeds precipitation and snow melt, and is raised when the inflow is larger. When the water content reaches the maximum value, additional precipitation becomes runoff. The dependence of evapotranspiration on soil moisture is parameterized by a "β-function". It usually allows for potential evaporation when the soil is wet and a reduced evaporation when the water level is low. While this approach provides a reasonable framework for the representation of land surface hydrological processes in GCMs, it obviously comprises shortcomings like the neglect of soil moisture dynamics or a stomatal control of transpiration by vegetation. Therefore, modelers started to develop land surface schemes that include e. g. a representation of vegetation which is physiologically reactive to atmospheric conditions. This is a first step toward a fully interactive coupled biosphere–atmosphere model which is a necessity when, for example, realistic numerical experiments regarding climate change scenarios or impact studies shall be conducted. Two outstanding approaches focusing on the aforementioned aims are the *Biosphere–Atmosphere Transfer Scheme* (*BATS*, Dickinson et al. 1986) and the *Simple Biosphere model* (*SiB*, Sellers et al. 1986). Apart from these models, numerous surface schemes were proposed that adopted specific features from these models or developed different approaches to be used in GCMs for climate simulations or *Numerical Weather Prediction (NWP)* (e. g. Warrilow et al. 1986, Abramopoulos et al. 1988, Noilhan and Planton 1989, Blondin 1991, Xue et al. 1991, Koster and Suarez 1992, Wood et al. 1992, Ducoudré et al. 1993, Verseghy et al. 1993, Viterbo and Beljaars 1995).

With this new generation of GCMs it became possible to study the impact of large scale changes in vegetation characteristics. For instance, evapotranspiration, surface air temperature, cloud formation and precipitation in the tropics and sub-tropics show significant sensitivity to the rooting depth of tropical vegetation, as indicated by Kleidon and Heimann (1998). They stated that there is evidence that most of the state-of-the-art GCMs underestimate the rooting depth of the vegetation, which may lead to large biases, especially in the simulation of the tropical climate system. A series of GCM experiments focused on the impacts of tropical deforestation (e. g. Dickinson and Henderson-Sellers 1988, Lean and Warrilow 1989, Shukla et al. 1990, Polcher and Laval 1994). These simulations agree in terms of predicting a reduced evapotranspiration and an increased surface temperature as consequences of the deforestation. But different results were found for the expected response of precipitation.

Polcher (1995) pointed out that the sensible heat flux may play an important role here, as its increase was found to lead to an enhanced number of convective events.

This large number of surface treatments provokes the call for intercomparison experiments. In particular, two international projects have been dedicated to that aim, which are the project on *Spatial Variability of Land Surface Processes* (*SLAPS*, Dooge et al. 1994, Polcher et al. 1996), which is already completed, and the ongoing *Project for Intercomparison of Land-surface Parameterization Schemes* (*PILPS*, Henderson-Sellers et al. 1993, Chen et al. 1997, Schulz et al. 1998). These projects were designed to systematically intercompare a large number of land surface schemes which are operational in current GCMs or NWP models. The PILPS science plan comprises of comparison and validation of the models, including sensitivity studies, ranging from zero-dimensional off-line simulations up to fully coupled three-dimensional global scale experiments.

In off-line — or stand-alone — simulations the surface schemes are forced by prescribed near-surface atmospheric conditions that were either derived from a GCM simulation or observed. Therefore, the surface schemes do not affect the atmospheric variables, and any feedback effects are excluded. In the intercomparisons the same forcings and corresponding surface parameters were used for all schemes. This procedure allows one to compare the behaviour of the various schemes and to examine the role of specific model characteristics, while excluding effects resulting from feedbacks with the atmosphere.

The analyses of the off-line intercomparisons show that the schemes behave very differently (e. g. Henderson-Sellers et al. 1996). It is even difficult to separate the models into different classes of typical behaviour (cf. Chen et al. 1997). Results like these show that it is very difficult to assess how future climate projections using current GCMs are influenced by their treatment of land surface processes (IPCC 1996). Preliminary results from a study presented by Polcher et al. (1998b), investigating the climate impact of doubling the atmospheric CO_2-concentration using four different GCMs, suggest that the uncertainties in climate change experiments due to land surface processes are comparable to those linked to other processes. The latter may include the treatment of clouds and water vapour or cloud-radiation feedbacks, which represent major uncertainties in current climate models as well.

PILPS just recently started to set up fully coupled global models to continue the intercomparison at the global scale. Therefore, no final results can be reported from this time. Previous studies using GCMs with different land surface codes were presented e. g. by Sato et al. (1989), who investigated the impact of replacing a simple bucket hydrological scheme by the sophisticated SiB model (Sellers et al. 1986), and Stamm et al. (1994), who replaced a bucket scheme by the more complex VIC model (Wood et al. 1992). Large differences were found in the simulated land surface fluxes. The bucket model commonly tends to compute higher evaporation than the more complex schemes, which contributes to a modified hydrological cycle. There are only very few publications in which two different complex land surface schemes implemented in the same atmospheric GCM are compared, with one of them not just being a simple bucket model. Peylin et al. (1997) compared two simulations with the National Center for Atmospheric Research (NCAR, Boulder) GCM coupled either to the BATS (Dickinson et al. 1986) or the SECHIBA (Ducoudré et al. 1993) land surface model, which were both regarded as complex. SECHIBA was originally the operational land surface scheme of the Laboratoire de Météorologie Dynamique (LMD, Paris) GCM. Considerable differences in the simulated climate were found on the regional scale, while on a global scale the effect appeared to be small.

This large number of studies, intercomparing land surface parameterization schemes on different temporal and spatial scales in numerous model set-ups (from off-line to fully coupled three-dimensional), has demonstrated that a great variety of approaches for representing land surface processes in numerical meteorological models currently exists, that lead to considerably different climate simulations. An important question that arises, and which is also a general research topic of this work, is what level of complexity of the land surface representation in GCMs is needed (Garratt 1993)? Very sophisticated models of the detailed processes in e. g. soil hydrology or vegetation may not be consistent with the degree of complexity of the representation of other components in the global climate system and, additionally, may be computationally too expensive. Simpler models with suitable parameterizations may provide comparable accuracy. Having this in mind, two models are compared in this thesis, both incorporating much of the computational simplicity of the bucket model but with a more realistic representation of vegetation (in terms of interception of precipitation or a physiological control of transpiration), and more advanced soil hydrology and surface runoff schemes, respectively.

The global scale GCM sensitivity experiments are very complex with so many degrees of freedom that the results are often difficult to interpret, thus they often remain very general. On the other hand, in off-line simulations feedback effects between surface and atmosphere are excluded which limits the transferability of their findings to the coupled land-atmosphere system. A compromise between these two cases is to use a coupled one-dimensional model of the entire vertical soil-atmosphere column (of a GCM). This will allow the study of surface-atmosphere interactions and feedbacks with a focus on the surface exchange processes, while no large scale atmospheric effects like horizontal advection complicate the interpretation of the results. Such a one-dimensional model will be utilized in this thesis for these reasons.

Another aspect of the meteorological models, beside the physical parameterization of the relevant processes, is the numerical realization of the coupling between land surface and atmosphere and its possible impact on the simulations. Very little attention has been paid to this in the past. Nevertheless, Polcher et al. (1998a) stated that "changes to the numerical framework of the land surface scheme may have a strong impact on the behavior of the scheme." Two commonly used coupling techniques are the implicit and the semi-implicit one. The former determines the prognostic variables at the surface and the lowest atmospheric level and the corresponding surface fluxes consistently at the same level in the time-stepping scheme. It is thus energy conserving. The latter uses the atmospheric and surface variables at different subsequent time levels to compute the surface fluxes. This requires a correction of the flux terms after the surface temperature has also been updated. To avoid an energy imbalance, this correction term needs to be taken into account in the calculations at the subsequent time step. Examples for land surface schemes used in GCMs, which are coupled implicitly to their host models, are SECHIBA or the surface scheme of the UK Meteorological Office (Warrilow et al. 1986). On the other hand, SiB or the surface scheme of the ECHAM4 GCM (Roeckner et al. 1996) are coupled semi-implicitly to their atmospheric hosts. ECHAM4 is the fourth generation of the ECHAM GCM which is a spectral climate model that was developed at the Max-Planck-Institut (MPI) für Meteorologie, Hamburg. Its land surface scheme will be denoted as ECHAM in this thesis. When comparing climate simulations of these GCMs, it is not a priori clear how they are affected by the different treatments of the numerical coupling, but it is reasonable to assume that it has some impact.

Against this background of land surface modelling in GCMs the central objectives of this

thesis are:

1. Select a few land surface schemes of a comparable degree of complexity (with ECHAM being one of them) out of the range of models that participated in the off-line intercomparison presented by Chen et al. (1997) and examine them in much more detail to provide insight in their key features and how these determine the simulated energy and water cycles.

2. Assess the impact of the numerical coupling technique between land surface and atmosphere in a one-dimensional version of the ECHAM4 climate model and compare this to the effect when the land surface scheme is replaced by one of the others selected in 1.

3. Extend the study in 2. to the fully coupled three-dimensional ECHAM4 GCM, with the intention to benefit from the findings in 1. and 2. for the interpretation of the global simulations. Evaluate the sensitivity of the simulated climate to the modifications of the land surface parameterization and the numerical coupling scheme.

Accordingly, the thesis is organized as outlined here: Three land surface schemes are selected from the Chen et al. (1997) off-line intercomparison study, which are ECHAM (Roeckner et al. 1992, 1996), SECHIBA (Ducoudré et al. 1993) and SSiB (*Simplified Simple Biosphere model*, Xue et al. 1991). The latter is a simplified version of SiB (Sellers et al. 1986). Their model characteristics are described in chapter 1.

A detailed evaluation of the three schemes mainly with respect to their simulated energy and moisture budgets and a description of the atmospheric forcing data used is given in chapter 2. The observations are also used for validation purposes of the quantities of the surface energy cycle. Additionally, sensitivity experiments with the ECHAM model are conducted, which investigate the impact of prescribed changes in land surface characteristics on the atmosphere and surface.

To address the issue of the numerical coupling technique between land surface and atmosphere, an implicitly coupled version of the ECHAM4 GCM has been developed as part of this thesis. It can be used for one-dimensional studies and as well for global scale simulations in different spatial resolutions. It is denoted as ECHAM4/IMPL in the thesis. Chapter 3 presents theoretical details of the different coupling techniques and an overview of their impact in the ECHAM4 and ECHAM4/IMPL one-dimensional models. A comprehensive evaluation of the energy residual term is given, that appears as part of the semi-implicit coupling, and how it affects the simulated surface fluxes and soil variables in comparison to the implicit scheme.

As outlined before in the list of central objectives of the thesis, the impact of these numerical aspects shall be compared to the effect when the land surface scheme is replaced by one of the others presented in chapter 2. SECHIBA has been selected for two reasons: Firstly, its thermodynamic treatment of the soil is more similar to that of ECHAM than it is in SSiB, which makes the new model easier to compare to the standard (or reference) one by avoiding too many drastic changes in the model architecture. Additionally, a somewhat peculiar behaviour is found regarding the soil hydrology in SSiB (chapter 2), where the deep soil drainage obviously plays a dominant role which is not yet fully understood. This seemed to indicate that choosing SSiB for the implementation in ECHAM4 would have introduced

more uncertainties making the interpretation of the results more difficult. SECHIBA is also implemented in the ECHAM4 GCM, as part of this thesis, using the implicit coupling technique. Therefore, the set of the three GCMs — ECHAM4, ECHAM4/IMPL and the so-called ECHAM4/SECHIBA — provides a complete ensemble of models to study the impact of the numerical coupling in a GCM and to compare this to the effects induced by a different land surface representation.

The aforementioned correction term, needed in the semi-implicit coupling to avoid an energy imbalance, is not implemented in the standard ECHAM4 GCM. Therefore, ECHAM4/-IMPL represents a clearly improved model in the physical point of view, as it provides a closed energy balance at the land surface. This makes it even more interesting to intercompare the three GCM versions on the global scale. This is done in chapter 4. First a global overview of the differences in the model simulations is given, followed by a number of analyses focusing on the regional impact. Both global and regional investigations include validation with observational data. Attempts are made to attribute identified changes between the simulations to differences in the representation of the various processes in the models.

The overall findings of the thesis are summarized in chapter 5 and recommendations for future investigations are given.

Chapter 1

Theoretical background and model descriptions

The surface energy balance in most meteorological situations is dominated by the total net radiation. Its solar component provides the forcing and the longwave part is usually a sink of energy at the surface. In the absence of water the surface temperature is mainly determined by the balance of these two flux terms. Besides them, the energy balance includes the turbulent fluxes of sensible and latent heat and the ground heat flux. The energy transfer from the surface to the atmosphere results in a generally heterogeneous temperature distribution, which yields spatial pressure gradients that drive the general atmospheric circulation. Thus, the circulation and climate in general are sensitive to changes in the surface energy fluxes, which is well known. Due to the close relations of the terms just mentioned, the surface energy balance is considered in GCMs as the link between atmosphere and land surface, with the surface temperature being the key variable.

The meaning of this quantity varies between different land surface schemes. It may be defined as the temperature of the ground, which is either a "layer" of infinitesimal thickness at the surface–atmosphere interface or the upper layer of a soil temperature finite difference scheme. Alternatively, it may describe the temperature of some level within the canopy. This will not further specified here. The interface between surface and atmosphere may be understood as a "layer" at the surface which is in contact with the atmosphere. Then the surface energy balance equation is given by:

$$C_S \frac{\partial T_S}{\partial t} = R_n + L \cdot E + H + G, \tag{1.1}$$

where T_S is the temperature representing the surface "layer" and C_S is the heat capacity per unit area. R_n is the total surface net radiation, $L \cdot E$ the latent heat flux (L is the latent heat of vaporization or sublimation of water, respectively, and E is the surface moisture flux), H is the sensible heat flux and G the ground heat flux. The net radiation R_n is given by

$$R_n = (1 - \alpha_S)R_{sd} + \epsilon R_{ld} - \epsilon \sigma T_S^4, \tag{1.2}$$

where R_{sd} and R_{ld} are the downward shortwave and longwave radiation, respectively. Here, α_S is the surface albedo, ϵ is the thermal emissivity, and σ is the Stefan–Boltzmann constant.

In the following sections the three land surface schemes ECHAM, SECHIBA and SSIB are described. Figure 1.1 gives a schematic overview of the schemes.

11

a)

			Symbols:
ECHAM	SECHIBA	SSiB	T_i: temperature of i-th soil layer
Heat Diffusion	Heat Diffusion	Force-Restore	T_s: surface temperature
5	7	2	T_{gs}: ground temperature (SSiB)

Symbols:

T_i: temperature of i-th soil layer

T_s: surface temperature

T_{gs}: ground temperature (SSiB)

T_d: deep soil temperature (SSiB)

T_a: air temperature within the canopy air space

T_c: canopy temperature

T_r: air temperature at reference height

Resistances:

r_a: aerodynamic resistance (between canopy air space and reference height (SSiB))

r_b: bulk boundary layer resistance

r_d: aerodynamic resistance between canopy air space and ground

ECHAM — Heat Diffusion — 5

SECHIBA — Heat Diffusion — 7

SSiB — Force-Restore — 2

layers for soil temperature

b)

Symbols:

q_r: Spec. humidity at reference height

q_{sat}: saturation value of q

e_r: vapor pressure at reference height

e_a: vapor pressure within the canopy air space

e_{sat}: saturation value of e

h: relative humidity

W_i: water content of i-th soil layer

Temperature of:

T_s: surface

T_{gs}: ground (SSiB)

T_c: canopy

Resistances:

r_a: aerodynamic

r_b: bulk boundary layer

r_c: bulk stomatal

r_d: aerodynamic

r_g: soil

r_0: architectural

ECHAM — Bucket, Arno

SECHIBA — Bucket, Choisnel

SSiB — Diffusion

Figure 1.1: Schematic representation of a) the soil temperature layers and the resistances for the calculation of sensible heat fluxes and b) the soil moisture layers and the resistances for the calculation of latent heat fluxes in ECHAM, SECHIBA and SSiB.

1.1 ECHAM

In the ECHAM model (Roeckner et al. 1992, 1996), the surface fluxes of momentum, heat and moisture are calculated by means of the classical aerodynamic formulae using the Monin-Obukhov similarity theory (e. g. Stull 1997):

$$F_\text{X} = \rho C_\text{D} |\vec{v}| (X_\text{a} - X_\text{S}), \tag{1.3}$$

where ρ is the density of air, C_D the drag coefficient for momentum (C_m) or the transfer coefficient for heat and humidity (C_h) and $|\vec{v}|$ the absolute value of the horizontal wind speed. The value of X_a may be identified with the atmospheric value of one of the mentioned quantities which are subject to the turbulent exchange, while X_S is its surface value. C_m and C_h are functions of the roughness length, which characterizes the roughness of the surface, and the Richardson number and are calculated by following the scheme as proposed by Louis (1979). For evaluating the moisture flux over land, each grid element is divided into four fractions. These fractions are: snow cover, water in the interception reservoir, vegetation and bare soil. This treatment of the vegetation is often referred to as "big leaf" approach, using mean values for parameters like surface resistance, leaf area index or albedo, not taking into account any information on the vegetation distribution within the grid box. The moisture flux E is calculated for each of the four fractions according to the following generic equation:

$$E = \rho C_\text{h} |\vec{v}| \beta [q_\text{a} - h q_\text{s}(T_\text{S}, p_\text{S})], \tag{1.4}$$

where q_s is the saturation specific humidity at surface temperature T_S and pressure p_S, and q_a is the atmospheric specific humidity at a reference level. The values of β and h have to be specified for each fraction:

- Snow sublimation and evaporation of water in the interception reservoir are assumed to be at the potential rate, i. e. $\beta = h = 1$.

- Evaporation from bare soil is limited by the relative humidity h at the surface, which is a function of the relative moisture in the upper soil. The maximum amount of water, that is available to bare soil evaporation, are the top 10 cm of the soil water column. For bare soil evaporation, $\beta = 1$.

- Based on Sellers et al. (1986), for transpiration β is specified as

$$\beta = \left[1 + \frac{C_\text{h} |\vec{v}| r_\text{c0}(\text{PAR})}{F(W_\text{S})} \right]^{-1}, \tag{1.5}$$

including the stomatal resistance $r_\text{c}(\text{PAR}, W_\text{S}) = r_\text{c0}(\text{PAR})/F(W_\text{S})$ which has control over the transpiration from vegetation. r_c0 depends on the *Photosynthetically Active Radiation (PAR)*:

$$\frac{1}{r_\text{c0}} = \frac{1}{kc} \left[\frac{b}{d\,\text{PAR}} \ln \left(\frac{d\,e^{k \cdot \text{LAI}} + 1}{d + 1} \right) - \ln \left(\frac{d + e^{-k \cdot \text{LAI}}}{d + 1} \right) \right], \tag{1.6}$$

where $d = (a + bc)/(c\text{PAR}), k = 0.9$, and LAI is the *Leaf Area Index*. PAR is taken as 55% of the net surface short wave radiation. The standard parameter values in

the GCM are $a = 5000$ J m^{-3}, $b = 10$ W m^{-2} and $c = 100$ s m^{-1}. In contrast, the values $a = 2582.01$ J m^{-3}, $b = 1.09$ W m^{-2} and $c = 110$ s m^{-1} are used for the ECHAM PILPS simulations that are presented in chapter 2. This is done according to the PILPS instructions (Chen et al. 1997). c/LAI represents the minimum value of r_{c0} when PAR is approaching infinity.

$F(W_\mathrm{S})$ is the *water stress factor* which is a function of the soil water content W_S and describes the availability of water in the root zone. It is given by:

$$F(W_\mathrm{S}) = \begin{cases} 1 & \text{if} \quad W_\mathrm{cr} \leq W_\mathrm{S} \leq W_\mathrm{Smax} \\ \frac{W_\mathrm{S} - W_\mathrm{pwp}}{W_\mathrm{cr} - W_\mathrm{pwp}} & \text{if} \quad W_\mathrm{pwp} < W_\mathrm{S} < W_\mathrm{cr} \\ 0 & \text{if} \quad 0\,\mathrm{m} \leq W_\mathrm{S} \leq W_\mathrm{pwp} \end{cases} \tag{1.7}$$

W_Smax is the *field capacity* which is defined as the maximum amount of water the soil can hold against gravity over periods of several days. W_cr is the *critical soil moisture* level at which soil moisture stress starts to reduce the transpiration of plants in the model. In the ECHAM4 standard model it is taken as 75% of W_Smax. W_pwp is the *permanent wilting point*, taken as 35% of W_Smax. It is defined as that soil water level at which the plants are not able anymore to further extract water from the soil. Therefore, when the soil water content is reduced down to W_pwp, transpiration stops.

For computing the transpiration component, h in (1.4) is set to 1.

The total moisture flux is computed as the area weighted average of the four components that are described above.

For the calculation of the soil temperature the concept of heat diffusion is used. The heat conduction equation is solved for five layers over land and land ice, following Warrilow et al. (1986). The temperatures are representative for the middle of each soil layer. The first soil layer in ECHAM is 6.5 cm deep, the second 25.4 cm, and the thicknesses of the other layers continuously increase with depth. The upper boundary condition is given by the net heat flux (radiative and turbulent) at the surface. At the lower boundary a zero heat flux condition is prescribed to ensure energy conservation in the coupled soil–atmosphere system. In the absence of snow the temperature of the first soil layer T_1 is regarded as land surface temperature T_S (see Fig. 1.1a). For a snow pack with a depth of less than a critical value of 2.5 cm water equivalent the surface energy balance equation is solved assuming the characteristics of bare soil. If the snow pack is deeper than the critical value, an extra snow layer with an own temperature T_Sn at the middle of the snow pack evolves. In this case, the surface temperature is determined by linear extrapolation from T_1 and T_Sn to the top of the snow pack.

To enable snow melt in ECHAM when the snow depth is below the critical value, T_S (which is equal to T_1) needs to be higher than the melting temperature. Otherwise, both T_Sn and T_1 need to exceed 0°C.

The water budget within the soil is computed for one layer with a prescribed field capacity (bucket model, Manabe 1969). The governing equation takes precipitation, snow melt, evapotranspiration, runoff and drainage into account. Interception of precipitation is treated using one canopy layer. The capacity of this canopy reservoir W_lmx is given by

$$W_\mathrm{lmx} = W_\mathrm{lmax}[(1 - \mathrm{vegrat}) + \mathrm{vegrat} \cdot \mathrm{LAI}], \tag{1.8}$$

Table 1.1: Comparison of the main characteristics of the different model versions of ECHAM used in the present study. B is the structure parameter used in the runoff scheme (cf. (1.9)), W_{lmax} is the maximum amount of water that can be held on one layer of leaf or bare ground (cf. (1.8)), c is a key parameter for calculating the stomatal resistance (cf. (1.6)), λ is the thermal conductivity in the soil, LAI is the leaf area index and vegrat is the vegetation ratio in the grid element. In the first five model versions of ECHAM, LAI and vegrat are set constant to their annual mean values. In the sensitivity test ECHVARI, these parameters follow their observed annual cycles, as shown in Fig. 1.2.

Model	B	W_{lmax} (mm)	c (s m^{-1})	λ (W K^{-1}m^{-1})	LAI	vegrat
ECHAM	0.2	0.1	110.0	2.0	1.3	0.956
ECHFLAT	0.025	0.1	110.0	2.0	1.3	0.956
ECHWL	0.2	1.0	110.0	2.0	1.3	0.956
ECHEVAP	0.2	0.1	40.0	2.0	1.3	0.956
ECHTEMP	0.2	0.1	40.0	1.0	1.3	0.956
ECHVARI	0.2	0.1	40.0	1.0	Vari.	Vari.

where W_{lmax} is the maximum amount of water that can be held on one layer of leaf or bare ground and vegrat is the vegetation ratio in the grid element.

In a simple bucket model surface runoff is produced by overflow when the soil water reservoir is saturated. Here, an advanced approach is chosen that accounts for sub-grid scale effects due to the heterogeneity within a grid area (*Arno scheme*, Dümenil and Todini 1992). It is assumed that the fraction s/S of the grid area in which the storage capacity is less than or equal to an assigned value w is given by

$$\frac{s}{S} = 1 - \left(1 - \frac{w}{w_{\max}}\right)^{B}.$$ (1.9)

The value of $w_{\max}$ is the maximum storage capacity in the grid element, and B is a structure parameter that is characteristic for the grid element. Its values range from 0.01 to 0.5. B takes into account the slope of the terrain, where a value of 0.01 represents very flat terrain which will allow a large fraction of precipitation to infiltrate the soil, while values approaching 0.5 indicate steep terrain where surface runoff will be more efficient. The drainage rate is a linear function of the soil moisture if it is between 5% and 90% of the field capacity. For higher values the drainage rate behaves like a potential function, and for lower values it is equal to zero. Infiltration and drainage do not occur if the soil is frozen.

In the sensitivity tests presented in section 2.3, five modified versions of the ECHAM land surface scheme have been used. They are identical to the reference version ECHAM but with some key land surface parameters changed (see Table 1.1 and Fig. 1.2).

The sixth modified version of ECHAM developed as part of this work is denoted as ECH7TL. The only modification compared to ECHAM is that it has seven soil temperature layers instead of five, and these layers are not as deep as in ECHAM.

In order to use the model for global experiments, global fields of several land surface parameters are necessary to define the surface boundary conditions. A global data set of annual mean land surface parameters has been compiled by Claussen et al. (1994) for the
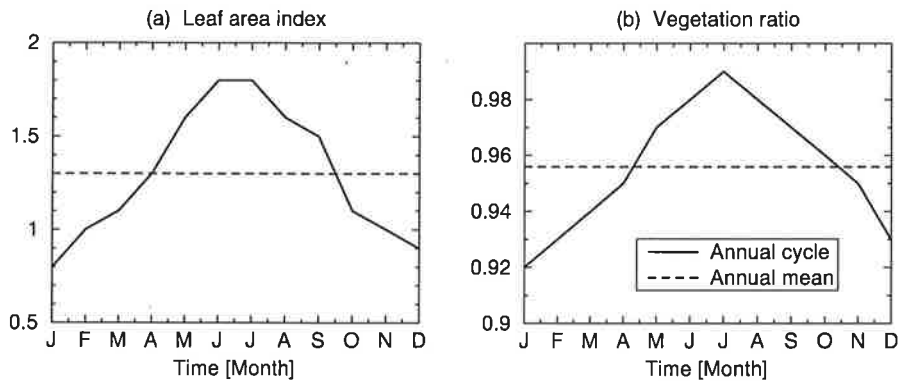
Figure 1.2: Annual cycles of (a) leaf area index and (b) vegetation ratio as observed at Cabauw (cf. Chen et al. 1997).

ECHAM4 GCM (Roeckner et al. 1996), including quantities like surface background albedo, LAI and fractional vegetation cover. This data set has been constructed by allocating parameter values from different sources to the major ecosystem complexes of Olson et al. (1983). In the presence of a snow cover the albedo is modified accordingly. The global distribution of the total soil water-holding capacity is derived from a high-resolution data set by Patterson (1990).

1.2   SECHIBA

The basic feature of the parameterization of SECHIBA (Ducoudré et al. 1993) is the representation of the transfer of heat and moisture between the atmosphere and the vegetated surface of the earth using a resistance formulation. In analogy to Ohm's law, surface sensible and latent heat fluxes are calculated as follows:

$$F_X \sim \frac{\text{potential difference}}{\text{resistance}} = \frac{\Delta X}{\sum_i r_i}. \tag{1.10}$$

The quantity X may be identified with temperature or specific humidity. The fluxes are driven by ΔX, the gradient of X between surface and a reference level in the atmosphere, and are limited by a sum of resistances r_i, which may be aerodynamic and/or surface resistances. The formulations of the land surface fluxes as given by (1.10) and (1.3) can be converted into each other.

Transpiration and canopy evaporation are computed using up to seven different vegetation types that may be present simultaneously in one grid element (besides bare soil). The moisture flux is calculated separately for each fractional surface cover class, and the total flux of the grid box is determined as an area weighted average. This technique is called the "mosaic approach" and takes into account the sub-grid scale distribution of the vegetation types. This distribution has been derived from the atlas by Matthews (1985). Figure 1.3 shows the fractional areas covered by bare soil and the seven different vegetation types (see Ducoudré et al. 1993) used in ECHAM4/SECHIBA (in T42 spatial resolution, cf. chapter 4). These vegetation maps can not directly be compared to the one used by the ECHAM
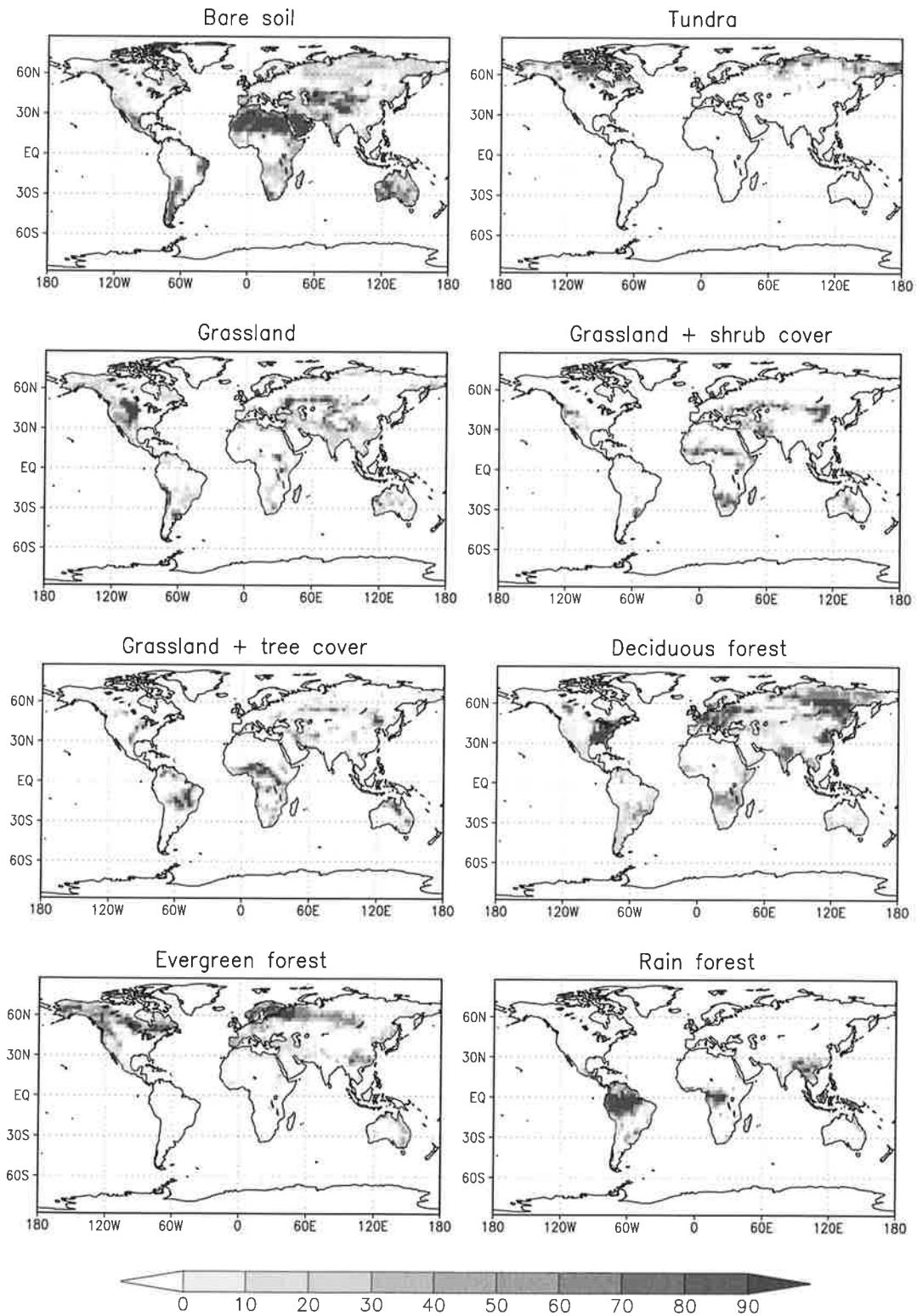
Figure 1.3: Global distributions of the fractional areas [%] covered by bare soil and the seven different vegetation types used in ECHAM4/SECHIBA (in T42 spatial resolution).

ECHAM4 T42

ECHAM4/SECHIBA T42

ECHAM4/SECHIBA T42 − ECHAM4 T42
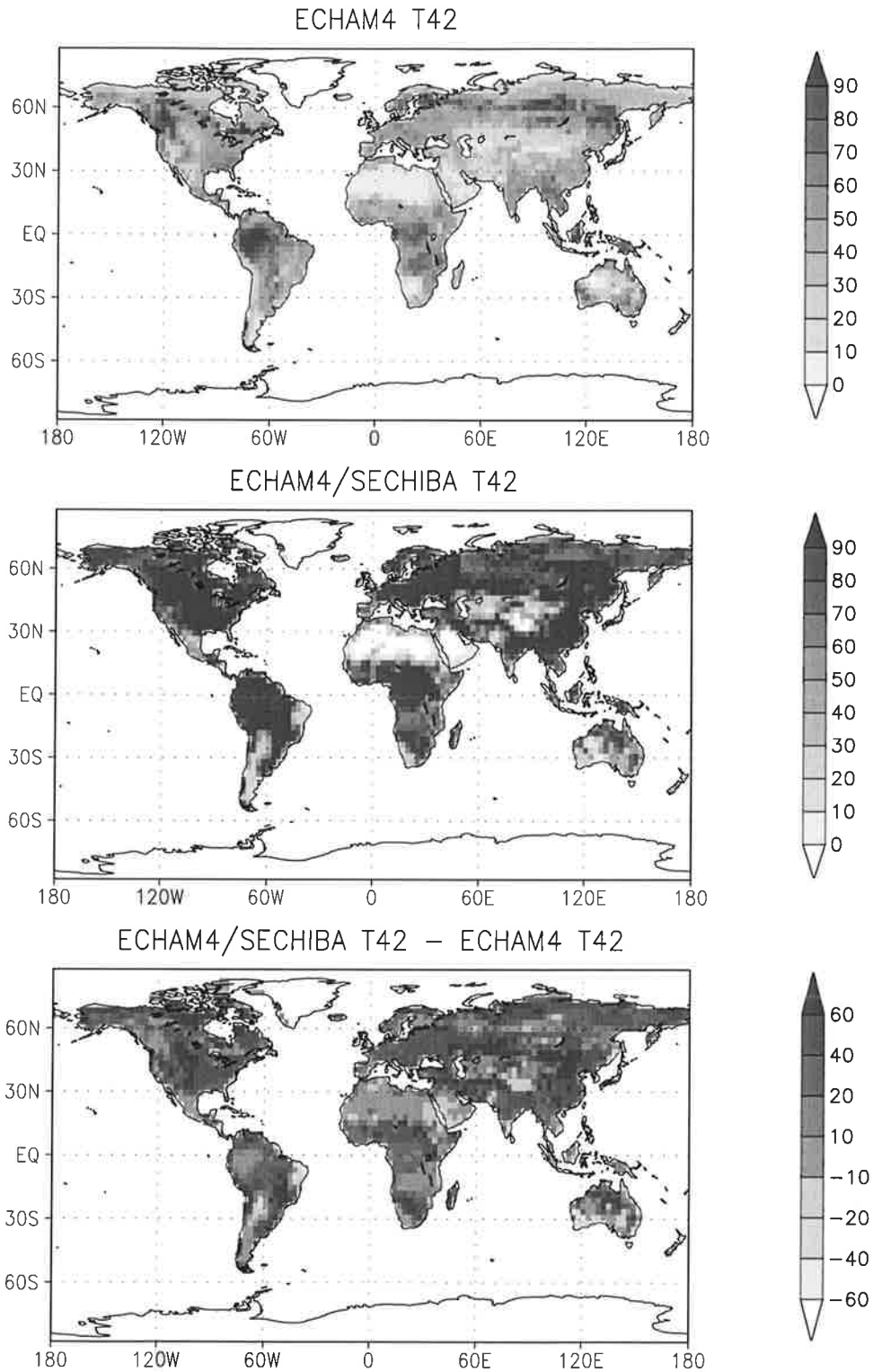
Figure 1.4: Global distributions of the total vegetation fraction (vegetation ratio) [%] as used in the ECHAM4 and ECHAM4/IMPL GCM versions (top panel) and in ECHAM4/SECHIBA (middle panel), both in T42 spatial resolution. The bottom panel shows the differences between the two maps.

ECHAM4 T42

ECHAM4/SECHIBA T42 (summer)

ECHAM4/SECHIBA T42 (winter)
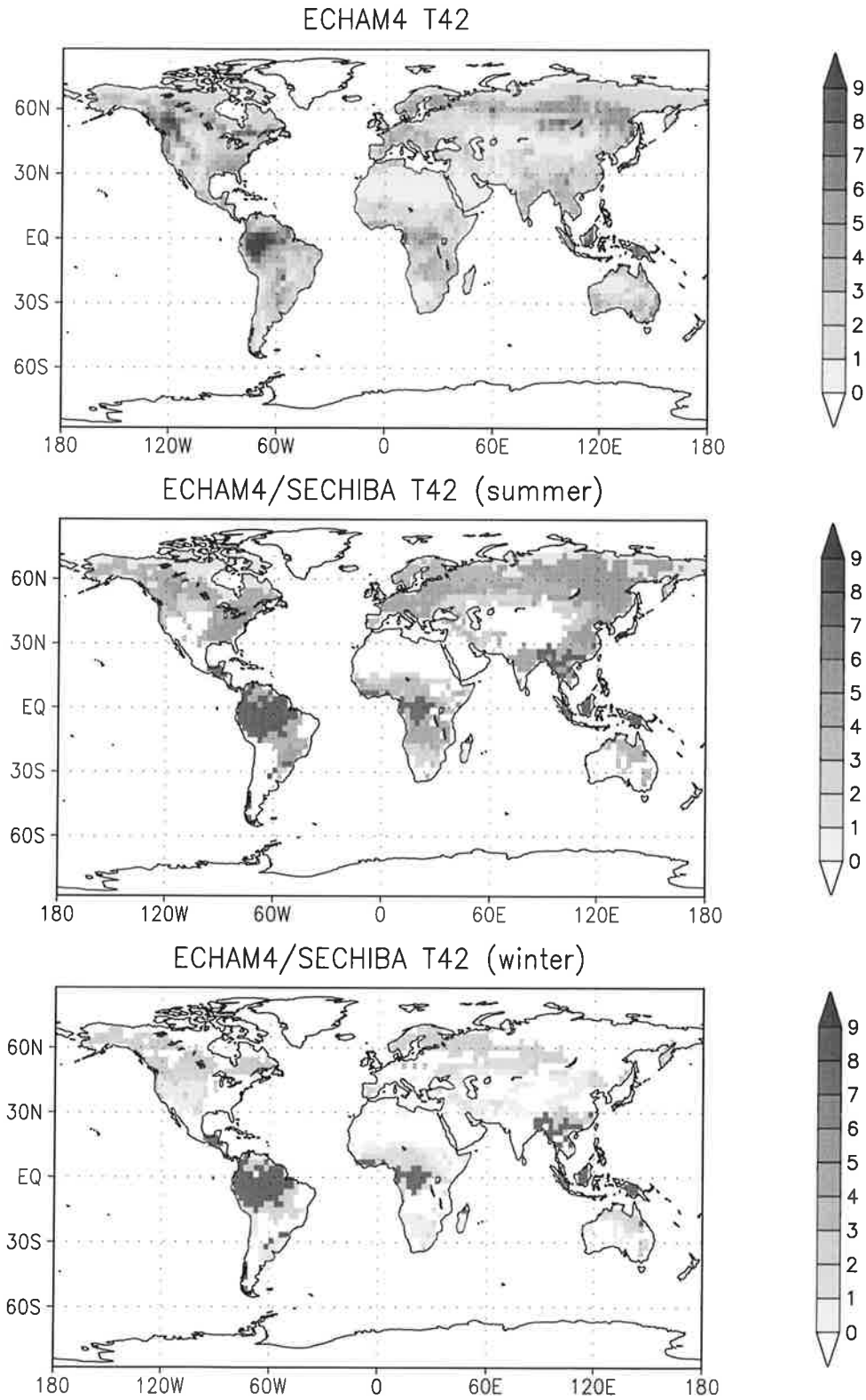
Figure 1.5: Global distributions of the annually constant LAI as used in the ECHAM4 and ECHAM4/IMPL GCM versions (top panel) and the LAI maximum values in the warm season (summer, middle panel) and the minima in the cold season (winter, bottom panel) in ECHAM4/SECHIBA, all in T42 spatial resolution.

ECHAM4/SECHIBA T42 (summer) − ECHAM4 T42

ECHAM4/SECHIBA T42 (winter) − ECHAM4 T42

ECHAM4/SECHIBA T42 (summer − winter)
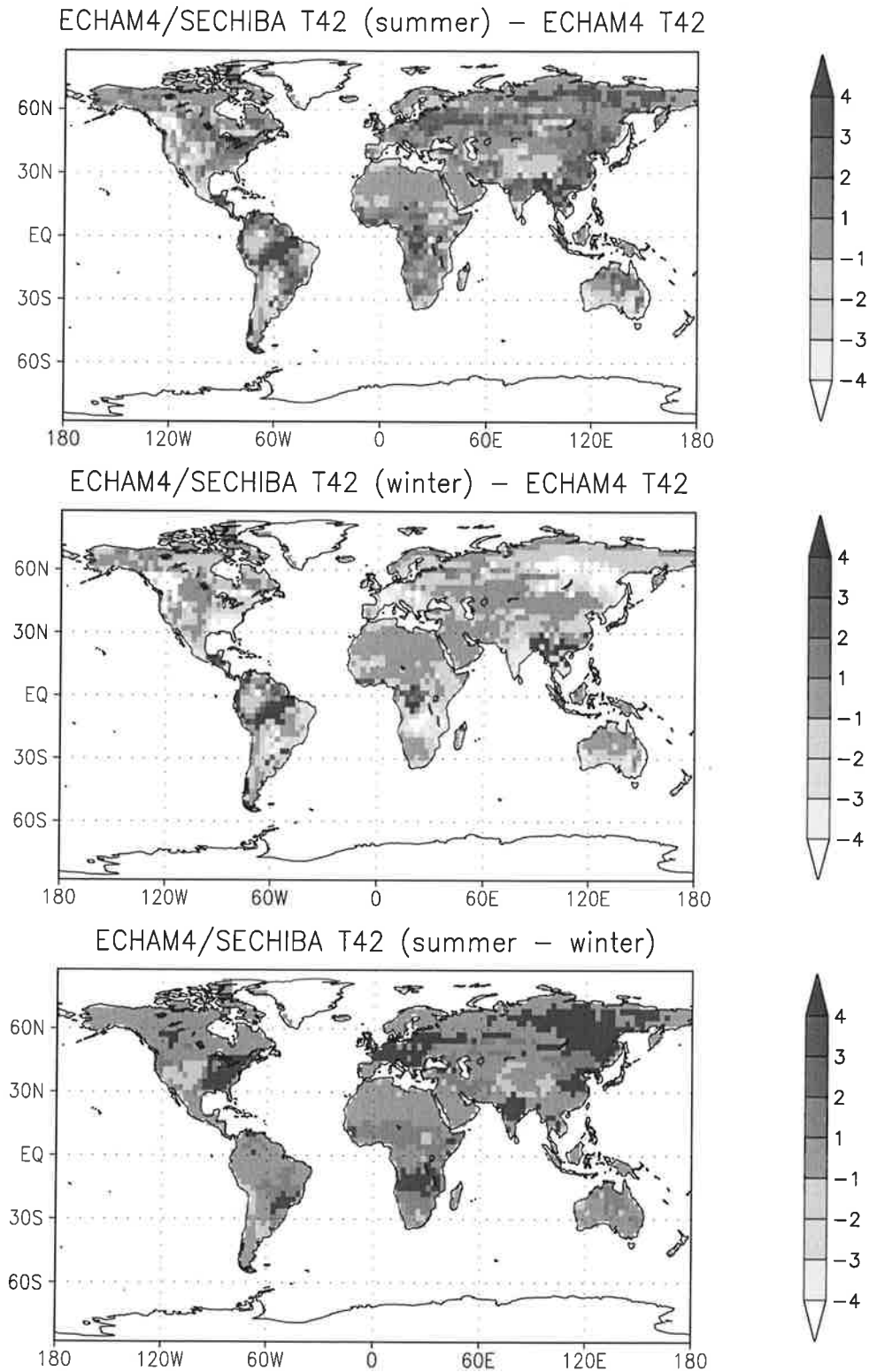
Figure 1.6: Differences between the global distributions of the ECHAM4/SECHIBA summer LAI and the annually constant LAI as used in the ECHAM4 and ECHAM4/IMPL GCM versions (top panel), the ECHAM4/SECHIBA winter LAI and ECHAM4 (middle panel) and the ECHAM4/SECHIBA summer and winter LAI (bottom panel), all in T42 spatial resolution.
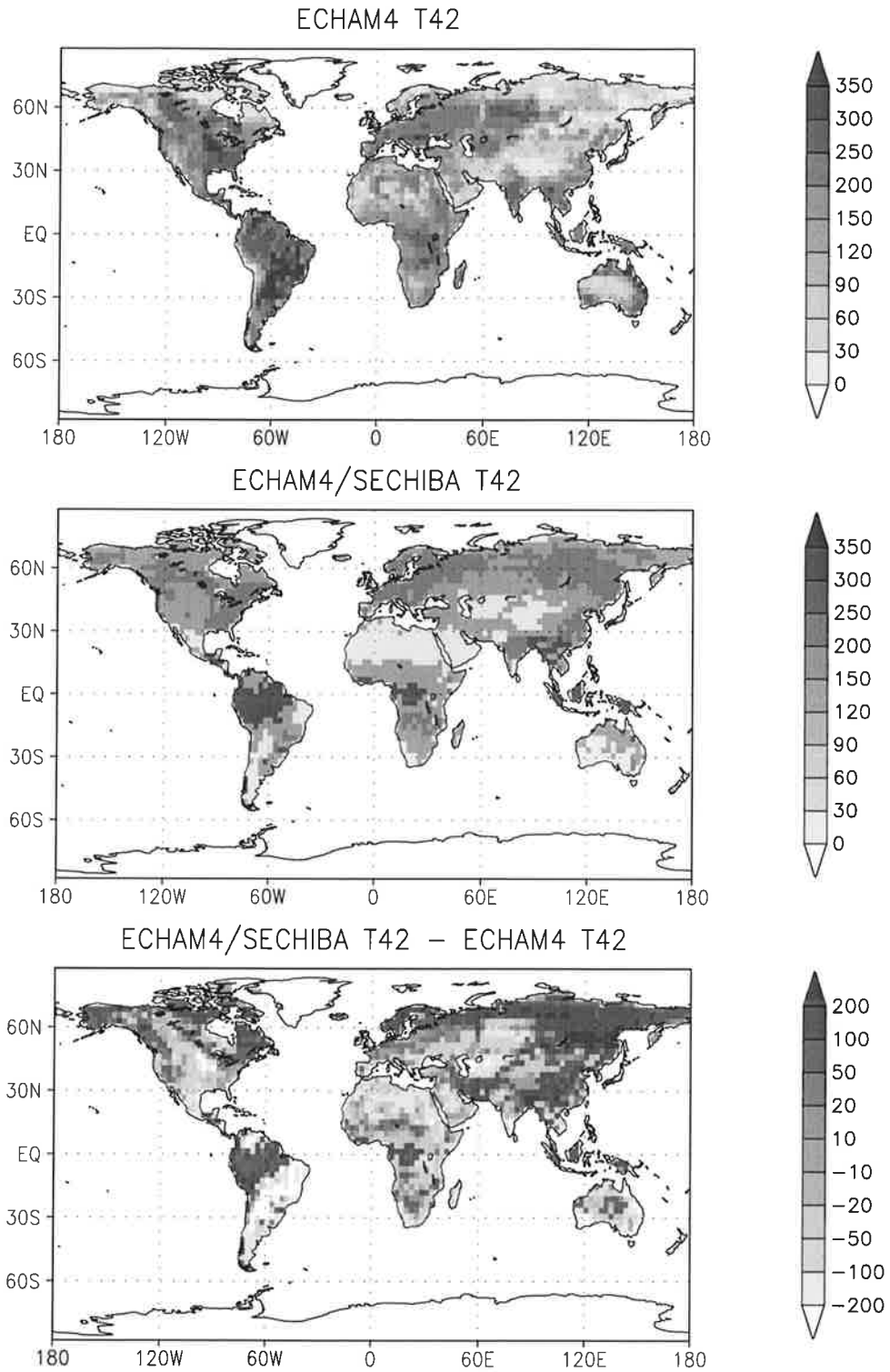
Figure 1.7: Global distributions of the plant-available soil water-holding capacity [mm] as used in the ECHAM4 and ECHAM4/IMPL GCM versions (top panel) and in ECHAM4/SECHIBA (middle panel), both in T42 spatial resolution. The bottom panel shows the differences between the two maps.

land surface scheme, because the latter specifies only the total vegetation fraction (vegetation ratio) in each grid box without information on the sub-grid scale distribution. In order to get an impression of the model differences, the aggregated total vegetation fraction in each T42 grid box in ECHAM4/SECHIBA is shown in Fig. 1.4 together with the distribution as used in the land surface scheme in the ECHAM4 and ECHAM4/IMPL GCM versions. Both maps show, as to be expected, very low values in deserts and mountainous regions (where non-zero values in the central Sahara Desert and Saudi Arabia in ECHAM4 appear to be unrealistic) and high values e. g. in the tropics. However, SECHIBA has a considerably larger vegetation cover in extended regions in Eurasia, America and central and southern Africa. The reason is that Claussen et al. (1994) specified the annual mean vegetation ratio in ECHAM4 as the arithmetic average of the values for the seasons of growing and dormancy, while the SECHIBA distribution refers to the high (growing season) values (Matthews 1985).

Generally, both parameterizations suffer from the fact that they do not resolve the annual cycle of the vegetation cover (which definitely has a high variation for many vegetation types like e. g. deciduous forest in the extratropics). Claussen et al. (1994) argue that the best thing to do in this case is to use annual arithmetic averages for the vegetation cover. Therefore, they will generally overestimate transpiration in the season of low insolation and underestimate it during high insolation. In the latter season transpiration is an important component of the surface moisture budget (depending on soil water availability). Therefore, underestimating the transpiration in this season will cause an higher absolute error than the overestimation at low insolation. This may serve as a reasoning for choosing a higher than the annual average vegetation fraction value (outside the tropics), as done in SECHIBA, to better represent the transpiration in the important season of high insolation.

In contrast to the seasonally constant vegetation fraction, a summer and a winter value of the LAI is specified for each vegetation type in SECHIBA. A seasonal cycle is calculated by linear interpolation between these values, depending on deep soil temperature which is not influenced by diurnal variations. Figure 1.5 compares the annually constant LAI global distribution of ECHAM4 (and ECHAM4/IMPL) to the maps of the LAI maximum values in the warm season and the minima in the cold season in ECHAM4/SECHIBA. For this illustration, the LAI values of the predominant surface cover class in each grid cell have been plotted. Both parameterizations show roughly the same global structure, and in many region of the globe the ECHAM4 LAI values are within the range between the two winter and summer extremes of the ECHAM4/SECHIBA LAI (cf. Fig. 1.6). Again, non-zero values in deserts in ECHAM4, where no plants are expected, appear to be unrealistic. Most striking differences between the summer and winter values in SECHIBA are visible in regions with deciduous forest, namely Europe, northeast Asia, eastern United States, India and southern Africa (Fig. 1.6). In these regions the LAI varies between 0 and 5 in winter and summer. Mainly due to the mosaic approach and the inclusion of the LAI seasonal cycle SECHIBA is expected to much better represent the global vegetation cover and the global and seasonal transpiration.

The global distribution of the total soil water-holding capacity in SECHIBA is determined according to the predominant surface cover class in each grid cell. Figure 1.7 shows the distributions of the plant-available soil water-holding capacity, that is the difference between field capacity and wilting level, as used in the land surface scheme in the ECHAM4 and ECHAM4/IMPL GCM versions and in ECHAM4/SECHIBA, both in T42 spatial resolution. The figure also shows that particularly large differences between the two maps are found in

Asia and South America.

A difference in SECHIBA to ECHAM is the formulation of the hydrological stress that limits the transpiration. In SECHIBA it is an exponential function of the ratio of the depth of dry soil above the water table and the total depth of the soil moisture layer where the water table is located. The evaporation of foliage water is controlled by the aerodynamic resistance and an architectural resistance, the latter representing the aerodynamic resistance between the leaves and the canopy top (see Fig. 1.1b).

The soil temperature is computed similar to ECHAM, using the heat conduction equation. But different from ECHAM, SECHIBA utilizes a discretization in seven layers that are not as deep, instead of five. For instance, the upper one is about two-thirds as deep as in ECHAM. A characteristic difference from ECHAM is the method used to determine the surface temperature (cf. Fig. 1.1a). In SECHIBA it is calculated using the surface energy balance equation and the soil properties obtained by an extrapolation of heat capacity and ground heat flux toward the surface. This procedure is expected to yield more realistic diurnal variations of the soil temperature profile and ground heat flux close to the surface.

In the presence of a snow pack the heat conduction equation is solved, using the thermal conductivity and heat capacity of snow. To enable snow melt in SECHIBA only the surface temperature, that is extrapolated from the two upper thermal layers to the surface as mentioned in the paragraph before, needs to be above the melting point. This is likely to produce a more realistic snow melt than ECHAM, in particular for deep snow packs.

The soil water is stored in two conceptual layers. The depths of the soil moisture reservoirs in the two other models, ECHAM and SSiB, are fixed, while in SECHIBA, the upper layer has a variable depth (*Choisnel scheme*, Choisnel 1977). If the soil is dry, an upper moisture layer will be created from top to bottom in the soil during a precipitation event. When the rain stops, first the soil moisture in the upper layer will be depleted by subsequent evaporation, again from top to bottom until the upper reservoir may disappear. Then evaporation continues from the lower reservoir. This design allows a fast response of bare soil evaporation to precipitation events, as the soil resistance which limits bare soil evaporation directly depends on the depth of dry soil above the water level in the uppermost moisture layer that contains water. Surface runoff only occurs when the soil is saturated, drainage is not computed.

1.3   SSiB

The parameterization of the SSiB model allows a detailed description of the land surface fluxes in the presence of different biome types, while their number is limited to one biome type per grid box. The fluxes are also computed by a resistance formulation. The model is described and extensively used in numerous studies (e. g. Xue et al. 1991, Xue and Shukla 1993).

In the SSiB model five components of the downward radiation flux through the lowest layer of the atmosphere are treated: direct beam and diffusive radiation in the visible and near-infrared wavelength intervals and diffusive thermal radiation. The surface albedo and the net-absorbed radiation at the canopy and at the ground are parameterized as functions of solar zenith angle and snow cover on the canopy and ground.

For the calculation of ground and deep soil temperature, the force-restore method (e. g. Deardorff 1978) is used. Additionally, a canopy temperature is computed. Hence, in contrast to the two other models, SSiB solves independent energy budges for canopy and ground.

For the interception of precipitation, one canopy water store is used. Infiltrated water may be stored in three soil layers. For the simulations at the Cabauw site (see chapter 2) their prescribed depths are 0.1, 0.9 and 9.0 m from top to bottom. Transfer of water between the layers is described by diffusion. In the Cabauw simulations the roots of the vegetation can penetrate the two upper layers, called the root zone. The water content of these two layers may be reduced by transpiration. From the third layer, the recharge layer, water can be abstracted by gravitational drainage. A snow cover can appear on the canopy and ground.

Chapter 2

Single point off-line simulations

2.1 The Cabauw observational data

The Cabauw site is located in the center of the Netherlands (at 51° 58' N, 4° 56' E). The flat terrain is almost completely covered with grass so that the vegetation ratio is nearly equal to 1. This means that the soil water is almost exclusively extracted by transpiration and not by bare soil evaporation. Details about the measuring program at Cabauw are given by Driedonks et al. (1978). The set of observational data includes the meteorological quantities that are used as atmospheric forcing to drive the land surface schemes, that is, solar and thermal downward radiation, precipitation, horizontal wind components, air temperature and specific humidity. As shown in Fig. 2.1, radiation, temperature and humidity undergo a marked annual cycle with a maximum in summer; the wind speed has a maximum in winter. For precipitation no annual cycle is obvious. For validation, measurements of sensible and latent heat fluxes, total net radiation, surface ground heat fluxes and soil temperature are available. The observations cover a 1-year period (the year 1987) at a time resolution of 30 min. It must be noted that the three schemes were all forced with the observational data at a 30-min time step Δt. In Fig. 2.1 the daily mean values were smoothed applying a 31-day running mean with periodic boundary conditions. The same procedure has been applied in most other figures in this chapter showing annual cycles of certain quantities. This was done only for the sake of clarity of the figures.

Studies of the data accuracy (Beljaars and Bosveld 1997) have shown that some observed quantities of the surface energy balance were seriously biased. Therefore, while the forcing variables of the PILPS Cabauw experiment have been extracted from an earlier version of the Cabauw data (Beljaars and Viterbo 1994), the energy fluxes for model validation were derived from a version of the Cabauw data which includes bias corrections (Beljaars and Bosveld 1997). The same procedure as described above was also applied to the Cabauw data by Chen et al. (1997) for the model intercomparison in PILPS. According to Chen et al. (1997) the remaining minor inconsistencies between the forcing and the validation data can be tolerated.
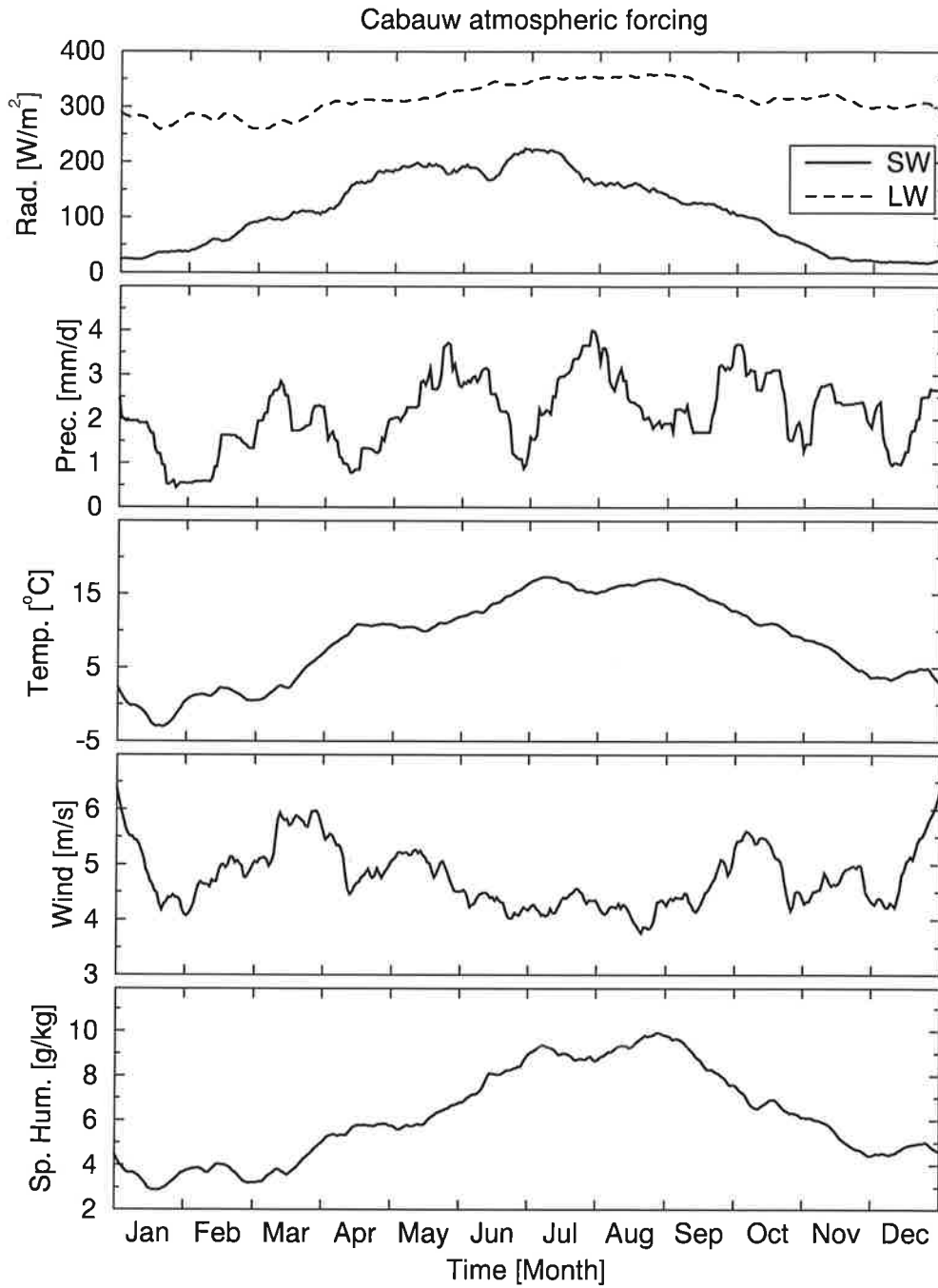
Figure 2.1: Annual cycles of the Cabauw observational atmospheric forcing quantities, that is, shortwave (SW) and longwave (LW) radiation (Rad.), precipitation (Prec.), atmospheric temperature (Temp.), absolute wind speed (Wind) and atmospheric specific humidity (Sp. Hum.). The three schemes were all forced with the observational data at a 30-min time step. For the clarity of the figure, the curves were smoothed using a 31-day running mean.

2.2 Model intercomparison

The basic idea of this model intercomparison is to use equivalent parameter values for soil and vegetation of every land surface scheme and to force them with the same atmospheric values. By this procedure the results of the simulations should only reveal similarities and differences of the model structures while excluding differences induced by feedbacks with the atmosphere or the choice of different parameter values. This study does not attempt to assess the quality of the land surface schemes. For this task several datasets would have to be used representing different climatological situations. This comparison shall only give a general idea about the features, properties and sensitivities of the models.

Parameters such as roughness length, leaf area index and albedo, and the initial values of the moisture reservoirs and temperatures were prescribed for all schemes in a consistent way. The third soil moisture layer of SSiB, the recharge layer, was set to saturation during the entire period of simulation. More details are given in Chen et al. (1997). Each model was run for a few years applying the 1-year forcing dataset repeatedly until equilibrium was reached.

2.2.1 Surface energy balance

Figure 2.2 shows the annual cycles of the surface temperature simulated by the individual models and also the observed surface radiative (effective) temperature T_{eff} and the soil temperature T_{S2} measured at a depth of 2 cm. T_{eff} is calculated from the observed upward longwave radiation. All curves show a clear seasonal variation with a minimum in January and a maximum in July. The value of T_{eff} is less than that of T_{S2} during the whole year with a difference in the range from 1 to 5°C. The three model surface temperatures are very close to each other and their curves are within the range of the two observed temperatures almost over the entire year. This behaviour is also represented by the annual mean temperature values which are 7.1°C for T_{eff}, 10.3°C for T_{S2}, 8.8°C for ECHAM, 9.0°C for SECHIBA and 8.7°C for SSiB. These simulated temperatures are all within the range between the observed T_{eff} and T_{S2}.

To better understand these results, the diurnal variations of the temperatures shall be discussed. An example for this is given in Fig. 2.3, which shows the diurnal variations of the surface temperature from 15 to 19 September as observed at Cabauw and as simulated by ECHAM, SSiB and SECHIBA. The diurnal cycles of the three model surface temperatures are very similar. But there is a tendency for the characteristic shape of the diurnal temperature curve of ECHAM to be closer to T_{S2} than that of the other models. This can be explained by a thermal damping of ECHAM's top soil layer which will be discussed in the following text.

As the ECHAM model soil temperatures are representative for the middle of each soil layer, the temperature T_1 of the top layer, which is 6.5 cm deep, is expected to be comparable with the measured value at a depth of 3.25 cm (cf. Fig. 1.1a). The amplitude of the diurnal soil temperature variation decreases with depth due to the heat conduction (diffusion) process in the soil. Additionally, there is a phase delay of the temperature signal with depth. Therefore the amplitude of the diurnal variations of the ECHAM model temperature is expected to be smaller than that of T_{S2} but, as seen in Fig. 2.3, it is larger instead. The temperature curve is within the range of T_{S2} and T_{eff} almost all the time. This behaviour is mainly due to the
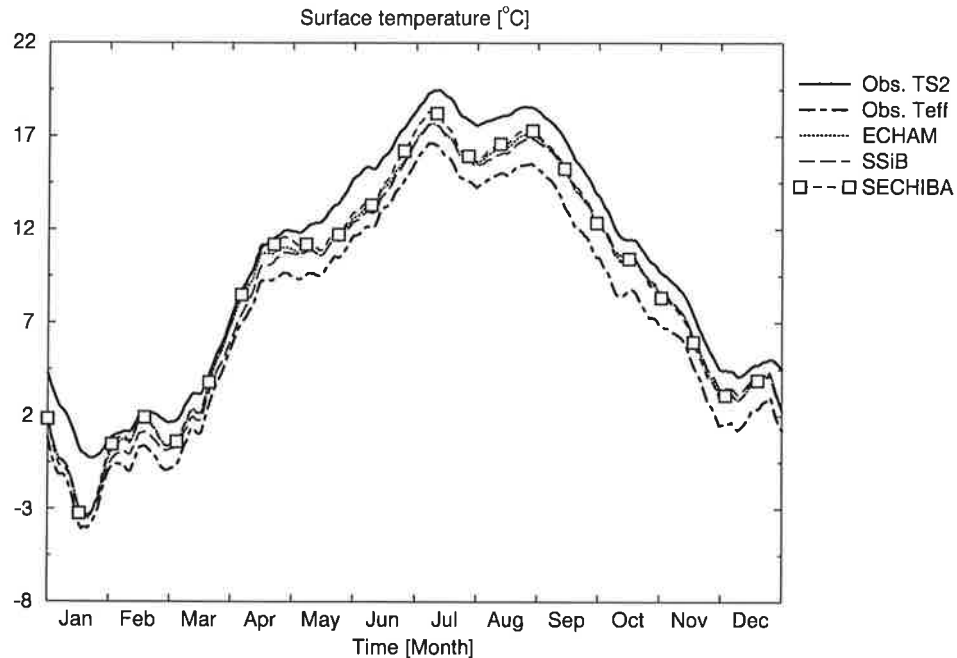
Figure 2.2: Annual cycles of soil temperature T_{S2} measured at a depth of 2 cm and observed surface radiative (effective) temperature T_{eff} compared to the surface temperatures as simulated by ECHAM, SSiB and SECHIBA. The observations were made at Cabauw. The curves were smoothed using a 31-day running mean.

discrepancy in the model that on the one hand the first model layer temperature T_1 represents the soil temperature at a depth of 3.25 cm according to the soil heat conduction scheme; on the other hand, it is **also** used as surface temperature for computing the atmospheric energy fluxes. (Thermal upward radiation and sensible and latent heat fluxes are computed using T_1 as land surface temperature (see Fig. 1.1a and (1.2), (1.3) and (1.4)).) In reality, the relevant surface temperature for these energy fluxes is the one which is "seen" by the atmosphere at the soil-vegetation–atmosphere interface. With regard to the thermal upward radiation, this is T_{eff}. For the turbulent energy fluxes, this is not T_1 either. As shown, this aspect of the model parameterization leads to some problems.

This may be explained using the diurnal evolution of surface temperature on 17 September as an example (cf. Fig. 2.3). During the night from 16 to 17 September T_{eff} and ECHAM's T_1 both decrease to a minimum value, but the minimum of T_{eff} is lower. In the early morning hours both begin to rise because of the incoming solar radiation. According to the model structure ECHAM can not represent a "skin temperature", therefore it rises more slowly than T_{eff} and is below it from about 0700 to 1300 UTC. This "thermal inertia of the surface layer" was also found by Betts et al. (1993) with a Cycle 39 version of the *European Centre for Medium-Range Weather Forecasts (ECMWF)* model. This is of relevance here since the ECHAM climate model was originally derived from an earlier version of the ECMWF model (Cycle 31). As ECHAM's temperature is used to compute thermal upward radiation and sensible and latent heat fluxes, these atmospheric energy fluxes are underestimated in the
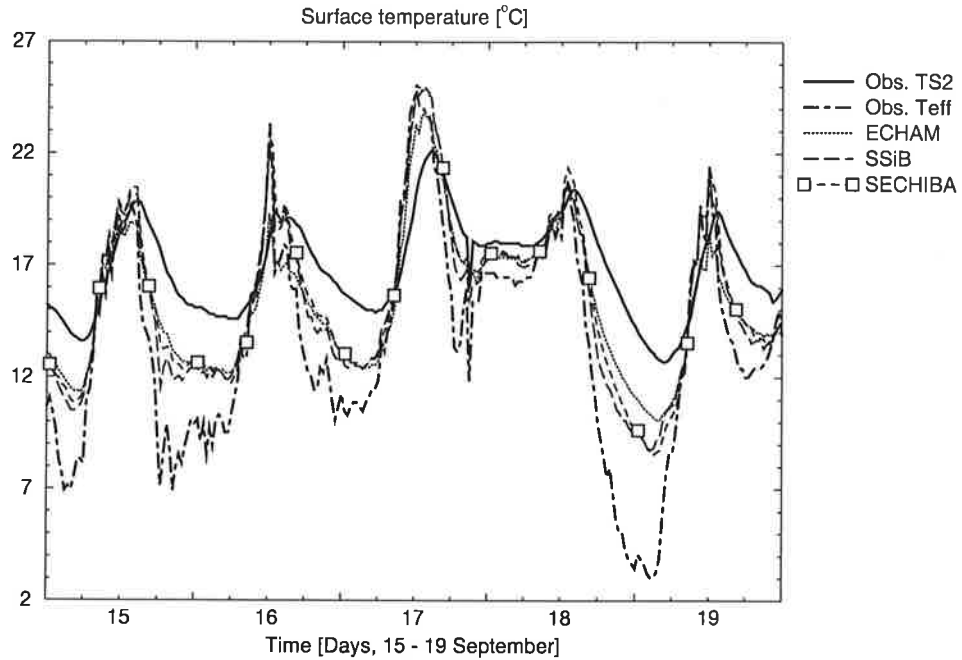
Figure 2.3: Diurnal cycles of soil temperature T_{S2} measured at a depth of 2 cm and observed surface radiative (effective) temperature T_{eff} from 15 to 19 September compared to the surface temperatures as simulated by ECHAM, SSiB and SECHIBA. The observations were made at Cabauw.
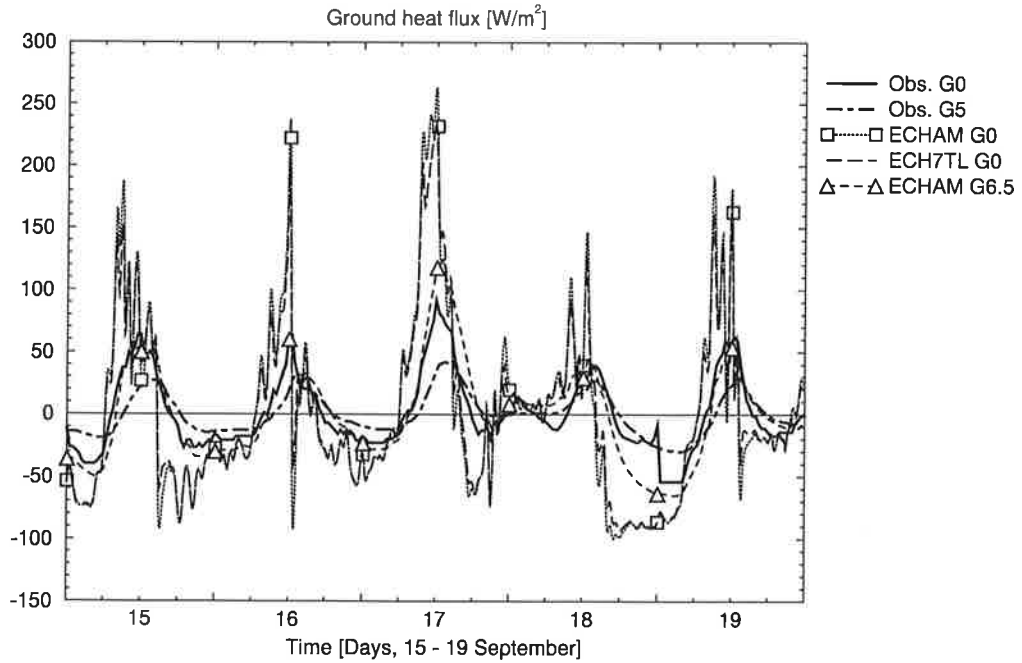
Figure 2.4: Diurnal cycles of surface ground heat flux $G0$ as observed at Cabauw from 15 to 19 September compared to the model results of ECHAM and ECH7TL. Additionally shown is the ground heat flux as measured at a depth of 5 cm (Obs. $G5$) and as simulated by ECHAM at a depth of 6.5 cm (ECHAM $G6.5$).

morning. The residual energy in the model has to go into the ground, which leads to a highly overestimated surface ground heat flux in the model as compared to the observation (cf. Fig. 2.4). The model shows a peak with a maximum of about 260 W m^{-2} in the surface ground heat flux on 17 September, while a peak of only about 90 W m^{-2} was observed.

In this context another aspect of the parameterization needs to be discussed. According to (1.1) the temporal evolution of the surface temperature T_S, which is equal to T_1 in ECHAM in the absence of snow (cf. Fig. 1.1a), is calculated from the balance of all vertical energy fluxes entering the surface layer. These are the atmospheric fluxes at the top and the ground heat flux at the bottom. Therefore, as shown in Fig. 1.1a, the suitable flux in ECHAM to be considered for validation of the surface energy balance and for comparison to the observed surface ground heat flux should be that one computed at the bottom of the surface layer, i. e. at a depth of 6.5 cm. This flux is denoted as $G6.5$ in Fig. 2.4 and indeed matches much better the observed surface ground heat flux than ECHAM's surface flux $G0$. This correspondence is due to the numerical finite difference scheme used to solve the soil heat conduction equation. But this means that the geometrical corresponding, i. e. at the same depth in the soil, measured and simulated heat fluxes can not be expected to be identical. Beside the surface flux $G0$ this is also shown by the measured ground heat flux at a depth of 5 cm which is included in Fig. 2.4 as well. The amplitude of the diurnal ground heat flux variation decreases with depth due to the heat conduction in the soil. This is similar to the behaviour of the soil temperature as discussed earlier. Therefore the amplitude of the diurnal variations of the ECHAM flux $G6.5$ is expected to be smaller than that of the measured $G5$ but it is larger instead.

As a consequence of the overestimated ground heat flux, in the sense that measured and simulated fluxes at the same depth in the soil are compared, the amplitude of the diurnal variations of the simulated soil temperature is overestimated as well. This is the reason why the temperature of the first soil layer in ECHAM, which is expected to represent the temperature at a depth of 3.25 cm, shows a too-high diurnal amplitude, which is even significantly higher than the one observed at a depth of 2 cm (T_{S2}). In the cooling phase during the second half of the day the processes described above are reversed. This causes an overestimation of the negative ground heat flux (cf. Fig. 2.4).

In SECHIBA the first soil layer is only 4.3 cm deep and the second is 12.9 cm deep. But the surface temperature at the soil–atmosphere interface is computed using the surface energy balance equation and the soil properties obtained by an extrapolation of heat capacity and ground heat flux toward the surface. The impact of this procedure on the simulated heat flux is analysed in sections 3.3 and 3.4 in more detail. It increases the dependence of surface temperature on atmospheric conditions by decreasing the effective heat capacity used in the surface energy balance equation. We would therefore expect the simulated surface temperature to be closer to the observed T_{eff} than the temperature of the first layer which is computed in the middle of the layer.

In SSiB surface radiative temperature is an average of canopy temperature and the upper ground temperature, the latter of which is calculated by the force-restore method. It represents the region in the soil that is influenced by the diurnal temperature wave. These are typically the top 10 cm (cf. Hillel 1982). This is of the same order as in the other two models. But by taking into account the lower heat capacity of the canopy, SSiB should be able to follow more closely the diurnal variations of the surface radiative temperature under vegetated conditions.
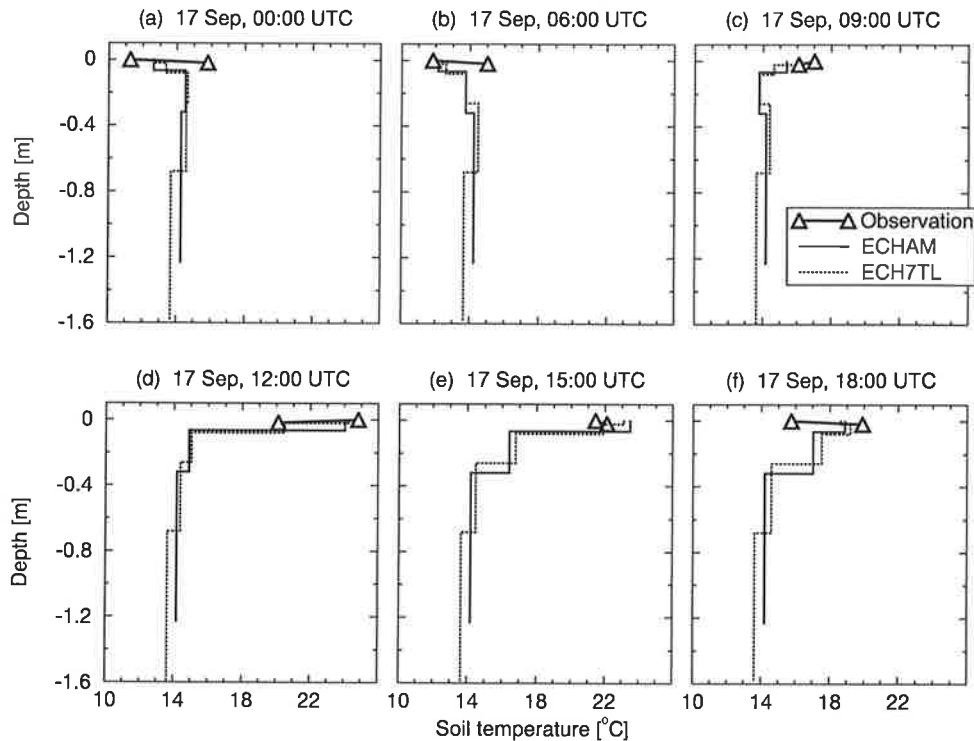
Figure 2.5: Soil temperature profiles as observed at Cabauw at different times on 17 September compared to the profiles as simulated by ECHAM and ECH7TL. The three upper layers of ECHAM and the five upper layers of ECH7TL are shown. The triangles indicate the values of the observed surface radiative (effective) temperature T_{eff} and the soil temperature T_{S2} measured at a depth of 2 cm.

In fact, during the evening hours of 15, 16 and 18 September SSiB better reproduces the fast decrease of surface temperature, which is seen in the evolution of T_{eff} (cf. Fig. 2.3), than ECHAM. At midday on 16 and 17 September and during the nighttime minimum on 19 September SSiB and SECHIBA are very similar. Due to their model structures these schemes show less damping of the diurnal surface temperature variations than ECHAM. So the simulated surface temperatures of all three schemes are consistent with their model structures. None of them is able to exactly match the evolution of the observed radiative temperature which would be necessary, for example, for a realistic computation of the thermal upward radiation (see also section 2.3.2).

Figure 2.5 compares six soil temperature profiles on 17 September as observed at Cabauw and as simulated by ECHAM and ECH7TL. Model version ECH7TL is identical to ECHAM, only the soil temperature layers are modified. ECH7TL has 7 layers instead of 5, and the depths are reduced. The original idea of choosing 7 layers was to compare this to SECHIBA, but then the layer depths were chosen smaller to get a visible effect. The first layer in ECH7TL is 2.1 cm deep instead of 6.5 cm in ECHAM, the second 6 cm instead of 25.4 cm etc. This version is used to test if due to an increased spatial resolution in the soil the simulated temperature profile can follow the diurnal variations of the observed one more closely. Figure 2.5 shows that the diurnal variations of the soil temperature (on 17 September) in ECHAM are represented by the upper 2 layers, and in ECH7TL by the upper 3–4 layers. The geometrical depths of the regions influenced by diurnal variations of temperature and
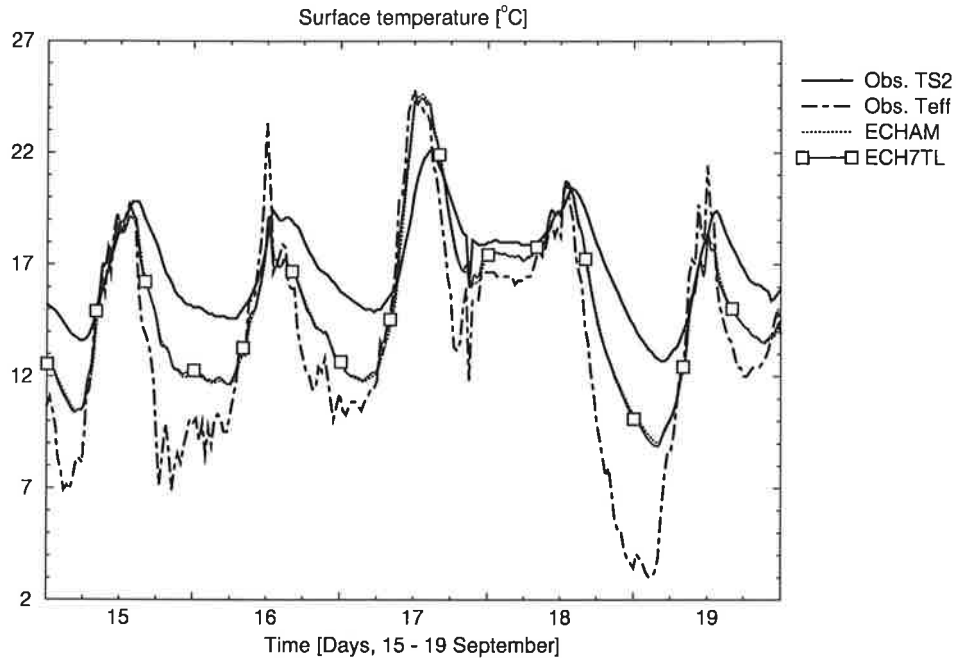
Figure 2.6: Diurnal cycles of soil temperature T_{S2} measured at a depth of 2 cm and observed surface radiative (effective) temperature T_{eff} from 15 to 19 September compared to the surface temperatures as simulated by ECHAM and ECH7TL. The observations were made at Cabauw.

the profiles are similar in both model versions. So the reproduction of the soil temperature profile does not change with the spatial resolution of the numerical scheme which is used to solve the heat conduction equation. This is a successful quality check for the numerical scheme.

But nevertheless, there is the tendency that the higher resolution scheme ECH7TL is closer to the observed profile. This can be seen, for example, in Fig. 2.5f, when in the cooling phase of the day the temperature of the first layer of ECH7TL has already been decreased below the temperature of the second layer, while this change in the profile can not be resolved by the thicker layers of ECHAM. However, here it can be concluded that there is only very little difference between the first soil layer temperature and the surface ground heat flux as simulated by ECHAM and ECH7TL (cf. Figs. 2.6 and 2.4). This means that the temperature of the top soil layer T_1 is mainly determined by the surface energy balance which is dominated by the atmospheric fluxes, but the use of layers with finite depths for the soil thermal discretization prevents T_1 from being able to closely follow the diurnal variations of T_{eff}. In ECHAM and ECH7TL these layers are still to deep. Using a finer discretization with a higher number of thinner layers would reduce the problem, but this would be computationally too expensive and would require shorter time steps for accuracy reasons, which is not acceptable for GCM applications. More suitable are the methodologies as used in SECHIBA or SSiB, or a so-called skin temperature formulation as presented by Viterbo and Beljaars (1995).

Now the total net radiation R_n which is given by (1.2) shall be considered. From the variables and parameters in this equation only the surface temperature T_S is computed by
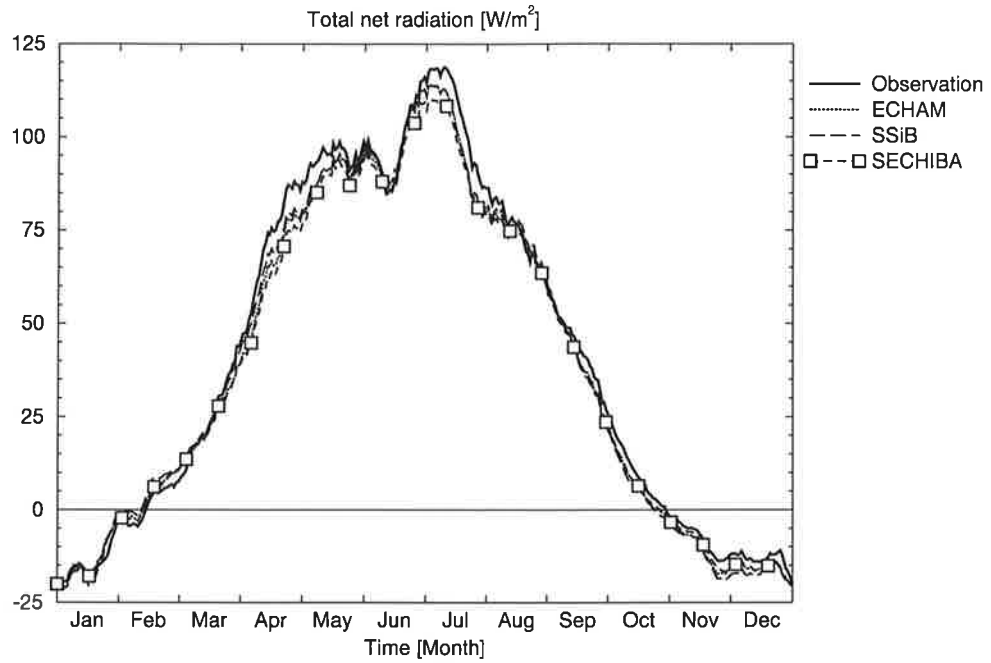
Figure 2.7: Annual cycle of total net radiation as observed at Cabauw compared to the model results of ECHAM, SSiB and SECHIBA. The curves were smoothed using a 31-day running mean.
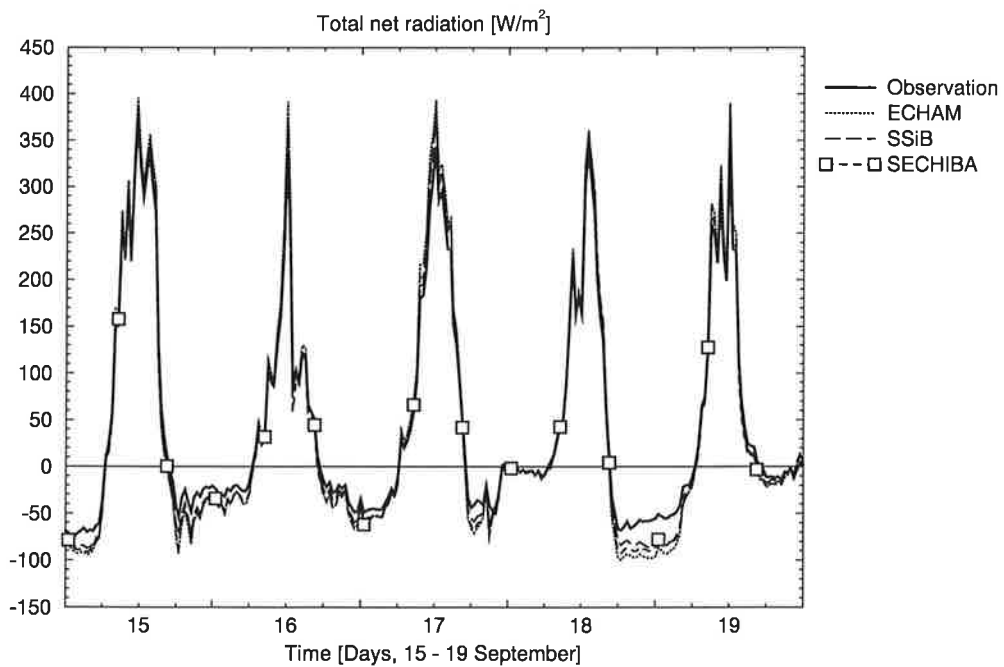
Figure 2.8: Diurnal cycles of total net radiation as observed at Cabauw from 15 to 19 September compared to the model results of ECHAM, SSiB and SECHIBA.
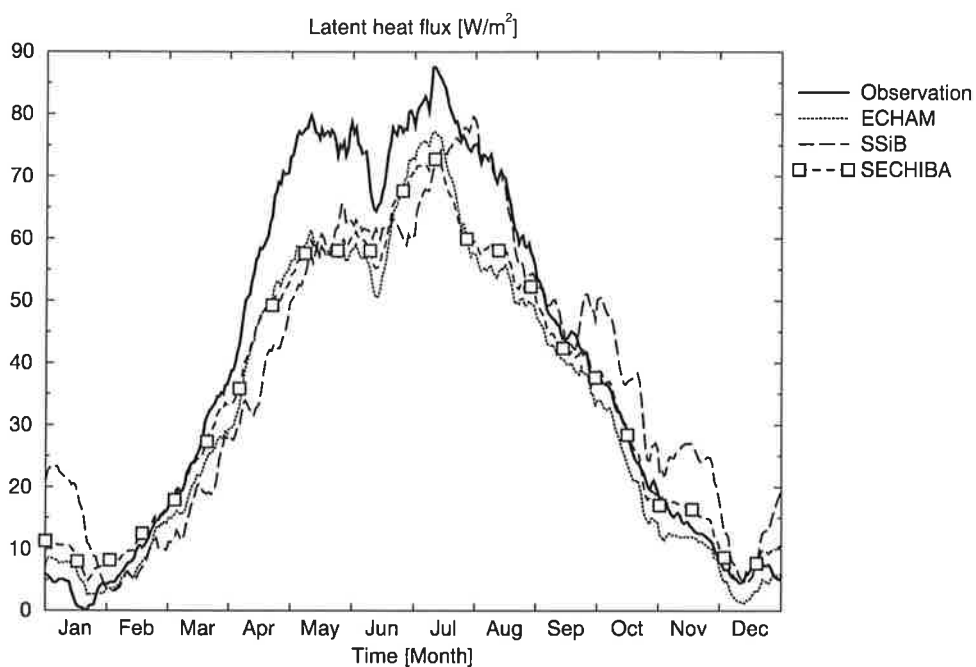
Figure 2.9: As Fig. 2.7 but for latent heat flux.
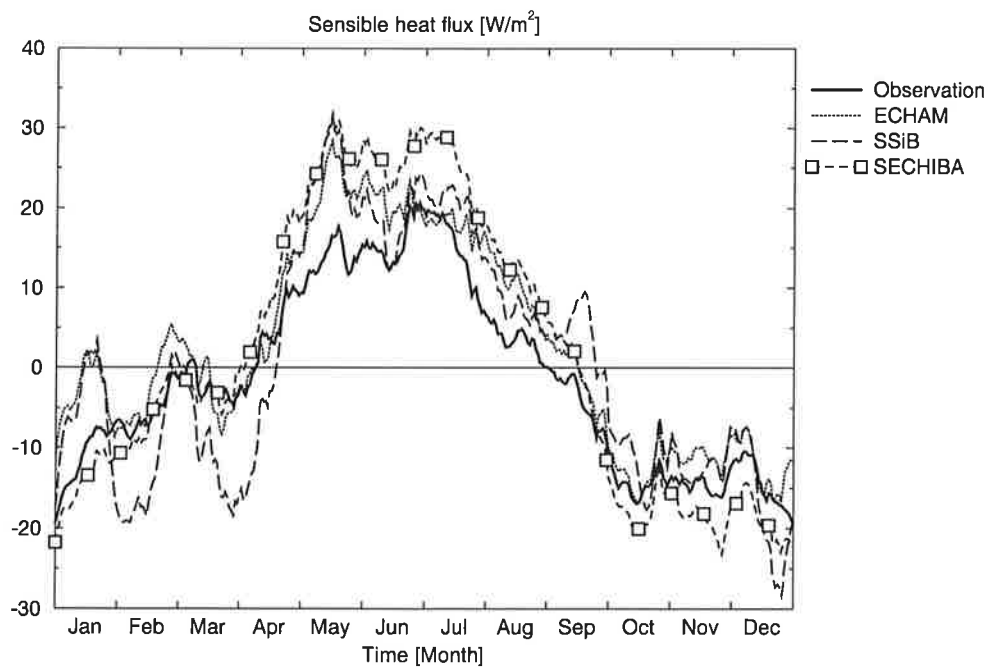
Figure 2.10: As Fig. 2.7 but for sensible heat flux.

the models. The downward radiation components are part of the atmospheric forcing, and ϵ and σ are constants. In ECHAM and SECHIBA the albedo α_S is set to the Cabauw estimated value 0.25 (in the absence of snow). In SSiB α_S is predicted every time step with diurnal variation, but the daily mean surface albedo is constrained to be close to 0.25. As shown in Fig. 2.7, R_n has a distinct seasonal cycle with a minimum of -20 W m^{-2}, on the basis of the 31-day running mean, in January and a maximum of 120 W m^{-2} in July representing the solar forcing. The observed annual mean value is 39.2 W m^{-2}, the simulated values are 38.1 W m^{-2} for ECHAM, 37.4 W m^{-2} for SECHIBA and 38.5 W m^{-2} for SSiB. The model curves are very close to each other and are also in good agreement with the Cabauw observations during most of the year. The models underestimate the net radiation by up to 10 W m^{-2} during some periods from April to July and from September to January. This is consistent with the simulated surface temperatures which are up to 2°C higher than the observed T_{eff}. Higher surface temperature causes enhanced upward longwave radiation, and the result is a decreased total net radiation if the other radiation components are fixed. The same behaviour is shown by the three models also on a diurnal timescale (cf. Fig. 2.8). Similar results were found by Betts et al. (1993).

Figure 2.9 illustrates the seasonal cycles of observed and modeled latent heat fluxes. The observation shows a minimum in January and two maxima in May and July. The three models roughly reproduce this evolution, but they underpredict the latent heat flux in spring and summer. ECHAM shows an underprediction over the entire year except January, SECHIBA in the months from April to August and SSiB from February to August. But from September to January SSiB simulates a too-high evaporation. SECHIBA also allows for a small overprediction in winter except in December. Underestimation by the models in spring and summer amounts to up to 20 W m^{-2}. This is also represented by the annual means of latent heat flux which is 40.5 W m^{-2} for the observation and 38.0 W m^{-2} for SSiB, followed by 35.7 W m^{-2} for SECHIBA, and 33.3 W m^{-2} for ECHAM.

SECHIBA and ECHAM are in agreement with each other and in good agreement with the observations concerning the phase of the annual cycle of latent heat flux. They show a maximum in May–June, which is followed by a coincident local minimum in the middle of June and a second maximum in July. SSiB's latent heat flux evolves differently. There is no local minimum in the middle of June, but two weeks later, and the second summer maximum is also delayed by more than two weeks. From the comparison to the annual cycle of sensible heat flux (Fig. 2.10) it becomes clear that SSiB's missing local minimum in latent heat flux in the middle of June is balanced by the sensible heat flux. Figure 2.10 shows a local minimum of sensible heat flux predicted by SSiB at that time which is less pronounced in the other model simulations or the observations.

The sensible heat flux is negative in winter and positive in summer. The models tend to be close to the observations in the months from October to April, but their behaviour is different. For instance, from January to April ECHAM and SSiB show some variations, and SSiB is somehow oscillating around the observation; on the other hand, SECHIBA agrees very well with it during this period. All three schemes overestimate the sensible heat flux during the summer months from May to September by up to 20 W m^{-2}. The observed annual mean is -1.3 W m^{-2}. ECHAM computes the highest annual mean at 2.6 W m^{-2} followed by SECHIBA with 1.6 W m^{-2} and then SSiB with 0.4 W m^{-2}.

From these considerations it becomes clear that the models show deficiencies in estimating the partitioning of the net radiation into latent and sensible heat flux, which are most obvious

in the summer. In this period the models show a systematic trend to underestimate latent heat flux and overestimate sensible heat flux. In the summer months ECHAM and SECHIBA behave similarly concerning the phase of variations of latent and sensible heat flux. SSiB shows a different phase, most obvious in latent heat flux. This distinctly different behaviour of the models is partly due to the different model structures applied to the surface moisture fluxes. This will be discussed in the next section.

2.2.2 Surface water balance

Figure 2.11 shows the annual evolution of the *relative plant-available soil moisture* in the root zone as computed by the different schemes. For the calculation of this variable, we first subtract the wilting level (see (1.7)) from the root zone soil water content, as simulated by the models, and from the field capacity, and then divide both quantities by each other. This means if the relative plant-available soil moisture is 0%, then the soil is at the wilting level (i. e. there is still moisture stored in the soil that is unavailable to plants). A relative soil moisture of 100% means that the soil is at field capacity. For the bucket-type models, ECHAM and SECHIBA, the field capacity is taken as the maximum soil water content. For SSiB the maximum value is the total saturation. This allows relative soil moisture values of more than 100% for SSiB. ECHAM and SECHIBA simulate annual cycles of soil moisture with maxima in January of more than 97% for ECHAM and 100% for SECHIBA and minima in July of about 36% and 68%, respectively. SSiB's relative soil water content stays in the range between about 98% and 119% throughout the year without showing an annual cycle. This was expected because the lowest soil layer was set to total saturation at every time step (cf. Chen et al. 1997), and this prohibits any rapid downward transport of soil water from the upper layers and acts as a restoring reservoir when the soil water in the upper layers is depleted by evapotranspiration. The annual mean relative plant-available soil moisture is highest in SSiB with 104.4% followed by SECHIBA with 96.1% and ECHAM with 75.1%.

Figures 2.12 to 2.14 show the annual cycles of precipitation, evapotranspiration, root zone drainage and surface runoff for the ECHAM, SECHIBA and SSiB models. The data were smoothed using a 31-day running mean. The precipitation is part of the atmospheric forcing that was used to drive the schemes and is therefore the same for each model. Precipitation is frequent during the whole year with an annual total of 776 mm. The maximum rainfall rate is 4 mm d^{-1} when filtered with a 31-day running mean. Daily mean values reach up to 23 mm d^{-1}. The three other quantities were simulated by the models.

In ECHAM there is a close correspondence of surface runoff to precipitation regarding the phase (cf. Fig. 2.12). If there is high or low precipitation, there is also enhanced or reduced runoff, respectively. The amplitude of runoff depends on precipitation rate and soil moisture. The Arno scheme, which is used in ECHAM, allows saturation of the soil to occur in parts of a grid element. The higher the soil water content, the larger the fraction of saturated area and the higher the part of precipitation that will go into surface runoff. This is reflected in Fig. 2.12. The ratio of runoff to precipitation is higher in March than in May–June, for instance. The reason is that in March the soil water content is higher than in May–June (Fig. 2.11).

The drainage rate is substantial from October to April. During the rest of the year it is almost zero. In ECHAM drainage rises linearly with the plant-available soil moisture between 0% and 75.7%. These are empirical threshold values. Above the 75.7% level drainage rises
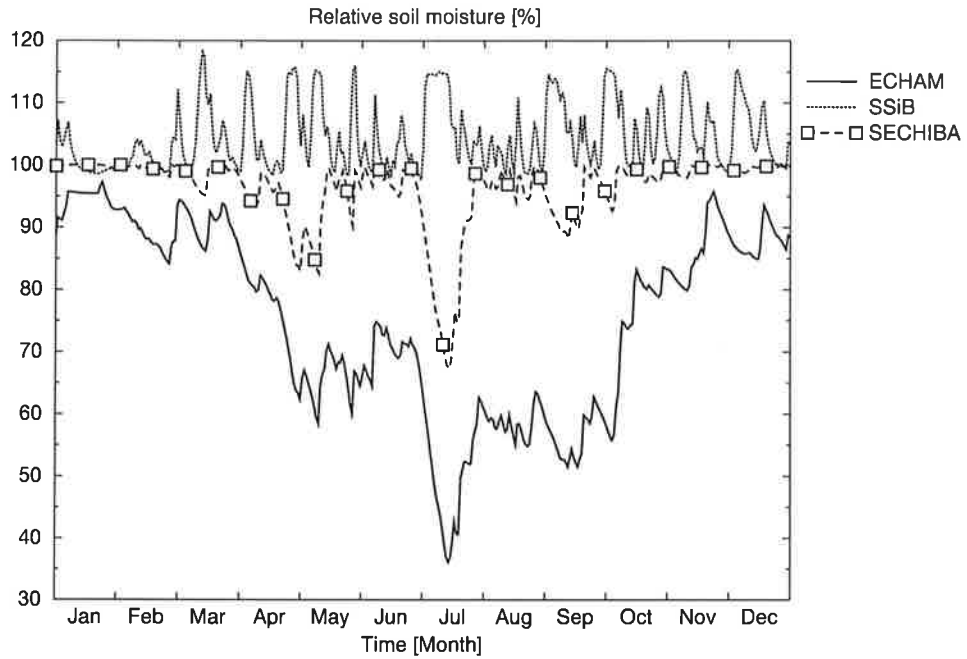
Figure 2.11: Annual cycles of relative plant-available soil moisture in the root zone for ECHAM, SSiB and SECHIBA. Shown are unsmoothed daily means.
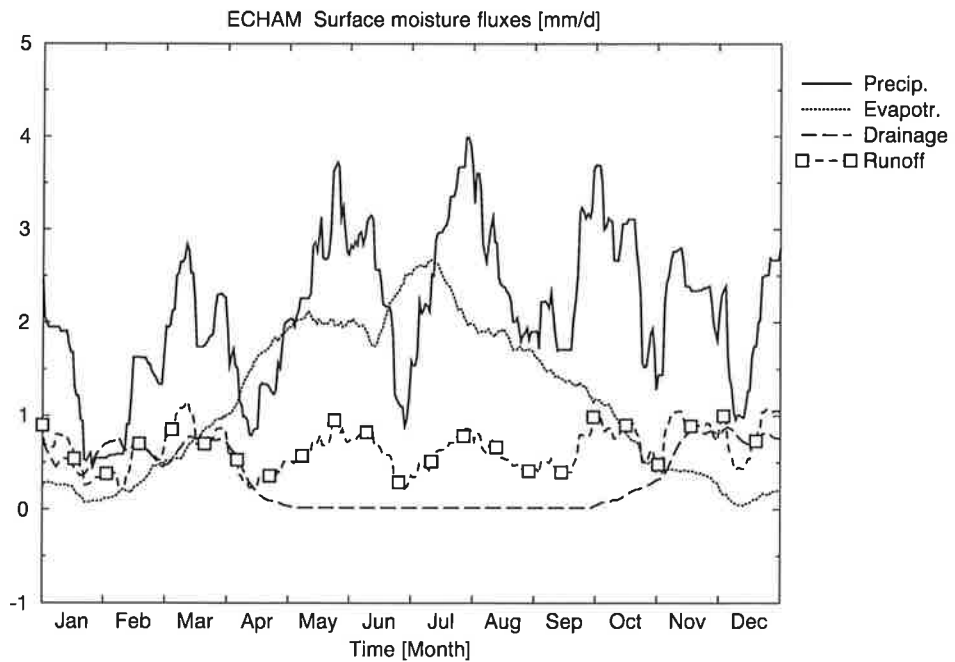
Figure 2.12: Annual cycles of precipitation, evapotranspiration, root zone drainage and surface runoff for ECHAM. The curves were smoothed using a 31-day running mean.
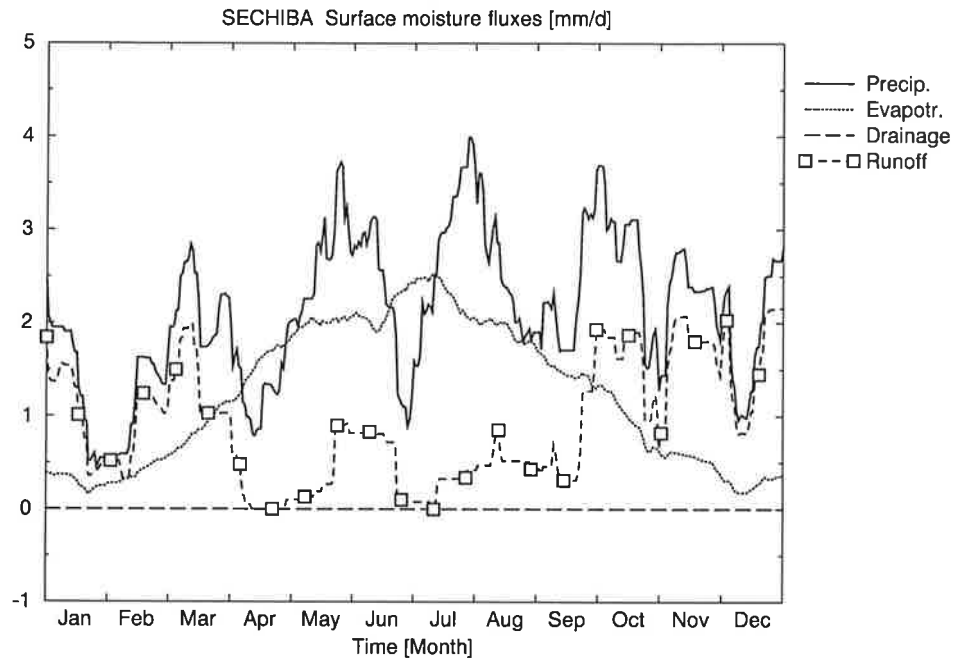
Figure 2.13: As Fig. 2.12 but for SECHIBA.
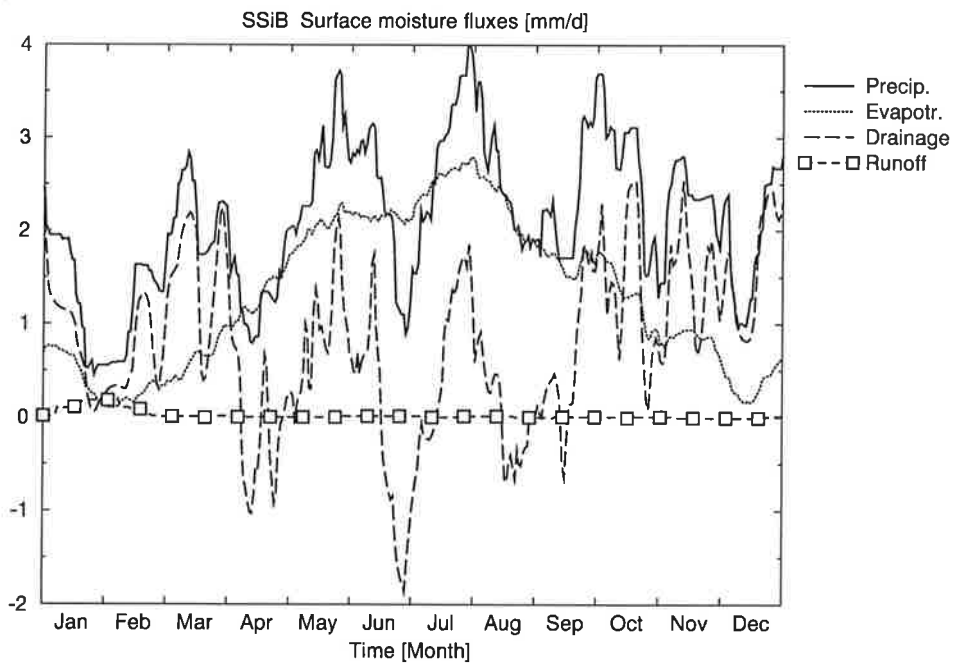
Figure 2.14: As Fig. 2.12 but for SSiB.

rapidly as a potential function. So the drainage rate is consistent with the evolution of soil moisture content that drops below 75.7% in April and exceeds this value again in October (Fig. 2.11). Observations of the root zone drainage at Cabauw are not available. Typical drainage rates observed at other sites are 0.6 mm d^{-1} in the Vindelälven catchment (Sweden) which was derived from meteorological observations (Hagemann and Dümenil 1998) and 0.5 to 0.8 mm d^{-1} in the catchments of Bothnian Bay and Bothnian Sea in winter (S. Hagemann 1996, pers. comm.; data provided by Carlsson). There is a good agreement with the ECHAM simulations at Cabauw (Fig. 2.12).

A comparison of Figs. 2.12 and 2.1 shows that the annual variations of evapotranspiration in ECHAM closely follow that of solar radiation.

Figure 2.13 shows the surface moisture fluxes of SECHIBA. The runoff has a similar phase relation to precipitation to ECHAM. But the amplitude has an annual cycle which is much more pronounced than in ECHAM. During the months from November to March a high part of the precipitation runs off. The reason is that in this period of time, the soil moisture is close to its maximum value (Fig. 2.11), so very little water can infiltrate. In April, the first half of May and in July runoff is lower than in ECHAM. In the second half of May and in June and August runoff is similar to ECHAM. These changes are due to the overflow runoff formulation in SECHIBA. In April–May and July soil moisture is reduced in both models because of decreased precipitation and simultaneously increasing evapotranspiration. The Arno scheme in ECHAM still produces substantial runoff in this situation, as previously discussed. But in SECHIBA soil moisture has to reach its maximum value again before runoff is produced. So ECHAM's surface runoff in summer closely follows the phase of precipitation, while the onset of the runoff in SECHIBA is a bit delayed due to the runoff scheme.

Due to the formulation of the Choisnel scheme SECHIBA has no root zone drainage. Similar to ECHAM the evolution of evapotranspiration is mainly determined by the amount of incoming solar radiation.

It can not be decided whether the surface water balance simulated by ECHAM or by SECHIBA is more realistic for the Cabauw site because there are no observations available for surface runoff, drainage and soil water content. According to Beljaars and Bosveld (1997) the Cabauw site is very wet during almost the entire year. Therefore, the annual cycle of the soil moisture simulated by SECHIBA seems to be more realistic than the one by ECHAM (Fig. 2.11). On the other hand the high water table at Cabauw is the result of a regulation by a system of ditches. It is likely to observe an annual cycle of soil moisture as the one by ECHAM at a different site in central Europe with flat terrain but without artificial soil moisture regulation.

In Fig. 2.14 SSiB's surface moisture fluxes are compared to each other. Surface runoff is close to zero throughout the year. This is consistent with the evolution of root zone soil moisture, which is below 70% of the total water-holding capacity during the entire year (Fig. 2.11), as surface runoff is mainly produced by infiltration excess. In contrast to ECHAM and SECHIBA, SSiB's root zone drainage shows a pattern similar to that of precipitation. Maxima and minima in the drainage rate are closely related to periods of high and low precipitation, respectively, throughout the year. During the months of low evapotranspiration from November to March a major part is lost through drainage. But during some periods in April, June and August–September, when precipitation is reduced but evapotranspiration is high, SSiB also allows negative drainage. This represents an upward motion of soil moisture
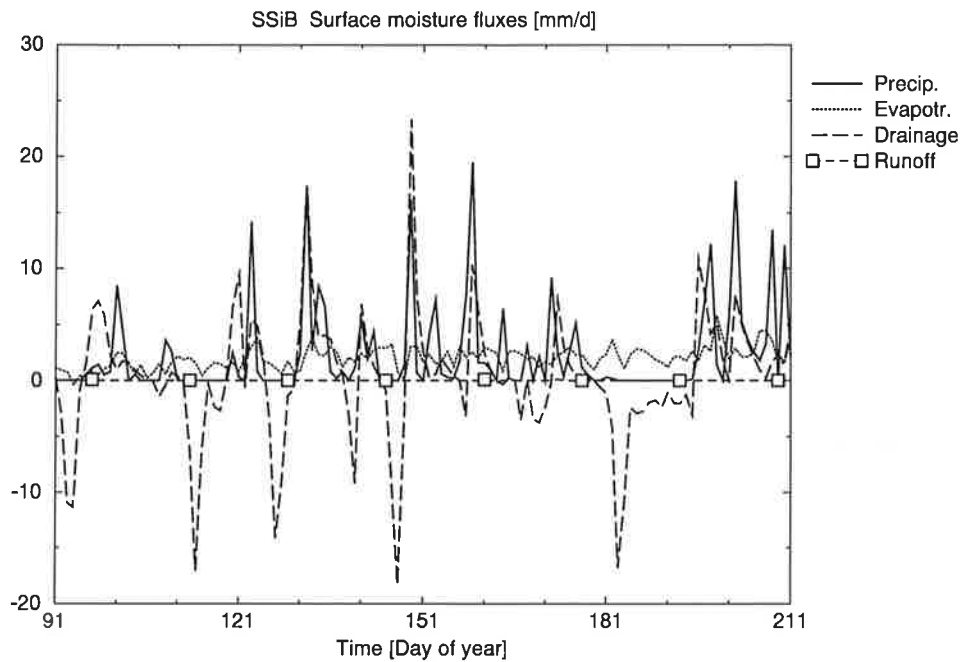
Figure 2.15: Evolution of precipitation, evapotranspiration, root zone drainage and surface runoff during the period from day 91 to day 211 as simulated by SSiB. Shown are unsmoothed daily means.
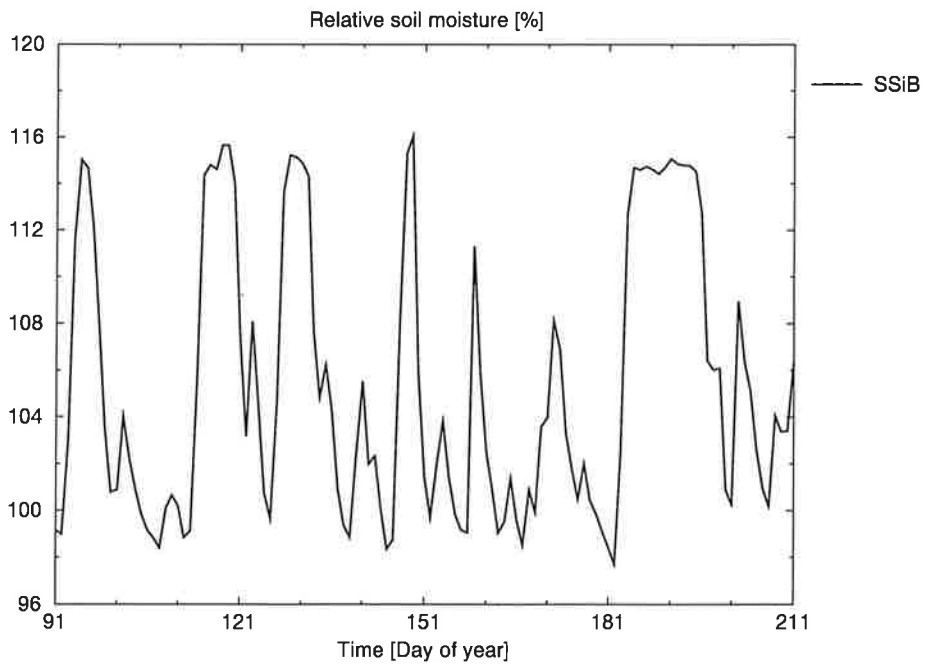
Figure 2.16: As Fig. 2.15 but for relative plant-available soil moisture in the root zone.

into the root zone which is possible because the exchange between the soil layers in SSiB is formulated as a diffusive process. SSiB is the only one of the three schemes compared in this study which allows recharge from the water table.

A comparison of Figs. 2.15 and 2.16 shows the relationship between precipitation, root zone drainage and soil moisture in SSiB in more detail. In these figures, daily means of the surface moisture fluxes and the relative plant-available soil moisture are compared for a period of 120 days starting from day 91. Precipitation events are often accompanied by downward drainage. Rises of soil moisture are caused by precipitation events or, apparently more often, by upward drainage. Reductions result from evapotranspiration or downward drainage. So in ECHAM and SECHIBA soil moisture is mainly influenced by precipitation and evapotranspiration, thus showing a distinct annual cycle; however, in SSiB the root zone drainage obviously plays an important role in the regulation of soil moisture. This is held at an almost constant value. In this context we have to emphasize that SSiB's lowest soil moisture layer was set to saturation during the entire simulation, as requested by the PILPS instructions (cf. Chen et al. 1997). Therefore, the water table stayed at a depth of 1 m, and water supply for the upward water motion from the recharge layer into the root zone was never restricted. This was supposed to represent the conditions at the Cabauw site. This feature may not be representative for SSiB in general but rather site or simulation dependent.

Another feature of the simulation results of SSiB can be identified from the comparison of Figs. 2.12 and 2.14. As mentioned before, evapotranspiration in ECHAM is mainly determined by the incoming solar radiation with maxima at the beginning of May and in the first half of July. In contrast to this, evapotranspiration in SSiB follows more closely the precipitation rate. Both quantities show maxima simultaneously in the second half of May and at the end of July. The annual variations correspond to each other also during the rest of the year. This different behaviour of SSiB gives rise to differences in the Bowen ratio compared to ECHAM and SECHIBA (cf. discussion in sections 2.2.1 and 2.3.1).

The results in Figs. 2.11–2.14 show that all three schemes have relatively similar annual cycles of simulated evapotranspiration. However, for the other hydrological components, each of the model simulations can be quite different. The surface runoff and drainage of ECHAM and SECHIBA show moderate variability, while their root zone soil moisture undergoes a pronounced annual cycle. In SSiB this is the other way around: the root zone soil moisture varies only in a small range, while the root zone drainage shows an annual cycle with a high variability. Although the models behave very differently internally, they are able to respond to the atmospheric forcing in a similar way.

2.3   Model sensitivity studies

In this section it shall be investigated if the underestimation of latent heat flux and overestimation of sensible heat flux in summer is due only to the systematic deficiencies in the parameterizations of the three models or if also a more careful choice of the appropriate parameter values for a realistic representation of the conditions at the Cabauw site can improve the simulations.
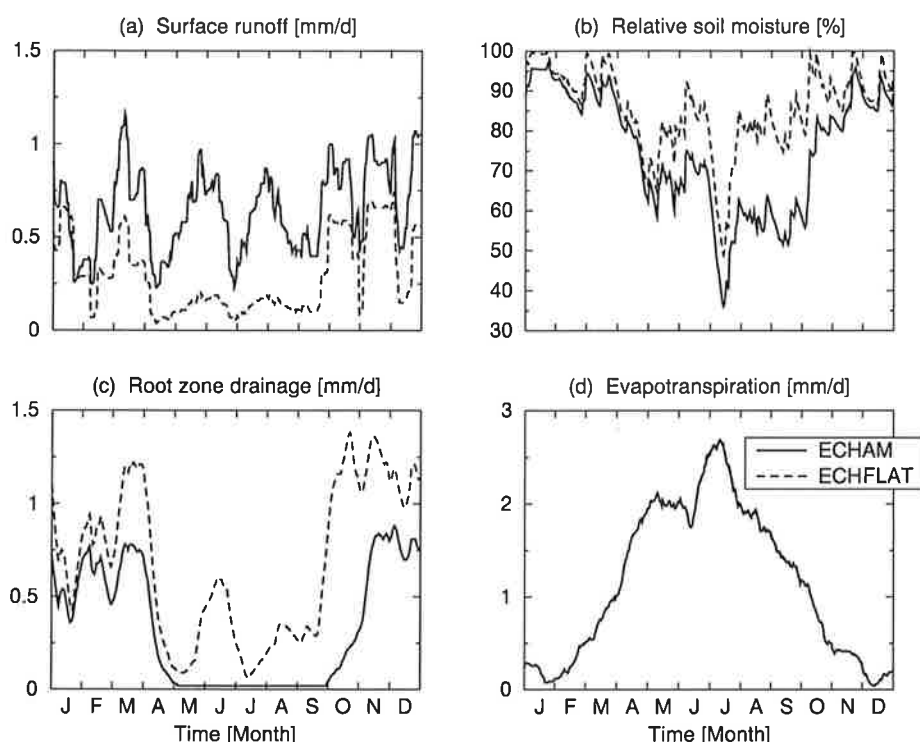
Figure 2.17: Comparison of the annual cycles of (a) surface runoff, (b) relative plant-available soil moisture, (c) root zone drainage and (d) evapotranspiration simulated by ECHAM and ECHFLAT. The curves were smoothed using a 31-day running mean except in (b).

2.3.1 Surface water balance

One could argue that due to the Arno scheme, runoff is calculated too high in ECHAM so that there is not enough water left for evapotranspiration. This could explain why evapotranspiration is underestimated. In ECHAM a structure parameter of $B = 0.2$ is used. This is a typical average value representing a moderate steepness of the terrain. Model version ECHFLAT uses a value of $B = 0.025$, that indicates a very flat terrain which may be more appropriate for the Cabauw site. Figure 2.17 shows that in fact surface runoff is reduced in ECHFLAT. More precipitation can infiltrate into the soil so that the relative plant-available soil moisture stays higher during the entire year. But as a result, the drainage rate is increased, in particular from October to March. The evapotranspiration itself is, however, almost insensitive to the variation of the structure parameter. The reason is that the relative plant-available soil moisture in ECHAM and ECHFLAT stays above the threshold value of the critical soil moisture (33.3% of the plant-available soil moisture) all year. Below this value, transpiration will be reduced by soil water stress; above this value, there is no water stress. In general, little differences in evapotranspiration between ECHAM and ECHFLAT are due to a changed bare soil evaporation which depends on relative soil moisture, but the fraction of bare soil in the grid area is very small. Therefore, this is not a way to improve the simulated annual cycle of latent heat flux for this particular site simulation.

Figure 2.18 shows the annual evolution of latent heat flux as a result of a changed minimum stomatal resistance r_{st0} (model version ECHEVAP) and maximum canopy water content W_{lmax} (version ECHWL). A reduction of r_{st0} and/or an increase of W_{lmax} gives higher
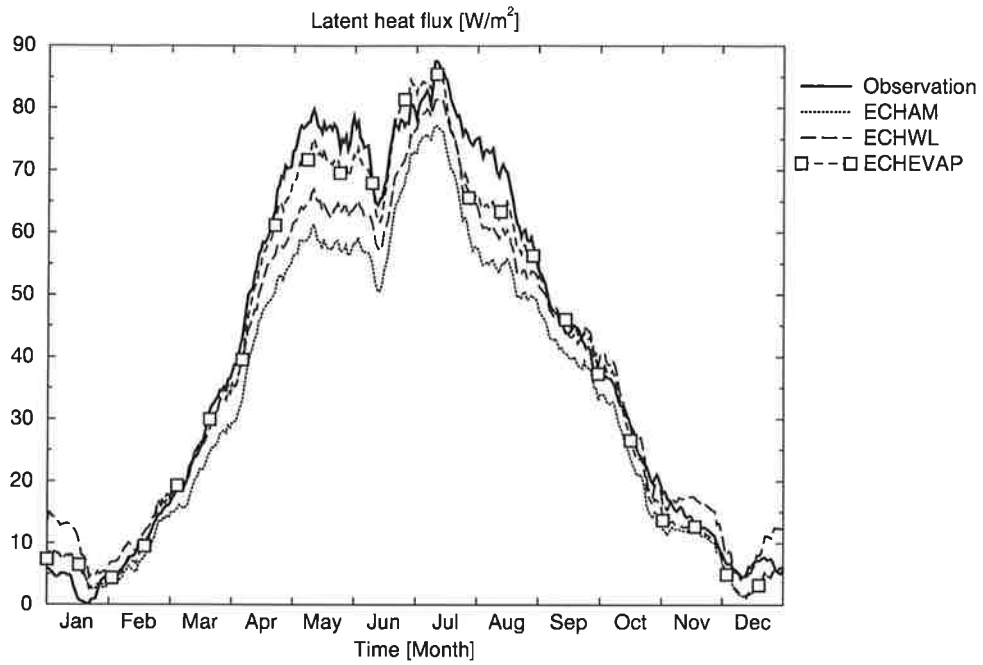
Figure 2.18: Annual cycle of latent heat flux as observed at Cabauw compared to the results of the models ECHAM, ECHWL and ECHEVAP. The curves were smoothed using a 31-day running mean.
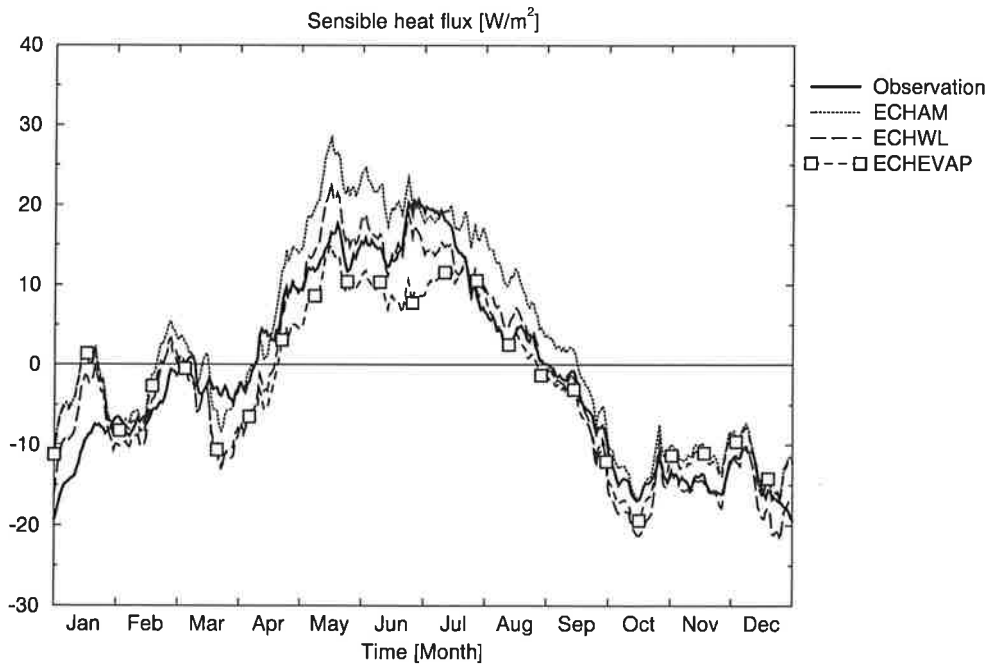
Figure 2.19: As Fig. 2.18 but for sensible heat flux.
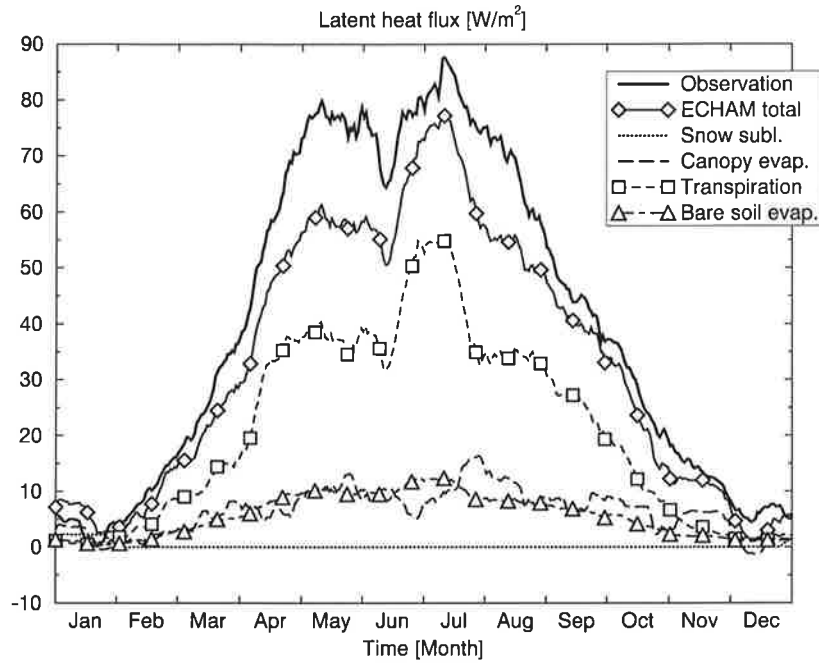
Figure 2.20: Contributions of snow sublimation, canopy evaporation, transpiration and bare soil evaporation to the total latent heat flux for ECHAM compared to the Cabauw observed latent heat flux. The curves were smoothed using a 31-day running mean.
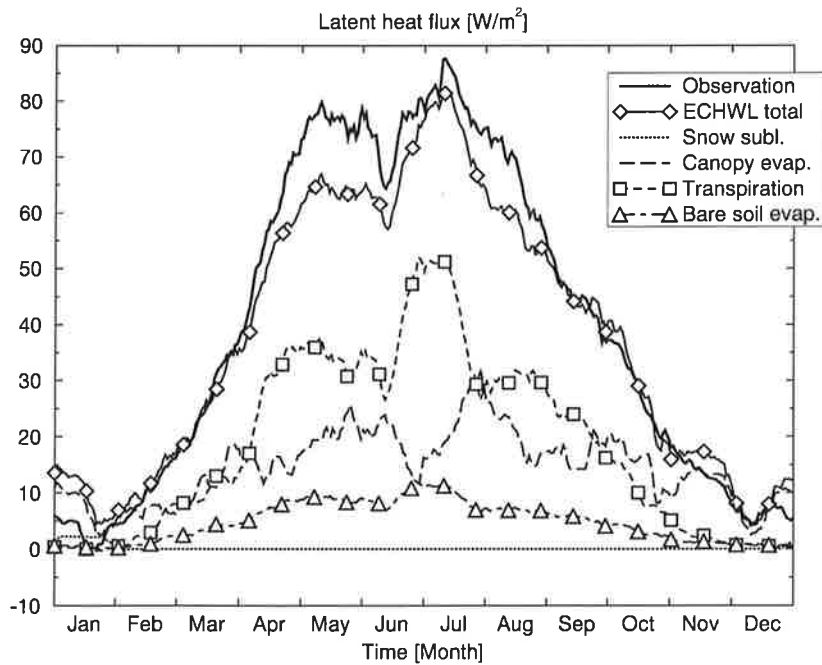
Figure 2.21: As Fig. 2.20 but for ECHWL.
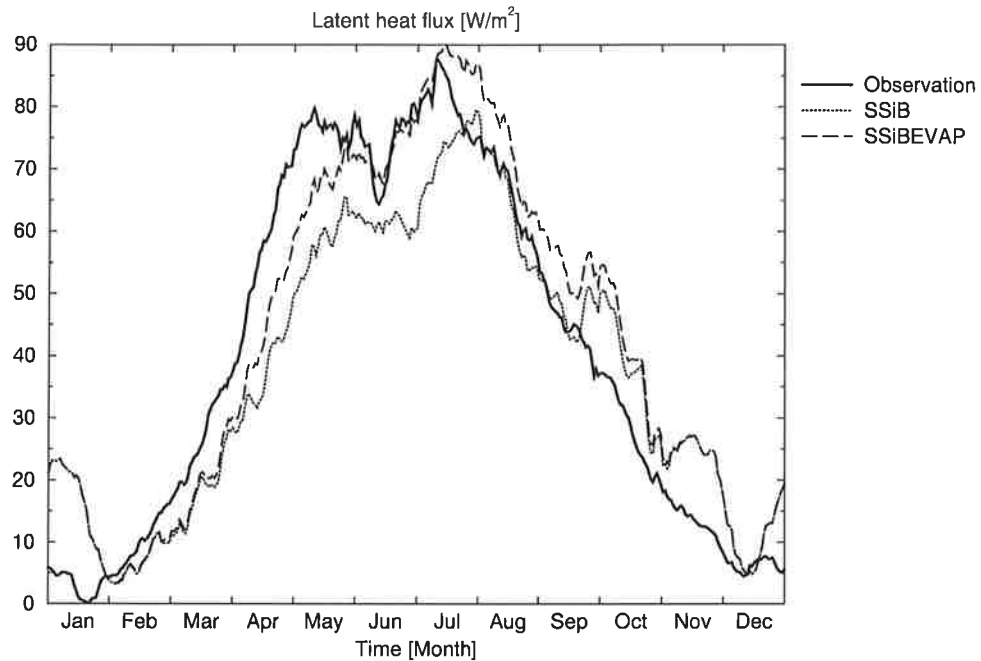
Figure 2.22: Annual cycle of latent heat flux as observed at Cabauw compared to the results of the models SSiB and SSiBEVAP. The curves were smoothed using a 31-day running mean.

evapotranspiration and lower sensible heat flux (cf. Fig. 2.19). The sensitivity to r_{st0} is greater than to W_{lmax} since a relatively smaller change has an even larger effect. The reason is that r_{st0} determines the stomatal resistance which controls transpiration, which is the major component of the latent heat flux in the simulations. This is illustrated by Fig. 2.20, which shows the contributions of snow sublimation, canopy evaporation, transpiration and bare soil evaporation to the total latent heat flux for ECHAM. The increase of the total latent heat flux in ECHWL in comparison to ECHAM is mainly due to an enhanced canopy evaporation, while the transpiration is reduced (cf. Figs. 2.20 and 2.21).

As seen in Fig. 2.18, latent heat flux (as computed from the ECHAM scheme) can be improved by prescribing a more appropriate stomatal resistance for the Cabauw ground cover than was specified in the PILPS study initially. The PILPS instructions specified the constant c and the LAI from which the stomatal resistance is computed (cf. section 1.1). In the original SiB scheme (Sellers et al. 1986), from which the stomatal resistance formulation in ECHAM was derived, the stomatal resistance of the standard ground cover (biome type 7) is calculated using a value of $c = 110$ s m^{-1}. This biome type was assumed to be appropriate for the Cabauw site. On the other hand, Dorman and Sellers (1989) indicate a different biome type for the location of Cabauw in their global dataset (i. e. broadleaf–deciduous trees with winter wheat, biome type 12). The ground cover part of this biome type has a value of $c = 25$ s m^{-1}. At Cabauw, this ground cover would be appropriate to match the observations. Koster (1995, pers. comm.) reports that the land surface scheme MOSAIC (Koster and Suarez 1992) gives better results when using the parameter set of this biome type. MOSAIC has a formulation of stomatal resistance similar to SiB. The ECHAM3 standard model uses the

combination of LAI = 4 and $c = 100$ s m^{-1} for all land points in the global GCM covered with vegetation. The PILPS instructions require a major change to LAI = 1.3 (annual mean) for the Cabauw site but specify only a small change to $c = 110$ s m^{-1}. As it uses an algorithm different from the original SiB, ECHAM requires a consistent modification of the c parameter in order to operate in a realistic way. The scheme gives best results for latent heat flux if a value of $c = 40$ s m^{-1} is chosen, as is shown in Fig. 2.18 for model version ECHEVAP. For an incoming solar radiation of 900 W m^{-2}, which is about the maximum value at the Cabauw site, the minimum stomatal resistance r_{st0} in model version ECHAM is 95 s m^{-1}, while it is 41 s m^{-1} in version ECHEVAP. The latter value compares very well with the observations of Russel (1980), which show surface resistance values of 40 s m^{-1} for a well-watered pasture.

Figure 2.22 compares the annual evolution of the latent heat flux as observed at Cabauw and the simulations of SSiB and the slightly modified model version SSiBEVAP. In SSiBEVAP a parameter value of $c = 25$ s m^{-1} is used (for reasons mentioned before). The value of the albedo computed by the model became lower than the value of 0.25 prescribed by PILPS. Therefore, in SSiBEVAP the albedo was adjusted to fit as closely as possible 0.25 for non snow-covered conditions. With these modifications the model's variations of evapotranspiration in the summer are in better agreement with the observations and ECHAM and SECHIBA. In particular, the simulation better meets the observed local minimum in June and the maximum in July. This seems to confirm the results of Koster as mentioned before. Why the evapotranspiration in SSiBEVAP in autumn and winter still follows the precipitation rate, such as SSiB does during the entire year, is not clear at this stage and is currently under investigation. In this context the root zone drainage seems to be important as it plays a major role in the regulation of soil moisture and is also likely to affect the evapotranspiration (cf. discussions in section 2.2.2 and Xue et al. 1996).

Sensitivity studies similar to the one conducted with ECHEVAP have shown that SECHIBA's latent heat flux also gets very close to the observations when the minimum stomatal resistance is reduced (V. Quiniou 1995, pers. comm.).

2.3.2 Surface energy balance

In the two modified versions of ECHAM which are presented in this section (ECHTEMP and ECHVARI (cf. Table 1.1)), a changed parameter value of $c = 40$ s m^{-1} as in ECHEVAP is used because, as in the section before, this value was found to be more appropriate for the Cabauw site. Therefore, a more realistic simulation is expected. The temperature top soil layer has an inertia that is due to the discretization of the soil layers in ECHAM. For this reason the ground heat flux tends to be too large in ECHAM (cf. section 2.2.1). This behaviour is also characteristic for the earlier version of the ECMWF scheme and is documented by Betts et al. (1993). As a consequence there is not enough energy left for the turbulent surface fluxes. This is obvious, for example, for ECHEVAP in the summer when the sum of simulated latent and sensible heat fluxes is less than observed (cf. Figs. 2.23 and 2.24).

One way to reduce the simulated ground heat flux is to decrease the soil thermal conductivity λ (cf. model version ECHTEMP). This consequently enhances the amplitude of the diurnal variations of the surface soil temperature (see Fig. 2.25). The simulated surface temperature gets closer to the observed effective radiative surface temperature, even closer than in SSiB and SECHIBA (cf. Fig. 2.3). This reduces the deviations of the simulated sensible heat flux especially in summer. But the feature remains that the diurnal evolution of the
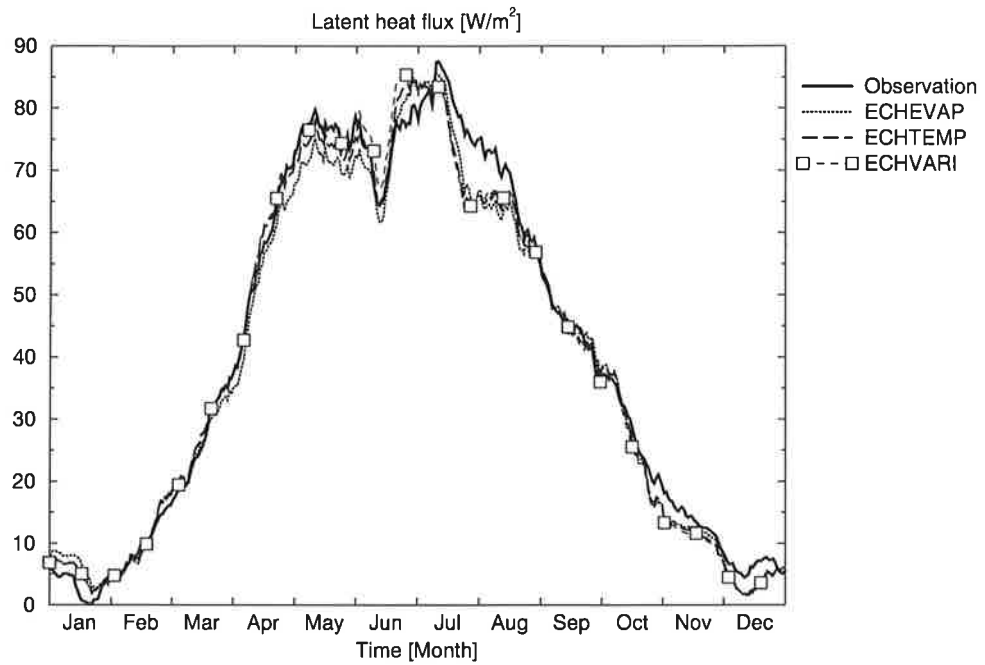
Figure 2.23: Annual cycle of latent heat flux as observed at Cabauw compared to the results of the models ECHEVAP, ECHTEMP and ECHVARI. The curves were smoothed using a 31-day running mean.
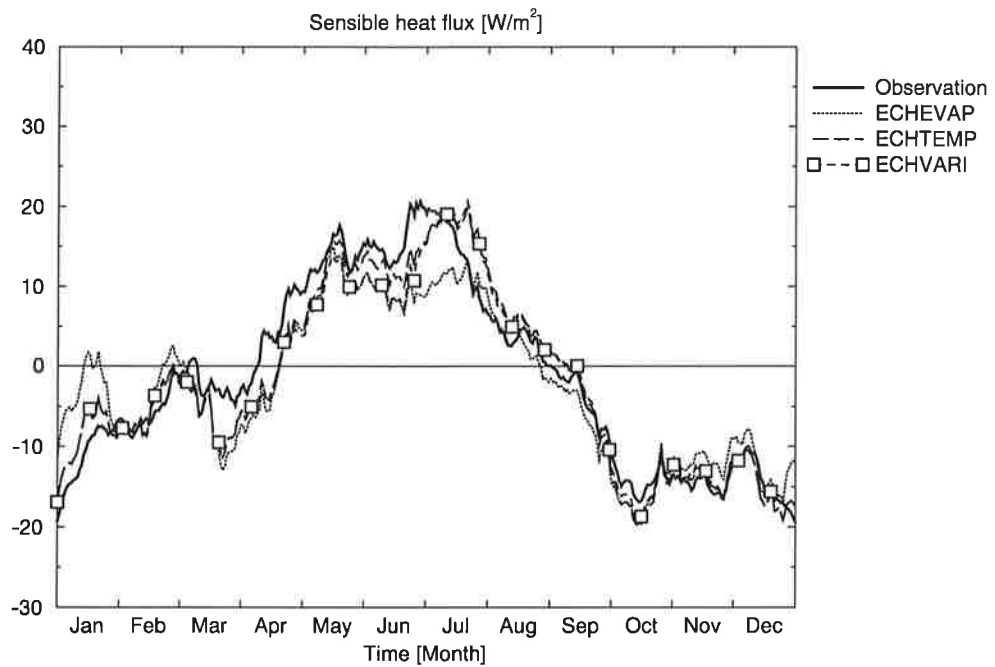
Figure 2.24: As Fig. 2.23 but for sensible heat flux.
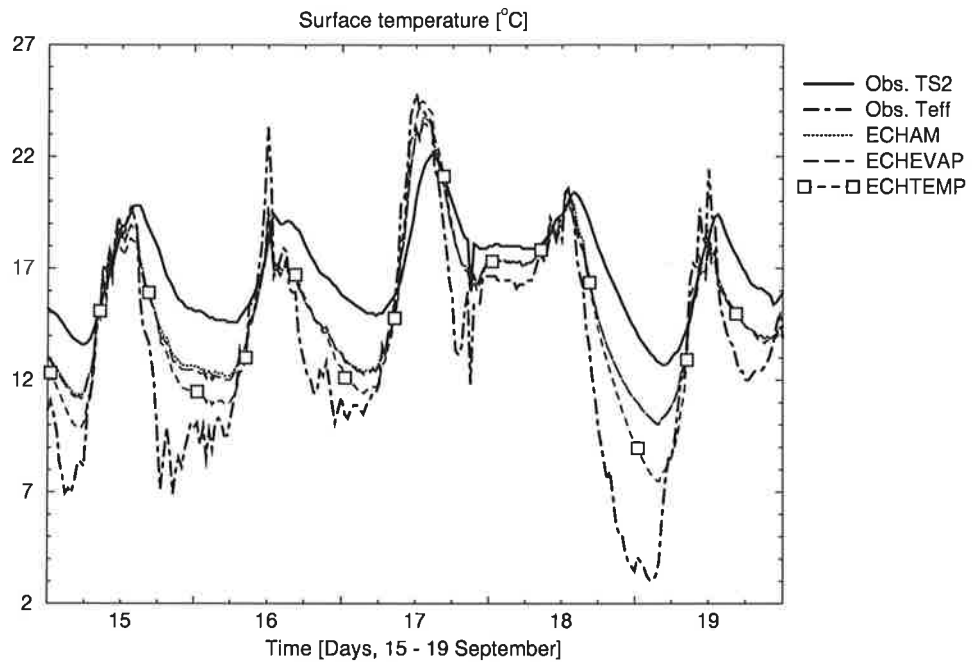
Figure 2.25: Diurnal cycles of soil temperature T_{S2} measured at 2-cm depth and observed surface radiative (effective) temperature T_{eff} from 15 to 19 September compared to the surface temperatures as simulated by ECHAM, ECHEVAP and ECHTEMP. The observations were made at Cabauw.
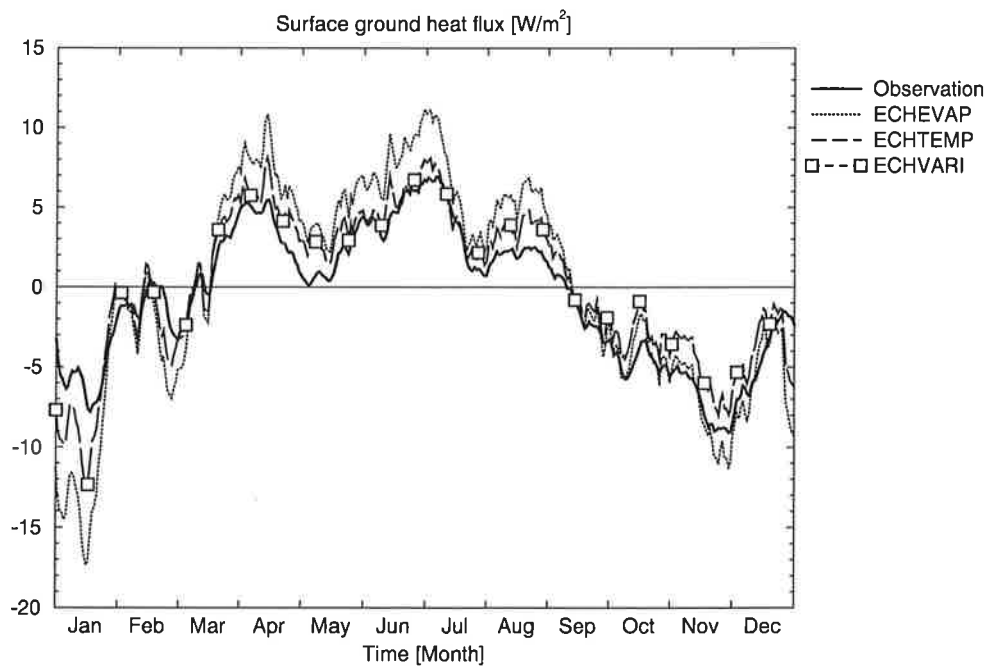
Figure 2.26: As Fig. 2.23 but for surface ground heat flux. ECHTEMP and ECHVARI show almost identical evolutions.

simulated surface temperature is delayed in phase compared to the observed T_{eff} (cf. Fig. 2.25). Due to the model structure this has to be expected. This can only be improved by changing the model structure, for example, by introducing a near-surface soil or vegetation layer with a small response time or a skin temperature as in Viterbo and Beljaars (1995). SSiB makes use of an independent canopy temperature, and SECHIBA tries to better represent the soil temperature profile; in fact, both models show a closer phase relation to the observed effective temperature than ECHAM (Fig. 2.3). Nevertheless, ground heat flux is closer to the observed in ECHTEMP (Fig. 2.26) and thus allows a more realistic partitioning of surface total net radiation into ground heat flux and turbulent surface fluxes. Sensitivity tests with the soil heat capacity showed only a very small effect for the simulated surface temperature.

The values that have been chosen for the soil thermal conductivity λ correspond to the cases of wet soil ($\lambda = 2$ W K^{-1} m^{-1} for ECHEVAP) and drier soil ($\lambda = 1$ W K^{-1} m^{-1} for ECHTEMP). They may be compared to the results of Beljaars and Bosveld (1997) who show an annual time series of daily values of λ which they derived from the Cabauw observations. Their results suggest that λ follows a seasonal cycle with higher values in winter and lower in summer. They compare their results to typical values tabulated by Hillel (1982), which cover a similar range as the values used in the different model versions of ECHAM. At about 0.8 W K^{-1} m^{-1}, the "observed" λ given by Beljaars and Bosveld (1997) is systematically lower. At the time of writing they were not able to give a reason for this behaviour. The standard value of λ used in the ECHAM3 GCM at Cabauw is 1.8 W K^{-1} m^{-1}, and in the ECHAM4 GCM 1.7 W K^{-1} m^{-1}. The value of λ used in ECHAM may also be compared to the range of values of λ in the CLASS scheme, where soil thermal conductivity depends on soil moisture (Verseghy 1991). During annual cycle simulations with CLASS for PILPS the interactively computed λ varied in the range between 1.5 W K^{-1} m^{-1} (wet soil) and 1.1 W K^{-1} m^{-1} (drier soil) (D. Verseghy 1995, pers. comm.). Figs. 2.23, 2.24 and 2.26 show that in the summer, when the soil gets drier, the simulated latent, sensible and ground heat fluxes in ECHTEMP are closer to the observations than in ECHEVAP, or both model simulations are almost similar. This may be seen as an indication that the simulation results are expected to be closer to the observations when taking the dependence of the soil thermal conductivity on soil moisture into consideration.

It should be emphasized that the sensitivity study with model version ECHTEMP does not imply that an exact agreement of the simulated surface temperature T_{S} of ECHTEMP and the observed radiative temperature T_{eff} is desired. Due to the model structure T_{S} is the soil temperature of the top 6.5 cm. The study shall only show that, if the interface variable of the land surface scheme to the atmosphere, the surface temperature, is closer to the observed T_{eff}, the ground heat flux and latent and sensible heat fluxes get closer to the observations.

If a time-varying LAI and vegetation ratio are used in ECHAM (as in version ECHVARI), the vegetation effect on evapotranspiration is expected to be represented more accurately than by constant values. Fig. 2.23 shows that the simulated latent heat flux in ECHVARI is even closer to the observation in May than in ECHTEMP. But in June it is overestimated. Correspondingly, sensible heat flux is underestimated during the same period (cf. Fig. 2.24). But in general the simulated turbulent fluxes are not very different in ECHTEMP and ECHVARI for this site. The reason is that two opposing effects tend to compensate each other when the parameters are changed. The increase of the vegetation ratio in May compared to the annual mean (cf. Fig. 1.2) reduces the bare soil part of the grid element and thus reduces

total evapotranspiration. This is due to the fact that in ECHAM daily evapotranspiration from a certain area is lower if it is covered with vegetation instead of bare soil, if the soil is relatively wet. On the other hand, the increase of the LAI enhances transpiration.

For this site and biome type it seems appropriate to use constant values for the parameters mentioned above. But for different biome types with more pronounced annual cycles of these parameters (like deciduous trees), it is expected that a more realistic representation of the vegetation, provided by time-varying values rather than constant parameter values, gives results e. g. for the energy fluxes closer to the observations. Future model development should incorporate this representation.

Chapter 3

Single column model studies

In the previous chapter the behaviour of the ECHAM land surface scheme has been analysed, when the model is integrated in off-line mode using atmospheric forcing. Therefore, feedback effects between the surface quantities and the atmospheric variables were excluded. In this chapter results from the one-dimensional (or single column) version of the ECHAM4 GCM (Roeckner et al. 1996) are presented. It calculates the entire vertical column, including the atmosphere and the soil, at one point, considering all physical processes included in the global model, e. g. radiation, vertical diffusion, formation of stratiform and convective precipitation and land surface processes. Thus feedback effects can be studied. Advective transport is either set to zero, or an advective forcing, extracted from a GCM simulation, is used. For the initialization, data from a GCM experiment are utilized, as well.

In the standard version of ECHAM4 the land surface and the atmosphere are coupled semi-implicitly, as explained in the next section. One major deficiency of this model structure in ECHAM4 is that the energy balance at the land surface is not closed. Under certain circumstances this can lead to significant errors in the components of the surface energy balance equation (1.1), which will be demonstrated in this chapter. Since the energy and moisture cycle are coupled via the latent heat flux, the components of the moisture cycle are altered in an erroneous way as well. It should be emphasized that this is not a problem of the land surface scheme itself, but mainly of the coupling procedure between land surface and atmosphere. This shows that the coupling procedure is an important issue for the model performance, which needs to be addressed. As a consequence, to investigate the impact of the coupling technique on the simulated model climate, a model version has been developed as part of this work, where land surface and atmosphere are coupled implicitly. This has the great advantage that the energy at the surface is conserved. This model version is denoted here as ECHAM4/IMPL. In the following section the basic elements of the two different numerical coupling techniques are explained.

3.1 Coupling between land surface and atmosphere

As noted already in section 1, solving the surface energy balance equation (1.1) is the most important task of any land surface scheme, as it closes the energy balance and determines the temperature at the surface. A discretization of (1.1), using a leapfrog time stepping scheme, leads to:

$$C_\text{S}\frac{T_\text{S}^{t+1} - T_\text{S}^{t-1}}{2\Delta t} = R_\text{n}^\text{coupl} + LE^\text{coupl} + H^\text{coupl} + G^\text{coupl}, \tag{3.1}$$

which gives the evolution of the surface temperature T_S over a $2\Delta t$ time step from time level $t-1$ to $t+1$. The meaning of the other quantities are as in (1.1). The superscripts of the flux terms on the right hand side of (3.1) indicate which numerical coupling technique between land surface and atmosphere is used.

The turbulent fluxes of latent and sensible heat in ECHAM4 are given as follows (notation as in (1.3) and (1.4)):

$$L \cdot E^\text{coupl} = L\rho C_\text{h}|\vec{v}|\beta[q_\text{a}^j - hq_\text{s}(T_\text{S}^i)], \tag{3.2}$$
$$H^\text{coupl} = \rho C_\text{h}|\vec{v}|[s_\text{a}^j - s_\text{S}^i]. \tag{3.3}$$

Here, s is the dry static energy which is defined as

$$s(z) = C_\text{p}T(z) + gz, \tag{3.4}$$

where C_p is the specific heat capacity of air at constant pressure, T the air temperature at height z above the ground and g the acceleration of gravity of the earth. i and j indicate the time levels of the variables. Their choice determines the type of coupling. Two different coupling procedures are discussed here, which are given by the following choices of i and j:

i = new time step $\quad = t+1, \quad j$ = new time step = $t+1$:   Implicit coupling,
i = previous time step = $t-1, \quad j$ = new time step = $t+1$:   Semi-implicit coupling.

In the next two sections it is described how the two different coupling techniques are applied to the surface energy balance equation. As the focus is on the coupling between land surface and atmosphere, and in order to simplify the equations, the expression for the ground heat flux will not be given. It is calculated from a heat diffusion equation in the soil, which is of the same type as the one used for the vertical diffusion in the lower atmosphere (see appendix A).

3.1.1   Implicit coupling

The objective of this method is to provide numerical stability of the solution of the equation and to calculate the prognostic variables and fluxes synchronously at the same level of time. This leads to a consistent solution for the atmospheric profiles of temperature and humidity including the surface conditions and the vertical heat fluxes.

In order to apply this method to the surface energy balance equation, the atmospheric values of temperature and humidity, used in the formulation of the surface heat fluxes, need to be known. As shown in appendix A, these quantities are related to the surface conditions by (A.7). In this equation the prognostic variable for level k is X_k^*/α. For the clarity of the implicit treatment of the surface energy balance equation, here we prefer to use the relations

$$q_\text{a}^{t+1} = E_{\text{q},N+1/2}^{t-1}q_\text{s}(T_\text{S}^{t+1}) + F_{\text{q},N+1/2}^{t-1}, \tag{3.5}$$
$$s_\text{a}^{t+1} = E_{\text{s},N+1/2}^{t-1}s_\text{S}^{t+1} + F_{\text{s},N+1/2}^{t-1}, \tag{3.6}$$

which give, similarly to (A.7), the variables at the lowest atmospheric level as functions of the surface conditions, but here both at time step $t+1$. The surface energy balance equation can also easily be formulated using the X_k^*/α variables, but here the description of the numerical scheme shall be kept as simple as possible. Thus, the expressions for the total net radiation (cf. (1.2)) and the latent and sensible heat fluxes (cf. (3.2), (3.3), (3.5) and (3.6)) become:

$$R_n^{\text{impl}} = (1 - \alpha_S)R_{sd} + \epsilon R_{ld} - \epsilon\sigma(T_S^{t+1})^4, \tag{3.7}$$

$$LE^{\text{impl}} = L\rho C_h|\vec{v}|\beta[(E_{q,N+1/2}^{t-1}q_s(T_S^{t+1}) + F_{q,N+1/2}^{t-1}) - hq_s(T_S^{t+1})], \tag{3.8}$$

$$H^{\text{impl}} = \rho C_h|\vec{v}|[(E_{s,N+1/2}^{t-1}s_S^{t+1} + F_{s,N+1/2}^{t-1}) - s_S^{t+1}]$$

$$= \rho C_h|\vec{v}|[(E_{s,N+1/2}^{t-1}C_P T_S^{t+1} + F_{s,N+1/2}^{t-1}) - C_P T_S^{t+1}]. \tag{3.9}$$

Inserting these expressions in (3.1) gives a fully implicit equation for the surface energy balance:

$$C_S\frac{T_S^{t+1} - T_S^{t-1}}{2\Delta t} = (1 - \alpha_S)R_{sd} + \epsilon R_{ld} - \epsilon\sigma(T_S^{t+1})^4$$

$$+ L\rho C_h|\vec{v}|\beta[(E_{q,N+1/2}^{t-1}q_s(T_S^{t+1}) + F_{q,N+1/2}^{t-1}) - hq_s(T_S^{t+1})]$$

$$+ \rho C_h|\vec{v}|[(E_{s,N+1/2}^{t-1}C_P T_S^{t+1} + F_{s,N+1/2}^{t-1}) - C_P T_S^{t+1}]$$

$$+ G^{\text{impl}}. \tag{3.10}$$

As an equation is desired that is linear in T_S, the nonlinear terms are replaced by their truncated Taylor expansions. These terms are the upward longwave radiation and the saturated specific humidity:

$$\epsilon\sigma(T_S^{t+1})^4 \approx \epsilon\sigma(T_S^{t-1})^4 + 4\epsilon\sigma(T_S^{t-1})^3(T_S^{t+1} - T_S^{t-1}) =: R_{lu}^{t+1}, \tag{3.11}$$

$$q_s(T_S^{t+1}) \approx q_s(T_S^{t-1}) + \frac{\partial q_s}{\partial T_S}\bigg|_{T_S^{t-1}} (T_S^{t+1} - T_S^{t-1}). \tag{3.12}$$

With this linearizations Eq. (3.10) can be resolved for T_S^{t+1}. Subsequently the back substitution can be performed, which yields the atmospheric profiles of temperature and humidity (see appendix A). The latent and sensible heat flux are calculated from (3.8) and (3.9). These expressions are incorporated in the surface energy balance equation (3.10) which ensures energy conservation in the coupled system, since the GCM consistently receives the same energy fluxes as used in the land surface scheme.

As the radiation module in ECHAM4 has already completed its calculations before the vertical diffusion component starts operation, care has to be taken of the upward longwave radiation concerning the energy conservation. Once the surface energy balance (3.10) is solved, the so-called radiative temperature will be computed which is related to R_{lu}^{t+1} (cf. (3.11)) by

$$R_{lu}^{t+1} = \epsilon\sigma(T_{\text{eff}}^{t+1})^4. \tag{3.13}$$

Passing the radiative temperature to the radiation scheme will ensure that the time-averaged balance of the longwave radiative fluxes is closed.

In the model versions ECHAM4/IMPL and ECHAM4/SECHIBA the soil temperature schemes are also coupled implicitly to the surface energy balance. This leads to a closed set

of equations which describe the vertical heat exchange in the entire column from the top of the planetary boundary layer to the bottom of the soil.

The implicit coupling method is numerically stable and it conserves energy, as the surface fluxes are consistent with the atmospheric profiles of temperature and humidity. Problems may arise, for instance, if the water supply is not sufficient for the calculated evaporation. This may happen because the fluxes are computed implicitly in (3.10), but with explicit coefficients. Therefore, a limiting condition like a soil moisture stress formulation may fail in effectively reducing excessive evaporation. This problem is avoided by a predictor-corrector method, as implemented in SECHIBA.

3.1.2 Semi-implicit coupling

In contrast to the implicit coupling, in this method the surface energy fluxes are calculated using the surface temperature value at the previous time step (cf. (3.2) and (3.3)). Thus, the following equations are obtained for the fluxes (see (3.7), (3.8)) and (3.9):

$$R_n^{\text{semi}} = (1 - \alpha_S)R_{\text{sd}} + \epsilon R_{\text{ld}} - \epsilon\sigma(T_S^{t-1})^4, \tag{3.14}$$

$$LE^{\text{semi}} = L\rho C_h|\vec{v}|\beta[(E_{q,N+1/2}^{t-1}q_s(T_S^{t-1}) + F_{q,N+1/2}^{t-1}) - hq_s(T_S^{t-1})], \tag{3.15}$$

$$H^{\text{semi}} = \rho C_h|\vec{v}|[(E_{s,N+1/2}^{t-1}C_P T_S^{t-1} + F_{s,N+1/2}^{t-1}) - C_P T_S^{t-1}]. \tag{3.16}$$

These formulations for the latent and sensible heat flux ((3.15) and (3.16)) are used to close the vertical diffusion scheme which computes the new atmospheric temperature and humidity profiles. In order to provide numerical stability when solving the surface energy balance equation (3.1), truncated Taylor expansions of the flux terms with respect to the (fast varying) surface temperature are used:

$$
\begin{aligned}
C_S \frac{T_S^{t+1} - T_S^{t-1}}{2\Delta t} &= R_n^{\text{semi}} + \left.\frac{\partial R_n}{\partial T_S}\right|_{T_S^{t-1}} (T_S^{t+1} - T_S^{t-1}) \\
&+ LE^{\text{semi}} + \left.\frac{\partial LE}{\partial T_S}\right|_{T_S^{t-1}} (T_S^{t+1} - T_S^{t-1}) \\
&+ H^{\text{semi}} + \left.\frac{\partial H}{\partial T_S}\right|_{T_S^{t-1}} (T_S^{t+1} - T_S^{t-1}) \\
&+ G^{\text{semi}}.
\end{aligned}
\tag{3.17}
$$

In ECHAM4 this equation is solved after the radiation and the vertical diffusion schemes have calculated the surface energy fluxes using (3.14), (3.15) and (3.16). Therefore, the fluxes that are balanced by the surface energy equation (3.17), and which correspond to the new value of the surface temperature, are different from those received by the atmosphere. This means that the energy balance at the surface is not closed in the model. It is not implied here that this is a principal deficiency of the semi-implicit method; but the imbalance has to be taken into account in the temperature calculation at the subsequent time step. This is not done in the standard ECHAM4 GCM. The surface residual energy, given by the sum of the three Taylor expansion terms in (3.17), is presumed to be small, but as shown later, this may not necessarily be the case in all situations. By design, the semi-implicit coupling only allows the surface temperature to feedback on the atmosphere at the subsequent time step, rather than simultaneously. More information on the coupling techniques can be found in Polcher et al. (1998a).

3.2 July simulation for central Europe

In this section results from the one-dimensional (1D) version of the standard ECHAM4 GCM (Roeckner et al. 1996) and the modified model versions ECHAM4/IMPL and ECHAM4/-SECHIBA are presented. As explained before, this set of three different model versions allows a systematic analysis of the impact of both the numerical coupling and the land surface parameterization on the simulated climate.

A 1D-simulation for July at a site in central Europe (54°N, 11°E) was performed with each of the three schemes, using the same initialization, taken from a previous ECHAM4 GCM simulation. An advective forcing was not applied. The vegetation is grass with a coverage of 80%. For the field capacity in ECHAM4 the typical value 0.23 m is chosen which yields a wilting point (i. e. 35% of the field capacity in the model, cf. (1.7)) of 0.08 m. Therefore, the maximum plant-available soil moisture, that is, the difference between field capacity and wilting level, amounts to 0.15 m. In the model structure of SECHIBA the wilting level is at zero by definition. Thus, the active soil moisture volume is equal to the maximum plant-available soil moisture. The three models were initialized at 7.7% of the plant-available soil moisture which represents very dry conditions. Here, some characteristic aspects of the numerical and physical differences between the three models can be analysed.

Figure 3.1 shows the diurnal variations of the surface energy fluxes of ECHAM4 for the first three days of the 1D-simulation. The total net radiation is characterized by periodically similar diurnal cycles with maxima of about 550 W m^{-2} at noon time and minima of about -80 W m^{-2} at the beginning of the nights. This energy should be balanced by the other flux terms of the surface energy equation and a change in surface temperature (cf. (1.1)). As the soil is very dry and there is almost no water in the interception reservoir, the evapotranspiration and thus latent heat flux is small on days 1 and 2. Therefore, the sensible heat flux dominates the flux terms which balance the net radiation. The surface energy residual term appears for reasons discussed in section 3.1.2. When formulating the equations for the semi-implicit coupling, it was assumed that this residual term, which represents an error in the surface/atmosphere energy balance, would be small compared to the physical fluxes. But as seen in Fig. 3.1, on day 1 and 2 the residual is actually of a magnitude similar to these fluxes. It is positive, which represents an energy loss at the surface due to the numerics. On day 3 the residual term shows a large negative peak at noon, while a very large positive peak appears in the latent heat flux, lasting for several hours and reaching a maximum value of about 1250 W m^{-2}, a completely unrealistic value! The energy flux is more than twice as high as that of the total net radiation. The ground heat and the sensible heat flux are inverted during this period, but the major part of the energy is provided by the residual term, that means it has no physical source but is artificially created by the numerics! Later in the afternoon of the same day there is another similar but smaller peak in the latent heat flux.

In order to get a better understanding of this behaviour, the moisture source of this enormous evapotranspiration shall be analysed. Figure 3.2 shows the different components that are aggregated to the total latent heat flux. During the first two days transpiration dominates, showing diurnal cycles of a realistic order of magnitude. Bare soil evaporation is zero during the entire period of simulation due to drought stress. The third day also starts with transpiration which is rapidly superposed by two peaks of canopy evaporation at noon and in the second half of the day. Why is the canopy evaporation so heavily overestimated?
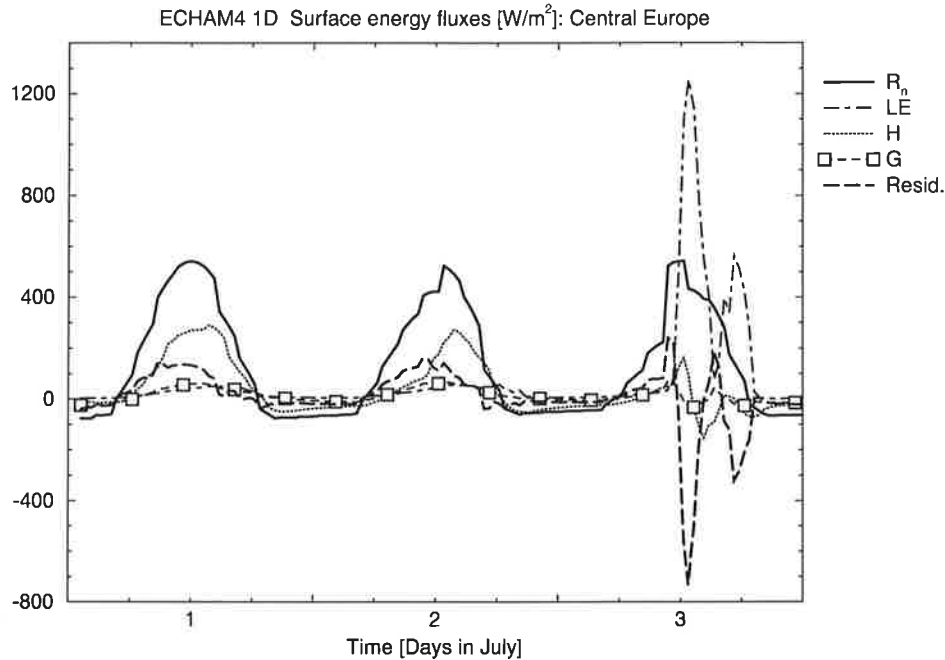
Figure 3.1: Diurnal cycles of total net radiation (R_n), latent heat flux (LE), sensible heat flux (H), ground heat flux (G) and the surface energy residual term as simulated by ECHAM4 1D from 1 to 3 July at a site in central Europe. Note that the residual is not small, which was assumed, but of the order of the physical fluxes or even much higher, leading to significantly erroneous flux simulations (e. g. on 3 July).

Figure 3.3 compares the total precipitation and evapotranspiration simulated by ECHAM4 on these three days. While there is not a large amount of rain on the first two days, two convective precipitation events take place on the third day coincidently with the canopy evaporation peaks; the higher one reaching a maximum value of about 42 mm d^{-1}. This implies, once the convective rain starts, the interception reservoir is moistened, allowing for canopy evaporation, which in turn triggers convective precipitation. The result is a positive feedback that is desirable when it evolves in a realistic way and which may be an important effect at certain locations, e. g. in the tropical rainforest. But in the example presented here the latent heat flux is highly overestimated due to the erroneous residual energy term, which is part of the semi-implicit coupling scheme implemented in the standard ECHAM4 GCM. This is a clear model deficiency and shows that great care needs to be taken in the choice of numerical methods applied.

The results presented above shall be compared to the case when an implicit coupling scheme is used, i. e. to ECHAM4/IMPL. Figure 3.4 shows the diurnal variations of the surface energy fluxes of ECHAM4/IMPL 1D from 1 to 3 July. The total net radiation evolves similarly as in ECHAM4 with diurnal cycles similar in shape and amplitude. The obvious difference to the semi-implicit model is the absence of a residual energy term. Comparing Figs. 3.1 and 3.4, this energy residual would appear to contribute mainly to the sensible heat flux on days 1 and 2 in the implicit model. This appears reasonable for the prevailing
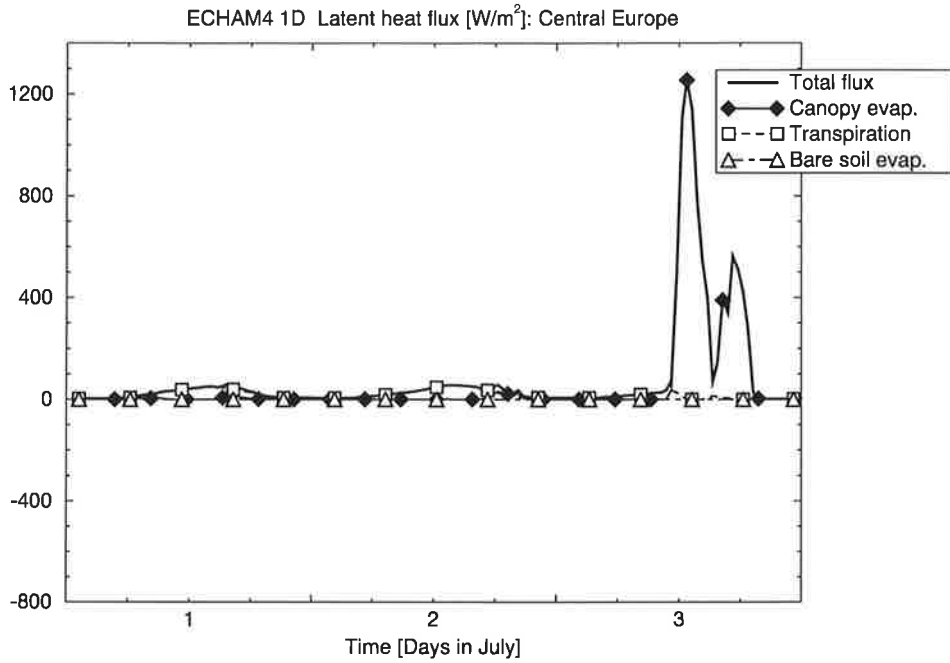
Figure 3.2: Contributions of canopy evaporation, transpiration and bare soil evaporation to the total latent heat flux as simulated by ECHAM4 1D from 1 to 3 July at a site in central Europe.
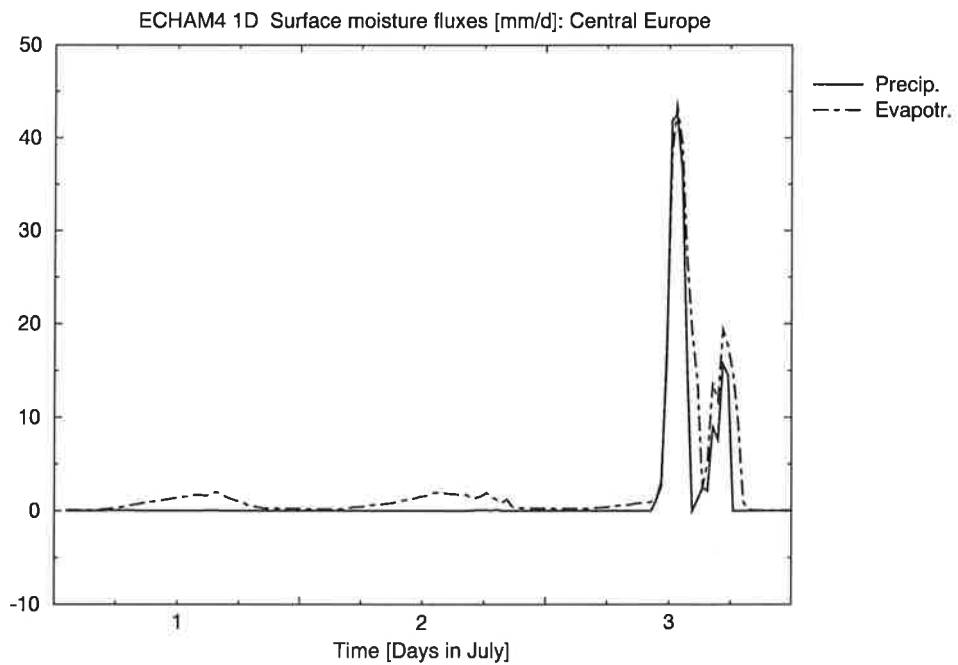
Figure 3.3: Diurnal cycles of precipitation and evapotranspiration as simulated by ECHAM4 1D from 1 to 3 July at a site in central Europe.

dry conditions. On day 3 the convective precipitation event appears again (see Fig. 3.5), but compared to that in ECHAM4 it is much smaller. As in ECHAM4 a positive feedback between convective precipitation and canopy evaporation occurs, but here the energy available for the latent heat flux is under much better control. It must be provided or compensated by the other surface energy fluxes or a change of surface temperature. As seen in Fig. 3.4, the total net radiative flux is about an upper limit for the latent heat flux on day 3, and when this limit is exceeded it is compensated by the sensible heat flux, which becomes negative at noon on day 3, and the ground heat flux. Additionally, the latent heat flux causes a distinct cooling of the surface, as shown later. Thus, the relations between the different quantities of the energy and moisture cycles just presented are physically reasonable. Due to the evaporation–precipitation feedback this has also implications for the precipitation. As shown, the semi-implicitly coupled ECHAM4 simulates an unrealistic high evaporation peak on day 3 which is associated with a maximum precipitation of about 42 mm d^{-1}. In ECHAM4/IMPL the corresponding precipitation maximum value is at about 21 mm d^{-1}, a much more realistic value under the conditions at this location.

The simulated energy fluxes in ECHAM4/SECHIBA, shown in Fig. 3.6, look essentially similar to those in ECHAM4/IMPL with respect to their orders of magnitude and the energy partitioning between the different fluxes. This is expected because the numerical coupling scheme is the same and the thermodynamic parts are very similar in both models. Furthermore, one of the main features of SECHIBA that makes it different to ECHAM, the mosaic approach for the treatment of the vegetation within a grid cell, does not apply here as only one biome type is used in these experiments. Therefore, the main differences between these schemes in this case are the soil hydrology scheme together with the soil moisture stress formulation. On the first day the evapotranspiration and thus the associated latent heat flux are higher in ECHAM4/SECHIBA compared to ECHAM4/IMPL; consequently, the sensible heat flux is lower. This is an artefact of the soil moisture initialization in combination with the different soil moisture stress term. Due to the enhanced transpiration, convective precipitation is triggered on the second day already (cf. Fig. 3.7), i. e. one day earlier than in ECHAM4/IMPL. As in the two other experiments, this is accompanied by a peak in canopy evaporation. The maximum precipitation value is similar as in ECHAM4/IMPL.

As expected, the higher latent heat flux in ECHAM4/SECHIBA on the first two days causes a lower surface temperature, best visible on day 2 (Fig. 3.8). On the third day a rapid cooling is seen in ECHAM4 as result of the peak in latent heat flux around noon (cf. Fig. 3.1). ECHAM4/IMPL shows a cooling on the third day as well, but not so pronounced. On days 1 and 2, when the energy partitioning between the different surface fluxes in ECHAM4 and ECHAM4/IMPL is comparably similar, the surface temperature of the two models shows a similar evolution as well. But there is a tendency for the temperature maxima to be slightly higher in ECHAM4/IMPL. This is due to the fact that in ECHAM4 some energy is lost to the energy residual. In ECHAM4/IMPL, this energy is mainly used, in this example, to increase maximum surface temperature and sensible heat flux, as discussed earlier.

Another feature of the ECHAM4 parameterization shall be mentioned here, concerning the soil moisture budget. Figure 3.9 shows the evolution of the relative plant-available soil moisture of the three models during the entire 30-day period of simulation. They are initialized at 7.7%. As on average, evapotranspiration exceeds precipitation in all three models, the soil water content decreases gradually in a similar way until the zero level is reached, which represents the wilting point. This is defined as that soil water level below which transpiration
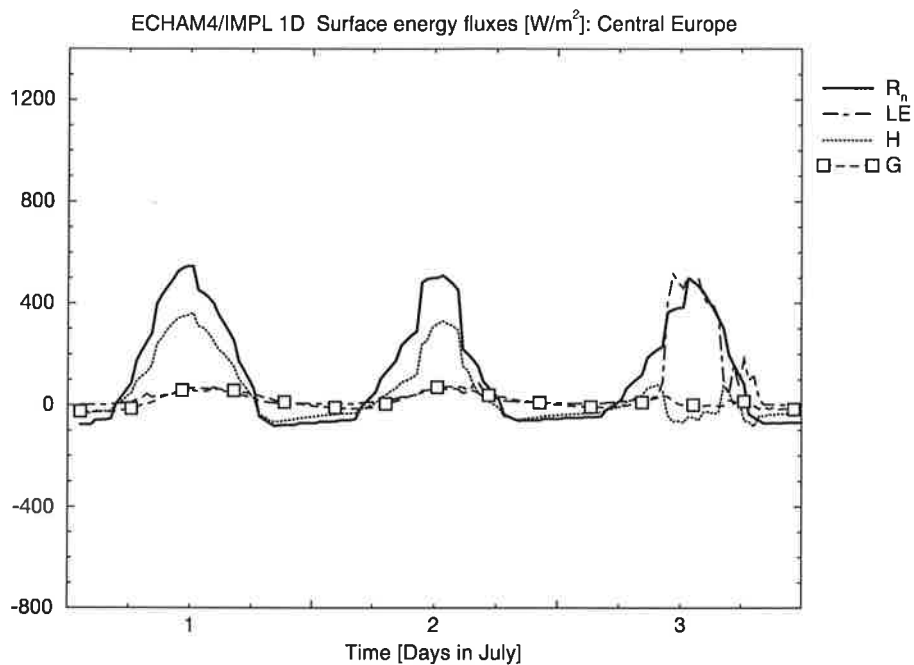
Figure 3.4: Diurnal cycles of total net radiation (R_n), latent heat flux (LE), sensible heat flux (H) and ground heat flux (G) as simulated by ECHAM4/IMPL 1D from 1 to 3 July at a site in central Europe.
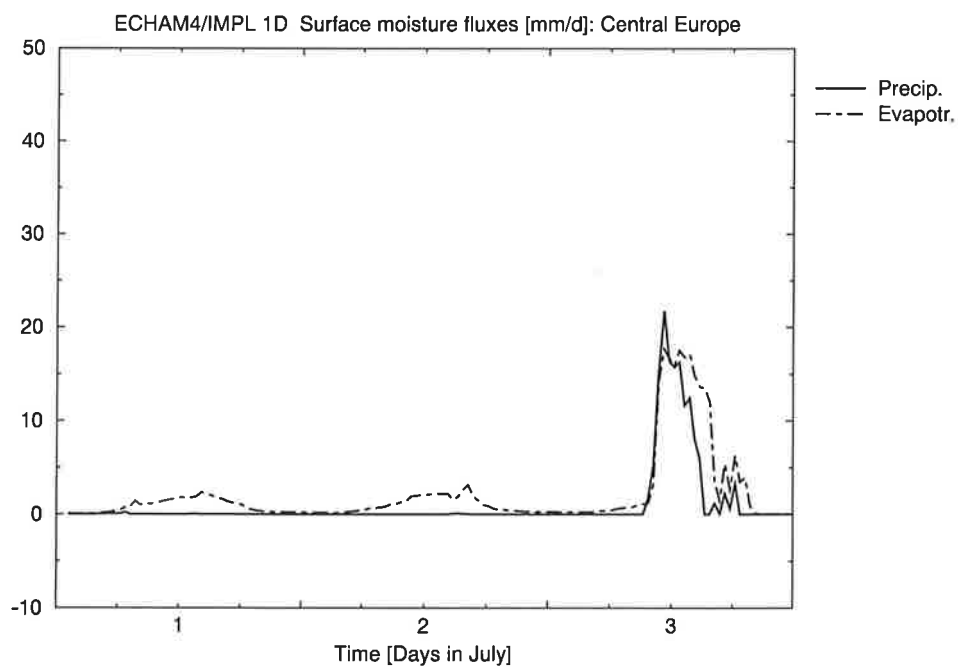
Figure 3.5: Diurnal cycles of precipitation and evapotranspiration as simulated by ECHAM4/IMPL 1D from 1 to 3 July at a site in central Europe.
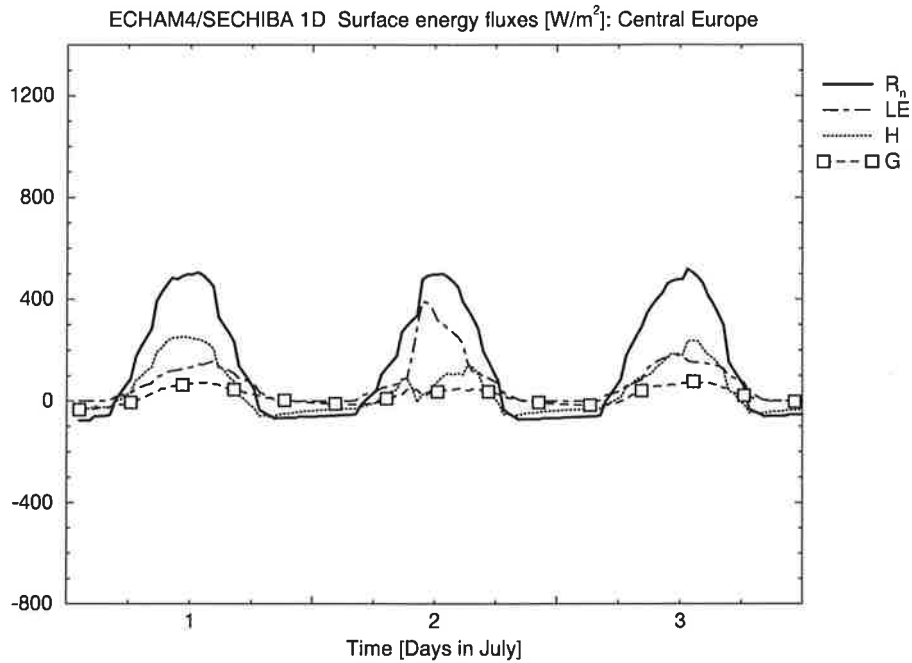
Figure 3.6: Diurnal cycles of total net radiation (R_n), latent heat flux (LE), sensible heat flux (H) and ground heat flux (G) as simulated by ECHAM4/SECHIBA 1D from 1 to 3 July at a site in central Europe.
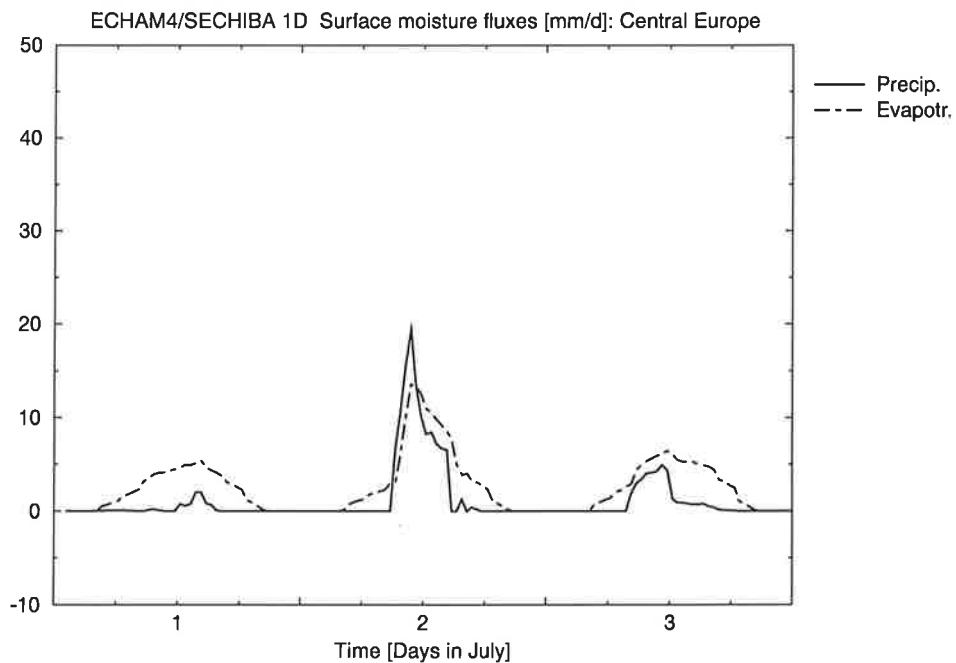
Figure 3.7: Diurnal cycles of precipitation and evapotranspiration as simulated by ECHAM4/-SECHIBA 1D from 1 to 3 July at a site in central Europe.
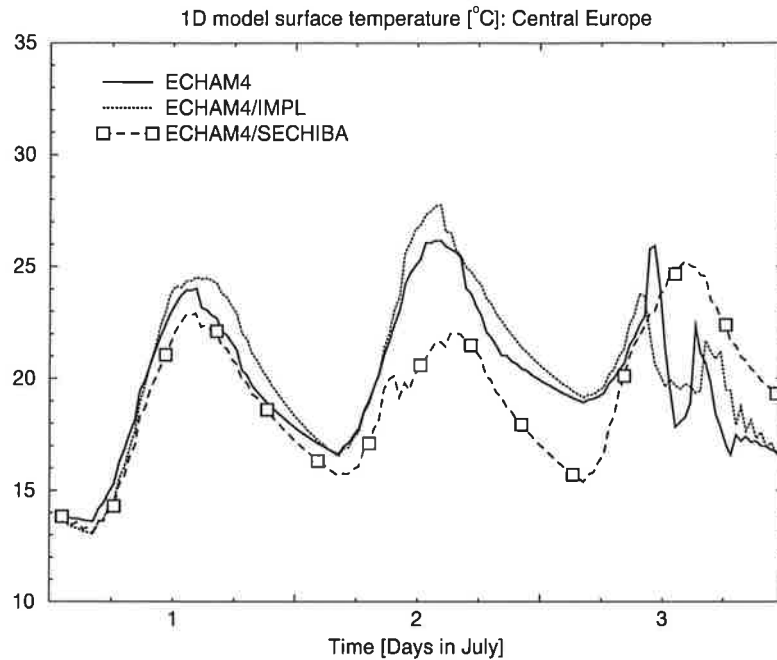
Figure 3.8: Diurnal cycles of surface temperature as simulated by ECHAM4, ECHAM4/IMPL and ECHAM4/SECHIBA 1D from 1 to 3 July at a site in central Europe.
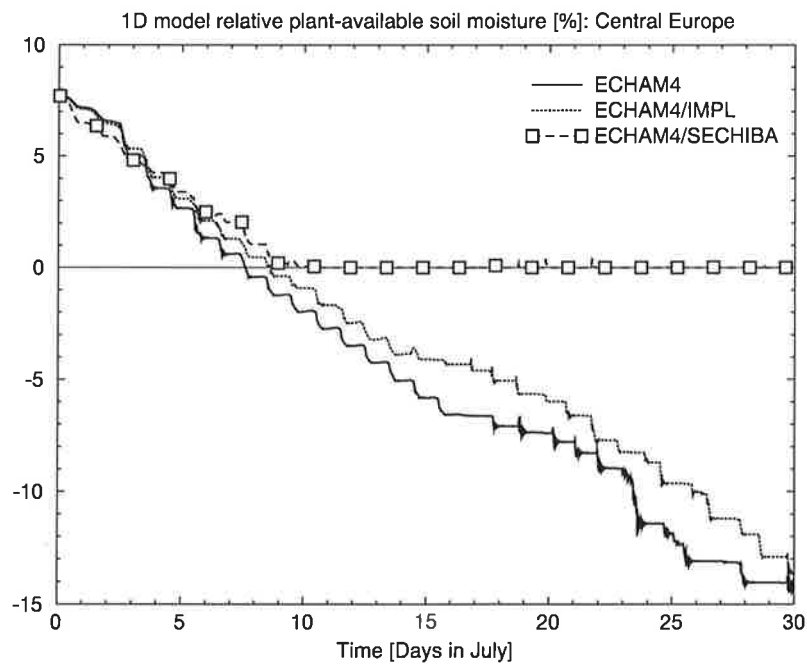
Figure 3.9: Evolution of relative plant-available soil moisture as simulated by ECHAM4, ECHAM4/-IMPL and ECHAM4/SECHIBA 1D from 1 to 30 July at a site in central Europe. The 0%-level indicates the wilting point. The ECHAM4 and ECHAM4/IMPL values below it are physically unrealistic, and they occur due to a coding error (cf. text).

is zero. At this point SECHIBA remains with a zero level while the water content of the other models further decreases. Bare soil evaporation is zero in ECHAM during this simulation due to drought stress. Therefore, only transpiration should be able to reduce the soil moisture in ECHAM4 and ECHAM4/IMPL according to the equations. But transpiration should stop at the wilting point by definition (see Eq. (1.7)), which is obviously not the case in these simulations! The reason is a pure coding error in ECHAM which allows the removal of additional water from the soil when required, which occurs when ever the calculated canopy evaporation exceeds the available water in the interception reservoir. This was not modified in ECHAM4/IMPL because the idea is to study the impact of the different numerical coupling in ECHAM4/IMPL while the physical equations remain completely unchanged. In SECHIBA such an effect is avoided by a predictor-corrector-method which reduces the canopy evaporation accordingly to the available water on the canopy. Besides that, due to a different formulation of the soil moisture stress SECHIBA additionally allows some bare soil evaporation in this situation. This can happen after heavy rain showers when the upper soil moisture layer is filled. This is the case on day 2, for instance (cf. Fig. 3.7). Furthermore, in SECHIBA the wilting level is at zero by definition. This appears to be a reasonable approach, as transpiration is zero, by definition, below it, and bare soil evaporation is very low there as well, or also zero as in ECHAM in this example. An exception is when there is water in the upper soil while the total soil column is very dry on the average, but this case is well-treated by the SECHIBA hydrology scheme.

In order to get an impression of the evolution of the surface temperature in the three models during the simulation, Fig. 3.10 shows the period from 16 to 19 July. On day 16 the temperatures in ECHAM4 and ECHAM4/IMPL increase similarly in the morning but at noon ECHAM4's temperature suddenly decreases while ECHAM4/IMPL's further rises. The reason is a peak in latent heat flux, enlarged by an energy supply from the residual (see Fig. 3.11). This effect, and the energy which is lost through the residual every day, tend to diminish the temperature increase in ECHAM4 during a warming phase, especially under dry conditions. Therefore, ECHAM4/IMPL shows a more pronounced diurnal temperature amplitude and generally higher temperature maxima during a warming phase. The surface temperature in ECHAM4/SECHIBA is even higher than in ECHAM4/IMPL for most of the time. The reason is that the soil moisture in SECHIBA can not be further reduced, which leads to a lower evapotranspiration and therefore less cooling. Sensitivity experiments with the same model set-up, but higher initial soil moisture, have shown that due to its soil hydrology and stress formulations, SECHIBA is generally more effective in keeping the water stored in the soil under dry and medium-wet conditions than ECHAM. Therefore, SECHIBA tends to simulate higher surface temperatures under these conditions.

On day 19 there is an example of a negative peak of the residual energy term in ECHAM4 of less than -1300 W m^{-2} supporting a very unrealistic latent heat flux of more than 1700 W m^{-2} (Fig. 3.11). This again forces an abrupt decrease of the surface temperature, followed by some oscillations during the subsequent time steps (see Fig. 3.10). Similar oscillations are also visible in the two other models at different times. They are mainly due to the leapfrog time stepping scheme used in the other physics modules of the atmospheric model, e. g. the vertical diffusion scheme. It is characterized by two different alternating chains of values which use a $2\Delta t$ time step to calculate the next value, while passing the other chain. For some reason these chains may diverge, especially after strong temperature gradients. This causes the oscillations. In order to reach a convergence of the two chains in such a situation,
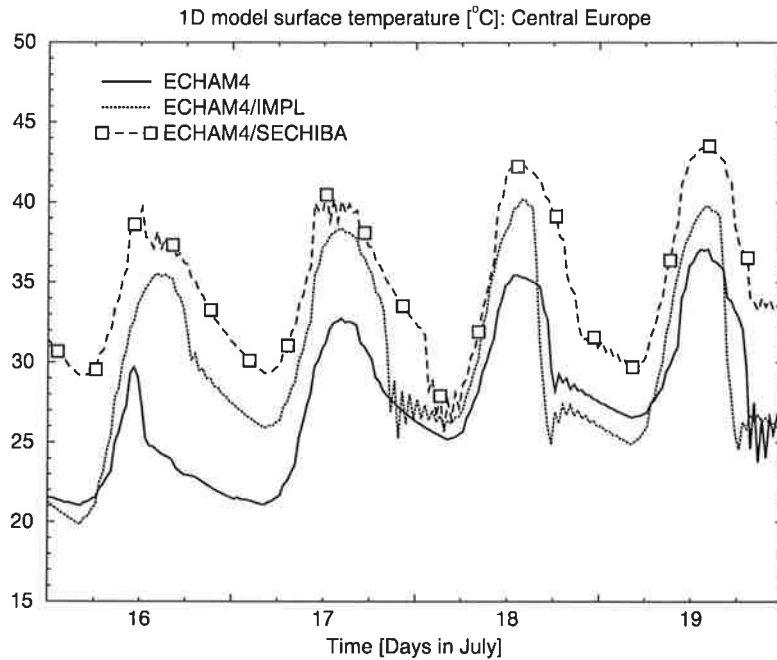
Figure 3.10: Diurnal cycles of surface temperature as simulated by ECHAM4, ECHAM4/IMPL and ECHAM4/SECHIBA 1D from 16 to 19 July at a site in central Europe.
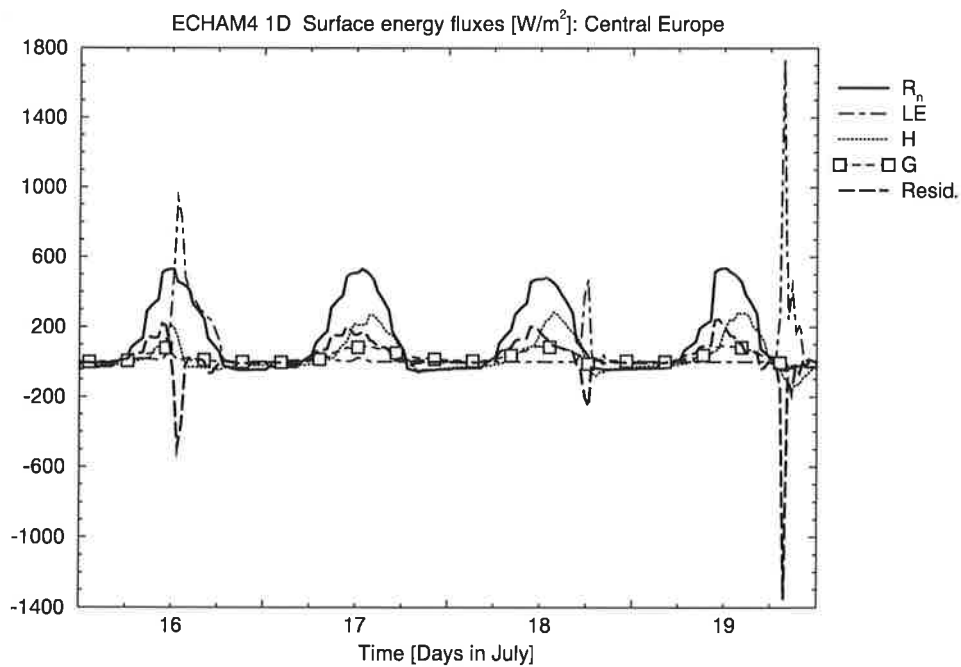
Figure 3.11: Diurnal cycles of total net radiation (R_n), latent heat flux (LE), sensible heat flux (H), ground heat flux (G) and the surface energy residual term as simulated by ECHAM4 1D from 16 to 19 July at a site in central Europe.

a time filter is used which connects them.

Former versions of the ECMWF numerical weather forecast model that used a semi-implicit coupling scheme had similar problems (L. Dümenil 1995, pers. comm.). The ECHAM climate model was originally derived from such an ECMWF model version. And its Cycle 48 version, which includes a skin temperature scheme that is implicitly coupled to the vertical diffusion module (Viterbo and Beljaars 1995), has to deal with that as well (P. Viterbo 1996, pers. comm.).

An oscillation problem also emerges in the soil moisture simulation in ECHAM4, in particular in the second half of the 30-day period (cf. Fig. 3.9). In ECHAM4/SECHIBA this is avoided by the use of a $1\Delta t$ forward time stepping scheme in the hydrology part of the model.

As demonstrated here, the land surface schemes of all three models suffer from the effect just described, causing oscillations of the simulated surface temperature. This happens in both the semi-implicitly and the implicitly coupled models to a comparably similar extent. But it shall be recalled that the implicit models have the great advantage of the conservation of energy.

3.3   May simulation for western Russia

In this section the different behaviour of the three models regarding the melting of snow shall be investigated. To enable snow melt in ECHAM, the upper soil layer needs to be warmer than the melting temperature, if the snow depth is below a critical depth of 2.5 cm water equivalent. It is recalled that the temperatures in the soil represent the values in the middle of the respective soil layers, which is at a depth of 3.25 cm for the top soil layer in ECHAM. If the snow pack is deeper than the critical value, an extra snow layer with an own temperature is added. In this case, to get snow melt both the temperature of the middle of the snow pack and the upper soil layer need to be higher than the melting temperature (while the temperature at the upper boundary of the snow pack is not allowed to exceed 0°C). This seems to be unrealistic, as besides the snow pack, the top soil layer needs to be heated, where the latter is only possible by heat conduction through the insulating snow pack. The effect of e. g. producing snow melt by contact with warm air at the surface is therefore poorly represented. For melting snow in SECHIBA only the surface temperature needs to be above the melting point. The temperature is extrapolated from the two upper thermal layers to the surface as shown in Fig. 1.1a. This is likely to produce a more realistic snow melt.

A 1D-simulation for May at a site in western Russia (60°N, 59°E) was performed with each of the three schemes with the same initialization, which was again taken from a previous ECHAM4 GCM simulation. The initial snow depth amounts to 15 cm water equivalent. Figure 3.12 shows the evolution of snow depth in the three models during the 30 days of simulation. All three models immediately start melting the snow and proceed until the snow cover has disappeared. In ECHAM4 and ECHAM4/SECHIBA the rate of decrease of snow depth is similar with a delay of ECHAM4/SECHIBA of 1–2 days. But on day 12 when the critical snow depth is reached, the melting slows down in ECHAM4. At that time the discretized extra snow layer disappears, and after that melting is not as efficient. Hence, the snow is completely melted first in ECHAM4/SECHIBA (day 14), followed by ECHAM4 (day
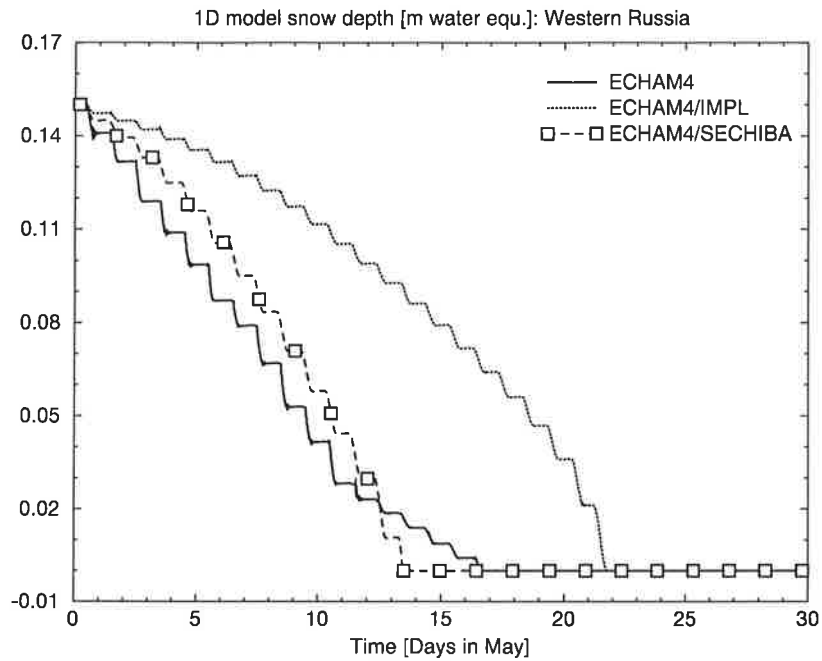
Figure 3.12: Evolution of snow depth as simulated by ECHAM4, ECHAM4/IMPL and ECHAM4/-SECHIBA 1D from 1 to 30 May at a site in western Russia.
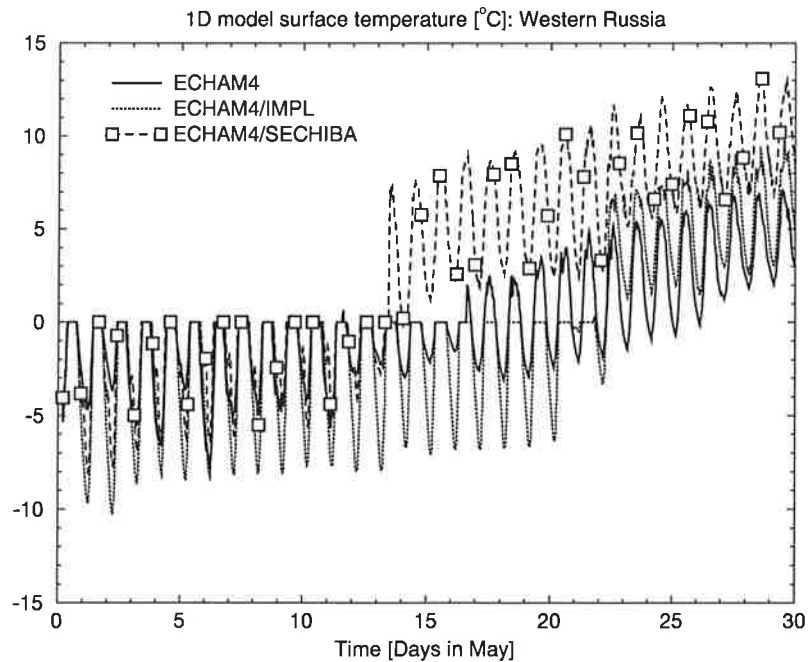
Figure 3.13: Evolution of surface temperature as simulated by ECHAM4, ECHAM4/IMPL and ECHAM4/SECHIBA 1D from 1 to 30 May at a site in western Russia.
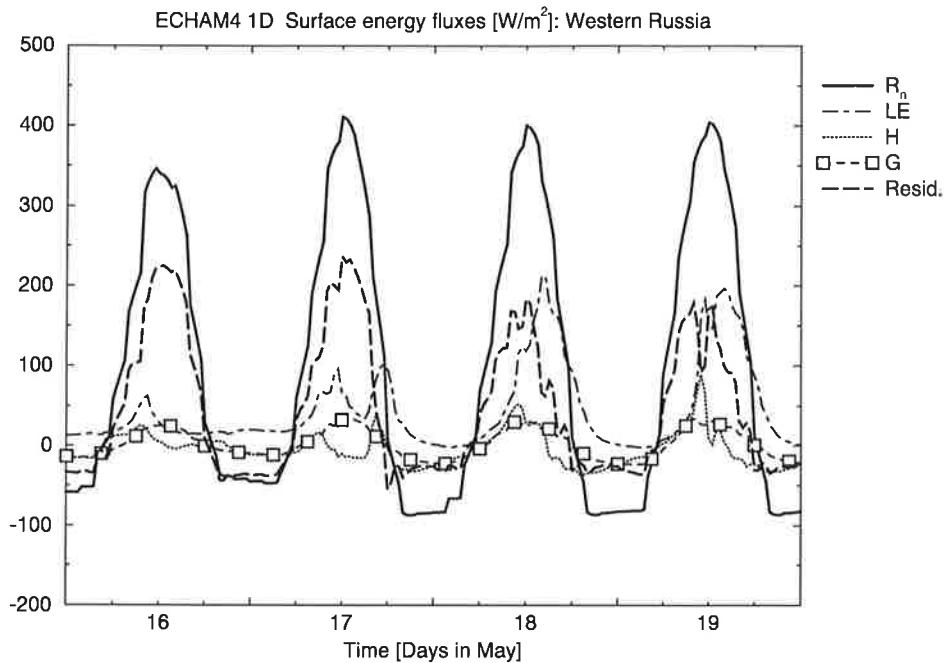
Figure 3.14: Diurnal cycles of total net radiation (R_n), latent heat flux (LE), sensible heat flux (H), ground heat flux (G) and the surface energy residual term as simulated by ECHAM4 1D from 16 to 19 May at a site in western Russia.

17). In ECHAM4/IMPL the melting is slow at the beginning, but it accelerates during the simulation until the snow is melted (day 22).

Figure 3.13 shows the diurnal cycles of the surface temperature of the three models over the same period of time as the previous figure. As long as there is snow on the ground the maximum surface temperature is fixed to the melting temperature of 0°C in all three models. If the temperature would exceed this value, due to balance of the surface energy fluxes, this additional energy amount would lead to melting. Once all snow is melted, the surface temperature can then exceed 0°C.

Figures 3.14 to 3.16 show the surface energy fluxes of the three models, each for a period of four days, centered around the time when the snow cover of the respective model has disappeared. Similar to the example for central Europe, presented in section 3.2, a large part of the available energy in ECHAM4 disappears in the energy residual (see Fig. 3.14). On 16 and 17 May, when there is still snow in ECHAM4, the residual peaks above 200 W m^{-2}, while the absolute ground and turbulent heat fluxes are significantly lower than 100 W m^{-2} most of the time. On the two following days, when the snow is melted, the maximum residual is still in the range of 150–200 W m^{-2}, which is of the order of magnitude of the latent heat flux. Thus, similar to the example for dry soil (cf. section 3.2), the semi-implicit coupling scheme shows significant numerical deficiencies regarding energy conservation when the soil is wet or snow covered.

In ECHAM4/IMPL (cf. Fig. 3.15), on the other hand, there is no energy loss through a residual term, and this mainly leads to more pronounced turbulent heat fluxes than in
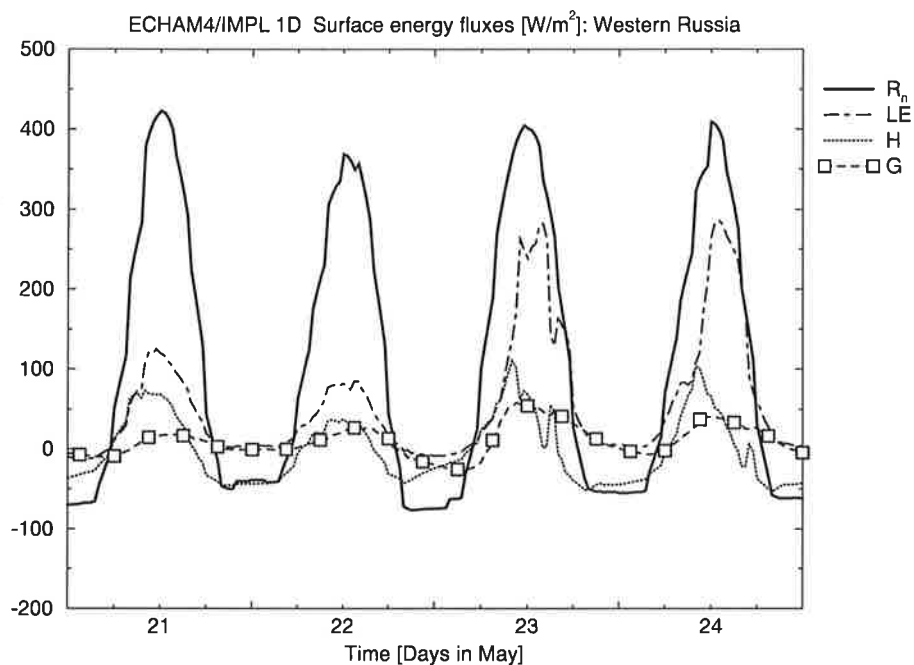
Figure 3.15: Diurnal cycles of total net radiation (R_n), latent heat flux (LE), sensible heat flux (H) and ground heat flux (G) as simulated by ECHAM4/IMPL 1D from 21 to 24 May at a site in western Russia.
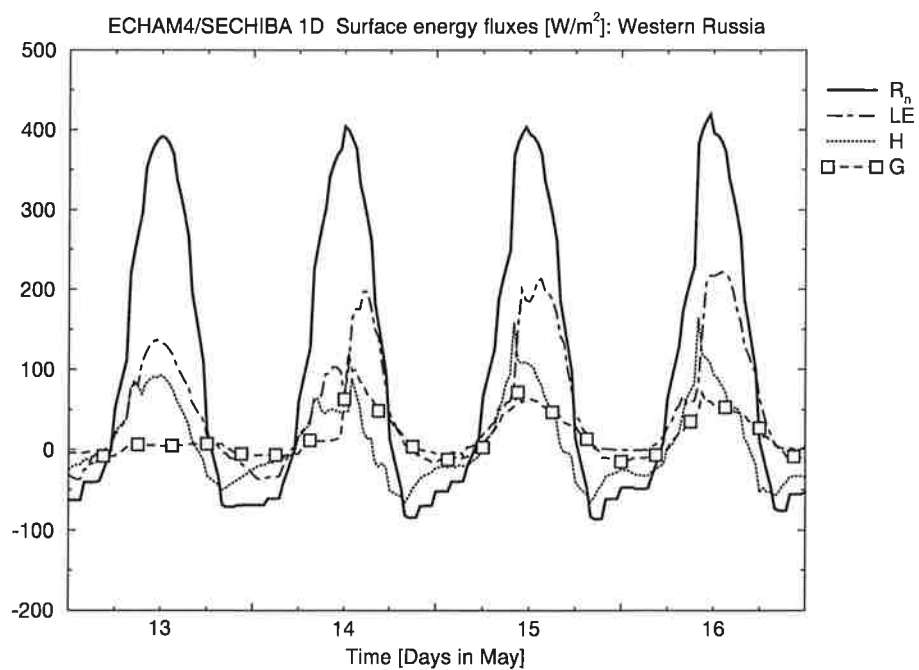
Figure 3.16: As Fig. 3.15 but for ECHAM4/SECHIBA from 13 to 16 May.
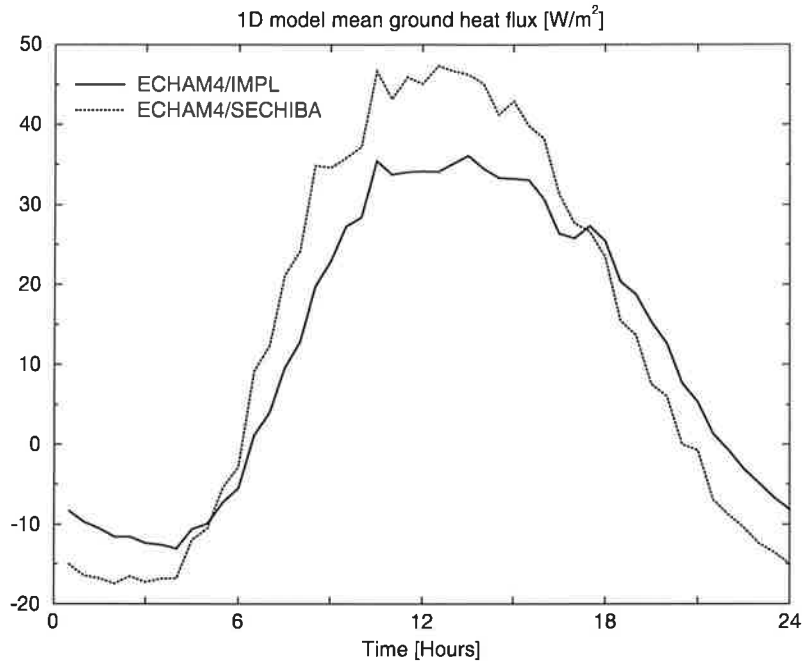
Figure 3.17: Multi-day average of the diurnal cycles of the ground heat flux as simulated by ECHAM4/IMPL and ECHAM4/SECHIBA. The flux simulations of both models were averaged over several days under similar atmospheric and soil conditions after the snow melt.

ECHAM4 and a much faster melting of snow (just before the snow pack vanishes, on 21 and 22 May, see Fig. 3.12). Furthermore, on 23 and 24 May, it produces a larger latent heat flux and a faster increase of the surface temperature after the snow melt (see Fig. 3.13). ECHAM4/SECHIBA behaves similar to ECHAM4/IMPL with the difference that the latent heat flux maxima on the days after the snow melt are smaller (cf. Fig. 3.16). The reason is that the interception storage in ECHAM4/SECHIBA is smaller at that time, causing a smaller canopy evaporation which is the main component of the total evapotranspiration. The maximum amount of water that can be held in the interception reservoir depends on the LAI. In ECHAM this is fixed in time, but in SECHIBA it is calculated interactively as a function of soil temperature. As the soil is still cold after the snow melt, the LAI in ECHAM4/SECHIBA is smaller than in ECHAM4/IMPL, which explains the smaller interception storage.

As mentioned in section 1.2, the surface energy balance equation in SECHIBA is solved using the soil properties obtained by an extrapolation of heat capacity and ground heat flux toward the surface. To assess the impact of this procedure, mean diurnal cycles of the ground heat flux as simulated by ECHAM4/IMPL and ECHAM4/SECHIBA are plotted in Fig. 3.17. For this figure the flux simulations of both models were averaged over a period of several days just after the snow is completely melted, while there are similar atmospheric and soil conditions in both models. Hence, these results do not represent two different meteorological situations in both models, but indicate systematic differences between the two parameterizations themselves. The figure shows that in ECHAM4/SECHIBA the diurnal cycle of the ground heat flux has a higher amplitude and is earlier in phase than in ECHAM4/IMPL.
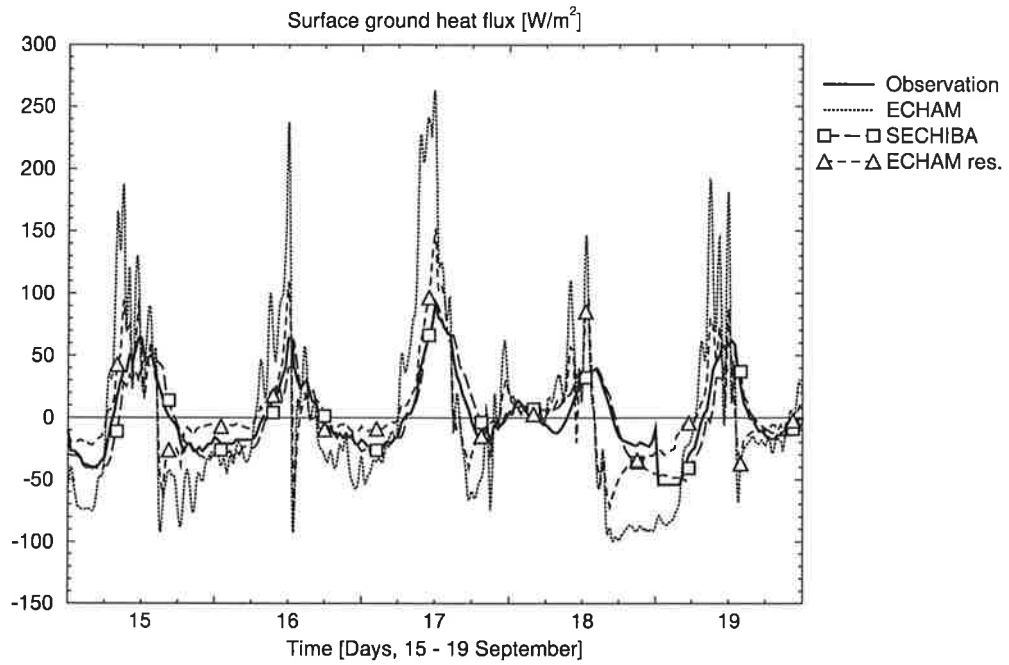
Figure 3.18: Diurnal cycles of surface ground heat flux as observed at Cabauw from 15 to 19 September compared to the model results of ECHAM and SECHIBA. ECHAM res. denotes the surface energy residual in ECHAM.
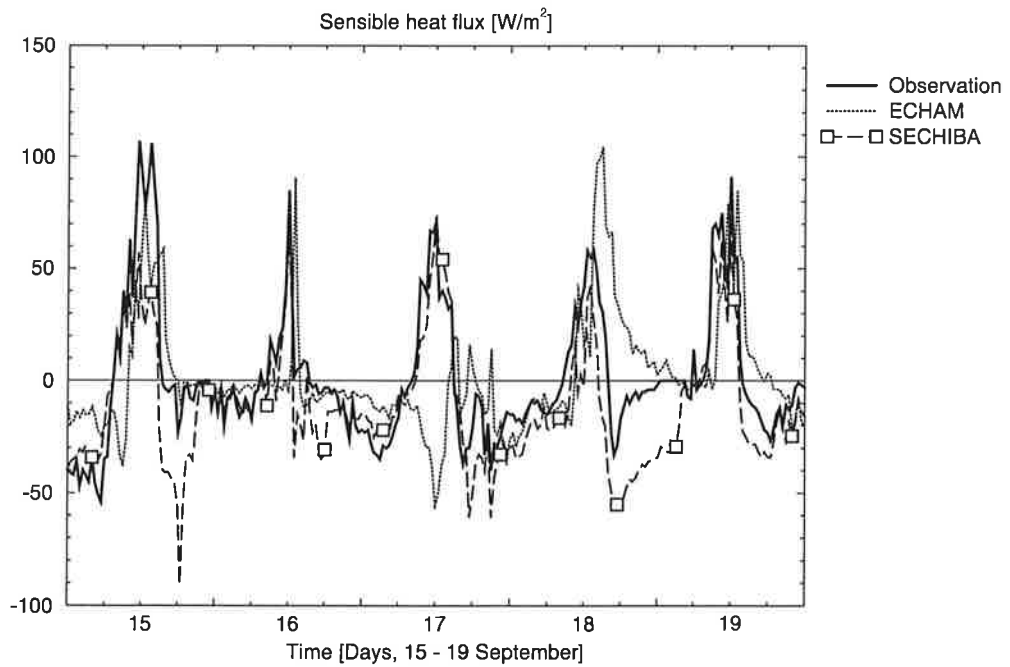
Figure 3.19: As Fig. 3.18 but for sensible heat flux.

This means that the extrapolation of the ground heat flux toward the surface in SECHIBA works as desired.

3.4   Comparison to the Cabauw observations

In order to verify that the numerical studies, which are the main focus of this chapter, are compatible with observational evidence, the Cabauw data set (cf. chapter 2) is used. For this reason a version of SECHIBA that is implemented in the ECHAM 1D model has been developed, which can also be forced by the atmospheric observations. As an example Fig. 3.18 compares the ECHAM and SECHIBA simulations of the ground heat flux to the observations. In section 2.2.1 the overestimation of the amplitude of the ground heat flux in ECHAM is discussed. In the morning hours before noon there is a too high downward flux into the soil and in the evening and night this situation is reversed. A comparison with Fig. 3.19 shows that the energy of the overestimated ground heat flux is missing or provided, respectively, to the sensible heat flux. Additionally, there is energy lost to or created by the energy residual term, respectively. The rise of the sensible heat flux in the morning is delayed by up to several hours and the decrease in the afternoon as well. This leads to a phase shift of its diurnal cycle. Two distinct examples for an erroneous sensible heat flux are on 17 and 18 September where even the sign, i. e. the vertical direction of the flux, is reversed.

The simulation of the ground heat flux by SECHIBA, which is very similar to the observation, is a remarkable improvement when compared to ECHAM (cf. Fig. 3.18). The sensible heat flux is significantly improved, too (Fig. 3.19). In particular, the simulation now much better meets the phase of the observed diurnal cycle. Together with the results of section 2.2.1 this shows that solving the surface energy balance equation with an implicit method, that prevents energy loss or creation by the numerics, in combination with a model structure as in SECHIBA, where the heat capacity and ground heat flux are extrapolated toward the surface, yields more realistic surface heat fluxes.

Chapter 4

Global experiments

As consequent extension of the intercomparison of the one-dimensional versions of the three GCMs ECHAM4, ECHAM4/IMPL and ECHAM4/SECHIBA in the previous chapter, here the models are compared in three-dimensional global experiments.

Each of the three models was integrated for a 10-year period after at least one year of spin-up. A T42 spatial resolution was chosen which is equivalent to about $2.8° \times 2.8°$ on a latitude–longitude grid. In all simulations an annual cycle of monthly mean climatological *Sea Surface Temperature (SST)* was used, and the land-sea-mask and glacier-mask and the distributions of background albedo and roughness length were identical. The underlying idea is to exclude differences between ECHAM and SECHIBA which are known to cause major modifications of the simulated climate and which were already studied in previous sensitivity experiments. For example, the albedo is a key parameter which determines the available energy at the land surface. This has a large impact on the general circulation of the atmosphere and the entire near surface climate (e. g. Charney et al., 1977), as already mentioned in the introduction of the thesis. Furthermore, Sud et al. (1988) found that also the roughness length has a significant influence on the large scale circulation and rain fall. By excluding these first-order differences which are directly caused by different values of important key parameters, this set-up allows one to study changes in the simulated atmospheric and near-surface variables which result from the altered land surface representations themselves.

4.1 Global model intercomparison

In this section a series of figures is presented (Fig. 4.1 – Fig. 4.13), which shall provide an overview of the global simulations of ECHAM4, ECHAM4/IMPL and ECHAM4/SECHIBA. Shown are a number of surface quantities and atmospheric fields that characterize the simulated energy and water cycles and atmospheric dynamics.

The figures are organized as follows: Each figure comprises eight panels (except Fig. 4.2) which are arranged in two columns, the left one for the Northern Hemisphere winter season (December-January-February, DJF), the right one for the summer season (June-July-August, JJA). An exception is Fig. 4.3, which shows the spring season (March-April-May, MAM) instead of the winter season. The top panels show the global distributions of the respective quantity as simulated by the standard — or control — model ECHAM4 (semi-
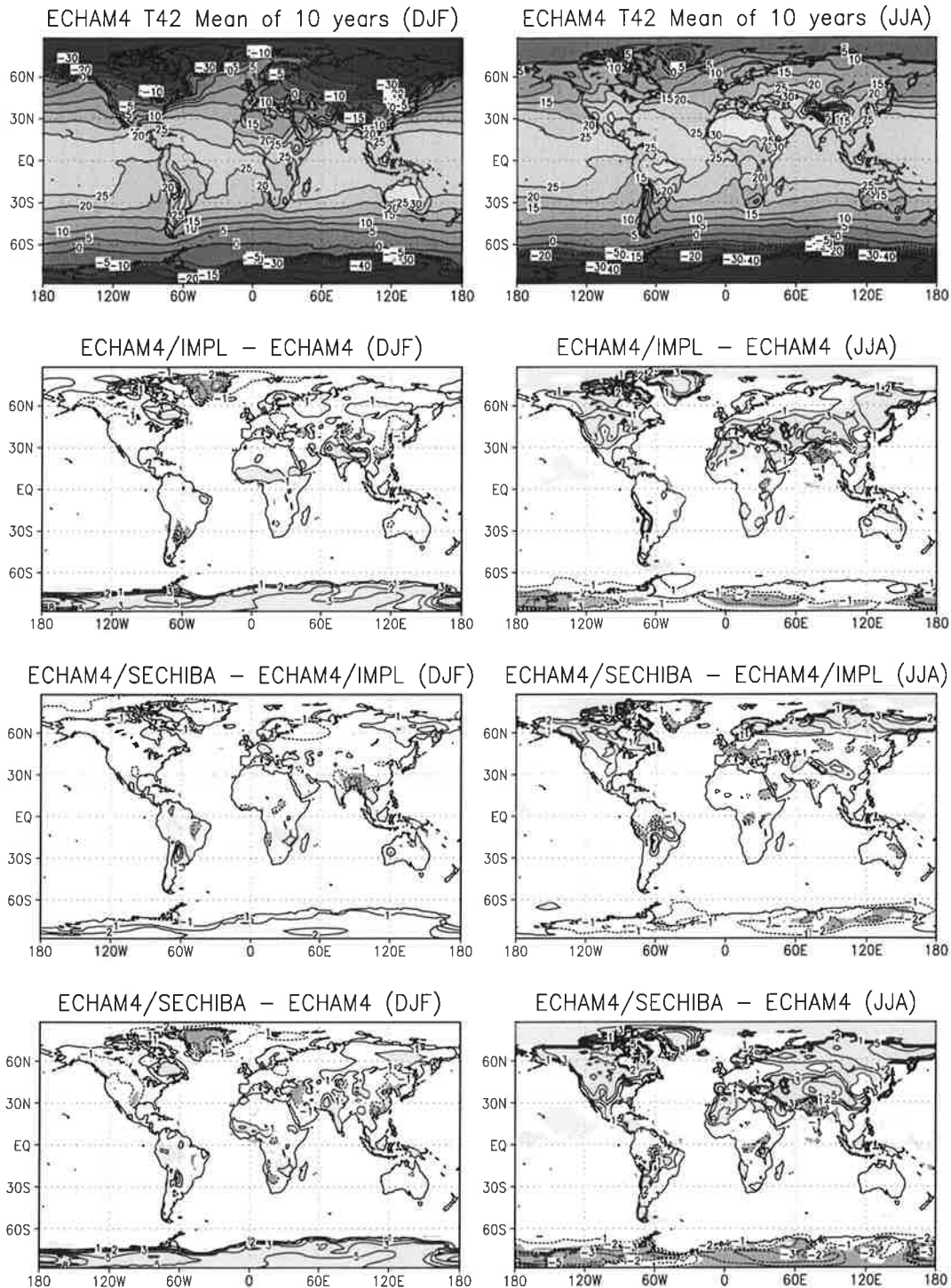
Figure 4.1: The top panels show DJF and JJA seasonal means of the global 2-meter air temperature [°C] as simulated by ECHAM4. The other panels show the model differences ECHAM4/IMPL - ECHAM4, ECHAM4/SECHIBA - ECHAM4/IMPL and ECHAM4/SECHIBA - ECHAM4. The shadings indicate the 95% confidence level of the Student t-test. Contours are at $0, \pm5, \pm10, \pm15, \pm20, \pm25, \pm30, \pm40$°C (top panels) and $\pm1, \pm2, \pm3, \pm5, \pm8$°C (lower six panels).

ECHAM4 T42 Mean of 10 years (DJF)

ECHAM4 T42 Mean of 10 years (JJA)
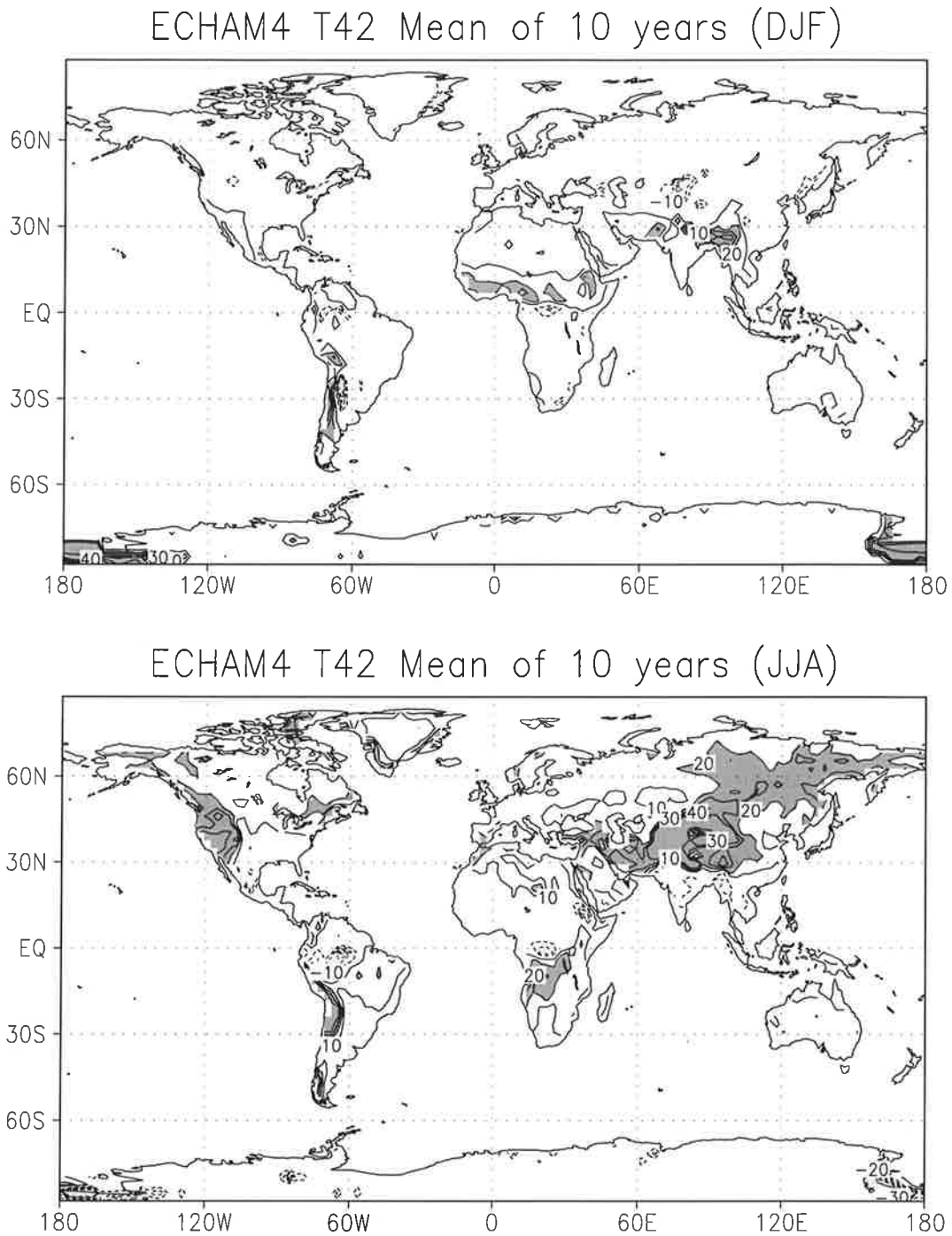
Figure 4.2: DJF (top panel) and JJA (bottom panel) seasonal means of the global land surface energy residual [W/m^2] which represents the error in the surface energy balance as simulated by ECHAM4. Positive values indicate regions where energy is lost for the physical system due to the numerical coupling, negative values indicate unphysical creation of energy by the numerics. The shadings depict regions with absolute values of more than 20 W/m^2. Contours are at $\pm 10, \pm 20, \pm 30, \pm 40$ W/m^2.

implicit). The second row of panels shows the differences of the first modified model version ECHAM4/IMPL (implicit) to the control model, the third row of panels the differences of the second modified (ECHAM4/SECHIBA, implicit) to the first modified model versions and the bottom panels the superposition of the second and third row panels, i. e. the differences of the second modified model version to the control model. Therefore, the second row of panels indicates the changes in the simulations due to the modified coupling technique from ECHAM4 to ECHAM4/IMPL, whereas the third row of panels reveals the effects of an altered land surface parameterization from ECHAM4/IMPL to ECHAM4/SECHIBA while the coupling scheme is unchanged. The total changes due to both model modifications are manifested in the bottom panels.

The figures show that there is a significant impact of the change of the coupling technique and the land surface scheme on most surface variables and atmospheric surface fields. The shaded areas indicate the 95% confidence level of the Student t-test. Generally more pronounced differences are found in the Northern Hemisphere summer season JJA than in the winter season DJF. Therefore, the following discussion of these results will mainly focus on the intercomparison of the three models in the JJA season.

4.1.1 Surface air temperature and related fields

Figure 4.1 shows the model differences of the global 2-meter air temperature. The temperature over large continental areas in the Northern Hemisphere is generally higher in JJA in the two modified model versions than in the standard ECHAM4.

For ECHAM4/IMPL this can be attributed to the model improvement compared to the standard ECHAM4 regarding the energy conservation at the land surface. Energy which was lost over wide regions of Eurasia and North America in JJA due to the implementation of the semi-implicit coupling scheme in ECHAM4 is conserved in ECHAM4/IMPL. Figure 4.2 shows the global distribution of the land surface energy residual in ECHAM4, which represents the error in the surface energy balance in the model. Positive values indicate regions where energy is lost for the physical system due to the numerical coupling, negative values indicate unphysical creation of energy by the numerics. The energy error is high in regions with large temperature changes (see Eq. (3.17)). These occur in regions of high insolation, especially when they are dry, due to the lack of evaporative cooling. This explains the zonally extended band of a high energy error between about 30° and 50°N with maxima in central southern Asia and the southwest of the United States. The Sahara desert, for instance, also receives a high insolation but there is no pronounced seasonal temperature trend within the JJA season in ECHAM4, therefore the energy errors associated with the daily raises and reductions of the surface temperature compensate each other. There are regions in northeast Russia and far northern America where ECHAM4 also exhibits enhanced surface energy errors, although they are not dry. The reason is that due to the late snow melt in these regions (cf. Fig. 4.3, top panels) they experience a considerable warming in June and July, whereas e. g. in west Eurasia the main warming period is earlier in the year.

As this error in the surface energy balance is corrected in ECHAM4/IMPL, the energy is conserved and may contribute to the heating of the surface, upward thermal radiation and/or turbulent surface heat fluxes. The former can be confirmed by comparing the global distribution of the surface air temperature difference between ECHAM4/IMPL and ECHAM4 in JJA (Fig. 4.1) and the regions of high energy balance errors in ECHAM4 (Fig. 4.2). Both
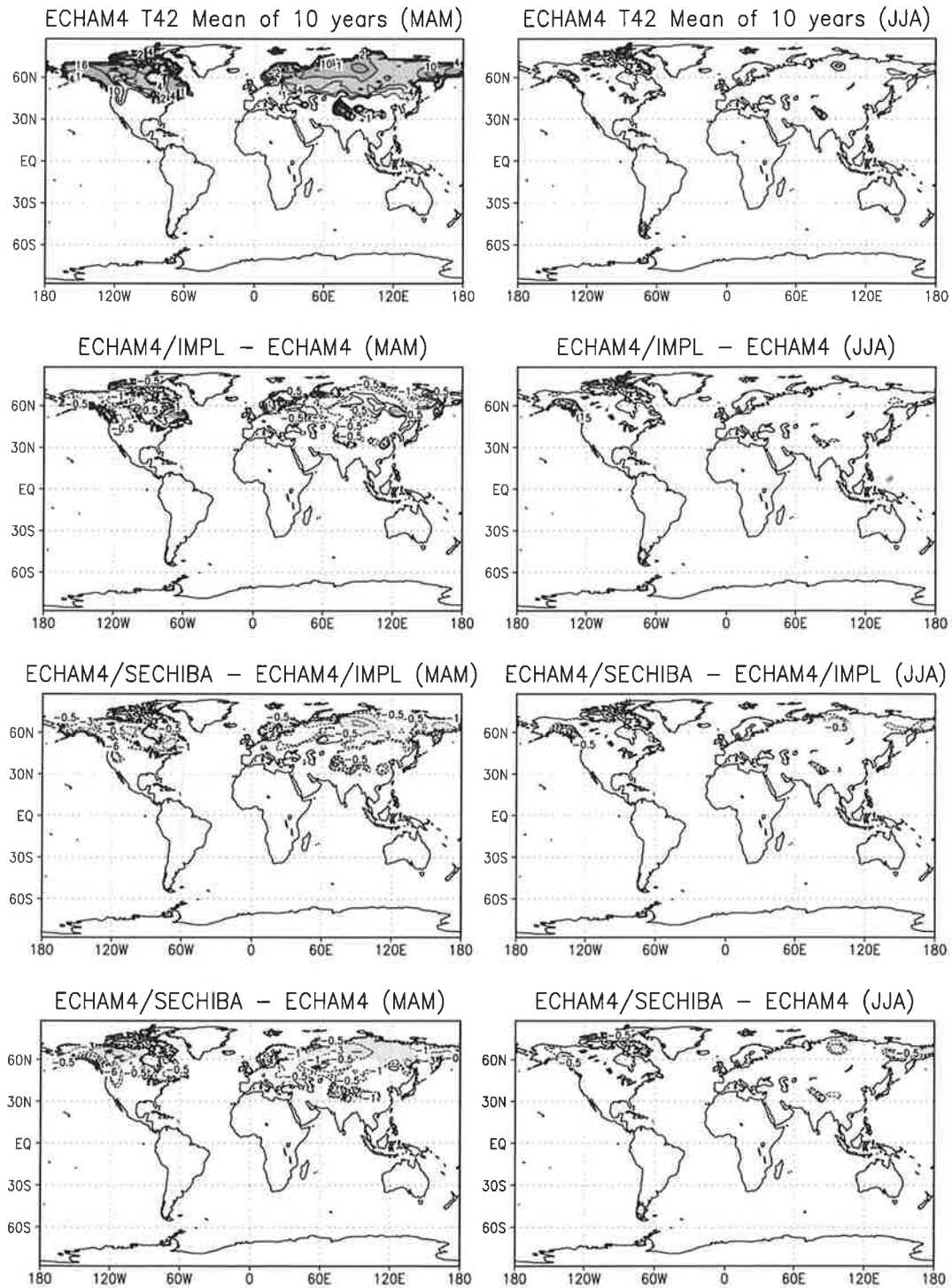
Figure 4.3: The top panels show MAM and JJA seasonal means of the global snow depth distribution [cm water equivalent] as simulated by ECHAM4. The other panels show the model differences ECHAM4/IMPL - ECHAM4, ECHAM4/SECHIBA - ECHAM4/IMPL and ECHAM4/SECHIBA - ECHAM4. The shadings indicate the 95% confidence level of the Student t-test. Contours are at 1, 2, 4, 10, 16 cm water equ. (top panels) and $\pm0.5, \pm1, \pm3, \pm6, \pm10$ cm water equ. (lower six panels).
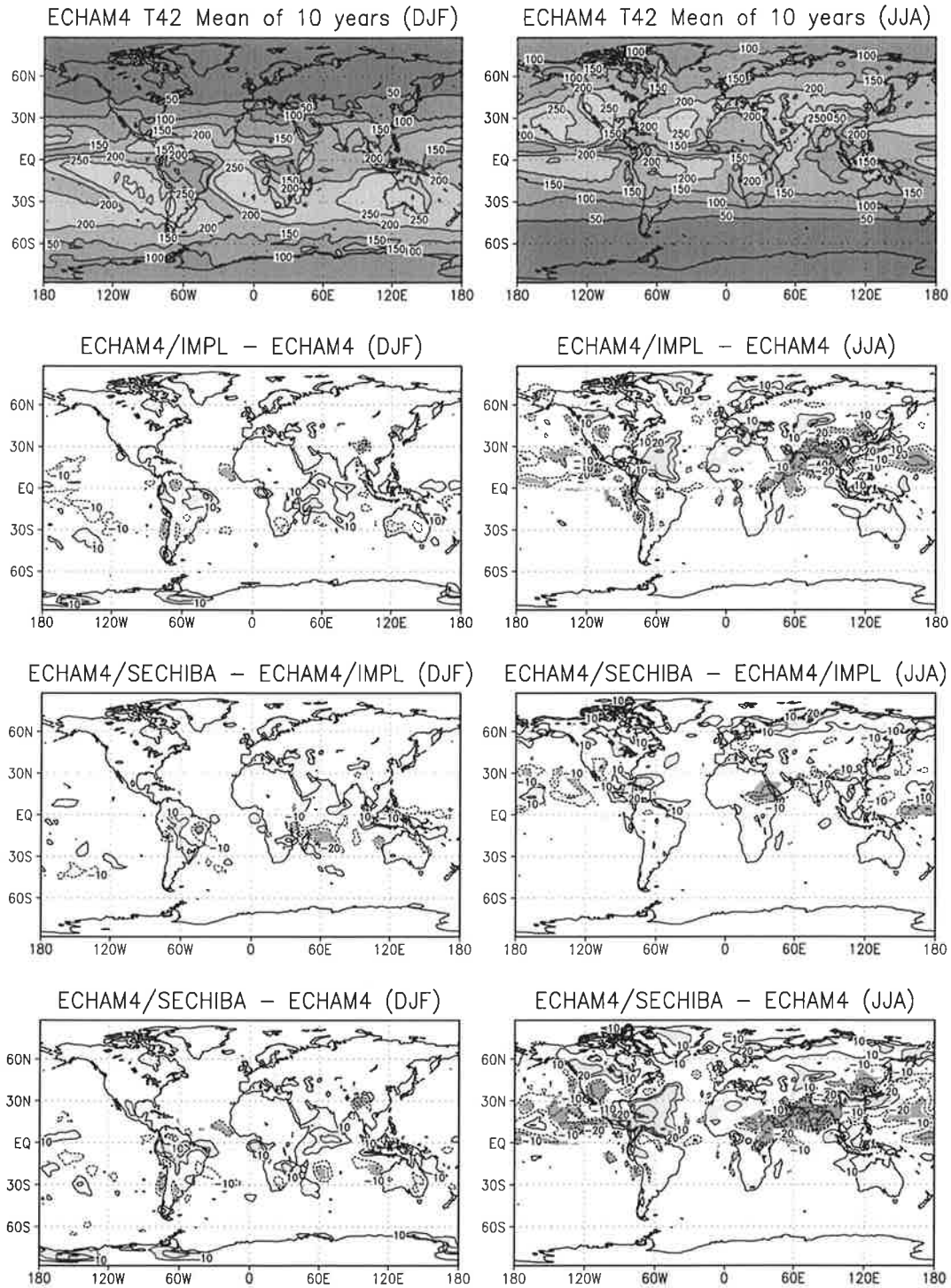
Figure 4.4: The top panels show DJF and JJA seasonal means of the global net surface solar radiation [W/m²] as simulated by ECHAM4. The other panels show the model differences ECHAM4/IMPL - ECHAM4, ECHAM4/SECHIBA - ECHAM4/IMPL and ECHAM4/SECHIBA - ECHAM4. The shadings indicate the 95% confidence level of the Student t-test. Contours are at 50, 100, 150, 200, 250, 300 W/m² (top panels) and ±10, ±20, ±40, ±60 W/m² (lower six panels).
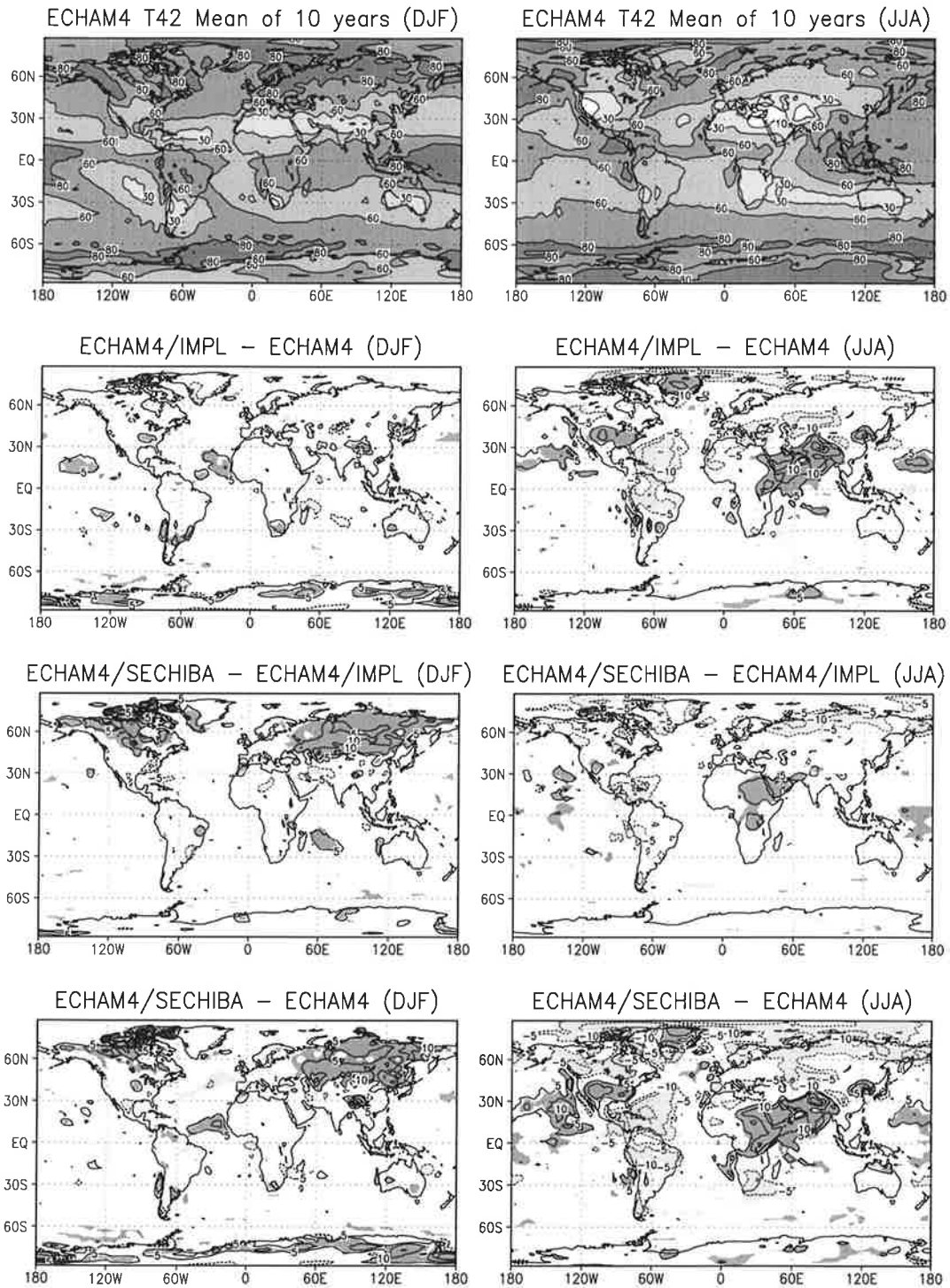
Figure 4.5: The top panels show DJF and JJA seasonal means of the global total cloud cover [%] as simulated by ECHAM4. The other panels show the model differences ECHAM4/IMPL - ECHAM4, ECHAM4/SECHIBA - ECHAM4/IMPL and ECHAM4/SECHIBA - ECHAM4. The shadings indicate the 95% confidence level of the Student t-test. Contours are at 10, 30, 60, 80% (top panels) and ±5, ±10, ±20, ±30% (lower six panels).
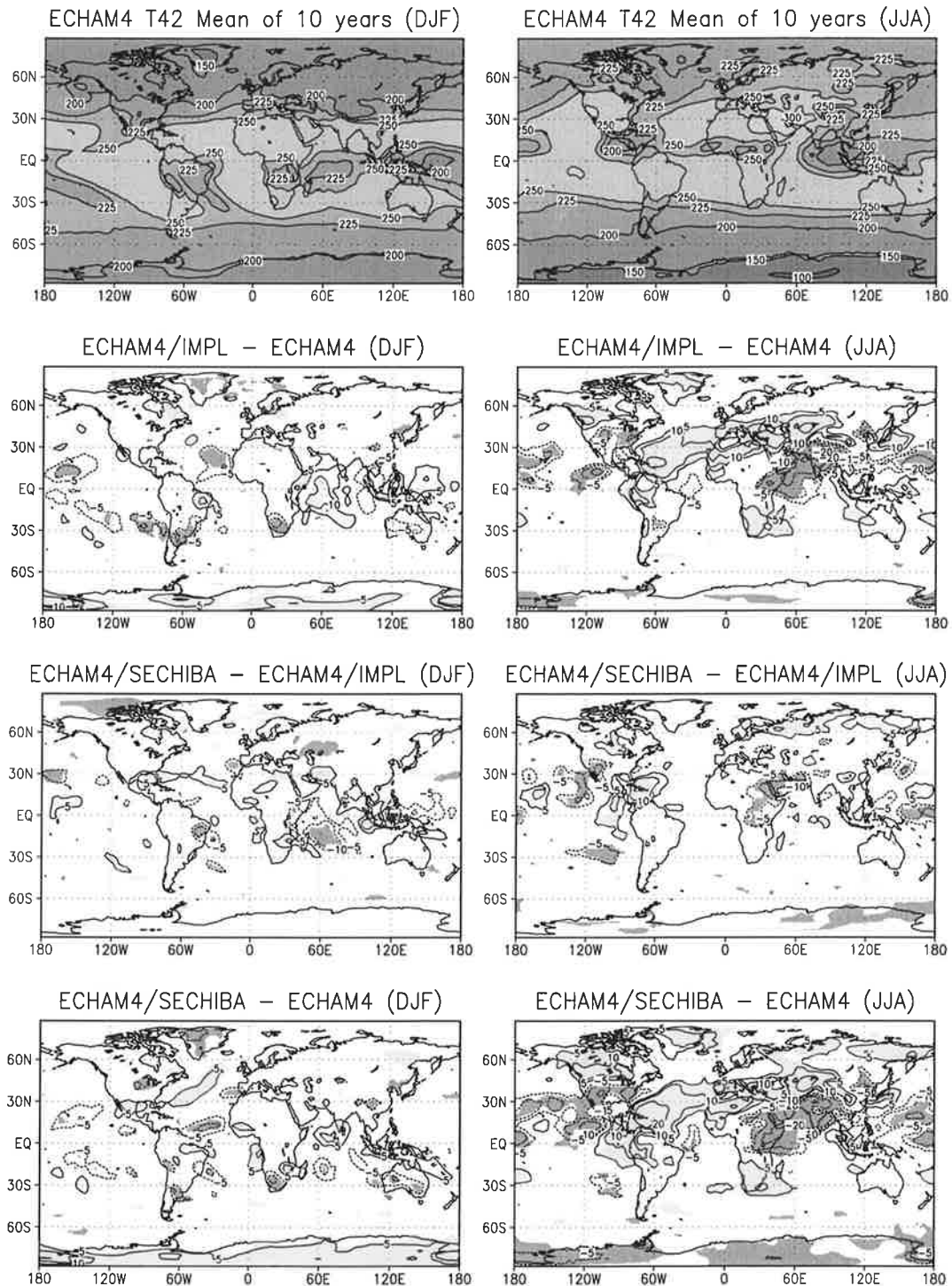
Figure 4.6: The top panels show DJF and JJA seasonal means of the global top thermal radiation (outgoing longwave radiation, OLR) [W/m^2] as simulated by ECHAM4. The other panels show the model differences ECHAM4/IMPL - ECHAM4, ECHAM4/SECHIBA - ECHAM4/IMPL and ECHAM4/SECHIBA - ECHAM4. The shadings indicate the 95% confidence level of the Student t-test. Contours are at 100, 150, 200, 225, 250, 300 W/m^2 (top panels) and $\pm 5, \pm 10, \pm 20, \pm 40$ W/m^2 (lower six panels).

show a good agreement in the regional distribution as well as in the locations of the maxima. A similar correspondence is found in DJF (India and Africa).

In ECHAM4/SECHIBA the increased surface air temperatures are mainly due to a different snow parameterization which accumulates less snow or allows the melting about one month earlier, respectively. The main reason is a different snow melt criterion (cf. discussion in section 3.3). Figure 4.3 shows that ECHAM4/SECHIBA simulates a significantly smaller snow depth than ECHAM4/IMPL in Canada, a wide region in Eurasia poleward of about 55°N, and in the region of the Tibetan plateau and the Himalaya in spring. Between ECHAM4/IMPL and ECHAM4 only non-uniformly distributed small differences in snow depth appear in these regions, and they are mostly not significant. The reduced snow cover in ECHAM4/SECHIBA causes a reduced surface albedo which leads to an enhanced absorption of solar radiation (see Fig. 4.4). The likely consequence is an increased surface temperature which in turn accelerates the melting of snow. Hence, here a snow – albedo – solar radiation – surface temperature positive feedback is found, that gradually increases the surface temperature, compared to ECHAM4/IMPL, over the weeks and months from spring to summer, which results in a temperature difference of more than 3°C in some Eurasian regions.

As a result of the enhanced surface and also tropospheric temperature the relative air humidity is reduced which leads to a reduced cloud cover, which further enhances the aforementioned feedback. In ECHAM4/SECHIBA this is best seen in JJA in northern Eurasia (Fig. 4.5). This mechanism is discussed in more detail in section 4.3.2 for a region in northeast Siberia. A similar behaviour is shown by ECHAM4/IMPL (compared to ECHAM4) in a region extending from the Baikal lake to the Caspian Sea and further on to southeast Europe. The raised surface temperature in this region is associated with a reduced cloud cover and an increased insolation.

A further comparison of the JJA maps of total cloud cover and solar radiation differences between the three models (Figs. 4.5 and 4.4) reveals an – expected – clear anti-correlation of these two quantities: an enhanced cloud cover is associated with a reduced surface solar radiation and vice versa. Very striking is the increased cloud cover in ECHAM4/IMPL (compared to ECHAM4) in a region covering the Indian subcontinent, parts of Saudi Arabia, the Indian Ocean and east Africa. This is related to an enhanced southeast Asian monsoon activity in ECHAM4/IMPL, which is further analysed in section 4.3.1. In ECHAM4/SECHIBA the cloud cover increase is even intensified over northeast and central Africa.

Analysing the *Outgoing Longwave* (or thermal) *Radiation (OLR)* at the top of the atmosphere can reveal some information on the height of the cloud top. As the emitted thermal radiation depends on the temperature of the emitting body and the tropospheric temperature decreases with height, there will be less OLR, relative to the surface thermal radiation, the higher the emitting clouds are. Figure 4.6 (top panels) shows the top thermal radiation as simulated by ECHAM4 in DJF and JJA. Very high clouds (i. e. low values of OLR) are found in the *InterTropical Convergence Zone (ITCZ)*. This is a region of low-level converging and high rising air. It roughly follows the position of the sun and is therefore usually located in the summer Hemisphere. This periodic motion between Southern and Northern Hemisphere is well represented in the DJF and JJA plots in Fig. 4.6. The figure also shows that ECHAM4/IMPL simulates higher clouds in JJA in a wide region over India and the northwest Indian Ocean and also some parts of the west and east Pacific in the domain of the ITCZ. This indicates an overall stronger convective activity in the ITCZ in ECHAM4/IMPL.

In ECHAM4/SECHIBA there are even higher clouds over northeast and central Africa. A comparison of these differences in the model simulations with the changes in the simulated total cloud cover (Fig. 4.5) shows an almost perfect agreement of the regions with an increased total cloud cover and those with a reduced OLR (which means an enhanced number of high clouds). Furthermore, there are regions with increased OLR, for instance in ECHAM4/IMPL in a band extending from central Eurasia westwards over southern Europe and north Africa, or in ECHAM4/SECHIBA at the north rim of Eurasia. These areas agree very well with regions of reduced total cloud cover and enhanced surface temperature (Figs. 4.5 and 4.1), which explains the increased upward thermal radiation.

4.1.2   Global water cycle

In this section the differences between the simulated global water cycles in the three models are discussed. Figure 4.7 presents the computed total surface evaporation. On the continents differences between the models are mainly determined by changes in available surface energy and moisture. This means, if there is enough water available in the soil to sustain the season of high evaporation, then the enhanced surface temperature in the two modified model versions can lead to a higher evaporation. In ECHAM4/IMPL (compared to ECHAM4) in JJA this is the case in northeast Russia and parts of central China. In most of these regions the relative plant-available soil moisture in ECHAM4 is higher than 60% up to 80% and more (Fig. 4.8). In ECHAM4/IMPL it is reduced by up to 20% but it stays around or not much below the value of the critical soil moisture. This is the level when soil moisture stress starts to reduce the transpiration (i. e. 61.5% of the plant-available soil moisture in the ECHAM4 land surface scheme, cf. Eq. (1.7)). In a large region extending from the Baikal lake to southern Europe and in the southern central USA and Mexico the soil moisture in ECHAM4/IMPL is reduced in JJA as well. In the Asian section this drying is persistent troughout the year, as the DJF plot shows. These regions are already relatively dry in ECHAM4, therefore the additional drying leads to a reduced evaporation which is likely to amplify the warming, especially in Asia (cf. Fig. 4.1).

The opposite effect of the mechanism just described is, that a cooling of the surface reduces the evaporation. This can be seen in ECHAM4/IMPL in JJA over the Indian peninsula. The soil moisture is unchanged or increased compared to ECHAM4.

Over the oceans the situation is different. As the same SST is prescribed in the three models, no differences in the evaporation as result of different evolutions of the surface temperature can occur as in the case over land. Furthermore, the limiting boundary condition regarding the availability of water as on continents does not exist over oceans. But changes in the simulated evaporation over oceans can be caused by an altered surface wind speed (see Eq. (1.4)). This is the case e. g. in ECHAM4/IMPL in JJA over large parts of the Indian Ocean. As a consequence of an enhanced southeast Asian summer monsoon circulation the surface wind speed is increased over the northwest Indian Ocean and the Bay of Bengal, which leads to a higher evaporation (Fig. 4.7). This serves as a source of humidity, which moistens the air which is advected over southeast Asia. As a result the atmospheric precipitable water in ECHAM4/IMPL is increased in this region compared to ECHAM4, as well as the cloud cover (Fig. 4.5). Figure 4.9 shows that this has also a considerable impact on the summer monsoon precipitation which is substantially increased over large areas. The Asian summer monsoon is discussed in more detail in section 4.3.1.
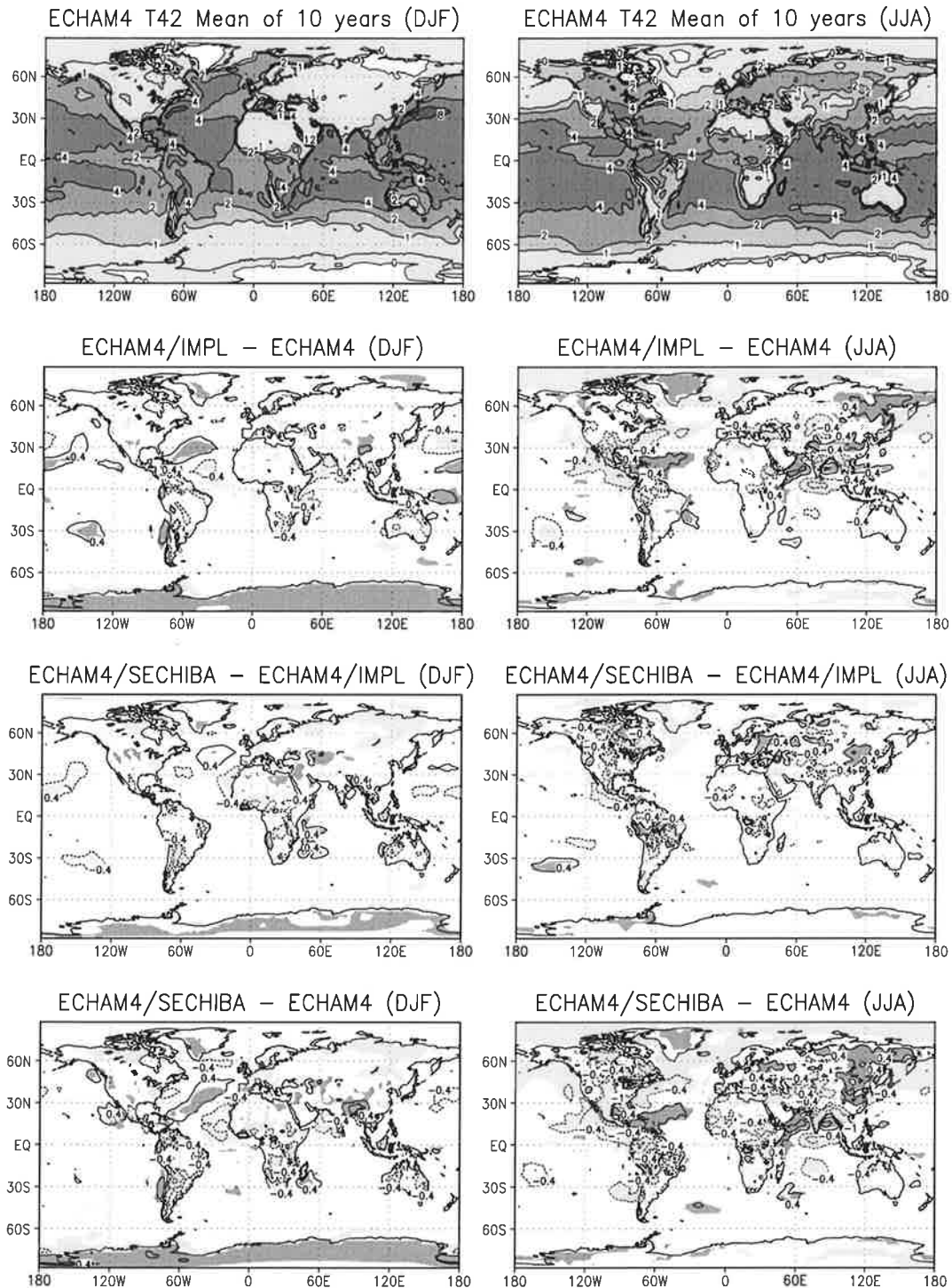
Figure 4.7: The top panels show DJF and JJA seasonal means of the global total surface evaporation [mm/d] as simulated by ECHAM4. The other panels show the model differences ECHAM4/IMPL - ECHAM4, ECHAM4/SECHIBA - ECHAM4/IMPL and ECHAM4/SECHIBA - ECHAM4. The shadings indicate the 95% confidence level of the Student t-test. Contours are at 0, 1, 2, 4, 8 mm/d (top panels) and ±0.4, ±1, ±3 mm/d (lower six panels).

ECHAM4 T42 Mean of 10 years (DJF)   ECHAM4 T42 Mean of 10 years (JJA)

ECHAM4/IMPL − ECHAM4 (DJF)   ECHAM4/IMPL − ECHAM4 (JJA)

ECHAM4/SECHIBA − ECHAM4/IMPL (DJF)   ECHAM4/SECHIBA − ECHAM4/IMPL (JJA)

ECHAM4/SECHIBA − ECHAM4 (DJF)   ECHAM4/SECHIBA − ECHAM4 (JJA)
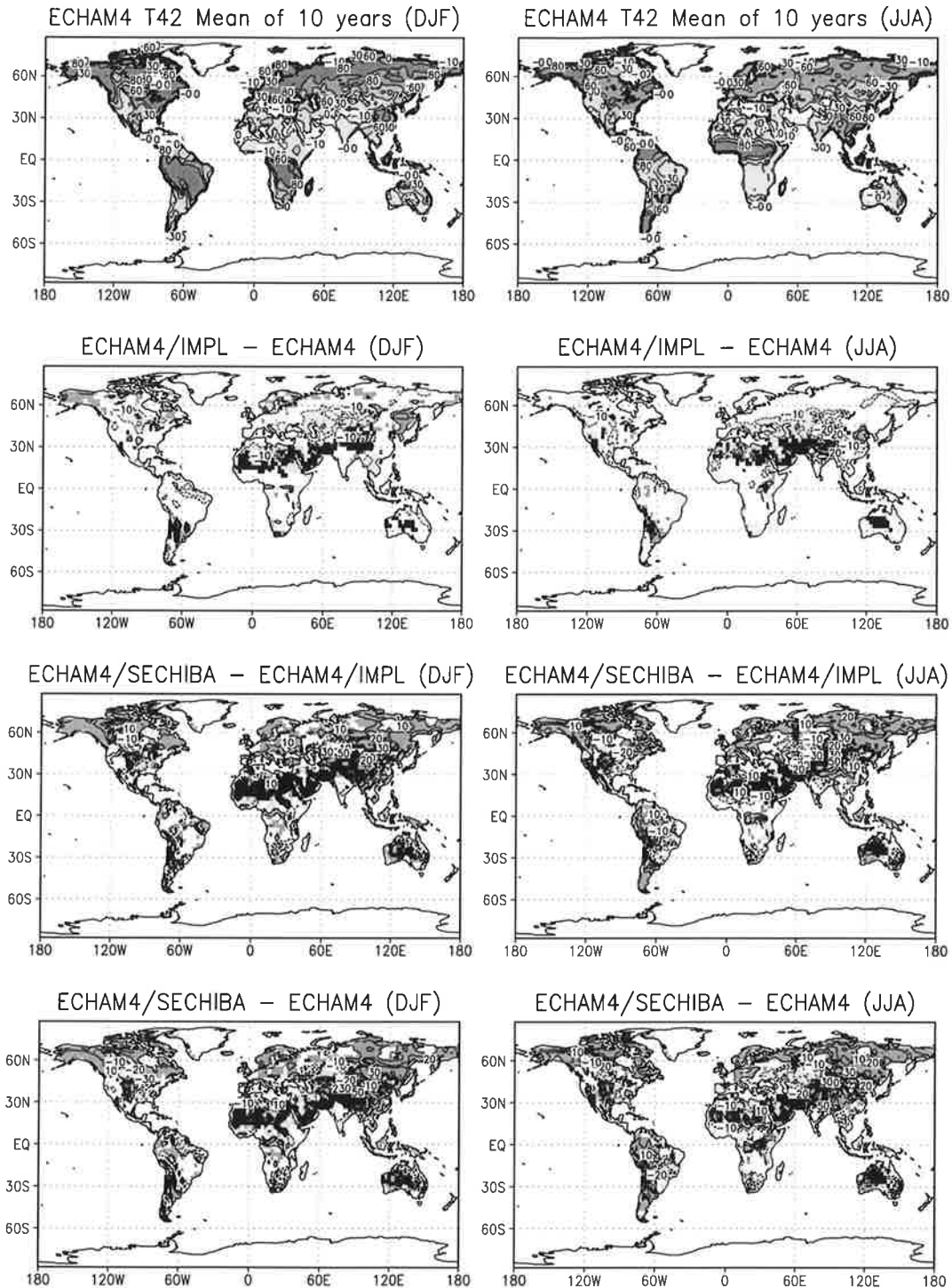
Figure 4.8: As Fig. 4.7 but for relative plant-available soil moisture [%]. The shadings indicate the 95% confidence level of the Student t-test, the black areas are regions where the soil water content in ECHAM4 (or ECHAM4/IMPL, respectively) is below the wilting level (cf. (1.7)) which is possible due to bare soil evaporation or the coding error that is discussed in section 3.2. The structure of the soil hydrology scheme in SECHIBA does not allow moisture values below the wilting level. Therefore these regions are excluded in the difference plots. Contours are at −10, 0, 30, 60, 80% (top panels) and ±10, ±20, ±30, ±50% (lower six panels).
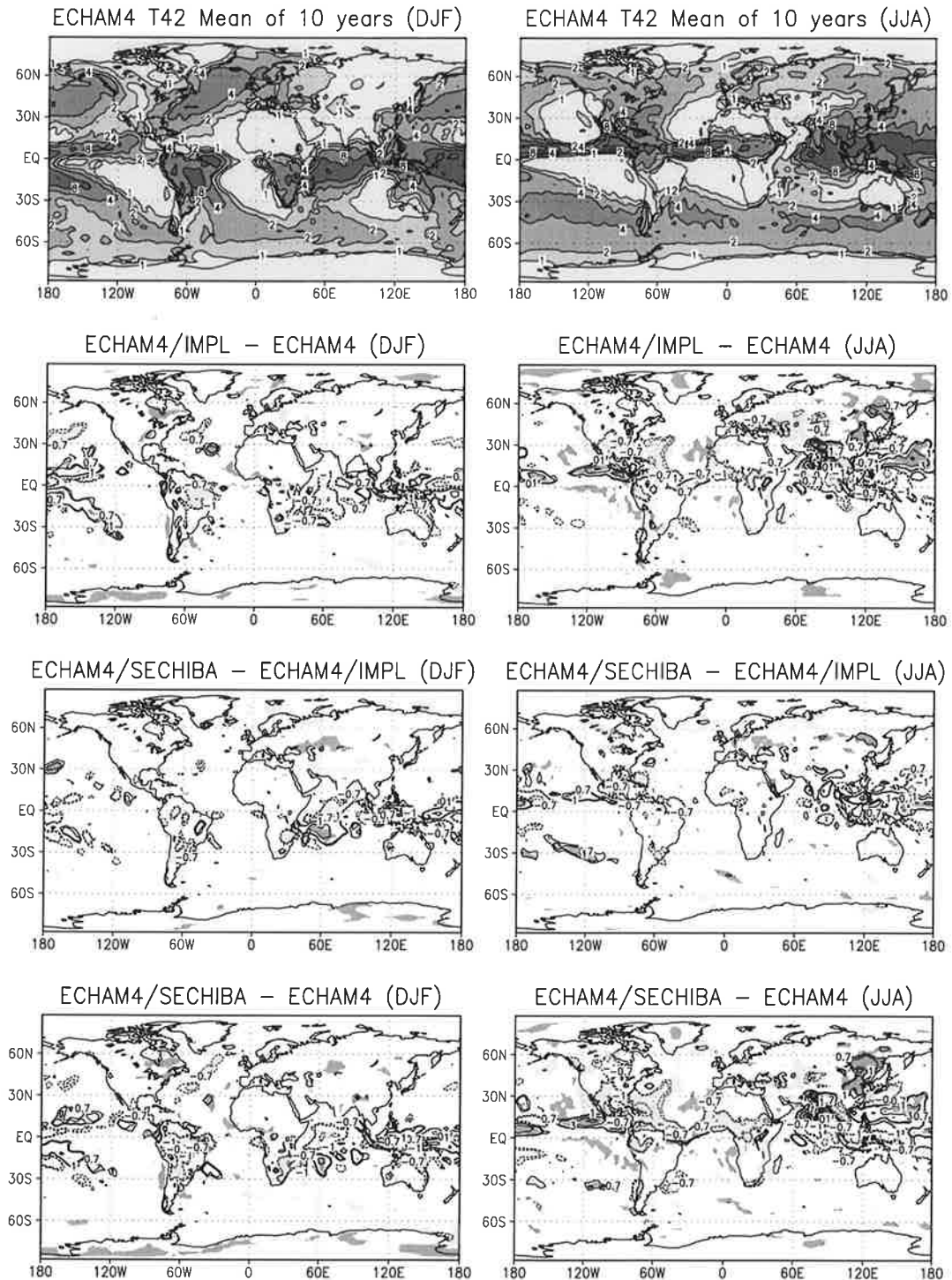
Figure 4.9: The top panels show DJF and JJA seasonal means of the global total precipitation [mm/d] as simulated by ECHAM4. The other panels show the model differences ECHAM4/IMPL - ECHAM4, ECHAM4/SECHIBA - ECHAM4/IMPL and ECHAM4/SECHIBA - ECHAM4. The shadings indicate the 95% confidence level of the Student t-test. Contours are at 1, 2, 4, 8, 16 mm/d (top panels) and $\pm 0.7, \pm 1, \pm 3, \pm 6$ mm/d (lower six panels).
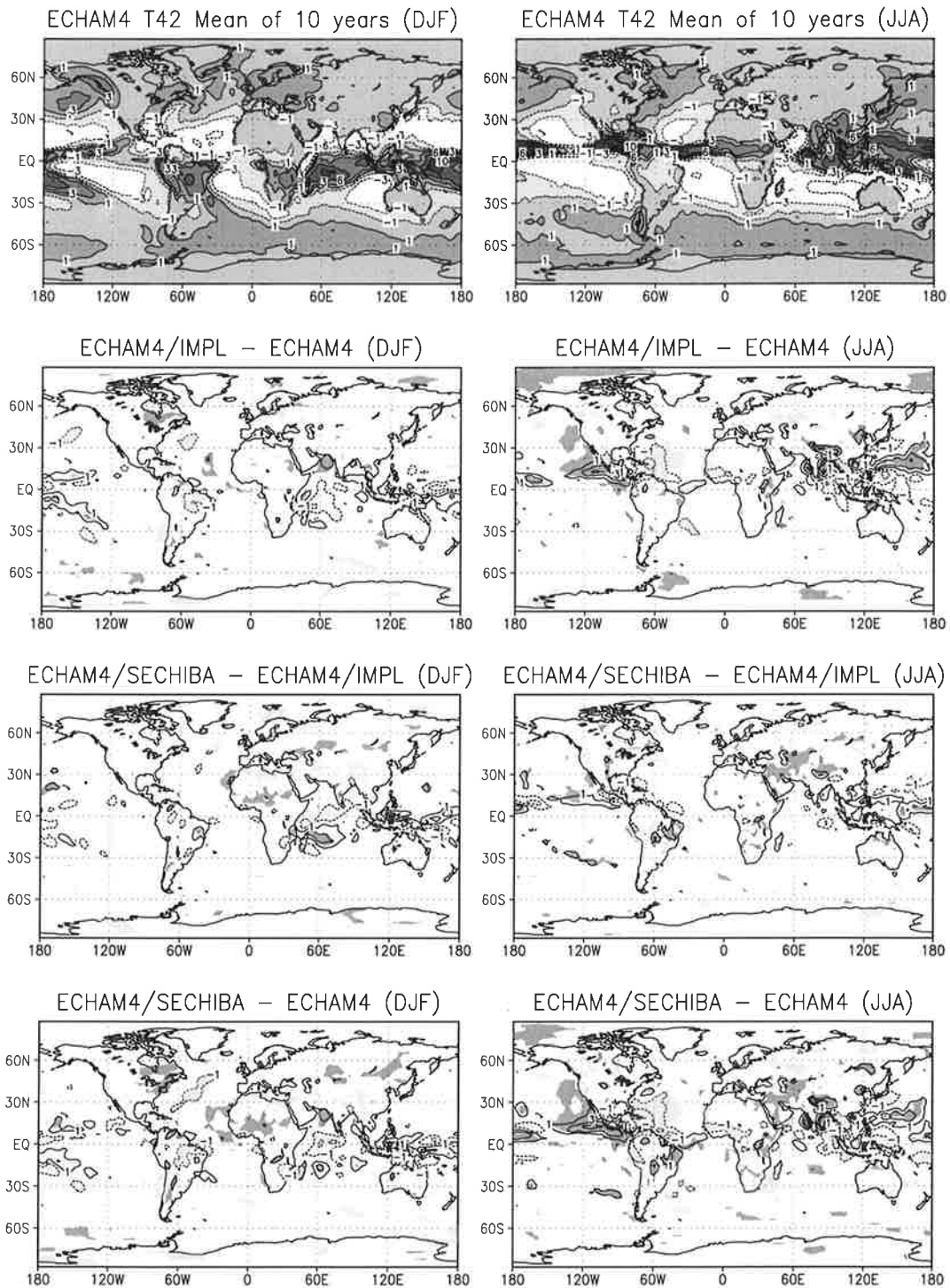
Figure 4.10: The top panels show DJF and JJA seasonal means of the global total precipitation - evaporation [mm/d] as simulated by ECHAM4. The other panels show the model differences ECHAM4/IMPL - ECHAM4, ECHAM4/SECHIBA - ECHAM4/IMPL and ECHAM4/SECHIBA - ECHAM4. The shadings indicate the 95% confidence level of the Student t-test. Contours are at -6, -3, -1, 1, 3, 6, 10, 15 mm/d (top panels) and $\pm 1, \pm 3, \pm 6$ mm/d (lower six panels).

Comparing the global differences of evaporation and precipitation in ECHAM4/IMPL to ECHAM4 in JJA (Figs. 4.7 and 4.9) shows that the patterns resemble each other. The differences of precipitation and evaporation (cf. Fig. 4.10) indicate that both change by almost the same amount in many regions. For instance, in northeast Asia precipitation and evaporation both increase but their difference shows no change. In the aforementioned region extending from central Asia to southern Europe precipitation and evaporation both decrease, again their difference is unchanged. Hence, these are two examples where the regional hydrological cycle in ECHAM4/IMPL is intensified or slowed down, respectively, by an alteration of the local (or regional) moisture recycling. This is mainly determined by local changes in the availability of surface energy and moisture.

The temporal evolution of the moisture content of a vertical atmospheric column extending from the Earth's surface to the top of the atmosphere is given by a continuity equation as the convergence of all moisture fluxes at the boundaries of the column. In the horizontal direction this is the convergence of air humidity which is advected into or out of the column, and in the vertical direction it is the difference between precipitation and evaporation at the surface. Averaged over long periods of time, e. g. seasons, the temporal change of the atmospheric moisture content of the column can be assumed to be small compared to the flux convergence terms in this equation, therefore a regional moisture convergence is directly given by precipitation minus evaporation in the region.

Figure 4.10 shows the moisture convergence where, for instance, the ITCZ, as simulated by ECHAM4 in DJF and JJA, is clearly depicted (top panels). The source regions of the moisture are to a large extent the subtropical oceans. The main differences of the moisture convergence in ECHAM4/IMPL in JJA occur in the tropics and subtropics, over continents as well as over oceans. They are mainly related to changes of the ITCZ. The moisture convergence in the Indian monsoon region increases as well as over the west Pacific at about 20°N. Southward of these regions the convergence tends to be reduced, which also seen in the Sahel in west Africa. Further changes occur over the oceans close to Central America. This suggests a large scale northward shift of the ITCZ in ECHAM4/IMPL in JJA which is likely due to the extensive warming of the Northern Hemisphere continental surfaces. This emphasizes the large scale global character of the ITCZ and its relation to the Asian monsoon circulation system (Gadgil et al. 1997).

In ECHAM4/SECHIBA, changes in the simulated evaporation in JJA compared to ECHAM4/IMPL (Fig. 4.7) are caused in many regions by a different soil water availability induced by different global distributions of total soil water-holding capacity in SECHIBA and ECHAM (cf. sections 1.1 and 1.2, Fig. 1.7). Examples for regions with smaller storage capacities in SECHIBA are the southern and central USA and eastern South America. In these regions less soil water is available to sustain episodes of high evaporation or little rain fall. In the USA this leads to a drying in the summer (JJA) (Fig. 4.8) which significantly reduces the evaporation. In eastern South America there is the dry season in JJA, and due to the smaller moisture reservoirs ECHAM4/SECHIBA simulates an intensified drying of the soil which also causes a decrease in evaporation. There is no change seen in the precipitation at the same time (Fig. 4.9) which means that there is an enhanced atmospheric moisture convergence in JJA (see Fig. 4.10).

The reverse mechanism is found further westwards in central and western South America between about 10° and 15°S. Larger soil water reservoirs in ECHAM4/SECHIBA allow for a higher available soil moisture and an increased evaporation in JJA (Fig. 4.7). A comparison of
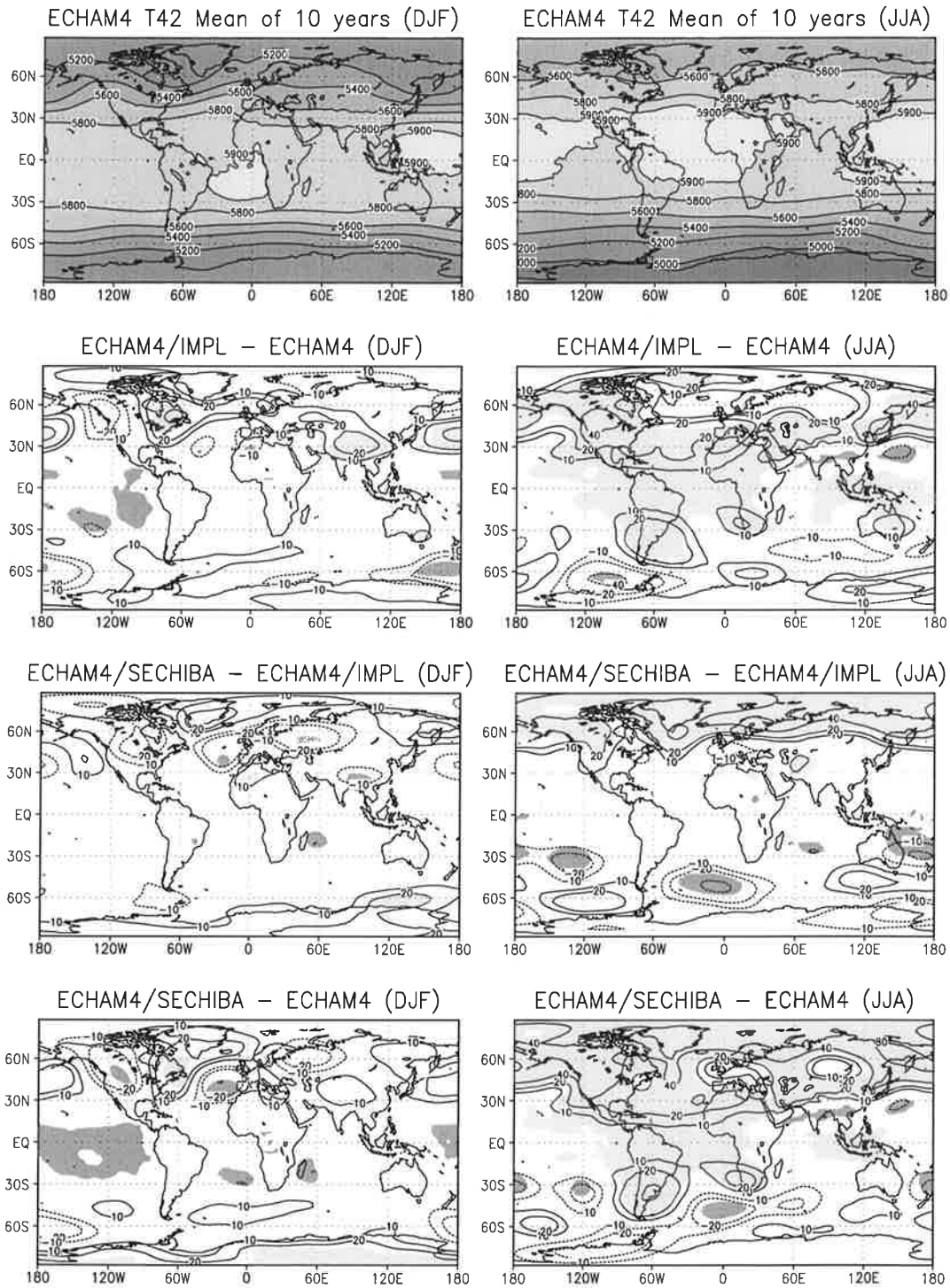
Figure 4.11: The top panels show DJF and JJA seasonal means of the global geopotential height [gpm] at 500 hPa as simulated by ECHAM4. The other panels show the model differences ECHAM4/IMPL - ECHAM4, ECHAM4/SECHIBA - ECHAM4/IMPL and ECHAM4/SECHIBA - ECHAM4. The shadings indicate the 95% confidence level of the Student t-test. Contours are at 5000, 5200, 5400, 5600, 5800, 5900 gpm (top panels) and $\pm 10, \pm 20, \pm 40, \pm 80$ gpm (lower six panels).
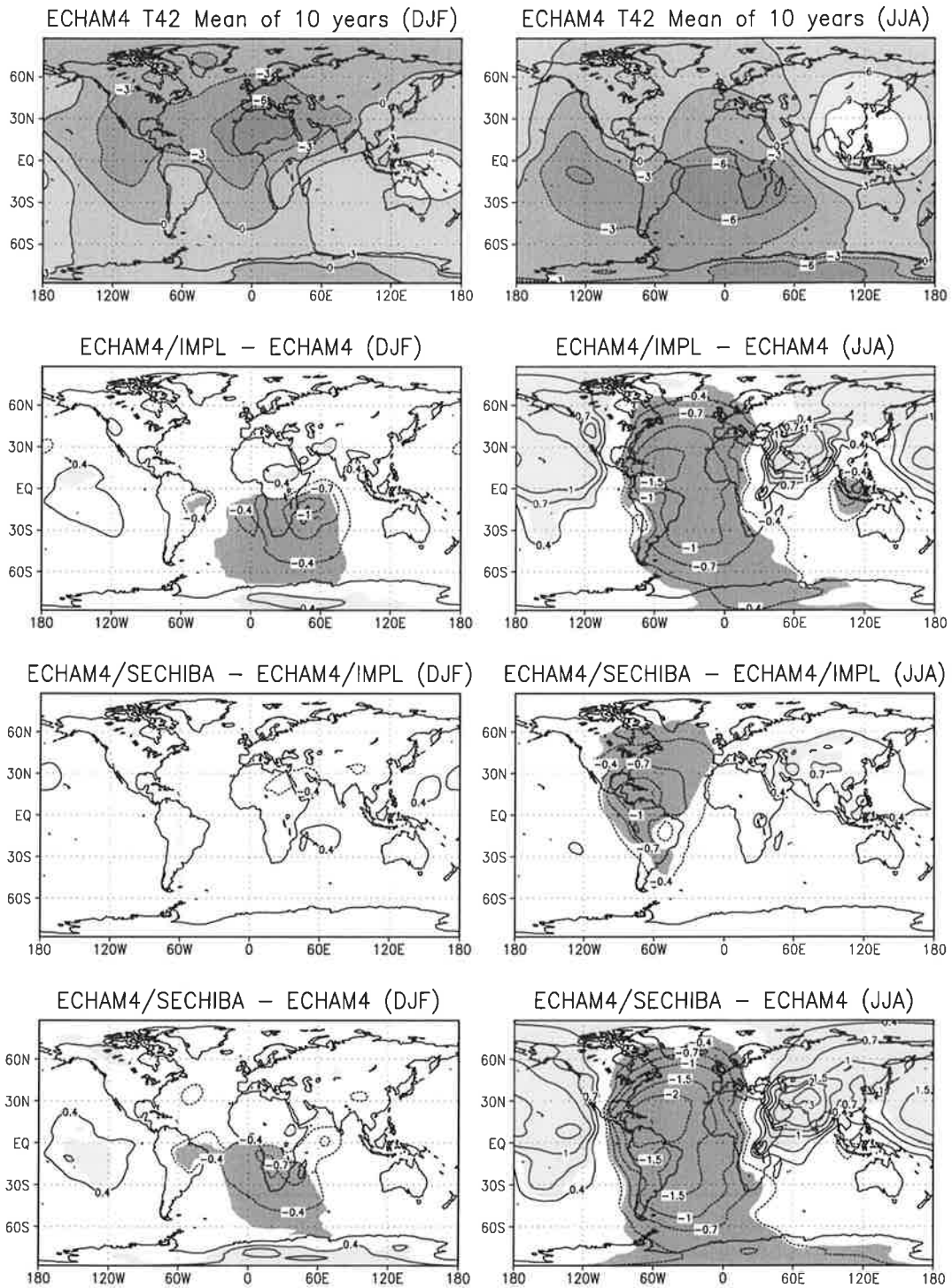
Figure 4.12: The top panels show DJF and JJA seasonal means of the global velocity potential [10^{-6} m^2/s] at 850 hPa as simulated by ECHAM4. The other panels show the model differences ECHAM4/IMPL - ECHAM4, ECHAM4/SECHIBA - ECHAM4/IMPL and ECHAM4/SECHIBA - ECHAM4. The shadings indicate the 95% confidence level of the Student t-test. Contours are at -6, -3, 0, 3, 6, $9 \cdot 10^{-6}$ m^2/s (top panels) and $\pm 0.4, \pm 0.7, \pm 1, \pm 1.5, \pm 2, \pm 3 \cdot 10^{-6}$ m^2/s (lower six panels).

ECHAM4 T42 Mean of 10 years (DJF)

ECHAM4 T42 Mean of 10 years (JJA)

ECHAM4/IMPL – ECHAM4 (DJF)

ECHAM4/IMPL – ECHAM4 (JJA)

ECHAM4/SECHIBA – ECHAM4/IMPL (DJF)

ECHAM4/SECHIBA – ECHAM4/IMPL (JJA)

ECHAM4/SECHIBA – ECHAM4 (DJF)

ECHAM4/SECHIBA – ECHAM4 (JJA)
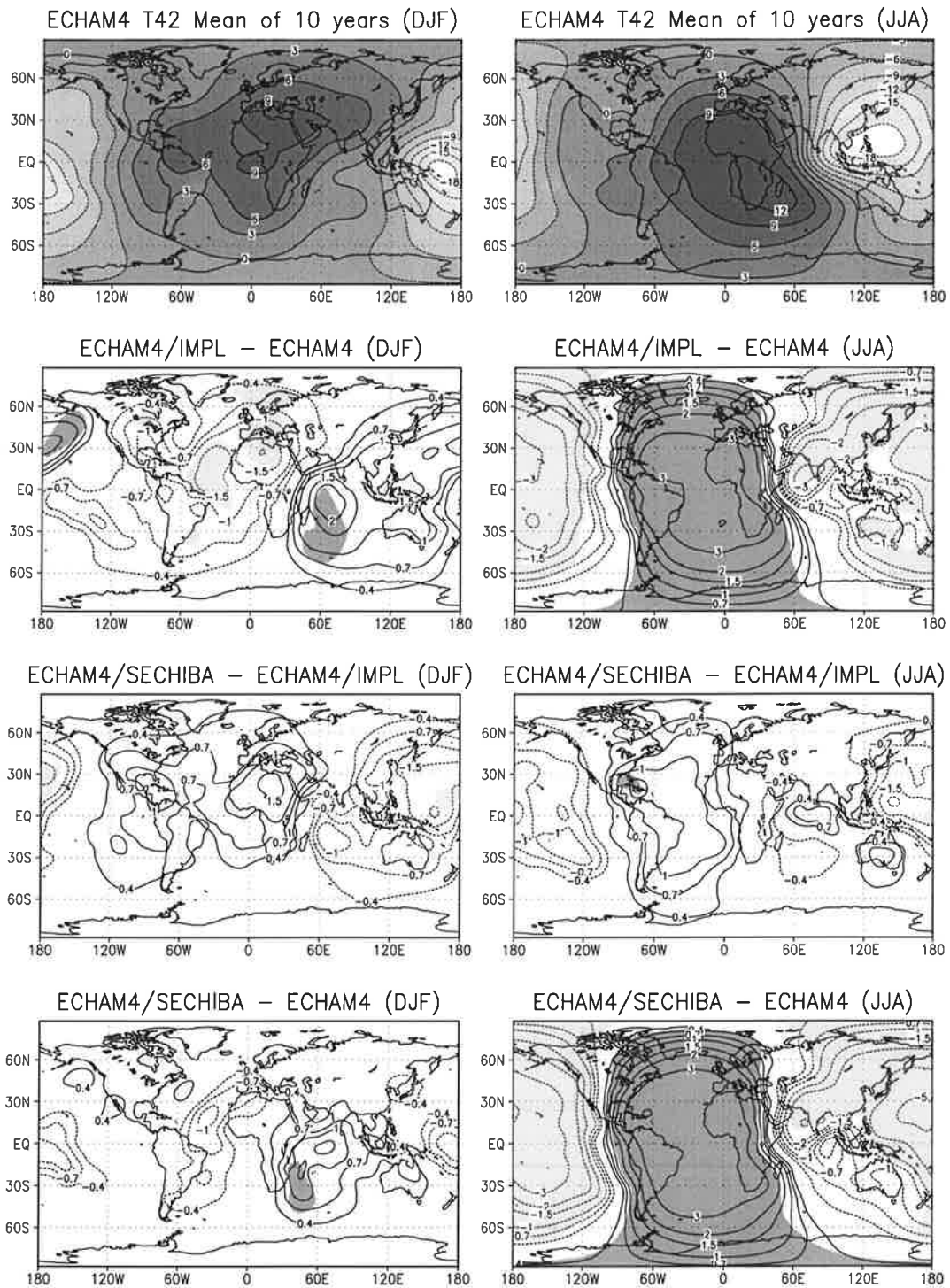
Figure 4.13: As Fig. 4.12 but for velocity potential $[10^{-6} \text{ m}^2/\text{s}]$ at 150 hPa. Contours are at -18, -15, -12, -9, -6, -3, 0, 3, 6, 9, $12 \cdot 10^{-6} \text{ m}^2/\text{s}$ (top panels) and $\pm 0.4, \pm 0.7, \pm 1, \pm 1.5, \pm 2, \pm 3, \pm 5$ $\cdot 10^{-6} \text{ m}^2/\text{s}$ (lower six panels).

these evaporation change patterns with the differences in the simulated surface temperature in ECHAM4/SECHIBA in JJA (cf. Fig. 4.1) shows the well-known relation between these two quantities: a reduced evaporation (and associated reduced latent heat flux) results in a warming of the surface and vice versa (here the temperature effect amounts up to 3°C). The importance of an accurate rooting depth distribution in climate models (which determines the plant-available soil moisture), especially in the tropics, has been demonstrated by Kleidon and Heimann (1998). They showed that by introducing deeper roots in the ECHAM4 GCM much more realistic annual cycles of simulated soil moisture and surface air temperature, compared to observations in Amazonia, are obtained. This confirms the importance of vegetative effects for the simulated regional climate.

In large areas in northeast Russia the relative plant-available soil moisture simulated by ECHAM4/SECHIBA is generally increased compared to ECHAM4/IMPL (Fig. 4.8) due to the different bucket size distribution in SECHIBA. It appears as a striking point of the evaporation in ECHAM4/SECHIBA that it is not changed, and in particular not enhanced, in most of this region (Fig. 4.7). This means that the soil water reservoirs in ECHAM4/IMPL in this region are already large enough to allow for an evaporation that is not limited by insufficient soil water supply. It is rather determined by the available surface energy in this region (energy limited) in both models.

4.1.3   Atmospheric dynamics

The altered temperature distributions in ECHAM4/IMPL and ECHAM4/SECHIBA in JJA cause significant changes of the simulated geopotential height (see Fig. 4.11). As indicated by changes in the simulated velocity potential in ECHAM4/IMPL (cf. Figs. 4.12 and 4.13), the circulation associated to the southeast Asian summer monsoon is intensified in this model version. It appears to be further enhanced in ECHAM4/SECHIBA. This is consistent with the increased moisture convergence in the Indian region in ECHAM4/IMPL and ECHAM4/SECHIBA (Fig. 4.10). The changes in the velocity potential further suggest that there is an intensified subsidence over the western central Atlantic Ocean and the Caribean Sea in JJA in the two modified models. This leads to a reduced total cloud cover (Fig. 4.5), which allows for a higher net surface solar radiation (Fig. 4.4). Furthermore, the total precipitation decreases in this region (Fig. 4.9).

In can be noticed that the changes in the velocity potential due to the modified numerical coupling in ECHAM4/IMPL are generally more pronounced than those due to the altered land surface parameterization in ECHAM4/SECHIBA. Even at the level of 150 hPa significant changes occur in the ECHAM4/IMPL simulation in JJA. However, there are almost no significant changes according to the Student t-test due to the altered land surface scheme in ECHAM4/SECHIBA, which appears to be reasonable.

4.2   Global model validation

In contrast to the standard ECHAM4 GCM, ECHAM4/IMPL and ECHAM4/SECHIBA conserve energy at the interface between land surface and atmosphere and thus verify one major observed fact.

Table 4.1: Comparison of three estimates of the annual mean world water balance and the calculations of ECHAM4, ECHAM4/IMPL and ECHAM4/SECHIBA. All moisture fluxes are given in mm/d. P, E and Y denote total precipitation, evaporation and total runoff, the subscripts L and O denote land and ocean.

	P_L	E_L	Y	$P_L - E_L$	P_O	E_O
Baumgartner and Reichel (1975)	2.05	1.31	0.74	0.74	2.93	3.23
Henning (1989)	1.97	1.21	0.76	0.76	2.87	3.18
Chahine (1992)	1.98	1.31	0.67	0.67	3.03	3.30
ECHAM4	2.07	1.40	0.626	0.669	3.09	3.37
ECHAM4/IMPL	1.95	1.33	0.577	0.620	3.08	3.34
ECHAM4/SECHIBA	1.87	1.26	0.628	0.616	3.07	3.33

4.2.1   World water balance

As a measure for the model performance regarding the simulation of the global water cycle Table 4.1 compares the three GCM versions to three estimates of the annual mean world water balance from different recent sources (Baumgartner and Reichel 1975, Henning 1989, Chahine 1992). There is some spread between these estimates (Henning 1989) which is due to an insufficient spatial sampling of the observed data, biases in the measurements and the assumptions in the assimilations methods.

Generally all three model versions are within or close to the ranges of values which are given by the estimates for the water fluxes over the global continents and oceans. Total precipitation and evaporation over the continents are largest in ECHAM4 which tends to overestimate these quantities when compared to the estimates. ECHAM4/IMPL simulates slightly less continental precipitation and evaporation and gets fairly close to the estimates. In ECHAM4/SECHIBA precipitation and evaporation over the continents are further reduced, and the precipitation tends to be underestimated. Over the oceans, simulated precipitation and evaporation are very similar and slightly overestimated in all three model versions, which appears to be reasonable as they only differ in their land surface representations. ECHAM4/SECHIBA shows the lowest values over the oceans and is close to the highest of the three estimates (by Chahine 1992).

Table 4.1 reveals another difference between the land surface schemes ECHAM and SECHIBA. Generally, the hydrological balance at the land surface is governed by a continuity equation. According to this equation the temporal evolution of the content of the surface (or soil) moisture store is equal to the total precipitation minus evaporation and total runoff. Averaged over long periods of time like one or a few years, the storage term in this equation is small compared to the flux terms, when the system is in or close to equilibrium. Therefore, the total precipitation minus evaporation over land is equal to total runoff, which is the case in the three estimates presented in Table 4.1. The three models show small discrepancies between these two values which are likely to be associated with snow accumulation over glaciers or ice melt processes.

4.2.2 Temporal and regional distributions

In this section the three GCM versions are validated against (climatological) observational data sets on the global scale. Six data sets were available for this purpose which include observations of surface key variables like precipitation, surface air temperature or snow pack.

4.2.2.1 Observational data for GCM validation

For validating the precipitation simulations of the three models a climatology released by the *Global Precipitation Climatology Project (GPCP)* is used that combines conventional rain gauge observations from world-wide more than 6700 stations with satellite measurements (Huffman et al. 1995). It may be regarded as the most reliable precipitation climatology available today (M. Stendel and K. Arpe 1998, pers. comm.). The GPCP has been established by the *World Meteorological Organization (WMO)* to provide global data sets of area-averaged and time-integrated precipitation based on all suitable observations (WMO/ICSU 1990, Rudolf et al. 1996). The data record used here has a spatial resolution of originally $2.5° \times 2.5°$ and comprises monthly mean values covering the period from July 1987 to December 1995, with December 1987 unavailable. Highest uncertainties exist over mountains, in regions with predominant solid precipitation and in deserts where rain fall is rare but heavy (Stendel and Arpe 1997).

The cloud cover simulations of the three GCM versions are compared to observational data of the *International Satellite Cloud Climatology Project (ISCCP)*. Detailed descriptions of the data processing algorithms and the available products are given by Rossow and Schiffer (1991) and Rossow and Garder (1993). Cloud detection is performed using measurements of infrared and visible radiances by operational geostationary weather satellites combined with data of at least one polar-orbiting satellite to provide almost global coverage. Derived quantities, that are used here for validation, are the total cloud cover and the high level cloud cover. The latter includes clouds with a top pressure of less than 440 hPa. The data record utilized here (ISCCP-C2 data set) has a spatial resolution of originally $2.5° \times 2.5°$ and consists of monthly mean values covering the period from July 1983 to December 1990. Compared to surface observations the ISCCP total cloud cover was found to be lower by 10% over land and 5%–25% in polar regions (Rossow et al. 1993).

A global climatology of monthly mean surface air temperature has been compiled by Legates and Willmott (1990), using terrestrial observations of shelter-height air temperature and shipboard measurements. Data from 17986 independent land station records and 6955 oceanic grid-point records have been taken into account. Most of the terrestrial data were compiled between 1920 and 1980, the oceanic measurements are from the period 1950 – 1979. These data were interpolated to a $0.5° \times 0.5°$ global grid. Potential discrepancies in the data set may be due to different instruments used in different countries. Some of them measure the air temperature at a height of 1.2 m, others at 2 m. Oceanic measurements are usually taken at a shipboard height of 12 m. Possible discrepancies were believed to be small on a global scale, therefore no correction was made by Legates and Willmott (1990) regarding this issue. A dense spatial coverage with land stations is available in some regions, e. g. in Europe or the USA. An extremely low coverage is apparent in Antarctica, Greenland and parts of north Canada, the Himalaya and the Tibetan plateau. Over the oceans, much of the Southern and Arctic Oceans are not covered. In these sparse data regions the climatology may contain

considerable deficiencies. For instance, in the region of the Himalayas the temperatures are known to be too warm by several degrees (K. Arpe 1997, pers. comm.).

A global monthly mean snow depth climatology is available from the *US Air Force Environmental Technical Applications Center (USAF/ETAC)* (Foster and Davy 1988). The data set has been distributed on the *International Satellite Land Surface Climatology Project (ISLSCP)* Initiative I CD-ROM set (Meeson et al. 1995). For this compilation snow depth data were obtained from as many sources as possible, worldwide. The quality of the climatology varies regionally and depends on the spatial density of the contributing stations. The time periods covered by the input data sets vary across the globe. The spatial resolution of the distributed data set is $1° \times 1°$ with a global coverage. Each data source was rated according to a 'high', 'fair' or 'low' confidence level. For instance, data from Canada, USA, Scandinavia and the former Soviet Union were rated to be 'highly confident'. However, in certain data sparse regions such as Antarctica, Greenland, China and various mountain areas, special procedures had to be developed to provide mean snow depths. These include e. g. the estimation of snow depth from the precipitation assuming an average snow density value. Most of these data sparse regions are rated with 'low confidence'.

Another observational data set, used in this work for comparison with model simulations, that is distributed on the ISLSCP CD-ROM (Meeson et al. 1995), is the *Earth Radiation Budget Experiment (ERBE)* S4 clear-sky surface albedo (Barkstrom 1984, Barkstrom et al. 1990). The goal of ERBE is to understand the radiation balance between the sun, earth, atmosphere and space, and to establish an accurate baseline data set for detection of climate changes. Identical ERBE instruments were flown on three different satellites providing a global coverage of the measurements. As part of ERBE, measurements of broadband shortwave radiation from scenes determined to be free of clouds were analysed and clear-sky albedos were derived. The data are provided as monthly means, and they cover the period from January 1987 to December 1988. Here, the average of the two years has been calculated. The spatial resolution is $1° \times 1°$. The ERBE clear-sky albedo values were validated by comparison with data from other satellite and aircraft observations of clear scenes. Errors may result from cloud contamination of the scene, instrument errors, sampling errors and uncertainties in models used in the processing. The random error is estimated to be of the order of 1%. Errors in the polar regions may be larger than this due to the inability to reliably distinguish between clouds and snow.

4.2.2.2   Comparison of the GCM simulations to observational data

Figure 4.14 shows the GPCP precipitation seasonal means for DJF (1988/89 – 1994/95) and JJA (1988 – 1995) and the differences between the three GCM versions and GPCP. In JJA ECHAM4 underestimates the precipitation at the west coast of India, over the Bay of Bengal and the western central Pacific in the ITCZ compared to GPCP. Overestimations occur in two regions over the Indian Ocean directly south of the Indian peninsula, over Malaysia and in the Sahel. All these biases are substantially improved in the implicitly coupled GCM versions ECHAM4/IMPL and ECHAM4/SECHIBA.

As discussed in section 4.1, changes in evaporation over the northern Indian Ocean (see Fig. 4.7) with subsequent modifications of the precipitation in this region (Fig. 4.9) in ECHAM4/IMPL in JJA (compared to ECHAM4) are caused by a different (intensified) southeast Asian summer monsoon circulation. More details on this are given in section 4.3.1.
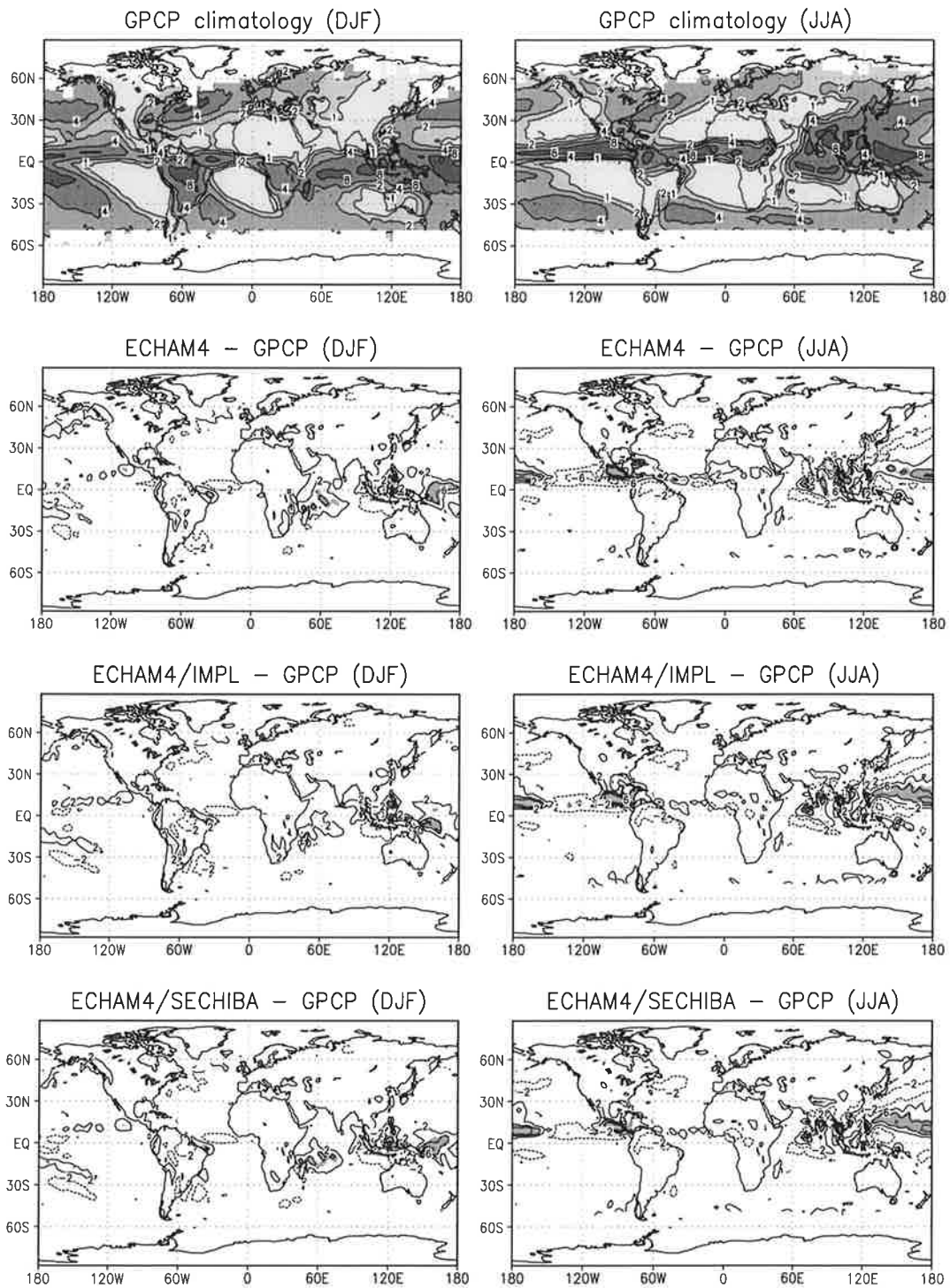
Figure 4.14: The top panels show DJF and JJA seasonal means of the global total precipitation [mm/d] as given by the GPCP climatology. The other panels show the differences ECHAM4 - GPCP, ECHAM4/IMPL - GPCP and ECHAM4/SECHIBA - GPCP. The shadings in the lower six panels indicate regions with absolute differences of more than 5 mm/d. Contours are at 1, 2, 4, 8, 16 mm/d (top panels) and ±2, ±6, ±10 mm/d (lower six panels).
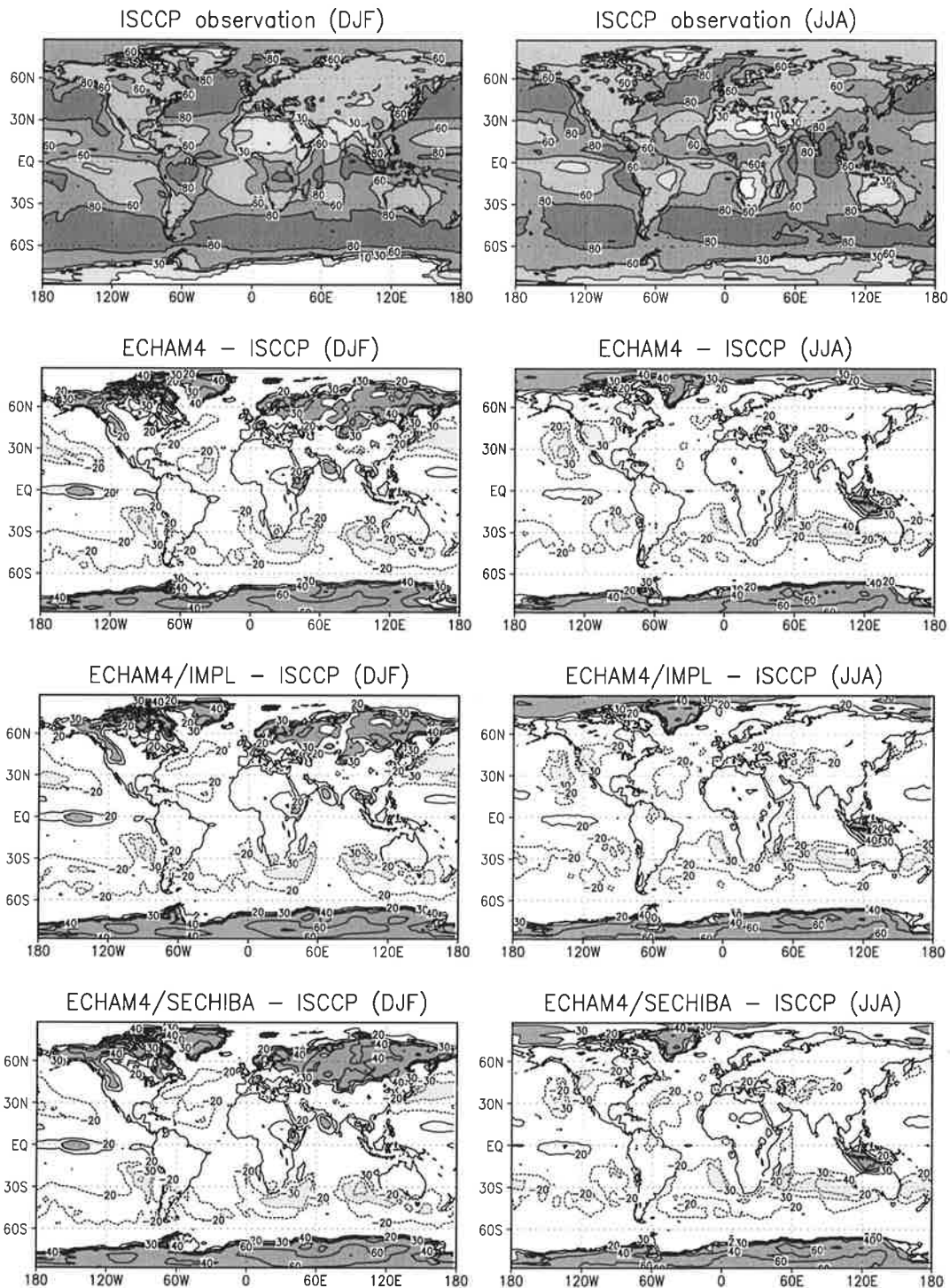
Figure 4.15: The top panels show DJF and JJA seasonal means of the global total cloud cover [%] as given by the ISCCP observations. The other panels show the differences ECHAM4 - ISCCP, ECHAM4/IMPL - ISCCP and ECHAM4/SECHIBA - ISCCP. The shadings in the lower six panels indicate regions with absolute differences of more than 30%. Contours are at 10, 30, 60, 80% (top panels) and $\pm 20, \pm 30, \pm 40, \pm 60\%$ (lower six panels).
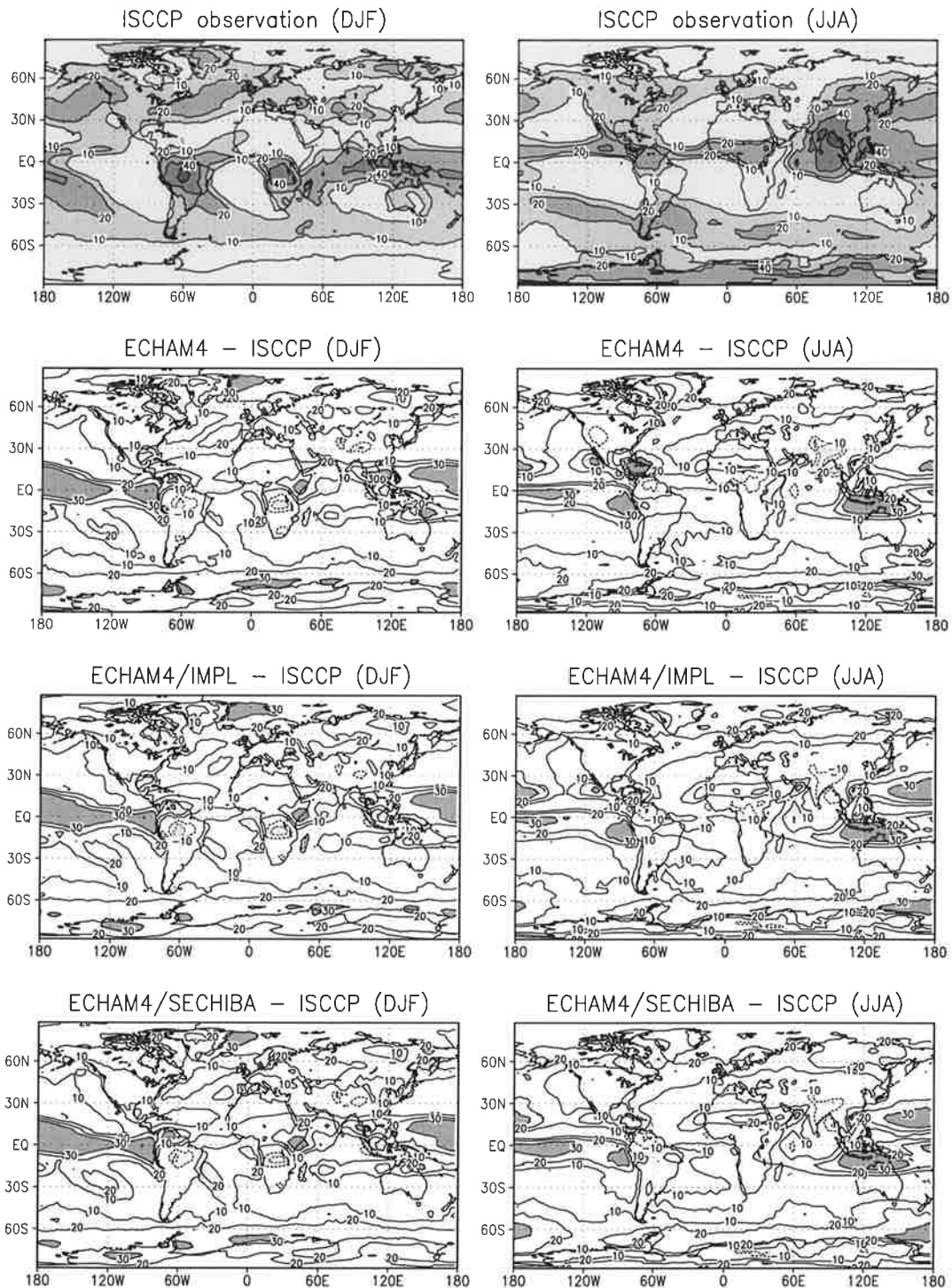
Figure 4.16: The top panels show DJF and JJA seasonal means of the global high level cloud cover [%] as given by the ISCCP observations. The other panels show the differences ECHAM4 - ISCCP, ECHAM4/IMPL - ISCCP and ECHAM4/SECHIBA - ISCCP. The shadings in the lower six panels indicate regions with differences lower than −20% or higher than 30%. Contours are at 10, 20, 40, 60% (top panels) and ±10, ±20, ±30% (lower six panels).

Furthermore, the ITCZ seems to be shifted northward and it shows an enhanced atmospheric moisture convergence over the Pacific Ocean in ECHAM4/IMPL in JJA which leads to a more realistic precipitation rate over the eastern Pacific and a higher bias in the precipitation over the western Pacific compared to GPCP. Overall, it can be concluded that the JJA tropical precipitation rates and distributions in the implicitly coupled GCM versions are much more realistic compared to the GPCP climatology than those of the ECHAM4 standard model. Wether the ECHAM land surface scheme or the SECHIBA parameterization yields better results can not be decided from this comparison.

Figure 4.15 shows the ISCCP multi-year averaged seasonal means of the total cloud cover for DJF (1983/84 – 1989/90) and JJA (1984 – 1990). Maxima are related to tropical convection and extratropical cyclones. Minima occur over deserts and the subtropical subsidence regions. All three GCM versions underestimate the total cloud cover over the north Pacific Ocean, in DJF more than in JJA, and over large parts of the oceans between about 20°S and 50°S troughout the year. Overestimations are seen over the Northern Hemisphere continents in DJF. Similar results were found by Lohmann (1996) with the ECHAM4 standard GCM. Also a modified model version with more advanced cloud microphysics did not significantly improve the problem. A further analysis of these discrepancies is beyond the scope of this work.

As discussed in section 4.1.1 the implicitly coupled GCM versions simulate a substantially increased cloud cover over the Indian region (cf. Fig. 4.5) compared to the standard ECHAM4 which is associated with the southeast Asian summer monsoon. As shown by Fig. 4.15 this leads to a considerably improved cloud cover representation in this region when compared to ISCCP measurements. Furthermore, the simulated cloud cover over west North America and the northeast Pacific Ocean is improved as well. However, over the northern subtropical Atlantic Ocean the cloud cover is reduced and becomes a bit too low compared to ISCCP.

Beside the total cloud cover the ISCCP products include the high level cloud cover, which is also used for validation here. For the GCMs the high level cloud cover is computed from the upper ten atmospheric model levels that cover the pressure range from about 400 hPa to 10 hPa, which is best comparable to the ISCCP data. Two main changes in the simulated high level clouds between the standard ECHAM4 GCM and the implicit versions are visible in Fig. 4.16 in JJA: an increase over the Indian region and a decrease over the Central American Oceans. Both are associated with changes in the circulation, as discussed in section 4.1.3, and are clear improvements when compared to the ISCCP observations.

Figure 4.17 shows the DJF and JJA seasonal mean differences between the simulated 2-meter air temperature of the three GCM versions and the surface air temperature given by Legates (short for Legates and Willmott (1990) climatology). Antarctica, Greenland, the Himalaya and Tibet region and the Southern and Arctic Oceans shall be excluded from this comparison because of the aforementioned uncertainties in the climatology in these regions. As the figure shows, ECHAM4 tends to be to warm by more than 3°C in some continental regions in JJA, namely mainly east- and northward of the Caspian Sea, in Saudi Arabia, in the southwest USA, in northeast Brazil and at the north rim of Eurasia. It tends to be too cold in northeast Siberia and in Alaska. ECHAM4/IMPL and ECHAM4/SECHIBA simulate higher surface temperatures in JJA over large mainly northern hemispheric continental areas due to different reasons that are disussed in detail in section 4.1.1. For the two aforementioned areas, which are too cold in ECHAM4, this means an improvement, but for the regions which are already too warm in ECHAM4 this bias is enhanced.
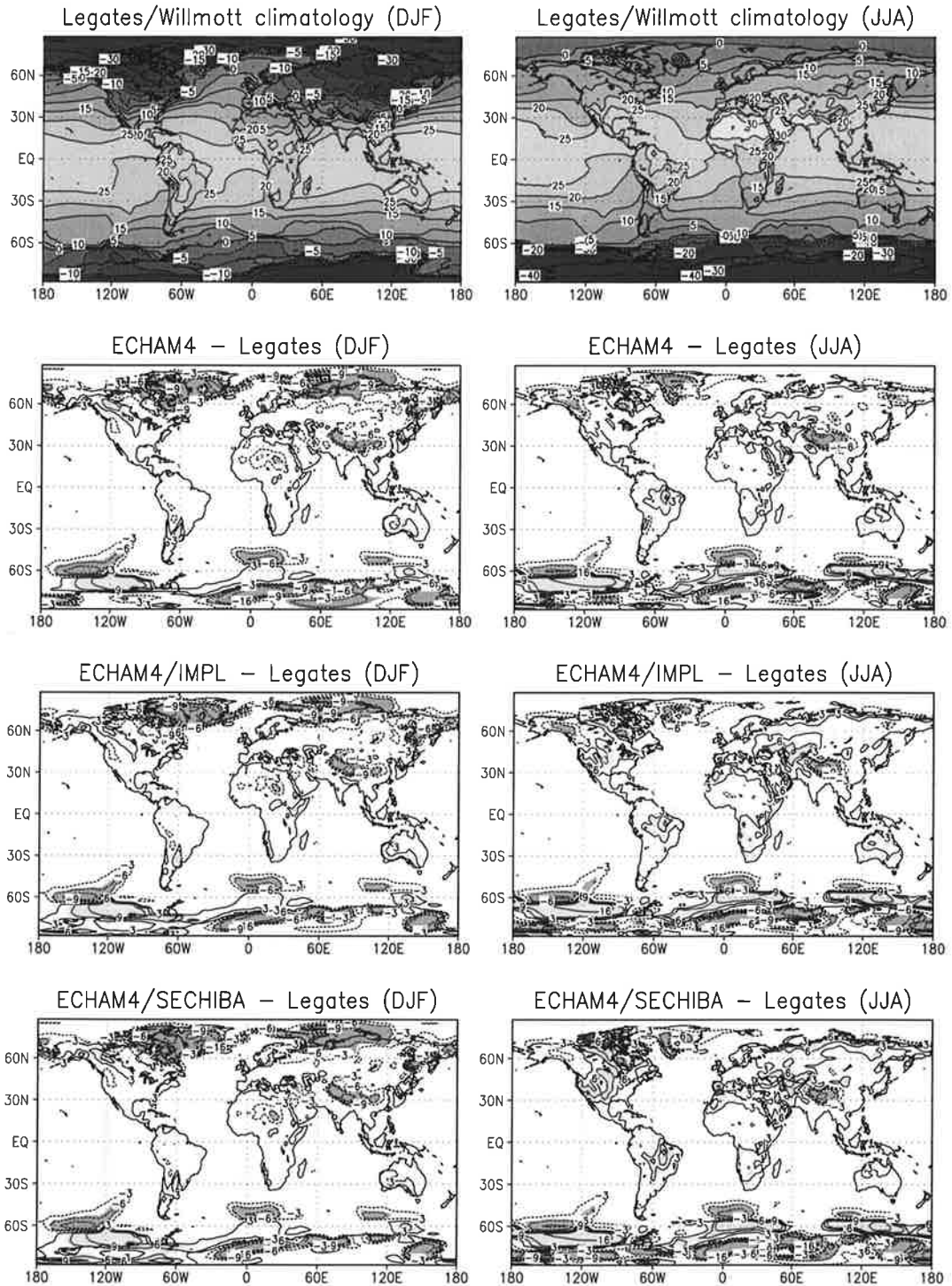
Figure 4.17: The top panels show DJF and JJA seasonal means of the global surface air temperature [°C] as given by the Legates/Willmott climatology. The other panels show the differences of the 2-meter air temperature simulated by the three GCM versions and Legates/Willmott. The shadings in the lower six panels indicate regions with absolute differences of more than 5°C. Contours are at $0, \pm 5, \pm 10, \pm 15, \pm 20, \pm 25, \pm 30, \pm 40$°C (top panels) and $\pm 3, \pm 6, \pm 9, \pm 16$°C (lower six panels).

This points to a principal problem which arises when a complex system that consists of many interacting components is tried to be modelled, using a set of simplifying equations and assumptions: reasonable results of the modelling approach, compared to observed data, may not necessarily mean that all processes are accurately represented, but it may very well be the case that there are still errors in different components of the system which compensate each other. When the ECHAM4 GCM was developed and calibrated for operational use, the 2-meter surface air temperature was one of the key parameters to judge the performance and calibration, and the model was adjusted accordingly (U. Schlese 1998, pers. comm.). As shown in Fig. 4.17 a reasonable representation of the absolute values as well as the seasonal cycle of the surface air temperature has been achieved in the ECHAM4 GCM (compared to Legates), although the energy is not conserved at the land surface, as demonstrated in chapter 3 and in section 4.1.1. This means that there are systematic model errors in the GCM that are revealed in the GCM version ECHAM4/IMPL which has a closed surface energy balance, what is clearly physically more realistic. Thus a new adjustment is needed for the implicit coupling scheme.

These systematic model errors may be embedded in the cloud parameterization, the representation of cloud–radiation feedbacks or the convection scheme, all of them being sources of major uncertainties in the ECHAM4 GCM and many other GCMs currently available. Further uncertainties may be contained in the calculation of vertical turbulent exchanges near the surface, the representation of the planetary boundary layer or the land surface processes, here especially in the global distributions of important parameter values that are used in these parameterizations. For instance, the background albedo in large regions around the Caspian and Black Sea, in North America and in large parts of South America, southern Africa and Australia, which is used in the three GCM versions, is underestimated by 2%–4% and sometimes more, when compared to ERBE albedo values which were derived from observed radiances at the top of the atmosphere utilizing the ECHAM3 radiation transfer code (Claussen et al. 1994, U. Lohmann 1997, pers. comm.). This is a likely reason which contributes to the overestimation of the surface air temperature of the three GCMs in most of these regions (cf. Fig. 4.17). Another parameter set which affects the surface temperature by controlling the evaporative cooling is the global bucket size distribution, as discussed in section 4.1.2. The surface air temperature in northeast South America is too high already in ECHAM4 and ECHAM4/IMPL in JJA, compared to Legates, in ECHAM4/SECHIBA it gets even higher due to the smaller SECHIBA bucket sizes in this region. This shows the need for accurate estimates for global bucket size distributions or associated rooting depths, respectively, for use in GCMs. This issue has recently started to draw special attention in the GCM community (e. g. Kleidon and Heimann 1998, de Rosnay and Polcher 1998).

Figure 4.18 shows that ECHAM4 and ECHAM4/IMPL simulate too deep snow packs in spring (MAM) in large parts of Eurasia, when compared to the USAF/ETAC snow climatology. This concerns in particular the snow melt regions, which indicates that the snow melt is simulated too late (by about one month). This is clearly improved in ECHAM4/SECHIBA, mainly due to the different snow melt criterion in SECHIBA which allows an earlier melting. However, in a region in Eurasia poleward of about 60°N and eastward of 90°E and in parts of Canada, all three GCM versions underestimate the snow depths in MAM which is most pronounced in ECHAM4/SECHIBA. These differences of the snow cover also affect the albedo of the three models. Figure 4.19 indicates that ECHAM4/SECHIBA shows the lowest overestimation of the albedo in the snow melt region in Eurasia in MAM, but
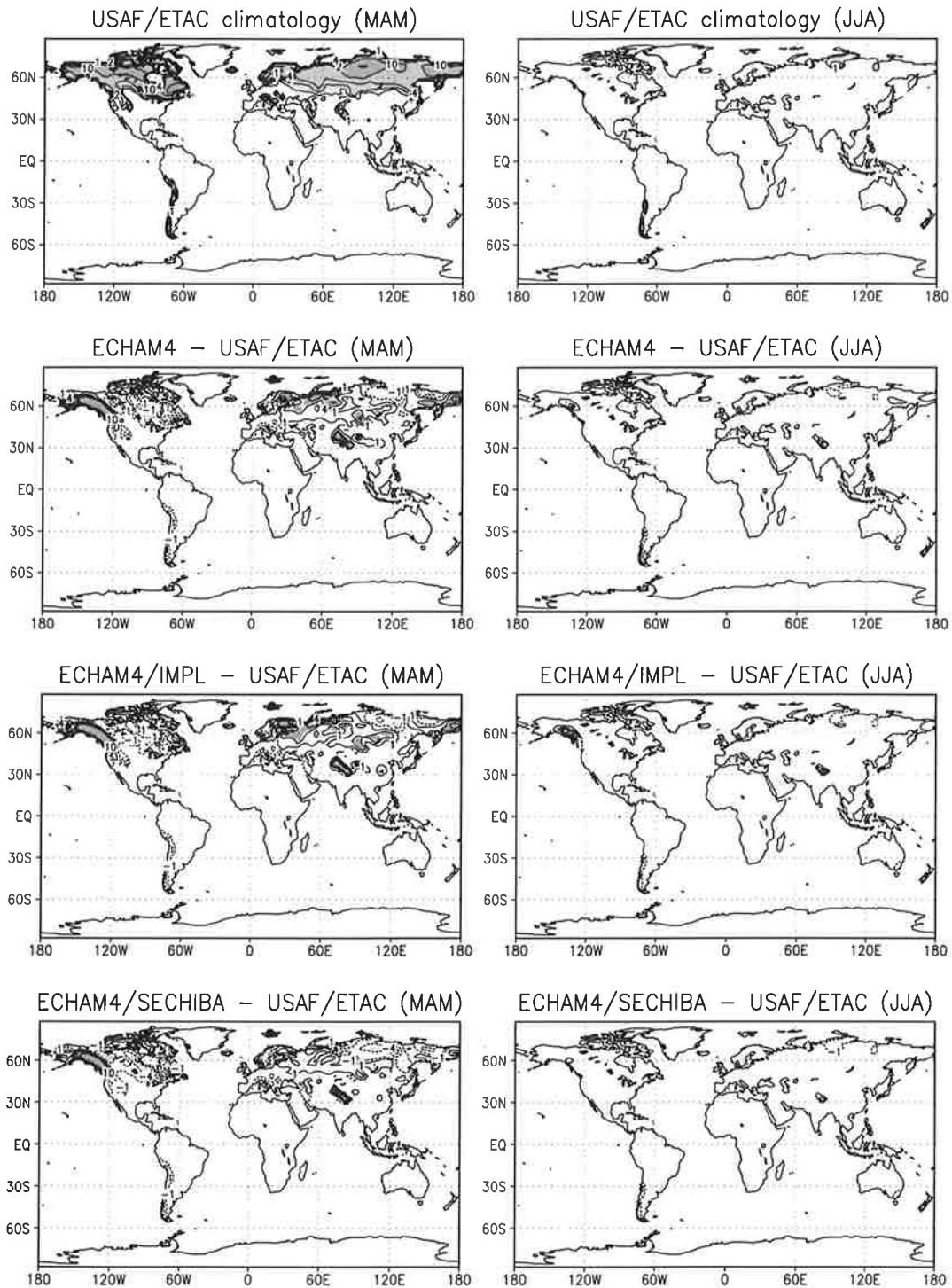
Figure 4.18: The top panels show MAM and JJA seasonal means of the global snow depth distribution [cm water equivalent] as given by the USAF/ETAC climatology. The other panels show the differences ECHAM4 - USAF/ETAC, ECHAM4/IMPL - USAF/ETAC and ECHAM4/SECHIBA - USAF/ETAC. The shadings in the lower six panels indicate regions with absolute differences of more than 5 cm water equivalent. Contours are at 1, 2, 4, 10, 16 cm water equ. (top panels) and $\pm1, \pm4, \pm7, \pm10$ cm water equ. (lower six panels).
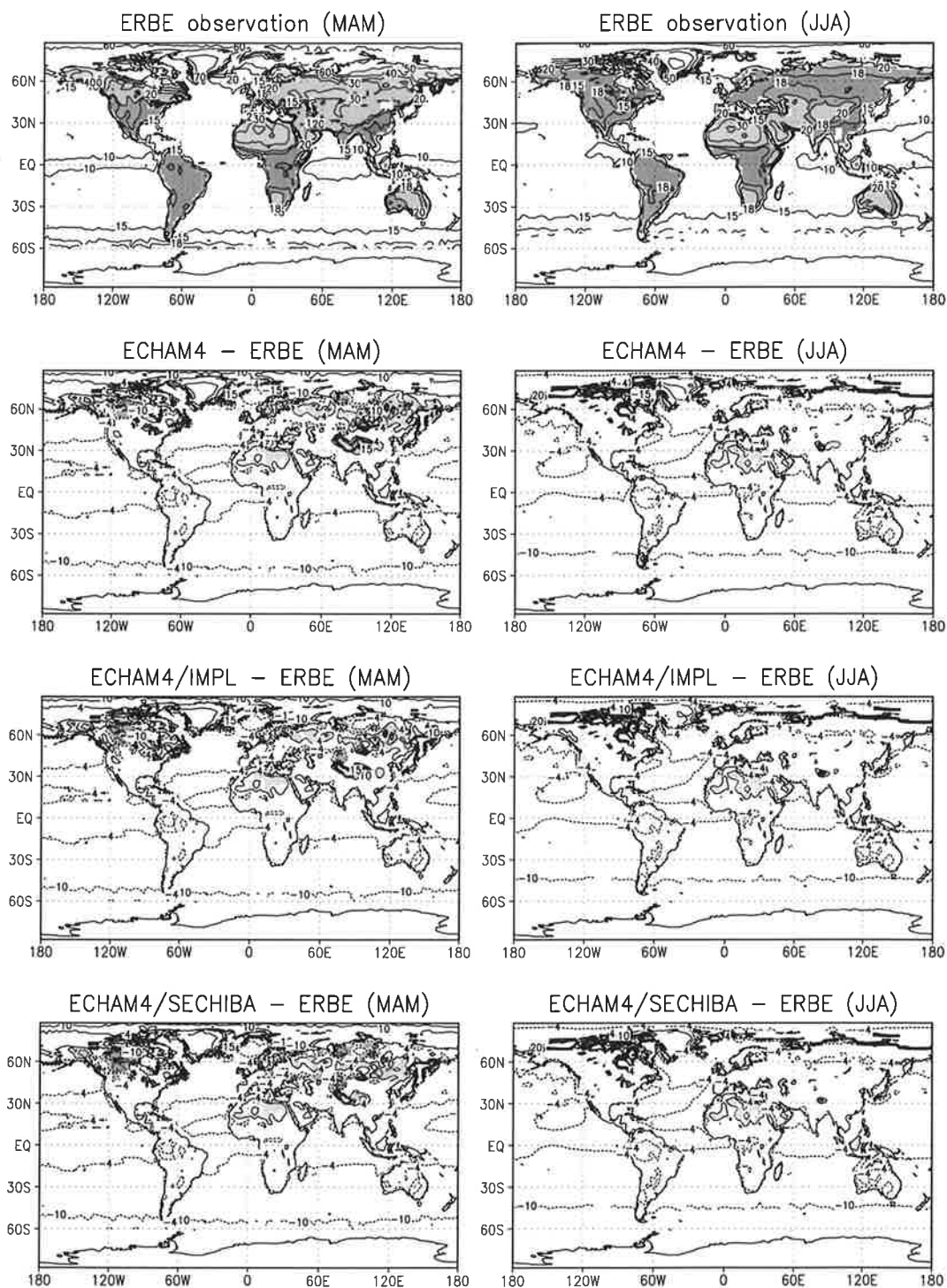
Figure 4.19: The top panels show MAM and JJA seasonal means of the global albedo distribution [%] as given by the ERBE observations. The other panels show the differences ECHAM4 - ERBE, ECHAM4/IMPL - ERBE and ECHAM4/SECHIBA - ERBE. The shadings in the lower six panels indicate regions with absolute differences of more than 6%. Contours are at 10, 15, 18, 20, 30, 40, 50, 60, 70% (top panels) and ±4, ±10, ±15% (lower six panels).

the highest underestimation in north central Eurasia, when compared to ERBE (although the satellite measurements need to be taken with great care in these regions due to the difficulties to reliably distinguish between clouds and snow). However, these results are consistent with the snow – albedo – solar radiation – surface temperature positive feedback, that is discussed in section 4.1.1 as a mechanism that gradually increases the surface temperature in ECHAM4/SECHIBA in northern Eurasia from spring to summer, compared to ECHAM4/IMPL.

The earlier snow melt in ECHAM4/SECHIBA is clearly an improvement which may provide better input for more realistic river discharge simulations as shown in section 4.3.2. But as demonstrated, the snow parameterization is still not satisfactory. An improvement would be expected from the use of a more sophisticated snow representation (e. g. Loth and Graf 1998).

4.3 Regional studies

From the global intercomparison and validation of the GCM versions ECHAM4, ECHAM4/-IMPL and ECHAM4/SECHIBA, presented in sections 4.1 and 4.2, certain key regions or processes, respectively, have been identified where substantial differences occur between the three models. In this section some of these regions are analysed in detail.

4.3.1 Asian summer monsoon

The global model intercomparison shows that there are significant differences in the representation of the southeast Asian summer monsoon in the three models regarding circulation, cloud formation, precipitation distribution and associated processes. The two implicitly coupled GCM versions generally simulate a more intense monsoon circulation. This is investigated in more detail in this section. For this reason the simulated atmospheric temperature and the zonal wind speed are compared to reanalysis data from ECMWF (Gibson et al. 1997) and the *National Center for Environmental Prediction (NCEP)* (Kalnay et al. 1996). Dümenil and Bauer (1998) have demonstrated that the reanalyses are a reasonable reference in this data sparse region.

Figure 4.20 shows the atmospheric temperature at 500 hPa in southeast Asia in July as given by the ECMWF and NCEP reanalyses and as simulated by the three GCM versions. Both reanalyses show pronounced local maxima of the temperature between 0°C and 1.5°C over the Tibetan plateau. ECHAM4 simulates two temperature maxima, both below −0.5°C and located too far southward or eastward, respectively. In ECHAM4/IMPL the local maximum temperature is increased by about 1°C, and in ECHAM4/SECHIBA by another 0.5°C, and in both modified model versions the warm region is shifted in west or northwest direction, respectively. This is more similar to the reanalyses. The maximum temperature in ECHAM4/IMPL is between 0°C and 0.5°C, and in ECHAM4/SECHIBA it is about 0.5°C higher. Both values are exactly in the range given by the reanalyses. The higher temperatures in the implicit models are explained by the changed coupling technique between land surface and atmosphere. The further increased temperature in ECHAM4/SECHIBA over the Tibetan plateau and the Himalayas is due to a more efficient snow melt, which is in good agreement with the USAF/ETAC snow climatology. Both effects are discussed in great
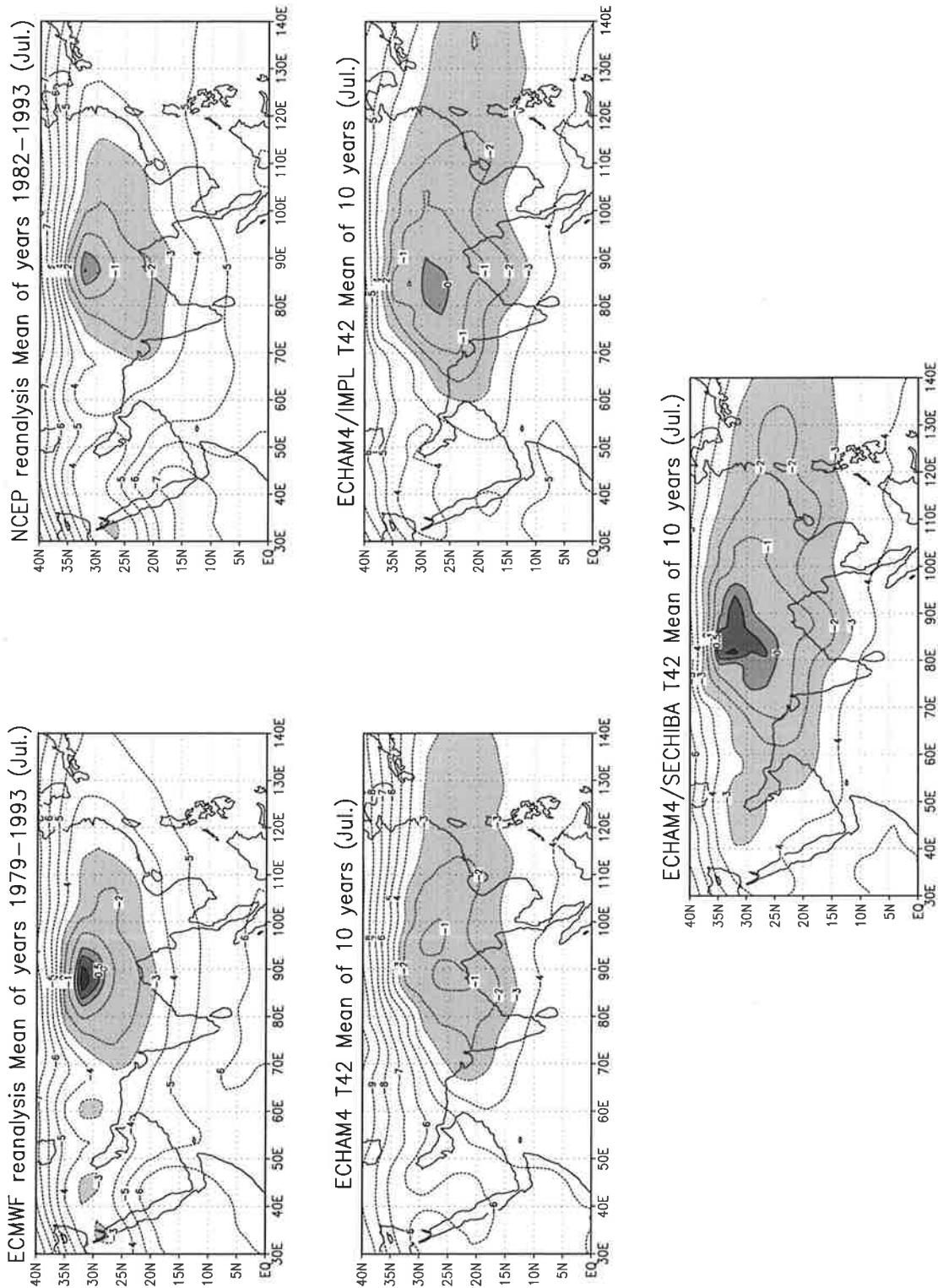
Figure 4.20: July monthly mean atmospheric temperature [°C] at 500 hPa in southeast Asia as given by the ECMWF and NCEP reanalyses compared to the simulations by ECHAM4, ECHAM4/IMPL and ECHAM4/SECHIBA. Contours are at $-10, -9, -8, -7, -6, -5, -4, -3, -2, -1, 0, 0.5, 1$°C.
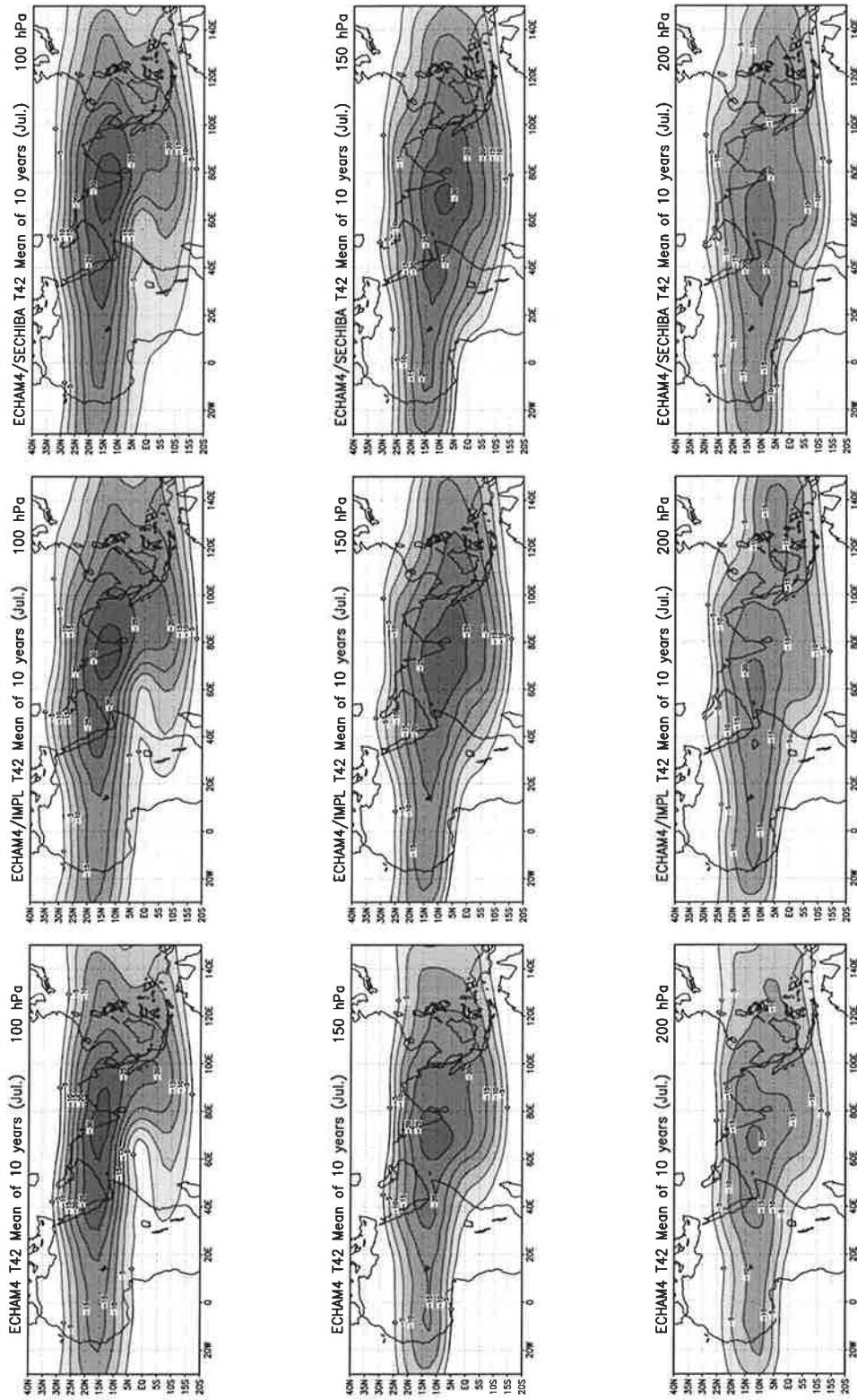
Figure 4.21: July monthly mean zonal wind [m/s] at the pressure levels 100 hPa, 150 hPa and 200 hPa in the monsoon region as simulated by ECHAM4, ECHAM4/IMPL and ECHAM4/SECHIBA. Contours are at $-35, -30, -25, -20, -15, -10, -5, 0$ m/s.
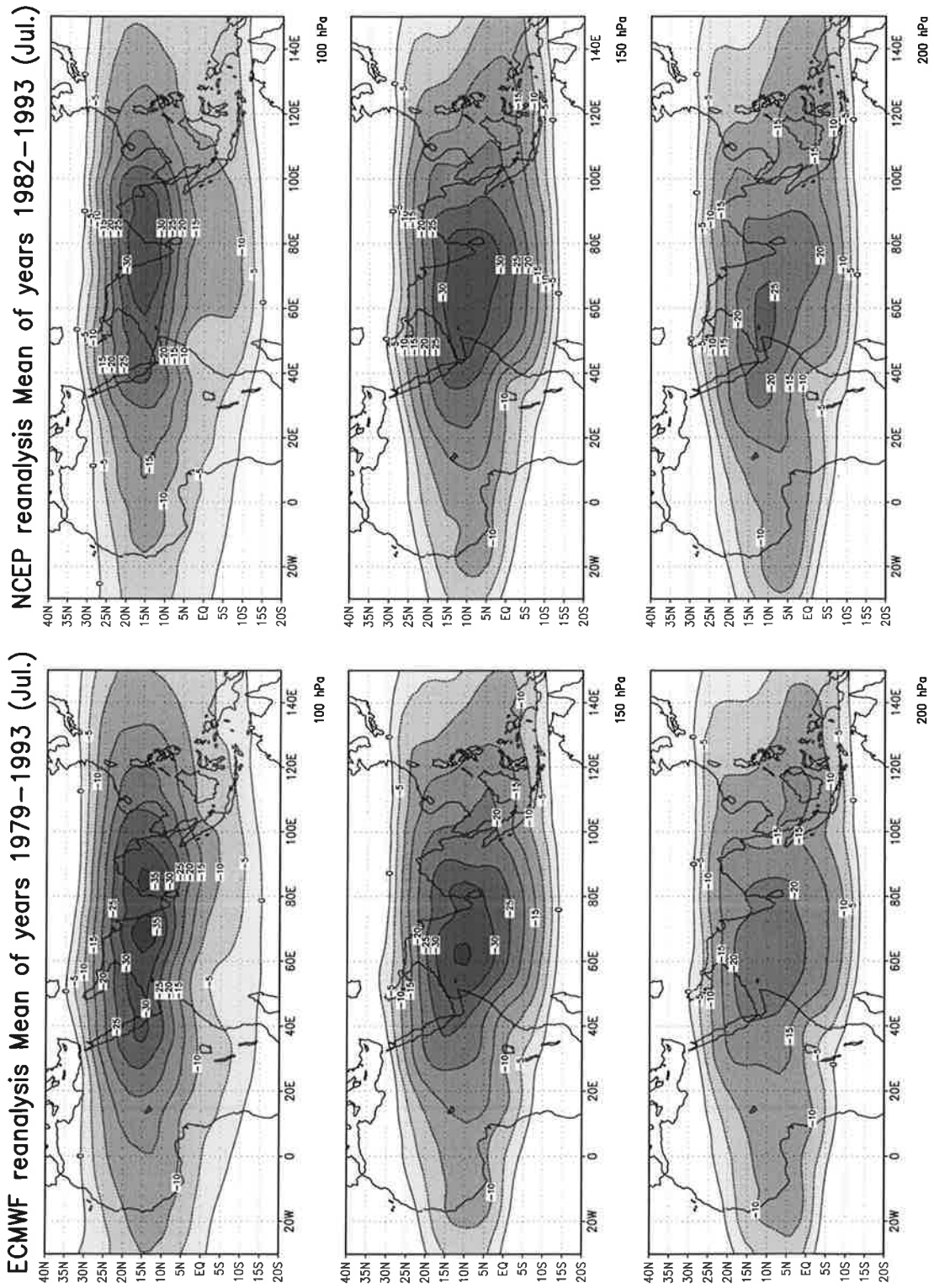
Figure 4.22: As Fig. 4.21 but for the ECMWF and NCEP reanalyses.
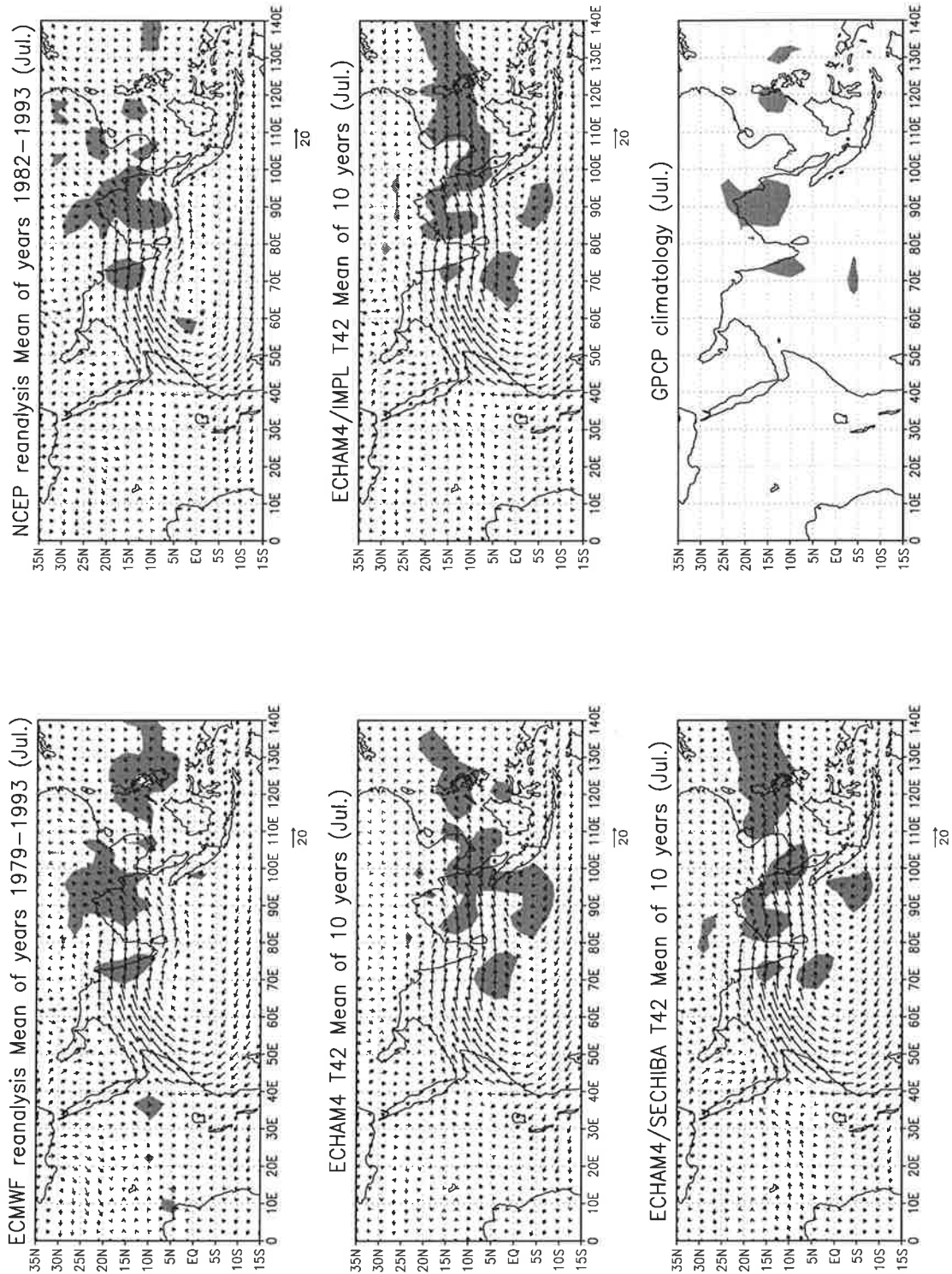
Figure 4.23: July monthly mean circulation [m/s] at 850 hPa in the Indian region as given by the ECMWF and NCEP reanalyses compared to the simulations by ECHAM4, ECHAM4/IMPL and ECHAM4/SECHIBA. The arrowlength for a wind speed of 20 m/s is indicated near the lower right corner of each panel. The shadings depict regions with a total precipitation of more than 10 mm/d, which may also be compared to the GPCP climatology.

detail in the previous sections. These changes lead to the enhanced 500 hPa atmospheric temperatures, seen in the simulations, which is an only slightly higher level than the Tibetan plateau.

The increased atmospheric temperature leads to a more pronounced high pressure system in the upper troposphere and an enhanced pressure gradient to the Southern Hemisphere. This intensifies the tropical easterly jet stream which is a component of the southeast Asian summer monsoon circulation and returns the air rising over the heated continent to the (Southern) winter hemisphere (e. g. Webster 1987). Figure 4.21 shows the zonal wind in the monsoon region in July at the pressure levels 100 hPa, 150 hPa and 200 hPa for the three model versions. In all three experiments the region of maximum wind speed at 100 hPa is located over the Indian peninsula, and it is shifted in western direction over the Indian Ocean at the lower levels. As expected, the two implicit models simulate higher wind speeds than the standard ECHAM4. This is best seen at 150 hPa where the region of absolute velocities exceeding 25 m/s in ECHAM4/IMPL has a larger extension than in ECHAM4, while ECHAM4/SECHIBA even exceeds 30 m/s. This is an improvement when compared to the ECMWF and NCEP reanalyses (Fig. 4.22). They show zonal wind speeds which are even slightly higher than the ECHAM4/SECHIBA results.

The lower branch of the Indian monsoon is represented by the Somali jet, advecting moist air from the Indian Ocean toward the Indian subcontinent. Figure 4.23 shows the circulation at 850 hPa in the Indian region in July as simulated by the three GCM versions. In ECHAM4 the Somali jet has an about 5 m/s weaker maximum velocity and a southward displaced position compared to the reanalyses. Consequently, the evaporation over the ocean is too small, and a large portion of the low level circulation does not reach into the Indian subcontinent (Dümenil and Bauer 1998). For these reasons, ECHAM4 simulates too little rainfall at the west coast of India compared to the reanalyses and the GPCP climatology (Fig. 4.23).

Both implicitly coupled models, ECHAM4/IMPL and ECHAM4/SECHIBA, much better represent the low level circulation including the Somali jet than ECHAM4. Due to this and the associated enhanced evaporation over the ocean (cf. Fig. 4.7), the precipitation patterns are substantially improved by providing increased rainfall at the west coast of India and over the northern Bay of Bengal, where it is too low in ECHAM4. An important aspect for the increase over the northern Bay of Bengal is an enhanced near-surface convergence in this region in ECHAM4/IMPL and ECHAM4/SECHIBA (Dümenil and Bauer 1998). Beside the two regions just mentioned, the two models additionally partly reproduce a rainfall maximum at the south rim of the Himalaya, which is also seen in the reanalyses. Furthermore, the erroneous rainfall maxima in ECHAM4, over the Indian Ocean westward of Indonesia, are reduced.

It can be concluded that ECHAM4/IMPL and ECHAM4/SECHIBA better represent the atmospheric temperature distribution at 500 hPa in the southeast Asian summer monsoon region than ECHAM4, which contributes to an improved monsoon circulation and precipitation compared to the ECMWF and NCEP reanalyses. It should be added that the modified snow cover in northern Eurasia in ECHAM4/SECHIBA probably also has an impact on the Asian summer monsoon (e. g. Douville et al. 1995).

Another possibility to assess the quality of the simulated hydrological cycle is to compare the modelled river discharge to observations. This quantity usually can easier be measured

Figure 4.24: The shaded areas indicate the catchments of the rivers Ganges/Brahmaputra and Kolyma.

with a higher accuracy than e. g. surface evaporation over a wide region. The data of the measured discharges of various large rivers of the earth are available from the *Global Runoff Data Centre (GRDC)* and are presented by Dümenil et al. (1993).

These data can not directly be compared to the GCM simulations because the ECHAM land surface scheme only calculates local surface runoff and drainage, but the river discharge is usually not computed by the atmospheric GCM (when not coupled to an ocean model). Therefore, use is made of the *Hydrological Discharge (HD)* model by Hagemann and Dümenil (1998). It uses the GCM calculated surface runoff and drainage as input and computes the resulting river discharge, taking into account the different time constants for transfer and retention of the water flow at the surface and in the deep soil, and of the river flow. The HD model operates on a scale of $0.5° \times 0.5°$ and can be applied to all rivers of the earth which can be resolved on this scale. It has extensively been tested by Hagemann (1998) in the catchments of most large rivers in the world. Only the simulations with the ECHAM scheme are suitable for this because it calculates both surface runoff and drainage. The SECHIBA model structure does not include a drainage term (cf. chapter 1), therefore the HD model can not be applied to the ECHAM4/SECHIBA simulations.

Two large river systems were selected for a comparison of simulated and observed discharges. The catchments of these rivers — Ganges/Brahmaputra and Kolyma — are shown in Fig. 4.24. They are representative for different climate regions and are dominated by different discharge regimes. The results for Ganges/Brahmaputra are presented in this section, those for the Kolyma in the next section.

The rivers Ganges and Brahmaputra provide a large portion of the discharge into the Bay
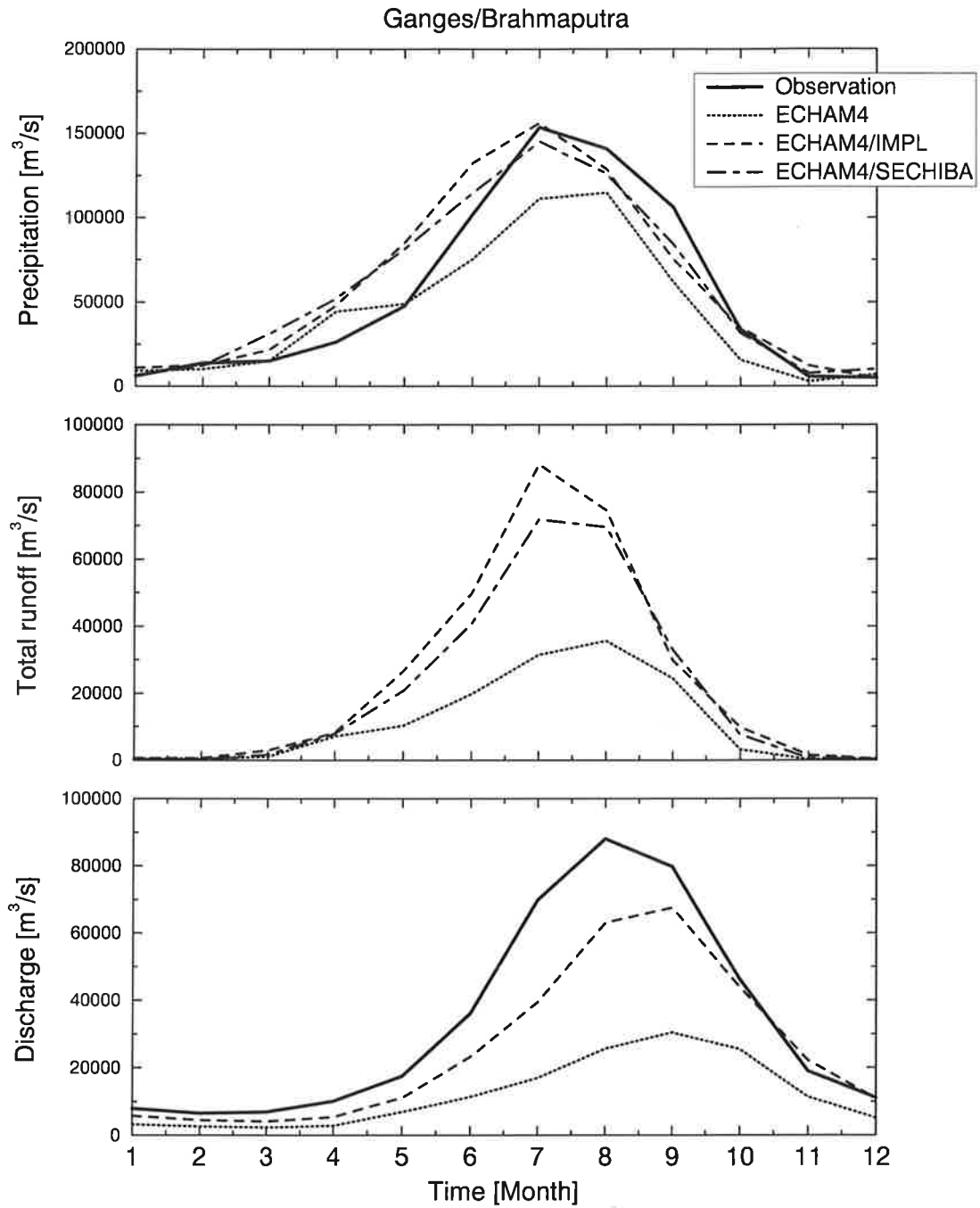
Figure 4.25: Monthly mean annual cycles of the Ganges/Brahmaputra catchment mean total precipitation [m³/s] and total runoff [m³/s] (i. e. surface runoff plus drainage) and river discharge [m³/s] for ECHAM4, ECHAM4/IMPL and ECHAM4/SECHIBA (no discharge) compared to observations of precipitation (GPCP) and discharge (GRDC).

of Bengal. As the rivers merge in their large delta, only the total catchment of both rivers will be considered here, as suggested by Hagemann (1998). Figure 4.25 shows the catchment mean total precipitation for Ganges/Brahmaputra as simulated by ECHAM4, ECHAM4/IMPL and ECHAM4/SECHIBA compared to the GPCP observations. The catchment area is 1,659,812 km^2 at the 0.5° resolution (Hagemann 1998). Using this value, the moisture flux units can be converted e. g. to mm/d. As the figure shows, ECHAM4 considerably underestimates the summer and autumn precipitation compared to the observation. ECHAM4/IMPL and ECHAM4/SECHIBA much better agree with the observed summer monsoon precipitation maximum. Other observations and also the ECMWF and NCEP reanalyses give even substantially higher rainfall values in summer (Hagemann 1998). This indicates that also the implicit models may still underestimate the summer rainfall in this region.

Figure 4.25 also shows the total runoff as simulated by the three models. On the whole it follows the simulated precipitation of each model, resulting in a low total runoff in ECHAM4 and much higher values in ECHAM4/SECHIBA and ECHAM4/IMPL. The third panel in Fig. 4.25 compares the river discharge of Ganges/Brahmaputra as computed by the HD model from the ECHAM4 and ECHAM4/IMPL simulations to the measurements given by GRDC. ECHAM4 drastically underestimates the discharge of Ganges/Brahmaputra due to a deficient representation of the summer monsoon precipitation in this region. Only 31% of the observed annual mean total runoff are reproduced by ECHAM4 (cf. Hagemann 1998). In ECHAM4/IMPL the discharge simulation is clearly improved compared to the GRDC measurements. The uncertainty of the measurements is more than 25% in the months of maximum discharge (Dümenil et al. 1993), which means that the ECHAM4/IMPL results are close to or within the uncertainty interval of the measurements.

This result gives further evidence, beside the direct comparison to the rainfall observations, that ECHAM4/IMPL clearly better represents the monsoon precipitation and consequently the entire hydrological cycle of the region.

4.3.2 Snow related processes in northeast Siberia

In the model intercomparison in section 4.1.1 several regions are identified in ECHAM4/IMPL and ECHAM4/SECHIBA where a reduced cloud cover is found in JJA which is associated with an increased surface temperature. The underlying mechanism shall be discussed here in more detail.

Figure 4.26 shows the atmospheric profiles of temperature, specific and relative humidity and cloud cover for a site in northeast Siberia at 65°N and 140°E. Both ECHAM4/IMPL and ECHAM4/SECHIBA simulate a higher JJA surface air temperature and a reduced total cloud cover at this location as compared to ECHAM4 (cf. Figs. 4.1 and 4.5). The reasons for this are discussed in section 4.1.1. The upper left panel in Fig. 4.26 shows that ECHAM4/IMPL simulates about 3°C higher temperatures near the surface than ECHAM4 at the selected site, and ECHAM4/SECHIBA is even warmer by another 3°C. This warming is also seen in the entire atmospheric column up to 200 hPa. At higher levels above 200 hPa the order of the profiles is partly reversed. Here ECHAM4/SECHIBA shows the lowest temperatures.

Due to the higher surface temperatures the evaporation is increased in the implicit models (cf. Fig. 4.7). This leads to an enhanced specific humidity in the entire troposphere in both models (Fig. 4.26). Although the specific humidity is increased, the atmospheric relative
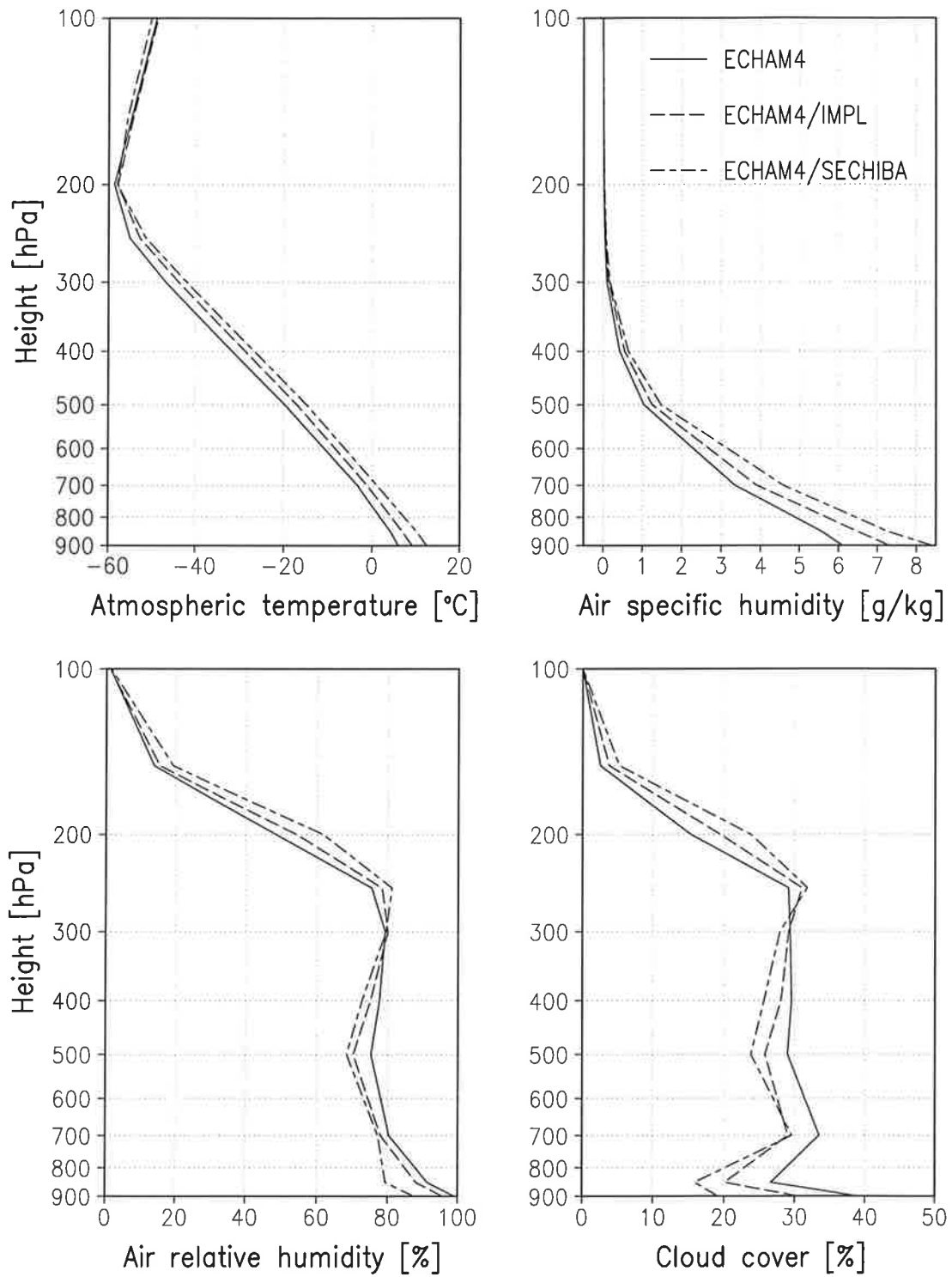
Figure 4.26: JJA seasonal mean vertical atmospheric profiles of temperature [°C], specific [g/kg] and relative [%] humidity and cloud cover [%] as simulated by ECHAM4, ECHAM4/IMPL and ECHAM4/SECHIBA at a site in northeast Siberia at 65°N and 140°E.
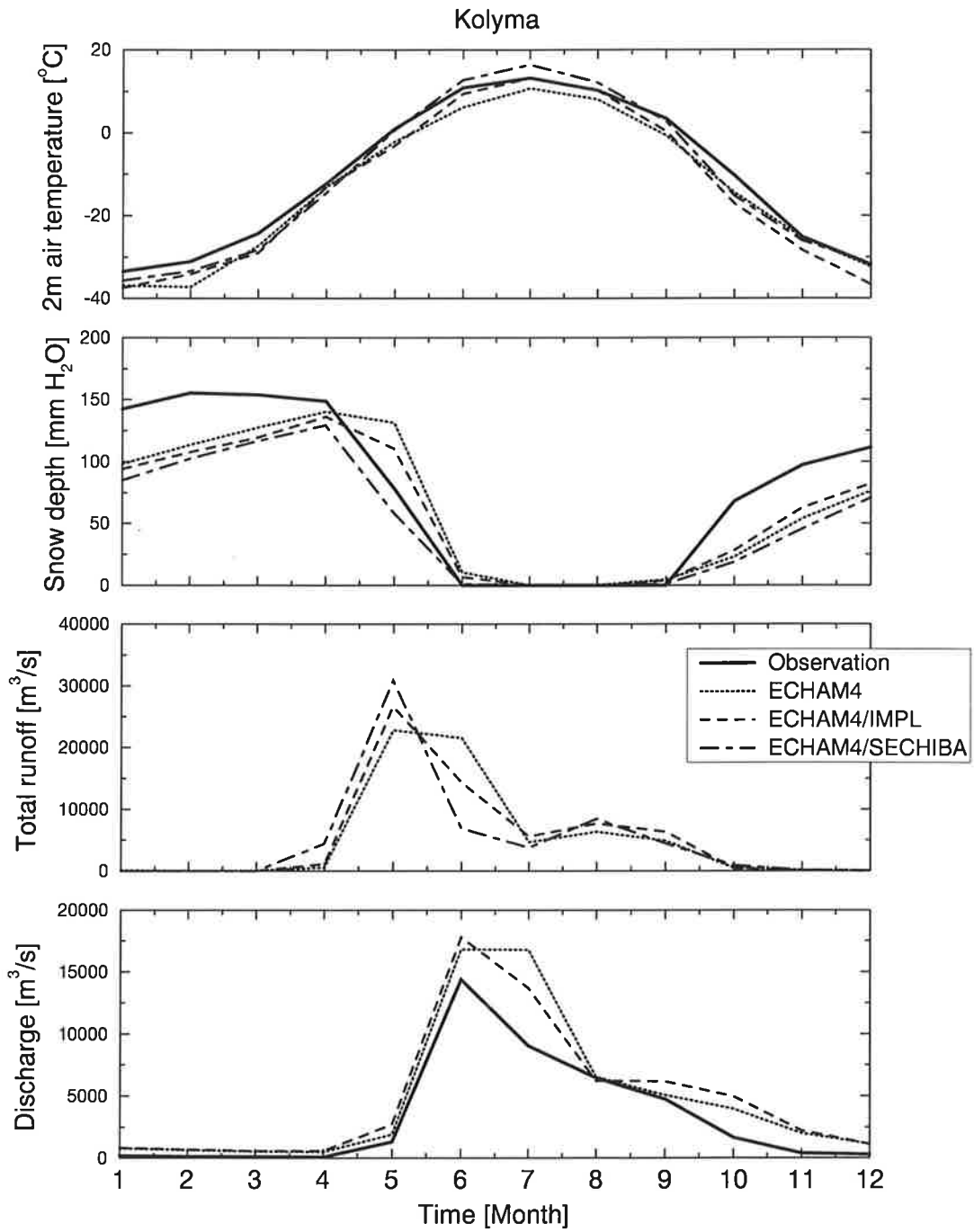
Figure 4.27: Monthly mean annual cycles of the Kolyma catchment mean 2-meter air temperature [°C], snow depth [mm water equivalent], total runoff [m³/s] (i. e. surface runoff plus drainage) and river discharge [m³/s] for ECHAM4, ECHAM4/IMPL and ECHAM4/SECHIBA (no discharge) compared to observations of surface air temperature (Legates/Willmott), snow depth (USAF/ETAC) and discharge (GRDC).

humidity is decreased in the implicit models up to a level of 300 hPa. At higher levels the order of the profiles is reversed. As a consequence of this behaviour, ECHAM4 simulates the largest cloud cover in the troposphere up to about 300 hPa and ECHAM4/SECHIBA the smallest. The difference between them is up to 10%. The ECHAM4/IMPL profile is between them (with one exception at 700 hPa). At levels higher than about 300 hPa, again, the order is reversed.

Hence, as a result of the enhanced land surface and tropospheric temperature the relative air humidity is reduced which leads to a reduced total cloud cover, while cirrus clouds increase. A similar mechanism has been found by Lohmann and Roeckner (1994), who tested the sensitivity of the cloud cover to changes of the SST. This may be an important positive feedback effect, amplifying the near-surface temperature raise in a global warming scenario. On the other hand, this may be interpreted as an indication for a deficient representation of the planetary boundary layer, as an increased evaporation does not lead to an increased cloud cover. This would be a damping effect, compensating for too pronounced surface temperature raises. If this compensation is missing, surface temperature biases may occur although the surface scheme is working accuratly.

The site just discussed is located very close to the catchment of the northeast Siberian river Kolyma which flows into the Arctic Ocean (cf. Fig. 4.24). The upper panel of Fig. 4.27 shows the annual cycles of the catchment mean 2-meter air temperature for the three GCM versions. ECHAM4 underestimates the temperature almost the entire year by up to 6°C compared to the Legates observations (cf. section 4.2.2.1). The two other models tend to simulate higher temperatures (except for ECHAM4/IMPL in October – December), in particular in the summer months. In this period ECHAM4/IMPL exactly agrees with Legates, while ECHAM4/SECHIBA overestimates it by about 3°C. ECHAM4 underestimates Legates by about 3°C, thus the order and the amounts of the temperature differences between the models are very similar to those seen in the profile plot (Fig. 4.26).

In ECHAM4/IMPL the higher temperature in JJA (compared to ECHAM4) is mainly due to the numerical coupling (cf. section 4.1.1), whereas in ECHAM4/SECHIBA it is associated with a different snow parameterization which allows for an earlier snow melt. This can be seen in the second panel of Fig. 4.27 which shows the simulated snow depths. All three models underestimate the snow pack during almost the entire snow period when compared to the USAF/ETAC climatology, while there is sufficient precipitation. Snow melt in ECHAM4 starts about one month too late which is a known deficiency of the ECHAM4 model. A delayed snow melt is found in all catchments of the largest rivers in north Russia and Canada (Hagemann 1998). ECHAM4/IMPL simulates the snow melt in the Kolyma catchment slightly earlier than that, and in ECHAM4/SECHIBA the time of snow melt is in very good agreement with USAF/ETAC (Fig. 4.27).

The simulated total runoff of all three models is predominated by the snow melt. The earlier in the year the snow melt occurs, the earlier is the maximum of total runoff. The lower panel of Fig. 4.27 shows the discharge computed by the HD model from the ECHAM4 and ECHAM4/IMPL simulations compared to the GRDC data. Both model discharges are too high in summer which is partly due to a discrepancy between the catchment area at the 0.5° resolution and the real area which is relevant for the discharge measurements (701,998 km^2 compared to the real area of 526,000 km^2). The reason is that the discharge station is not directly located at the river mouth but a bit upstream, whereas only the total catchment area is available in the 0.5° data set (S. Hagemann 1998, pers. comm.). Taking this into account

ECHAM4 still overestimates the discharge by 18% (Hagemann 1998). This is consistent with a too high simulated precipitation in spring and summer. Beside this, there is an uncertainty in the GRDC data of more than 30% in the months of maximum discharge (Dümenil et al. 1993), which means that both models are consistent with the observations except for ECHAM4 in July.

Generally, ECHAM4/IMPL tends to produce an earlier discharge than ECHAM4 which is due to an earlier snow melt and agrees better with the GRDC data. Since ECHAM4/-SECHIBA agrees very well with the USAF/ETAC snow observations regarding the melting time an even better discharge simulation may be expected from that. Therefore, it would be desirable to be able to apply the HD model to ECHAM4/SECHIBA. This would require a modification of the soil hydrology formulation to include a drainage term. This has been done by Ducharne et al. (1998), and it is one of the future perspectives for ECHAM4/SECHIBA.

4.3.3 Evaporation over Europe

In this section observations of evaporation over land at seven European sites are presented that have been used by Wild et al. (1996) to test the accuracy of the simulated evaporation in high resolution versions of the ECHAM3 and ECHAM4 GCMs. The data are shortly described by Wild et al. (1996). Shown are seasonal cycles of monthly mean evaporation which are based on multi-year station measurements for most of the sites. The Cabauw data (Beljaars and Bosveld 1997) cover a period of one year, and they are presented in chapter 2.

Figure 4.28 compares the observed seasonal cycles of evaporation at the different sites and the simulations of ECHAM4, ECHAM4/IMPL and ECHAM4/SECHIBA at the respective grid points. The simulated seasonal atmospheric forcing in the European region is similar in all three models (see section 4.1). Furthermore, there are only small differences between the bucket size distributions in ECHAM and SECHIBA in this region (cf. Fig. 1.7). Wild et al. (1996) demonstrated that the simulated seasonal surface radiation in ECHAM4 is in good agreement with observations in this region. This was found to be a major improvement compared to the previous GCM version ECHAM3, which tends to overestimate the surface radiation in summer and autumn in this region. The comparison of the different sites shows that the two models with the ECHAM surface parameterization tend to compute higher evaporation than ECHAM4/SECHIBA in winter and spring and/or lower in summer (Fig. 4.28). The latter model tends to better agree with the observations in the majority of the sites, best seen at Rietholzbach, Gross Lüsewitz and Cabauw. Certainly, comparisons between point measurements and GCM grid point simulations, especially at the relatively coarse T42 resolution, must be interpreted with caution. However, similar results for ECHAM4 were found at the higher $1.1° \times 1.1°$ resolution used by Wild et al. (1996). This indicates that this behaviour is not specifically dependent on resolution but rather a consequence of the model parameterization.

Figure 4.29 shows the contributions of snow sublimation, canopy evaporation, transpiration and bare soil evaporation to the total evaporation for ECHAM4/IMPL at the seven sites. The transpiration clearly follows the annual (solar) cycle with very low values in winter and high values in summer at all sites. At near mountain sites and in Stockholm there is some contribution by snow sublimation which appears to be reasonable. High total evaporation values in the first half of the year are mainly caused by evaporation from the canopy (especially at Rietholzbach and Zürich) or bare soil. In the second half of the year bare
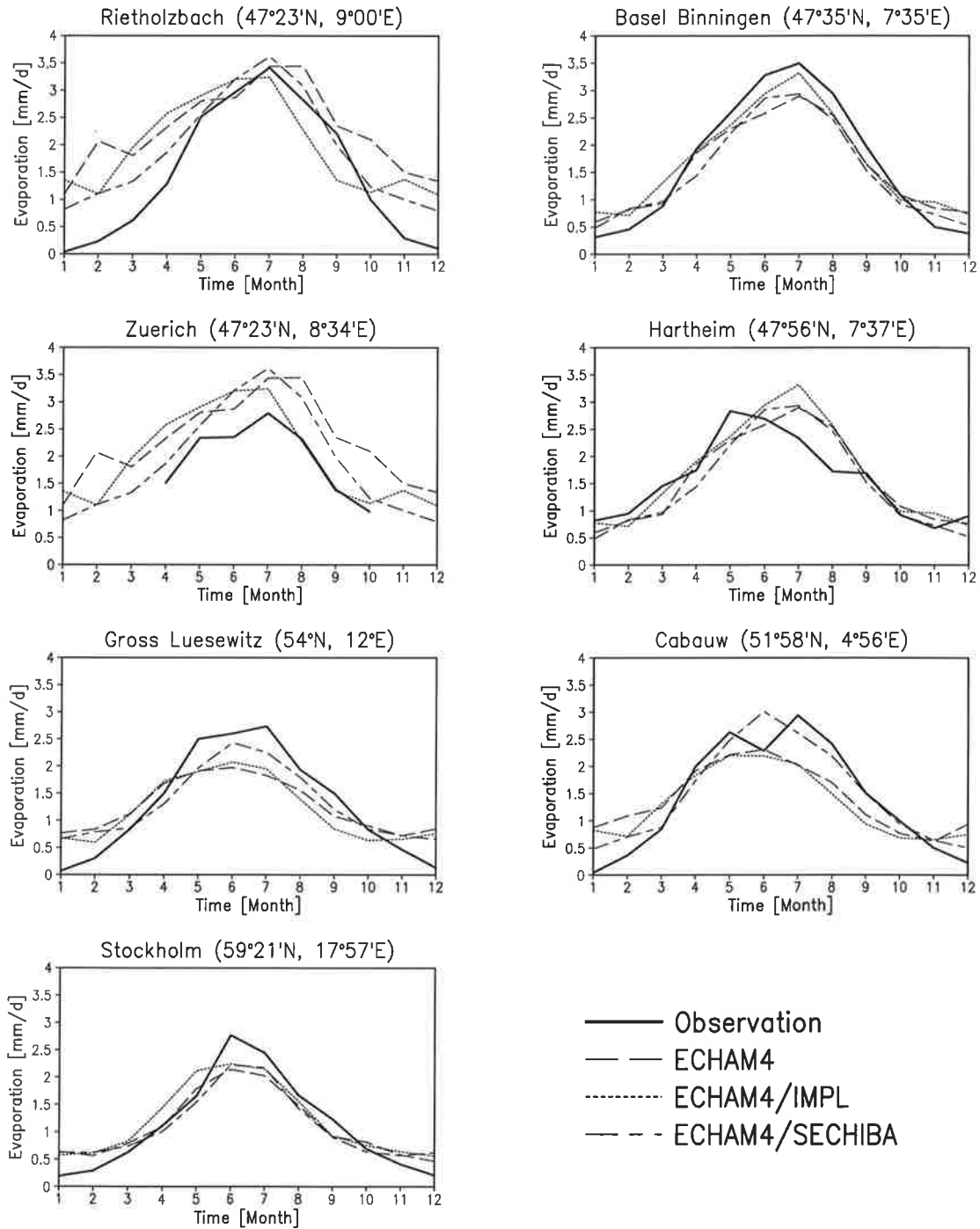
Figure 4.28: Monthly mean annual cycles of evaporation [mm/d] as simulated by ECHAM4, ECHAM4/IMPL and ECHAM4/SECHIBA compared to station measurements at seven different sites in Europe. The geographical locations are given. The observations are from Wild et al. (1996), the Cabauw data from Beljaars and Bosveld (1997).
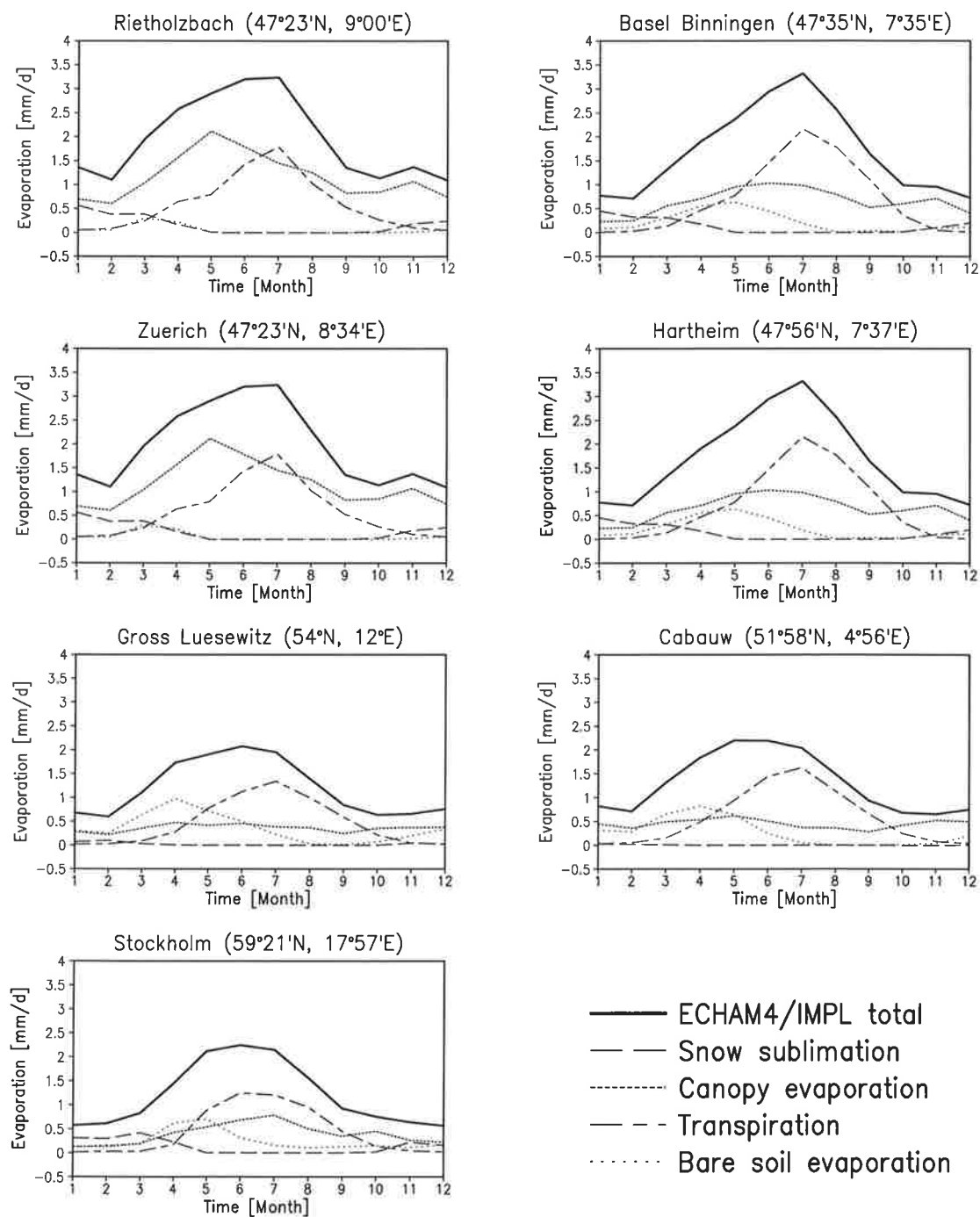
Figure 4.29: Contributions of snow sublimation, canopy evaporation, transpiration and bare soil evaporation to the total evaporation [all in mm/d] for ECHAM4/IMPL at the seven European sites from Fig. 4.28.
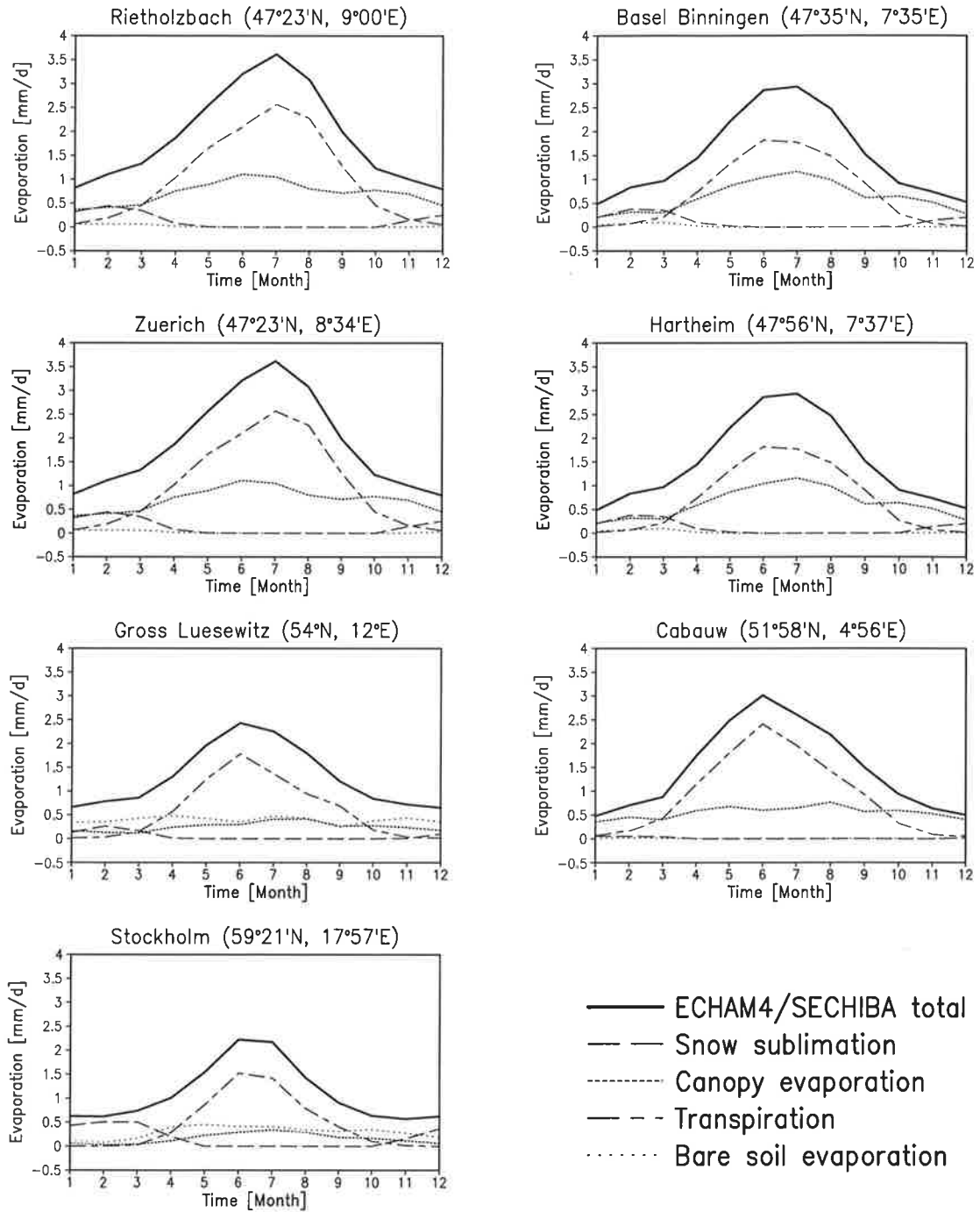
Figure 4.30: As Fig. 4.29 but for ECHAM4/SECHIBA.

soil evaporation ceases due to a drying of the soil, since the model structure allows bare soil evaporation only from the top 10 cm of the soil moisture reservoir.

In ECHAM4/SECHIBA (Fig. 4.30) transpiration and snow sublimation are roughly similar as in ECHAM4/IMPL. The most striking differences are the reduced bare soil evaporation in ECHAM4/SECHIBA in spring and the reduced canopy evaporation at Rietholzbach and Zürich, also in spring. The former is attributed to the substantially higher vegetation cover in ECHAM4/SECHIBA in the European region. As shown in Fig. 1.4, ECHAM4/SECHIBA specifies vegetation ratios in most parts of Europe of more than 90%, while in ECHAM4/-IMPL they are mostly between 40% and 50%. Consequently, the latter model allows for a higher bare soil contribution.

The results of ECHAM4/IMPL for the Cabauw point may be compared to the off-line simulations with ECHAM using the observed atmospheric forcing and appropriate parameter values for the site (chapter 2). Figure 2.20 shows that the bare soil contribution in the off-line simulations in winter and spring is clearly lower than in ECHAM4/IMPL at the Cabauw point (Fig. 4.29). This is due to the observed annual mean vegetation ratio of 95.6% which is specified for the off-line experiment, representing the dense grass cover at the site. Consequently, there is only very little overestimation of total evaporation in winter. At the Cabauw point in ECHAM4/IMPL a vegetation fraction of 42% is specified. Consistently, this leads to the higher bare soil evaporation in winter and spring, which explains the difference between the off-line and the GCM results. On the one hand this is an example for the difficulties one faces when trying to compare measurements, representing a grass area of the order of 1 ha, and GCM simulations, where one grid element covers large parts of The Netherlands and Belgium, which can definitely not be treated like just a rather huge grassland. On the other hand it emphazises the importance and the need for accurate global parameter sets in GCMs. In particular, the use of annual mean values for parameters that obviously are subject to high seasonal variations, like the vegetation cover in many regions of the world, is a model simplification which may induce large errors in the simulations. This is an issue that should be addressed to as part of the very next efforts to improve the model.

Another difference between ECHAM and SECHIBA is that the latter uses a seasonally varying LAI rather than an annual constant one (cf. section 1.2). This is one step in the direction just mentioned. The temporal constant LAI was identified by Wild et al. (1996) to cause problems in the simulations of evaporation in ECHAM at these European sites. Here, the seasonally varying LAI prevents ECHAM4/SECHIBA from the high spring canopy evaporation found in ECHAM4/IMPL (at Rietholzbach and Zürich, Figs. 4.29 and 4.30), since the size of the interception reservoir is directly computed from the LAI. Furthermore, the seasonal cycle of the LAI in ECHAM4/SECHIBA allows for a higher annual amplitude of the simulated transpiration than in ECHAM4/IMPL, which appears to be intuitively reasonable and also to be an improvement when compared to the observations in Fig. 4.28. This evaluation shows, that further efforts need to be made to improve the representation of the vegetation in the ECHAM4/IMPL GCM and that SECHIBA provides some important perspectives for this issue.

Chapter 5

Conclusions and future perspectives

Land surface processes have a significant impact on near-surface climate phenomena. They determine, among other things, surface sensible and latent heat fluxes and the radiation budget, and thus influence atmosphere and land characteristics, such as temperature and humidity, cloud formation and the entire structure of the planetary boundary layer. It is therefore important to include land surface processes in a realistic way in models for climate simulations or numerical weather prediction. The component of an atmospheric general circulation model that is responsible for the representation of these processes is the land surface parameterization scheme, which essentially simulates the surface energy and moisture cycles.

Another aspect of the meteorological models, beside the physical parameterization of the relevant processes, is the numerical realization of the coupling between land surface and atmosphere and its possible influence on the simulations. It is reasonable to assume that it has an impact, but very little attention has been paid to this in the past.

Therefore, to more substantially assess the role of the land surface in the entire climate system, the questions of interest are:

- Which aspects of the land surface parameterization are most important for the simulation of the atmosphere or the climate of the Earth in general?

- What is the impact of the numerical coupling between land surface and atmosphere on the climate simulations?

- What is the relative importance of both the physical parameterization and the numerical coupling for the global model performance?

These questions were the main focus of this thesis. A further general research topic of this work was, what level of complexity of the land surface representation in GCMs is needed. In order to address these items, the following methodology was chosen:

The results of the standard ECHAM4 GCM, in which land surface and atmosphere are coupled semi-implicitly in a way that the energy balance at the land surface–atmosphere interface is not closed (which is a major deficiency), were compared to those of the two modified model versions ECHAM4/IMPL and ECHAM4/SECHIBA. These versions were developed as part of this thesis. In contrast to the standard ECHAM4, they incorporate an implicit

coupling technique which has as one major advantage: the conservation of energy at the land surface. The implicit and semi-implicit coupling techniques are standard methodologies used in current GCMs. ECHAM4 and ECHAM4/IMPL are identical with respect to all physical parameterizations they apply, the only difference is the coupling. Therefore, they can be used to investigate the impact of the coupling technique on the simulated climate. On the other hand, the comparison of ECHAM4/IMPL and ECHAM4/SECHIBA reveals the influence of different land surface parameterizations, both coupled to the atmosphere in the same way. Therefore, this set of three different model versions allows a systematic analysis of the impact of both the numerical coupling and the physical parameterization on the model climate.

The thesis was organized for a detailed evaluation of the land surface schemes in a hierarchy of model set-ups, from off-line experiments, through one-dimensional to global three-dimensional. In the off-line section, the three land surface schemes ECHAM, SECHIBA and SSiB, which were developed for use in GCMs, were compared, mainly with respect to their simulated energy and moisture budgets. SECHIBA was found to incorporate a thermodynamic treatment of the soil which is more similar to that of ECHAM than to that of SSiB. Furthermore, a somewhat peculiar behaviour was found in SSiB regarding its soil hydrology, where the deep soil drainage obviously plays a dominant role. Therefore, SECHIBA had been selected for the implementation in the ECHAM4 GCM, to make the new model easier to compare to the standard one. The guiding principal was to avoid too many drastic changes in the model architecture and probable additional uncertainties, which may have further complicated the interpretation of the results. ECHAM and SECHIBA still incorporate a number of various different features which may allow one to regard them as representatives of significantly different approaches from the range of the large number of currently existing land surface models.

Single point off-line simulations

In this thesis, results from off-line simulations, using ECHAM, SECHIBA and SSiB, have been presented where the schemes were driven by identical atmospheric forcing, extracted from the Cabauw observational dataset of 1987. The energy and water cycles of the models were compared, and the quantities of the energy cycle were validated against the Cabauw data. Differences in the components of energy and hydrological cycle as simulated by the schemes were explained by characteristic differences in the model architectures. Additional studies were performed with the schemes to test the sensitivities to certain parameters and to improve the model behaviour.

The three models are different in their structures but, nevertheless, they simulate similar annual cycles of surface temperature and total net radiation. These results are consistent with the Cabauw observations. On a diurnal timescale the simulations reveal a principal conceptual problem of the surface temperature calculation when using a finite difference scheme for solving the the soil heat conduction equation. This can be seen for ECHAM which shows deficiencies in modelling the diurnal variations of surface temperature and ground heat flux. This is due to the fact that the temperature of the top soil layer, which has a depth of 6.5 cm, is used with two different meanings: firstly as part of the soil temperature finite difference scheme, and secondly as surface value for computing the atmospheric surface energy fluxes (in the absence of snow). This causes some inconsistencies. Using a finer discretization with

a higher number of thinner layers near the surface would reduce the problem. It was found that this would be computationally too expensive and would require shorter time steps for accuracy reasons, which is not acceptable for GCM applications.

SECHIBA applies a more sophisticated approach by solving the surface energy balance equation with the soil properties obtained by an extrapolation of heat capacity and ground heat flux toward the surface. In SSiB, the surface radiative temperature is computed as an average of the temperatures of the upper ground and the canopy of vegetation. The latter has a much lower heat capacity than the ground. Due to these model formulations, SECHIBA and SSiB capture more accurately the observed diurnal variations of the surface temperature. This may be even more improved by introducing a skin temperature formulation (see also Viterbo and Beljaars (1995) who report on the improvement of the ECMWF land surface scheme by the implementation of a skin temperature).

Differences between the three models occur in the simulations of the turbulent heat fluxes regarding amplitude as well as phase. All three models underestimate latent heat flux and overestimate sensible heat flux in summer. In ECHAM and SECHIBA, evapotranspiration is mainly determined by incoming solar radiation which appears to be realistic when compared to the observations. In SSiB, evapotranspiration seems to follow the precipitation rate. However, on an annual timescale the simulated evapotranspiration of all three models is relatively similar in their Cabauw experiments. In contrast to this, the model simulations for the other hydrological components, such as surface runoff, drainage and the variations of root zone soil moisture, are quite different. This is explained by the different philosophies of the models, especially in SSiB, where the root zone soil moisture appears to be strongly controlled by unexpected high upward and downward vertical water fluxes in the soil.

It has been shown that a model with a relatively simple soil hydrology like ECHAM, only using one soil moisture reservoir, can successfully reproduce the observed latent heat flux at Cabauw. But this requires a careful choice of the appropriate parameter values characteristic for the site to be used. It was found that the annual cycles of the turbulent heat fluxes in ECHAM, SECHIBA and SSiB are very sensitive to the surface resistance, for example. If a value for the minimum stomatal resistance that is appropriate for the site is chosen, simulated latent and sensible heat fluxes get close to the observations.

Single column model studies

A principal (intended) restriction in off-line simulations is the exclusion of feedback effects between land surface and atmosphere, which is necessary if well-defined atmospheric conditions imposed to the land surface scheme are desired. In order to also study the interactions between land surface and atmosphere, the one-dimensional versions of the standard ECHAM4 GCM and the two modified models ECHAM4/IMPL and ECHAM4/SECHIBA were used.

The simulations of these three one-dimensional models were compared under different climatic conditions. Their behaviours were analysed for a simulation of July at a central European site under prevailing dry conditions and a simulation of May at a site in western Russia during snow melt followed by wet soil conditions. For all three situations the behaviour of the energy residual term in ECHAM4 was investigated, which is part of the semi-implicit coupling and represents an error in the surface/atmosphere energy balance. It was found not to be negligibly small, but rather to be of an order of magnitude similar to the physical

fluxes of e. g. latent or sensible heat. This term serves as artificial (numerical) sink or source of energy at the surface which may significantly alter the surface energy balance. Due to this, unrealistic high latent heat flux values of more than 1700 W/m^2 were found in the July simulation. Only a very little portion of this energy may be provided by other physical terms of the energy balance. For instance, in this particular case, more than 1300 W/m^2 were compensated by the energy residual. This had also a negative effect for the convective precipitation that was triggered by the evaporation, associated with the latent heat flux. This model behaviour represents a clear deficiency in ECHAM4 and shows that great care needs to be taken in the choice of numerical methods applied. In the case of a GCM, this means that, beside other things, the numerical coupling between surface and atmosphere needs to be properly designed to ensure that the surface energy balance can be realistically calculated. As the energy and water cycles are coupled via the latent heat flux or evapotranspiration, respectively, a proper numerical treatment has important implications also for the surface moisture balance.

These results were compared to ECHAM4/IMPL which utilizes an implicit coupling technique with a closed land surface–atmosphere energy balance. Here, the energy, which was lost to (or created by) the numerical scheme in ECHAM4, is conserved for the physical processes. Similar to ECHAM4, a positive feedback between convective precipitation and canopy evaporation occurs in the July simulation, but here the energy available for the latent heat flux is more realistically controlled. An extreme overestimation of latent heat flux (and associated precipitation) peaks and an energy loss due the numerics, such as in ECHAM4, are avoided in ECHAM4/IMPL. This was found to result in a more pronounced diurnal cycle of surface temperature and generally higher temperature maxima during a warming phase.

Furthermore, a coding error in the ECHAM parameterization was identified which allows the removal of additional water from the soil when required, which occurs whenever the calculated canopy evaporation exceeds the available water in the interception reservoir. This was found to lead to a reduction of the soil water content below the wilting level by transpiration, which should not be possible by definition of the wilting point. In SECHIBA such an effect is avoided by a predictor-corrector-method which reduces the canopy evaporation accordingly to the available water on the canopy. Additionally, due to its soil hydrology and stress formulations, SECHIBA was found to be generally more effective in keeping the water stored in the soil under dry and medium-wet conditions than ECHAM. Therefore, SECHIBA tends to simulate higher surface temperatures under these conditions. Besides that, SECHIBA additionally allows some bare soil evaporation even under prevailing dry conditions, as a result of a different formulation of the soil moisture stress. This may occur as a response to heavy rain showers when the upper soil moisture layer, which is part of the Choisnel soil hydrology scheme, is filled. This was found to be a reasonable approach.

As mentioned above, both ECHAM4/IMPL and ECHAM4/SECHIBA tend to simulate higher surface temperatures than ECHAM4 under dry conditions, for the reasons discussed. This was actually found in the global experiments using these three models in arid regions.

Numerical instabilities in the calculation of the surface temperature, which occur in ECHAM4 in certain situations with associated rapid surface temperature changes, were found not to be avoided by the implicit coupling. They occur to a similar extent, but one has to keep in mind that the implicit models offer the important advantage of conserving energy at the land surface–atmosphere interface.

In SECHIBA the surface energy balance equation is solved using the soil properties obtained by an extrapolation of heat capacity and ground heat flux toward the surface. It was found that due to this in ECHAM4/SECHIBA the diurnal cycle of the ground heat flux has a higher amplitude and is earlier in phase than in ECHAM4/IMPL, which is desired. A comparison with the Cabauw observational data showed that solving the surface energy balance equation with an implicit method, that prevents energy loss or creation by the numerics, in combination with this particular model structure in SECHIBA, yields more realistic surface heat fluxes.

Global experiments

For a comparison of the three GCM versions ECHAM4, ECHAM4/IMPL and ECHAM4/-SECHIBA on the global scale, each of the three models was integrated for a 10-year period after at least one year of spin-up. A T42 spatial resolution was chosen which is equivalent to about $2.8° \times 2.8°$ on a latitude–longitude grid. In all simulations an annual cycle of monthly mean climatological SST was used, and the land-sea-mask and glacier-mask and the distributions of background albedo and roughness length were identical.

A significant impact of the change of the coupling technique and the land surface scheme on most surface variables and atmospheric surface fields was found. For most variables the change of the coupling scheme appears to produce larger differences than the modifications in the land surface parameterization. Generally more pronounced differences appear in the northern hemispheric summer season (JJA) than in the winter season (DJF).

The 2-meter air temperature over large continental areas in the Northern Hemisphere was found to be generally higher by up to 3–5°C in JJA in the two modified model versions than in the standard ECHAM4. For ECHAM4/IMPL this was attributed to the model improvement compared to the standard ECHAM4 regarding the energy conservation at the land surface–atmosphere interface. Energy amounts of regionally more than 40 W/m^2 in the JJA seasonal mean, which are lost in ECHAM4 over wide areas of Eurasia and North America due to the implementation of the semi-implicit coupling scheme, are conserved in ECHAM4/IMPL. Therefore, here this energy can be used for physical processes, e. g. for heating the land surface and lower atmosphere.

In ECHAM4/SECHIBA the increased surface air temperature of up to about 3°C in JJA was found to be mainly due to a different snow parameterization which allows an earlier snow melt. It induces a snow – albedo – solar radiation – surface temperature feedback. As a result of the enhanced surface and also tropospheric temperatures the relative air humidity is reduced which leads to a reduced cloud cover, further enhancing this feedback. The earlier snow melt has been shown to be in good agreement with the USAF/ETAC snow climatology and to be consistent with ERBE albedo measurements.

When comparing the model results to the Legates/Willmott climatology, ECHAM4 was found to reasonably represent the absolute values as well as the seasonal cycle of the surface air temperature (with some overestimations in Eurasia and the southwest USA in JJA), although the energy is not conserved at the land surface. This means that there are systematic model errors in the GCM which compensate the error at the surface. These were detected by the GCM versions ECHAM4/IMPL and ECHAM4/SECHIBA which have closed surface energy balances (which is clearly physically more realistic), resulting in higher surface air

temperatures in many regions. Thus a new adjustment of the GCM is needed for the implicit coupling scheme.

The changed temperature distributions in ECHAM4/IMPL and ECHAM4/SECHIBA were found to cause significant changes of the geopotential height. As indicated by changes of the velocity potential, the southeast Asian summer monsoon is intensified in ECHAM4/-IMPL. It appears to be further enhanced in ECHAM4/SECHIBA. This is confirmed by an enhanced moisture convergence in the Indian region in ECHAM4/IMPL and ECHAM4/-SECHIBA.

All three GCM versions were found to be in good agreement with the ranges of global annual mean precipitation and evaporation over continents and oceans as given by three different estimates of the world water balance.

The precipitation in the implicit models was found to be altered mainly in the tropics and subtropics. In the Indian region, rain fall occurs that is locally enhanced by more than 6 mm/d in JJA, which is associated with an intensified Asian summer monsoon. In other regions an increased precipitation was found due to a northward shifted and partly intensified ITCZ. A comparison to the GPCP precipitation climatology indicated that the distribution and the rates of the southeast Asian summer monsoon rain fall are considerably improved in ECHAM4/IMPL and ECHAM4/SECHIBA. Furthermore, overestimated rain fall rates in ECHAM4 over northern Africa in JJA are improved in the modified models as well. ISCCP satellite data confirmed that the total and high cloud covers, which are increased over India in JJA by more than 20% and 10% in the two implicit models, respectively, are much more realistic than those simulated by ECHAM4.

The evaporation in the two modified GCM versions was found to change by up to 1 mm/d. This is caused by an altered wind speed over the oceans, and a changed availability of energy or soil water at the land surface. The latter shows the importance of accurate global data sets of the soil water-holding capacity for realistic simulations of the global near-surface water cycle. The same holds for global data sets of albedo, which determines the available energy at the land surface, or certain vegetation parameters.

Regional studies

One focus of the regional studies conducted was the intercomparison of the representation of the Asian summer monsoon in the three models, which was found to be generally more intense in the two implicitly coupled GCM versions.

The ECMWF and NCEP reanalyses both show pronounced local maxima between 0°C and 1.5°C of the atmospheric temperature at 500 hPa over the Tibetan plateau in July. The reanalyses have been shown to be a reasonable reference in this data sparse region (Dümenil and Bauer 1998). The temperatures as simulated by ECHAM4/IMPL and ECHAM4/-SECHIBA were found to be in this range. In contrast, ECHAM4 simulated two temperature maxima, both displaced and too cold. The higher temperatures in the implicit models were explained by the changed coupling technique between land surface and atmosphere. The further increased temperature in ECHAM4/SECHIBA over the Tibetan plateau and the Himalayas is due to a more efficient snow melt, which was found to be in good agreement with the USAF/ETAC snow climatology. These changes lead to the enhanced 500 hPa atmo-

spheric temperatures, seen in the simulations, which is only slightly higher than the Tibetan plateau.

The increased atmospheric temperatures in the implict models were found to lead to more pronounced high pressure systems in the upper troposphere and enhanced pressure gradients to the Southern Hemisphere. This intensified the tropical easterly jet stream, which is the upper branch of the southeast Asian summer monsoon circulation, which was in better agreement with the reanalyses. The lower branch of the Indian monsoon, advecting moist air from the Indian Ocean toward the Indian subcontinent, was also found to be considerably improved in the implicit models, with respect to both stream patterns and wind velocities. Due to this, and the associated enhanced evaporation over the ocean, the precipitation patterns were substantially improved at the west coast of India and over the northern Bay of Bengal compared to the reanalyses and the GPCP precipitation climatology. In these regions, rain fall was found to be too low in ECHAM4. The improvement of the summer monsoon precipitation in ECHAM4/IMPL was also confirmed by comparison of the simulated river discharge of the Ganges/Brahmaputra to observations.

For a site in northeast Siberia the mechanism was analysed, which leads to a reduced cloud cover in JJA in ECHAM4/IMPL and ECHAM4/SECHIBA as compared to ECHAM4. It was found that, although the specific humidity is increased in the lower and middle troposhere by enhanced surface evaporation, the atmospheric relative humidity is decreased in the implicit models due to an increased temperature at the surface and almost in the entire troposhere. This leads to a reduced cloud cover. This may be interpreted as an indication for a deficient representation of the planetary boundary layer, as an increased evaporation does not lead to an increased cloud cover.

For the Kolyma catchment in northeast Siberia ECHAM4 was found to simulate the snow melt with a delay of about one month, which is also seen in all catchments of the largest rivers in north Russia and Canada. ECHAM4/IMPL simulated the snow melt in the Kolyma catchment slightly earlier than that, and in ECHAM4/SECHIBA the time of snow melt was in very good agreement with USAF/ETAC. Therefore, ECHAM4/IMPL tended to produce an earlier discharge than ECHAM4 which agrees better with the river discharge data. Since ECHAM4/SECHIBA agreed very well with the USAF/ETAC snow observations regarding the melting time, an even better discharge simulation would be expected from that.

As third regional study, the simulated annual cycles of evaporation of the three GCM versions were compared to measurements at seven different sites in Europe. Additionally, the different components of the total fluxes, such as snow sublimation, transpiration or evaporation from the canopy or bare soil were analysed for ECHAM4/IMPL and ECHAM4/SECHIBA. It was found that a seasonally varying LAI, as implemented in SECHIBA, appears to improve the simulated seasonal cycles of transpiration and canopy evaporation, when compared to ECHAM which utilizes an annual constant LAI. This evaluation showed that further efforts need to be made to improve the representation of the vegetation in the ECHAM4/IMPL GCM and that SECHIBA provides some important perspectives for this issue.

Future perspectives and model development

An extension of the studies presented in this thesis would be the intercomparison of ECHAM4, ECHAM4/IMPL and ECHAM4/SECHIBA in an experimental set-up as used in the *Atmo-*

spheric Model Intercomparison Project (AMIP) (Gates 1992). In the AMIP simulations the interannually varying SST, as observed over several years (1979–1988 in the original AMIP experiments), is provided to the atmospheric models as lower boundary condition, rather than a climatological mean SST as in the simulations presented in this work. It would be interesting to study interannual variability in the implicit models, induced by the varying SST, e. g. with respect to the simulated Asian summer monsoon circulation and precipitation and its probable interactions with El Niño events.

A further possibility is the coupling of the implicit GCM versions to an ocean general circulation model. The standard semi-implicit ECHAM4 has already been coupled to an ocean model. It would be interesting to test if the implicit coupling has a positive effect on the flux correction, needed in many ocean–atmosphere coupled GCMs to avoid drift. The implicit coupling technique may have an important effect for the representation of the energy balance on sea ice, since large variations of the temperature occur there. However, it is not expected to have a pronounced effect at the ocean–atmosphere interface, since water has a large heat capacity which causes diurnal sea surface temperature variations to be small. An exception are the tropical oceans that receive high insolation. In a model set-up including an ocean model, which resolves the diurnal temperature cycle in the upper layers, an implicit coupling would be expected to be more important.

A general restriction of the presented studies and the available data sets was that the impact of one important feature of SECHIBA, the sub-grid scale distribution of the vegetation types, on the simulated climate in comparison to ECHAM, was very difficult to evaluate. Global climatologies of surface air temperature or precipitation can generally not serve as criteria, whether the big leaf or the mosaic approach leads to more realistic results. For this issue, a set of evaporation measurements would be needed, covering a region with heterogeneous vegetation distribution. Such a data set could help to demonstrate the advantages of the mosaic approach.

Based on the results of this work some recommendations for the future development of the ECHAM GCM will be given. The main result is that in future a model architecture should be used which conserves energy at the land surface–atmosphere interface as in the implicitly coupled ECHAM4/IMPL. The semi-implicit coupling technique in the current standard ECHAM4 was found to induce too large errors in the surface–atmosphere energy balance, significantly affecting both energy and water cycle variables, which is not acceptable. ECHAM4/IMPL needs similar computer resources as ECHAM4 with respect to storage capacity and CPU time (ECHAM4/SECHIBA needs slightly more).

A next step in (land surface) model development would be an interchange or combination of those components of the compared models, which have been found to produce best results. This procedure leads to a model with a comparable complexity as the source models. These components are:

- Discretization of the soil heat conduction equation and calculation of the surface temperature, using the surface energy balance equation, using the soil properties obtained by an extrapolation of heat capacity and ground heat flux toward the surface (from SECHIBA).

- Bucket soil hydrology utilizing the Choisnel scheme (from SECHIBA). This could be upgraded by the multi-column soil moisture scheme (a column for each surface type within one grid element) by de Rosnay and Polcher (1998).

- Arno scheme for computing surface runoff and drainage (from ECHAM). This has already implemented in the Choisnel scheme by Ducharne et al. (1998). It allows an application of the HD model for computing river discharge from the GCM output.

- Seasonally varying LAI (from SECHIBA).

- Sub-grid scale distribution of the vegetation types should be included, although observational evidence for the advantage of this approach is difficult to demonstrate due to the aforementioned reasons (from SECHIBA). However, some advantageous aspects of the mosaic approach in comparsion to observational data have been shown by de Rosnay and Polcher (1998).

- Snow parameterization and melting criterion from SECHIBA.

Additionally, improved global parameter data sets are needed for LAI, vegetation cover and background albedo, the two latter also with seasonal cycles. These may be provided from measurements by a new generation of satellites which will begin within the next few years (see e. g. Wanner et al. 1997 or Lucht 1998 for the retrieval of high-resolution albedo data sets from satellite observations).

Furthermore, the specification of different soil bucket depths in ECHAM4/IMPL and ECHAM4/SECHIBA was found to lead to differences in the simulated evaporation and, consequently, surface air temperature (e. g. in South America). A comparison with observations revealed biases in the temperature simulation which may be attributed to an underestimated evaporation. Kleidon and Heimann (1998) found that an increase of the ECHAM4 bucket depths in large parts of the tropics reduced the simulated surface air temperature during the dry season, in agreement with observations at certain Brazilian sites. They argued that the existence of 18-meter root depths, which were found in the evergreen forest at the margin of the Amazon basin, may give observational evidence for choosing correspondingly large bucket sizes (or soil water-holding capacities) in the ECHAM4 GCM at these places. This approach appears to be questionable since the bucket concept assumes a homogeneous distribution of roots and available water in the bucket. This assumption may hold for one-meter deep roots in a soil in the extratropics, but it can certainly not represent a soil with 18-meter deep roots in Amazonia.

A more realistic approach is that of de Rosnay and Polcher (1998) who use root profiles, which are known for many vegetation types on the whole globe. This concept is already implicitly included in the Choisnel scheme. The scheme by de Rosnay and Polcher (1998) is also available in combination with the Arno scheme.

Such a model set-up, including the components listed before, would be expected to produce more realistic simulations (after an adjustment to the other GCM components) than the currently operational standard ECHAM4 GCM, while not substantially increasing the degree of complexity of the model or the necessary computer resources.

Further improvement of the model would require significantly more effort. For instance, a more realistic snow parameterization would be desirable, including snow aging and other important processes. These could be represented by a multi-layered snow model, requiring considerably more resources.

Furthermore, to stay compatible with the development of models concerning biogeochemical processes, it appears to be necessary to provide soil hydrological models including several

layers for soil moisture in the future. For instance, the methane emissions from natural wetlands depend significantly on the depth of the soil water table (e. g. Walter et al. 1996). Therefore, accurate soil hydrological models will be a prerequisite for future coupled water–carbon cycle modelling activities.

Finally, this thesis has shown that the accurate representation of land surface processes is essential for realistic climate simulations in GCMs.

Appendix A

Numerical scheme for the vertical diffusion

The turbulent exchange of heat and humidity at the surface and their turbulent vertical transport in the lower atmosphere is described as a diffusive process. The equation for the vertical diffusion which is solved in the ECHAM4 model is:

$$\frac{\partial X(z,t)}{\partial t} = \frac{1}{\rho(z,t)}\frac{\partial}{\partial z}\left(\rho(z,t)K(z,t)\frac{\partial X(z,t)}{\partial z}\right) = \frac{1}{\rho(z,t)}\frac{\partial J_X(z,t)}{\partial z}, \qquad (A.1)$$

where X may be identified with the dry static energy s or the specific humidity q. K is the exchange coefficient and J_X (positive downwards) is the vertical turbulent flux of X. ρ is the air density, t is time and z is the vertical coordinate.

In order to solve (A.1) over the entire atmospheric column, numerical boundary conditions are needed. At the top of the planetary boundary layer a zero flux condition is chosen. At the surface, bulk formulae for the surface sensible and latent heat fluxes as given by (1.3), which take into account the surface properties, are introduced for J_X. Thus, the entire vertical turbulent transport including the surface fluxes can be computed with (A.1). This shows how closely linked the land surface and the vertical diffusion schemes are.

In ECHAM4 (A.1) is solved numerically using a discretization in the vertical and in time. Figure A.1 gives a schematic representation of the vertical discretization. It shall be assumed that the computation is performed from the T–th atmospheric level (top) to the N–th level (bottom). Variables are calculated at full levels (solid lines) and fluxes at intermediate levels (dashed lines). X_S denotes the surface value of X. Equation (A.1) is solved implicitly using a leapfrog time stepping scheme. The computation starts at the previous time step, denoted as $t-1$, when all variables are known. The equation is solved with explicit coefficients, that means that the values of ρ and K at time $t-1$ are used. The system is integrated over a $2\Delta t$ time step ($1\Delta t$ at the first time step), yielding the new values at time $t+1$. The discretization of (A.1) results in the following finite difference scheme for level k ($k = \text{T}, \text{T}+1, \ldots, \text{N}$):

$$\frac{X_k^{t+1} - X_k^{t-1}}{2\Delta t} = \frac{g}{\Delta p_k}\left(\rho_{k+1/2}^{t-1}K_{k+1/2}^{t-1}\frac{X_{k+1}^* - X_k^*}{\Delta z_{k+1/2}} - \rho_{k-1/2}^{t-1}K_{k-1/2}^{t-1}\frac{X_k^* - X_{k-1}^*}{\Delta z_{k-1/2}}\right). \qquad (A.2)$$
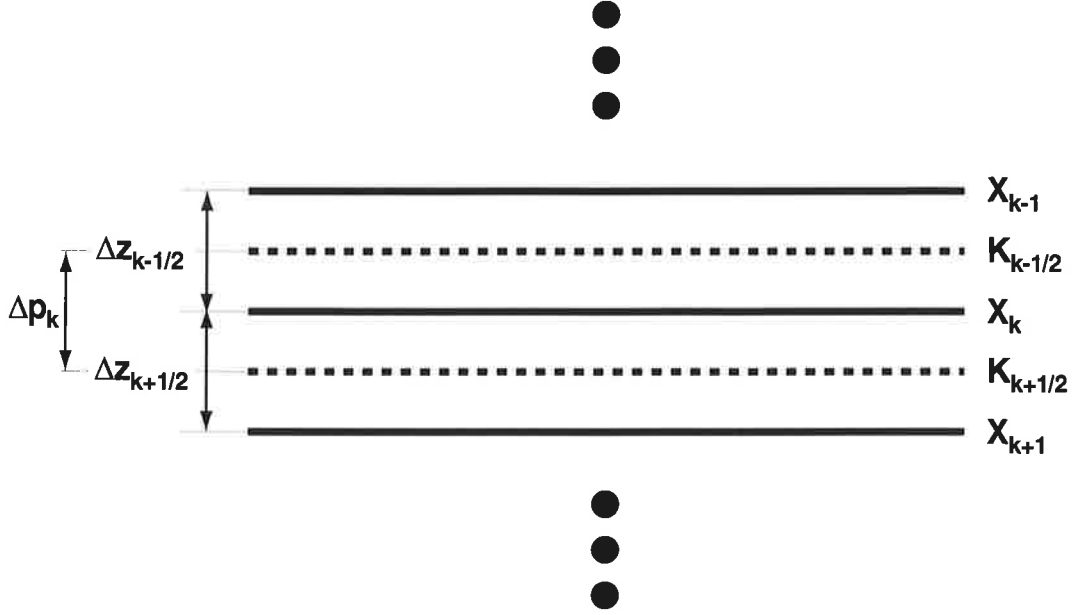
Figure A.1: Schematic representation of the full and intermediate levels used for the discretization of the vertical diffusion equation.

g is the acceleration of gravity of the earth and Δp_k is the pressure difference between two adjacent intermediate levels, both are induced here through the hydrostatic equation. X_k^* is given by

$$X_k^* = \alpha X_k^{t+1} + (1 - \alpha)X_k^{t-1} \qquad \text{with} \qquad \alpha = 1.5\,. \tag{A.3}$$

Equation (A.2) can be written as

$$-\frac{A_{k+1/2}^{t-1}}{\Delta p_k}\frac{X_{k+1}^*}{\alpha} + \left(1 + \frac{A_{k+1/2}^{t-1}}{\Delta p_k} + \frac{A_{k-1/2}^{t-1}}{\Delta p_k}\right)\frac{X_k^*}{\alpha} - \frac{A_{k-1/2}^{t-1}}{\Delta p_k}\frac{X_{k-1}^*}{\alpha} = \frac{X_k^{t-1}}{\alpha}, \tag{A.4}$$

when using the definition

$$A_{k+1/2}^{t-1} := 2\Delta t\;\alpha\;g\;\frac{\rho_{k+1/2}^{t-1}\,K_{k+1/2}^{t-1}}{\Delta z_{k+1/2}}. \tag{A.5}$$

Rewriting of (A.4) leads to

$$-\hat{A}_{k+1/2}^{t-1}\frac{X_{k+1}^*}{\alpha} + \hat{B}_{k+1/2}^{t-1}\frac{X_k^*}{\alpha} - \hat{C}_{k+1/2}^{t-1}\frac{X_{k-1}^*}{\alpha} = \frac{X_k^{t-1}}{\alpha} \tag{A.6}$$

with the coefficients

$$\hat{A}_{k+1/2}^{t-1} = \frac{A_{k+1/2}^{t-1}}{\Delta p_k},$$

$$\hat{B}_{k+1/2}^{t-1} = \left(1 + \frac{A_{k+1/2}^{t-1}}{\Delta p_k} + \frac{A_{k-1/2}^{t-1}}{\Delta p_k}\right),$$

$$\hat{C}^{t-1}_{k+1/2} = \frac{A^{t-1}_{k-1/2}}{\Delta p_k}.$$

This system of equations is solved using an algorithm proposed by Richtmyer and Morton (1967). It allows to reduce the system (A.6) to a set of equations of the form

$$\frac{X^*_k}{\alpha} = E^{t-1}_{k+1/2}\frac{X^*_{k+1}}{\alpha} + F^{t-1}_{k+1/2} \tag{A.7}$$

which can be explicitly solved (see below). The coefficients $E^{t-1}_{k+1/2}$ and $F^{t-1}_{k+1/2}$ are given by

$$E^{t-1}_{k+1/2} = \frac{\hat{A}^{t-1}_{k+1/2}}{\hat{B}^{t-1}_{k+1/2} - \hat{C}^{t-1}_{k+1/2}E^{t-1}_{k-1/2}}, \tag{A.8}$$

$$F^{t-1}_{k+1/2} = \frac{X^{t-1}_k/\alpha + \hat{C}^{t-1}_{k+1/2}F^{t-1}_{k-1/2}}{\hat{B}^{t-1}_{k+1/2} - \hat{C}^{t-1}_{k+1/2}E^{t-1}_{k-1/2}}. \tag{A.9}$$

As the coefficients of (A.2) are explicit, this is also true for (A.4) and (A.6). Therefore, $E^{t-1}_{k+1/2}$ and $F^{t-1}_{k+1/2}$ are calculated at time $t-1$. From these equations together with the zero flux condition at the top (i. e. $\hat{C}_{T+1/2} = 0$), one can calculate the $E_{k+1/2}$ and $F_{k+1/2}$ iteratively from top to bottom of the vertical column, that is in order of increasing k ($k = T, T+1, \ldots, N$). For $k = N$ in (A.7), there is a value for X^*_{N+1} needed. This is the surface value of X. Depending on the type of coupling between land surface scheme and atmosphere, the value at time $t-1$ or $t+1$ will be used (see section 3.1). Using this boundary condition at the bottom, the X^*_k can be calculated iteratively from (A.7) in order of decreasing k ($k = N, N-1, \ldots, T$). This back substitution yields the vertical profile of X at the new time step.

References

Abramopoulos, F., C. Rosenzweig, and B. Choudhury, 1988: Improved ground hydrology calculations for global climate models (GCMs): Soil water movement and evapotranspiration. *J. Climate*, **1**, 921–941.

Barkstrom, B. R., 1984: The Earth Radiation Budget Experiment (ERBE). *Bull. Amer. Meteor. Soc.*, **65**, 1170–1185.

Barkstrom, B. R., E. F. Harrison, and R. B. Lee, 1990: Earth Radiation Budget Experiment, preliminary seasonal results. *Eos, Trans. Amer. Geophys. Union*, **71**, February 27.

Baumgartner, A., and E. Reichel, 1975: *The World Water Balance*. Elsevier, Amsterdam, 179 pp.

Beljaars, A. C. M., and F. C. Bosveld, 1997: Cabauw data for the validation of land surface parameterization schemes. *J. Climate*, **10**, 1172–1193.

Beljaars, A. C. M., and P. Viterbo, 1994: The sensitivity of winter evaporation to the formulation of aerodynamic resistance in the ECMWF model. *Bound.-Layer Meteor.*, **71**, 135–149.

Betts, A. K., J. H. Ball, and A. C. M. Beljaars, 1993: Comparison between the land surface response of the ECMWF model and the FIFE-1987 data. *Quart. J. Roy. Meteor. Soc.*, **119**, 975–1001.

Blondin, C., 1991: Parameterization of land-surface processes in numerical weather prediction. In: Schmugge, T. J., and J. C. André (Eds.), *Land Surface Evaporation: Measurements and Parameterization*, Springer-Verlag, Berlin, 31–54.

Brubaker, K. L., D. Entekhabi, and P. S. Eagleson, 1993: Estimation of continental precipitation recycling. *J. Climate*, **6**, 1077–1089.

Chahine, M. T., 1992: The hydrological cycle and its influence on climate. *Nature*, **359**, 373–380.

Charney, J. G., W. J. Quirk, S.-H. Chow, and J. Kornfield, 1977: A comparative study of the effects of albedo change on drought in semi-arid regions. *J. Atmos. Sci.*, **34**, 1366–1385.

Chen, T. H., A. Henderson-Sellers, P. C. D. Milly, A. J. Pitman, A. C. M. Beljaars, J. Polcher, F. Abramopoulos, A. Boone, S. Chang, F. Chen, Y. Dai, C. E. Desborough, R. E. Dickinson, L. Dümenil, M. Ek, J. R. Garratt, N. Gedney, Y. M. Gusev, J. Kim, R. Koster, E. Kowalczyk, K. Laval, J. Lean, D. Lettenmaier, X. Liang, J.-F. Mahfouf, H.-T. Mengelkamp, K. Mitchell, O. N. Nasonova, J. Noilhan, A. Robock, C. Rosenzweig, J. Schaake, C. A. Schlosser, J.-P. Schulz, Y. Shao, A. B. Shmakin, D. L. Verseghy, P. Wetzel, E. F. Wood, Y. Xue, Z.-L. Yang,

and Q. Zeng, 1997: Cabauw experimental results from the Project for Intercomparison of Land-surface Parameterization Schemes. *J. Climate*, **10**, 1194–1215.

Choisnel, E., 1977: Le bilan d'énergie et le bilan hydrique du sol. *La Météorologie*, **VI**, **11**, 103–133.

Claussen, M., U. Lohmann, E. Roeckner, and U. Schulzweida, 1994: A global data set of land-surface parameters. *Max-Planck-Institut für Meteorologie*, Rep. 135, Hamburg, 35 pp.

Deardorff, J. W., 1978: Efficient prediction of ground surface temperature and moisture, with inclusion of a layer of vegetation. *J. Geophys. Res.*, **83**, 1889–1903.

Dickinson, R. E., and A. Henderson-Sellers, 1988: Modelling tropical deforestation: A study of GCM land-surface parameterizations. *Quart. J. Roy. Meteor. Soc.*, **114**, 439–462.

Dickinson, R. E., A. Henderson-Sellers, P. J. Kennedy, and M. F. Wilson, 1986: Biosphere–Atmosphere Transfer Scheme (BATS) for the NCAR Community Climate Model. *National Center for Atmospheric Research*, Tech. Note NCAR/TN-275+STR, Boulder, 69 pp.

Dooge, J. C. I., M. Bruen, and A. Dowley, 1994: Spatial variability of land surface processes. *Centre for Water Resources Research*, Rep. LSP/94/19, University College Dublin, 145 pp.

Dorman, J. L., and P. J. Sellers, 1989: A global climatology of albedo, roughness length and stomatal resistance for atmospheric general circulation models as represented by the Simple Biosphere model (SiB). *J. Appl. Meteor.*, **28**, 833–855.

Douville, H., J.-F. Royer, and J.-F. Mahfouf, 1995: A new snow parameterization for the Météo-France climate model. Part II: Validation in a 3-D GCM experiment. *Climate Dyn.*, **12**, 37–52.

Driedonks, A. G. M., H. van Dop, and W. Kohsiek, 1978: Meteorological observations on the 213 m mast at Cabauw in the Netherlands. *Proc. Fourth Symp. Meteor. Observ. and Instrum.*, Denver, Amer. Meteor. Soc., 41–46.

Ducharne, A., K. Lavel, and J. Polcher, 1998: Sensitivity of the hydrological cycle to the parametrization of soil hydrology in a GCM. *Climate Dyn.*, **14**, 307–327.

Ducoudré, N. I., K. Laval, and A. Perrier, 1993: SECHIBA, a new set of parameterizations of the hydrologic exchanges at the land–atmosphere interface within the LMD atmospheric general circulation model. *J. Climate*, **6**, 248–273.

Dümenil, L., and H.-S. Bauer, 1998: The tropical easterly jet in a hierarchy of GCMs and in reanalyses. *Climate Dyn.*, submitted. [Also: *Max-Planck-Institut für Meteorologie*, 1998, Rep. 247, Hamburg, 45 pp.]

Dümenil, L., and E. Todini, 1992: A rainfall-runoff scheme for use in the Hamburg climate model. In: O'Kane, J. P. (Ed.), *Advances in Theoretical Hydrology: A Tribute to James Dooge*, European Geophysical Society Series on Hydrological Sciences, **1**, Elsevier Science Publishers, Amsterdam, 129–157.

Dümenil, L., K. Isele, H.-J. Liebscher, U. Schröder, M. Schumacher, and K. Wilke, 1993: Discharge data from 50 selected rivers for GCM validation. *Max-Planck-Institut für Meteorologie*, Rep. 100, Hamburg.

Foster, D. J., and R. D. Davy, 1988: Global snow depth climatology. *USAF Environmental Technical Applications Center*, USAFETAC/TN-88/006, Scott Air Force Base, Illinois, 48 pp.

Gadgil, S., S. Sajani, and participating modelling groups of AMIP, 1997: Monsoon precipitation in the AMIP runs. Draft report of results from an AMIP diagnostic subproject, *Climate Dyn.*, submitted. [Also: *Centre for Atmospheric and Oceanic Sciences*, Indian Institute of Science, Bangalore.

Garratt, J. R., 1993: Sensitivity of climate simulations to land-surface and atmospheric boundary-layer treatments – a review. *J. Climate*, **6**, 419–449.

Gates, W. L., 1992: AMIP: The Atmospheric Model Intercomparison Project. *Bull. Amer. Meteor. Soc.*, **73**, 1962–1970.

Gibson, J. K., P. Kallberg, S. Uppala, A. Hernandez, A. Nomura, and E. Serrano, 1997: The ECMWF Re-Analysis (ERA). 1. ERA description. *European Centre for Medium-Range Weather Forecasts*, ECMWF Re-Analysis Project Report Series No. 1, Reading, 71 pp.

Hagemann, S., 1998: Entwicklung einer Parameterisierung des lateralen Abflusses für Landflächen auf der globalen Skala. PhD thesis, *Max-Planck-Institut für Meteorologie*, Examensarbeit 52, Hamburg, 121 pp.

Hagemann, S., and L. Dümenil, 1998: A parametrization of the lateral waterflow for the global scale. *Climate Dyn.*, **14**, 17–31.

Henderson-Sellers, A., Z.-L. Yang, and R. E. Dickinson, 1993: The Project for Intercomparison of Land-surface Parameterization Schemes (PILPS). *Bull. Amer. Meteor. Soc.*, **74**, 1335–1349.

Henderson-Sellers, A., K. McGuffie, and A. J. Pitman, 1996: The Project for Intercomparison of Land-Surface Parameterization Schemes (PILPS): 1992 to 1995. *Climate Dyn.*, **12**, 849–859.

Henning, D., 1989: *Atlas of the Surface Heat Balance of the Continents.* Gebrüder Borntraeger, Berlin.

Hillel, D., 1982: *Introduction to Soil Physics.* Academic Press, 364 pp.

Huffman, G. J., R. F. Adler, B. Rudolf, U. Schneider, and P. R. Keehn, 1995: Global precipitation estimates based on a technique for combining satellite-based estimates, rain gauge analysis, and NWP model precipitation information. *J. Climate*, **8**, 1284–1295.

IPCC, 1996: Climate change 1995 – The science of climate change. *Intergovernmental Panel on Climate Change*, Contribution of Working Group I to the Second Assessment Report, Houghton, J. T., L. G. Meira Filho, B. A. Callander, N. Harris, A. Kattenberg, and K. Maskell (Eds.), WMO-UNEP, Cambridge University Press, 572 pp.

Kalnay, E., M. Kanamitsu, R. Kistler, W. Collins, D. Deaven, L. Gandin, M. Iredell, S. Saha, G. White, J. Woollen, Y. Zhu, M. Chelliah, W. Ebisuzaki, W. Higgins, J. Janowiak, K. C. Mo, C. Ropelewski, J. Wang, A. Leetmaa, R. Reynolds, R. Jenne, and D. Joseph, 1996: The NCEP/NCAR 40-year reanalyses project. *Bull. Am. Meteor. Soc.*, **77**, 437–471.

Kleidon, A., and M. Heimann, 1998: The effect of deep rooted vegetation on the simulated climate of an atmospheric general circulation model. Part I: Mechanism and comparison to observations. *Climate Dyn.*, submitted. [Also: *Max-Planck-Institut für Meteorologie*, 1998, Rep. 249, Hamburg, 25 pp.]

Koster, R. D., and M. J. Suarez, 1992: Modeling the land surface boundary in climate models as a composite of independent vegetation stands. *J. Geophys. Res.*, **97**, 2697–2715.

Koster, R. D., J. Jouzel, R. Suozzo, G. Russell, W. Broecker, D. Rind, and P. Eagleson, 1986: Global sources of local precipitation as determined by the NASA/GISS GCM. *Geophys. Res. Lett.*, **13**, 121–124.

Lean, J., and D. A. Warrilow, 1989: Simulation of the regional climatic impact of Amazon deforestation. *Nature*, **342**, 411–413.

Legates, D. R., and C. J. Willmott, 1990: Mean seasonal and spatial variability in global surface air temperature. *Theor. Appl. Climatol.*, **41**, 11–21.

Lohmann, U., 1996: Sensitivität des Modellklimas eines globalen Zirkulationsmodells der Atmosphäre gegenüber Änderungen der Wolkenmikrophysik. PhD thesis, *Max-Planck-Institut für Meteorologie*, Examensarbeit 41, Hamburg, 143 pp.

Lohmann, U., and E. Roeckner, 1994: The influence of cirrus cloud-radiative forcing on climate and climate sensitivity in a general circulation model. *Max-Planck-Institut für Meteorologie*, Rep. 126, Hamburg, 48 pp.

Loth, B., and H. F. Graf, 1998: Modelling the snow cover for climate studies. Part I: Long-term integrations under different climatic conditions using a multi-layered snow-cover model. *J. Geophys. Res.*, accepted. [Also: *Max-Planck-Institut für Meteorologie*, 1996, Rep. 190, Hamburg, 30 pp.]

Louis, J.-F., 1979: A parametric model of vertical eddy fluxes in the atmosphere. *Bound.-Layer Meteor.*, **17**, 187–202.

Lucht, W., 1998: Expected retrieval accuracies of bidirectional reflectance and albedo from EOS-MODIS and MISR angular sampling. *J. Geophys. Res.*, **103**, 8763–8778.

Manabe, S., 1969: Climate and the ocean circulation. I. The atmospheric circulation and the hydrology of the earth's surface. *Mon. Wea. Rev.*, **97**, 739–774.

Matthews, E., 1985: Atlas of archived vegetation, land-use and seasonal albedo data sets. *NASA*, Tech. Memo. 86199.

Meeson, B. W., F. E. Corprew, J. M. P. McManus, D. M. Myers, J. W. Closs, K.-J. Sun, D. J. Sunday, and P. J. Sellers, 1995: ISLSCP Initiative I – global data sets for land-atmosphere models, 1987–1988. *NASA*, CD-ROM, vol. 1-5.

Milly, P. C. D., and K. A. Dunne, 1994: Sensitivity of the global water cycle to the water-holding capacity of land. *J. Climate*, **7**, 506–526.

Mintz, Y., 1984: The sensitivity of numerically simulated climates to land-surface boundary conditions. In: Houghton, J. T. (Ed.), *The Global Climate*, Cambridge University Press, 79–105.

Noilhan, J., and S. Planton, 1989: A simple parameterization of land surface processes for meteorological models. *Mon. Wea. Rev.*, **117**, 536–549.

Olson, J. S., J. A. Watts, and L. J. Allison, 1983: Carbon in live vegetation of major world ecosystems. *Oak Ridge National Laboratory*, ORNL-5862, Oak Ridge.

Patterson, K. A., 1990: Global distributions of total and total-available soil water-holding capacities. M. S. thesis, Dept. of Geography, University of Delaware, 119 pp.

Peylin, P., J. Polcher, G. Bonan, D. L. Williamson, and K. Laval, 1997: Comparison of two complex land surface schemes coupled to the National Center for Atmospheric Research general circulation model. *J. Geophys. Res.*, **102**, 19413–19431.

Polcher, J., 1995: Sensitivity of tropical convection to land surface processes. *J. Atmos. Sci.*, **52**, 3143–3161.

Polcher, J., and K. Laval, 1994: The impact of African and Amazonian deforestation on tropical climate. *J. Hydrol.*, **155**, 389–405.

Polcher, J., K. Laval, L. Dümenil, J. Lean, and P. R. Rowntree, 1996: Comparing three land surface schemes used in general circulation models. *J. Hydrol.*, **180**, 373–394.

Polcher, J., B. McAvaney, P. Viterbo, M.-A. Gaertner, A. Hahmann, J.-F. Mahfouf, J. Noilhan, T. Phillips, A. Pitman, C. A. Schlosser, J.-P. Schulz, B. Timbal, D. L. Verseghy, and Y. Xue, 1998a: A proposal for a general interface between land-surface schemes and general circulation models. *Global Planet. Change*, submitted.

Polcher, J., J. Crossley, C. Bunton, H. Douville, N. Gedney, K. Laval, S. Planton, P. R. Rowntree, and P. Valdes, 1998b: Importance of land-surface processes for the uncertainties of climate change: A European project. *GEWEX News*, International GEWEX Project Office, World Climate Research Programme, **8**, No. 2, 11–13.

Richtmyer, R. D., and K. W. Morton, 1967: *Difference methods for initial-value problems.* 2nd ed., Interscience Publishers (John Wiley & Sons), New York.

Roeckner, E., K. Arpe, L. Bengtsson, S. Brinkop, L. Dümenil, M. Esch, E. Kirk, F. Lunkeit, M. Ponater, B. Rockel, R. Sausen, U. Schlese, S. Schubert, M. Windelband, 1992: Simulation of the present-day climate with the ECHAM model: Impact of model physics and resolution. *Max-Planck-Institut für Meteorologie*, Rep. 93, Hamburg, 171 pp.

Roeckner, E., K. Arpe, L. Bengtsson, M. Christoph, M. Claussen, L. Dümenil, M. Esch, M. Giorgetta, U. Schlese, U. Schulzweida, 1996: The atmospheric general circulation model ECHAM4: Model description and simulation of present-day climate. *Max-Planck-Institut für Meteorologie*, Rep. 218, Hamburg, 90 pp.

de Rosnay, P., and J. Polcher, 1998: Modeling root water uptake in a complex land surface scheme coupled to a GCM. *Hydrol. Earth Sys. Sci.*, accepted.

Rossow, W. B., and L. C. Garder, 1993: Cloud detection using satellite measurements of infrared and visible radiances for ISCCP. *J. Climate*, **6**, 2341–2369.

Rossow, W. B., and R. A. Schiffer, 1991: ISCCP cloud data products. *Bull. Amer. Meteor. Soc.*, **72**, 2–20.

Rossow, W. B., A. W. Walker, and L. C. Garder, 1993: Comparison of ISCCP and other cloud amounts. *J. Climate*, **6**, 2394–2418.

Rudolf, B., H. Hauschild, W. Rüth, and U. Schneider, 1996: Comparison of raingauge analyses, satellite-based precipitation estimates and forecast model results. *Adv. Space Res.*, **7**, 53–62.

Russell, G., 1980: Crop evaporation, surface resistance and soil water status. *Agric. Meteor.*, **21**, 213–226.

Sato, N., P. J. Sellers, D. A. Randall, E. K. Schneider, J. Shukla, J. L. Kinter III, Y.-T. Hou, and E. Albertazzi, 1989: Effects of implementing the Simple Biosphere model in a general circulation model. *J. Atmos. Sci.*, **46**, 2757–2782.

Schulz, J.-P., L. Dümenil, J. Polcher, C. A. Schlosser, Y. Xue, 1998: Land surface energy and moisture fluxes: Comparing three models. *J. Appl. Meteor.*, **37**, 288–307.

Sellers, P. J., Y. Mintz, Y. C. Sud, and A. Dalcher, 1986: A Simple Biosphere Model (SiB) for use within general circulation models. *J. Atmos. Sci.*, **43**, 505–531.

Shukla, J., and Y. Mintz, 1982: Influence of land-surface evapotranspiration on the earth's climate. *Science*, **215**, 1498–1501.

Shukla, J., C. Nobre, and P. J. Sellers, 1990: Amazon deforestation and climate change. *Science*, **247**, 1322–1325.

Stamm, J. F., E. F. Wood, and D. P. Lettenmaier, 1994: Sensitivity of a GCM simulation of global climate to the representation of land-surface hydrology. *J. Climate*, **7**, 1218–1239.

Stendel, M., and K. Arpe, 1997: Evaluation of the hydrological cycle in reanalyses and observations. *Max-Planck-Institut für Meteorologie*, Rep. 228, Hamburg, 52 pp.

Stull, R. B., 1997: *An Introduction to Boundary Layer Meteorology.* Kluwer Academic Publishers, Dordrecht, 670 pp.

Sud, Y. C., J. Shukla, and Y. Mintz, 1988: Influence of land surface roughness on atmospheric circulation and precipitation: A sensitivity study with a general circulation model. *J. Appl. Meteor.*, **27**, 1036–1054.

Verseghy, D. L., 1991: CLASS – a Canadian land surface scheme for GCMS. I. Soil model. *Int. J. Climatol.*, **11**, 111–133.

Verseghy, D. L., N. A. McFarlane, and M. Lazare, 1993: CLASS – a Canadian land surface scheme for GCMS, II. Vegetation model and coupled runs. *Int. J. Climatol.*, **13**, 347–370.

Viterbo, P., and A. C. M. Beljaars, 1995: An improved land surface parameterization scheme in the ECMWF model and its validation. *J. Climate*, **8**, 2716–2748.

Walter, B. P., M. Heimann, R. D. Shannon, J. R. White, 1996: A process-based model to derive methane emissions from natural wetlands. *Geophys. Res. Lett.*, **23**, 3731–3734.

Wanner, W., A. H. Strahler, B. Hu, P. Lewis, J.-P. Muller, X. Li, C. L. Barker Schaaf, and M. J. Barnsley, 1997: Global retrieval of bidirectional reflectance and albedo over land from EOS MODIS and MISR data: theory and algorithm. *J. Geophys. Res.*, **102**, 17143–17162.

Warrilow, D. A., A. B. Sangster, and A. Slingo, 1986: Modelling of land surface processes and their influence on European climate. *Meteorological Office*, Met O 20 Tech. Note DCTN 38, Bracknell, 92 pp.

Webster, P. J., 1987: The elementary monsoon. In: Fein, J. S., and P. L. Stephens (Eds.), *Monsoons*, Wiley Intersciences Publications, New York, 3–32.

Wild, M., L. Dümenil, and J.-P. Schulz, 1996: Regional climate simulation with a high resolution GCM: surface hydrology. *Climate Dyn.*, **12**, 755–774.

WMO/ICSU, 1990: The Global Precipitation Climatology Project – Implementation and data management plan. *World Meteorological Organization*, WMO/TD 367, Geneva, 45 pp. and 6 appendices.

Wood, E. F., D. P. Lettenmaier, and V. G. Zartarian, 1992: A land-surface hydrology parameterization with subgrid scale variability for general circulation models. *J. Geophys. Res.*, **97**, 2717–2728.

Xue, Y., and J. Shukla, 1993: The influence of land surface properties on Sahel climate. Part I: Desertification. *J. Climate*, **6**, 2232–2245.

Xue, Y., P. J. Sellers, J. L. Kinter, and J. Shukla, 1991: A simplified biosphere model for global climate studies. *J. Climate*, 4, 345–364.

Xue, Y., F. J. Zeng, and C. A. Schlosser, 1996: SSiB and its sensitivity to soil properties – a case study using HAPEX-Mobilhy data. *Global Planet. Change*, **13**, 183–194.

Acknowledgments